



Provided by the author(s) and University of Galway in accordance with publisher policies. Please cite the published version when available.

Title	Space based observations of marine phytoplankton in NE Atlantic waters
Author(s)	Jordan, Catherine
Publication Date	2024-04-11
Publisher	NUI Galway
Item record	http://hdl.handle.net/10379/18143

Downloaded 2024-05-02T14:48:29Z

Some rights reserved. For more information, please see the item record link above.





OLLSCOIL NA GAILLIMHÉ
UNIVERSITY OF GALWAY

Space based observations of marine phytoplankton in NE Atlantic waters

by Catherine Jordan M.Sc. B.Sc.

Thesis submitted to the University of Galway for the Degree of
Doctor of Philosophy

June 2023

Department of Earth and Ocean Science

School of Natural Sciences

University of Galway

Supervisors: Professor Peter Croot and Dr Caroline Cusack

Head of Department: Dr Tiernan Henry



Marine Institute
Foras na Mara

Table of Contents

List of Figures	v
List of Tables	vii
Declaration	viii
Funding	ix
Acknowledgements	x
General Abstract	xiii
1. General Introduction	1
1.1.1 Phytoplankton	1
1.1.2 Aquaculture.....	5
1.1.3 Climate change	5
1.1.4 Phytoplankton Functional Types	7
1.1.5 Harmful Algae in Irish Waters.....	7
1.1.6 Fundamentals of Ocean Colour	8
1.1.7 Colour Producing Agents or Optically Active Constituents.....	10
1.1.8 Case 1 and Case 2 waters.....	10
1.1.9 Phytoplankton/Chlorophyll absorption.....	12
1.1.10 CDOM absorption.....	13
1.1.11 Suspended Sediments	14
1.1.12 Remote Sensing	15
1.1.13 Ocean Colour Sensors.....	15
1.1.14 Chlorophyll Algorithms	16
1.1.15 HABS from Ocean Colour.....	18
1.1.16 Deriving fluorescence from Remote Sensing	20
1.1.17 Attenuation Coefficient and K_d (490) Algorithm.....	20
1.1.18 Importance of Validation	21
1.2 Chapter Summary.....	24
2. Chapter 2:.....	26
<i>In situ</i> Attenuation Coefficient and Satellite Derived K_d (490) in Irish Coastal and Oceanic Waters	26
2.1 Abstract	26
2.2 Introduction	27
2.2.1 Phytoplankton Absorption	28
2.2.2 Water absorption	28

2.2.3	CDOM absorption	29
2.2.4	Remote sensing	29
2.3	Material and Methods.....	32
2.3.1	Study Area.....	32
2.3.2	Attenuation Coefficient.....	33
2.3.3	Satellite Data	34
2.4	Results	35
2.5	Discussion	45
2.6	Conclusions	49
3.	Chapter 3:.....	51
	Documenting a Continuous and Autonomous Above-Water Hyperspectral Radiometry System on a Research Vessel in the NE Atlantic	51
3.1	Abstract	51
3.2	Introduction	53
3.2.1	Ocean Colour	53
3.2.2	Satellite Validation.....	53
3.2.3	Hyperspectral Radiometers	54
3.2.4	Data Management Quality Management Framework (DM-QMF).....	57
3.2.5	Objectives of this Chapter.....	59
3.3	Methods	59
3.3.1	Study Area.....	59
3.3.2	TriOS RAMSES Hyperspectral Radiometer System On Board The RV Celtic Explorer.....	59
3.3.3	Process Flow	61
3.3.4	Satellite Data Match Up.....	63
3.3.5	<i>In situ</i> Chlorophyll Analysis	64
3.3.6	Statistical Analysis	64
3.3.7	Marine Institute Data Management Quality Management Framework (DM-QMF)	65
3.3.8	Data Catalogue	65
3.3.9	Digital Objective Identifier	66
3.3.10	Performance Evaluation	66
3.3.11	Celtic Explorer	67
3.4	Results	68
3.5	Discussion	70
3.6	Conclusion.....	77

4. Chapter 4:.....	78
Using the Red Band Difference Algorithm to Detect and Monitor a <i>Karenia</i> spp. Bloom Off the South Coast of Ireland, June 2019	78
4.1 Abstract	78
4.2 Introduction	79
4.2.1 Objectives of this Study	83
4.3 Materials and Methods	84
4.3.1 Study Area.....	84
4.3.2 Satellite Imagery	85
4.3.3 Lagrangian Particle Tracking.....	86
4.3.4 <i>In situ</i> Data	87
4.4 Results	88
4.5 Discussion	94
4.6 Conclusion.....	99
5. Chapter 5:.....	101
Combining Satellite Imagery and the HABscope in Irish waters	101
5.1 Abstract	101
5.2 Introduction	102
5.3 Methods	104
5.3.1 Phytoplankton Research Surveys CV21015 and CV21021	104
5.3.2 Red Band Difference Satellite imagery.....	104
5.3.3 HABscope	105
5.4 Results	106
5.5 Discussion	110
6. Summary Chapter	115
6.1 Summary of thesis	115
6.1.1 Chapter 2	116
6.1.2 Chapter 3	117
6.1.3 Chapter 4	119
6.1.4 Chapter 5	120
6.2 Summary of products available from this PhD	121
6.3 Future Studies.....	121
7. References.....	123
Appendices	141
Appendix A1. Matlab Scripts	141

Appendix A2. Data Management Plan Checklist.....	190
Appendix A3. Hyperspectral Radiometer Software Set Up.....	193
Appendix A4. Requirements and Acceptance Criteria.....	197
Appendix A5. Daily RBD image for the 27th June 2019.....	200
Appendix A6. Full Species count lists for Cork, Oysterhaven and Kinsale	201
Appendix A7. Phytoplankton counts from CV19018	213
Appendix A8. RBD values V Surface Cell counts.....	223
Appendix A9. HABscope conversion chart	224
Appendix A10. Communication of PhD thesis to the public	225

List of Figures

Figure 1 Diagram illustrating all the elements involved in phytoplankton blooms along with seasonal trends. Source online: https://slideplayer.com/slide/15767305/	4
Figure 2 Diagram illustrating the wavelengths of light interacting with different properties at or just below the ocean surface, which shapes the surface reflectance. Online Source: https://seos-project.eu/oceancolour/oceancolour-c01-p02.html	9
Figure 3 An example of light absorption spectra for marine algal pigments. Much of the visible spectrum is utilised by different pigments at different wavelengths. Copyright Yarish et al. (2012).	13
Figure 4 An example of the mean relative contributions of Detritus, Phytoplankton, CDOM, and Water to total light absorption at wavelengths between 300 and 700 nm for the NAAMES dataset. Copyright Allen et al. (2020).....	14
Figure 5 The difference between a multispectral ocean colour sensor (VIIRS) capabilities beside the future PACE OLI hyperspectral satellite for identifying HABs. Source: https://pace.oceansciences.org/about.htm	19
Figure 6 Study area broken into three sections: stations from CE19009 and CV18012; Aran Grounds and Western Irish Sea (WIS).....	32
Figure 7 (A) TriOS RAMSES irradiance sensor inside frame (B) Sensor being deployed off the ship.....	34
Figure 8 In situ Kd490nm values for CV18012 and CE19009 research surveys	36
Figure 9 In situ chlorophyll surface values for all stations sampled during CE19009 (May 24th June 6th 2019)	36
Figure 10 Examples of in situ attenuation coefficient plots generated at CV18012: Aran grounds, Stratified and Mixed water stations and open water CE19009 with error bars.....	38
Figure 11 (A) Daily satellite derived Kd490 data from dates during CV18012. (B) Daily satellite derived Kd490 data from dates during CE19009	39
Figure 12 (A) Monthly satellite derived Kd490 average data from dates during CV18012. (B) Monthly satellite derived Kd490 average data from dates during CE19009.....	40
Figure 13 Monthly climatology averages for Kd(490) from January to November (1999 - 2019).....	42

Figure 14 Monthly climatology averages for Chlorophyll from January to November (1999 - 2019).....	43
Figure 15 (A) Full year percentage data coverage generated between 1997 and 2019. (B) July percentage data coverage generated between 1997 and 2019. (C) December percentage data coverage generated between 1997 and 2019.....	44
Figure 16 (A) A TriOS RAMSES-ACC hyperspectral cosine irradiance meter for $E_s(\lambda)$ downwelling solar irradiance and 2 TriOS RAMSES ARC hyperspectral radiance meters; 1 for measuring radiance $L_{sfc}(\theta_{sfc}, \Phi_{Sun}, \lambda)$ emerging from the sea surface and 1 for measuring sky leaving radiance $L_{sky}(\theta_{sky}, \Phi_{Sun}, \lambda)$ on the port side of the vessel (B) 2 TriOS RAMSES ARC hyperspectral radiance meters; 1 for measuring radiance $L_{sfc}(\theta_{sfc}, \Phi_{Sun}, \lambda)$ emerging from the sea surface and 1 for measuring sky leaving radiance $L_{sky}(\theta_{sky}, \Phi_{Sun}, \lambda)$ (C) RV Celtic Explorer with an arrow pointing to the platform the sensors are mounted on, above the bridge (D) a screen grab of the TriOS Ramses software MSDA_XE where the sensors are controlled from.	61
Figure 17 Process Flow that visually describes the steps from Manufacturer calibration to Rrs Data output.	62
Figure 18 Detailed process flow describing each data processing step from accessing the raw data to the final data	63
Figure 19 A screen grab from the data catalogue from www.data.marine.ie	66
Figure 20 Track paths of the RV Celtic Explorer during 2019, 16 research surveys were conducted during this year covering a total of 42,147 nautical miles over the course of 320 days.....	67
Figure 21 (A) Stations from both CE19009 and CE19010 research survey (B) Stations that were compared with satellite derived data	68
Figure 22 Remote Sensing Reflectance Plots from CE19010 ST03,32,43,60 and CE19009 ST26, 35	70
Figure 23 Linear Regression plots between ESA-CCI CMEMS derived Rrs value and above-water radiometry values (A) 443 nm, (B) 490 nm, (C) 510 nm and (D) 560 nm	71
Figure 24 (A) Map of study area in the Celtic Sea. (B) In situ sample locations are noted as points and the polygon location for the particle tracking model is outlined by the black line. Bathymetry is represented in metres.	85
Figure 25 Sentinel-3a OLCI images with RBD algorithm displaying the phytoplankton bloom progression between 29th May 2019 and 23rd July 2019 (A–H). Colours	

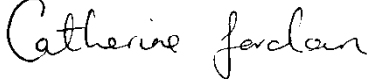
indicate relative fluorescence, with warmer colours representing higher fluorescence indicative of higher bloom concentration.	89
Figure 26 OC5 IFREMER Level 4 Chlorophyll a data from the HAB bulletin weeks 24–28 (A–F) 4th June 2019 to 8th July 2019.....	90
Figure 27 Particle tracking model simulation results display current driven bloom dispersal on the left (A–D). Maps show the density distribution of particles on 08/06/2019, 15/06/2019, 22/06/2019, and 29/06/2019 compared with Sentinel-3a OLCI images with RBD weekly composites on the right (E-H).	91
Figure 28 In situ <i>Karenia</i> spp. cells/L counts for inshore stations in Cork Harbour, Oysterhaven, and Kinsale from the national monitoring programme June–August 2019.....	92
Figure 29 Sentinel-3a OLCI image with RBD algorithm from 10 July 2019. The red circles indicate cell concentrations determined using light microscopy for in situ samples collected on CV19018 on the same date. The grey colour in the image represents cloud cover.....	93
Figure 30 Coastal currents (red) and the Shelf Edge Current (green) adapted from Hill et al. (2008)	97
Figure 31 Stations from CV21015 and CV21021	104
Figure 32 HABscope set up on research survey CV21015.....	106
Figure 33 Red Band Difference satellite imagery from the weeks research surveys CV21015 (A) and CV21021 (B) took place	107
Figure 34 Screen grab from a HABscope video demonstrating two cells identified using the neural network programme trained to recognise <i>Karenia</i> spp. cells.....	108
Figure 35 A bubble map of <i>K. mikimotoi</i> in situ microscope results overlaid onto RBD satellite imagery during CV21021 survey dates	109
Figure 36 Screen grab from the HABscope to illustrate a mixed assemblage of phytoplankton species and the neural network technology identifying <i>Karenia</i> spp. amongst other species	109

List of Tables

Table 1 Statistics Summary Table.....	72
---------------------------------------	----

Declaration

I, Catherine Jordan, certify this thesis is my own research and any work presented within this thesis has not been used to obtain a degree elsewhere.

Signed: 

Date: 27/06/2023

Funding

This project (Grant-aid Agreement No. CF/17/03/01) was carried out with the support of the Marine Institute and funded under the Marine Research Programme by the Irish Government.



Further funding for travel to Oldenburg (Germany), NOAA (USA) and NASA (USA) was provided by the Marine Institute Networking and Travel Grants and a Ryan Institute travel grant.

Acknowledgements

Firstly, I would like to thank my *exceptional* supervisors Professor Peter Croot and Dr Caroline Cusack. I could not have completed this PhD without you both supporting me along the way. The blend of both your supervision styles helped me get this thesis finished, granted having your PhD student have babies along the way may not have been your idea of the ideal student but you both helped me incorporate real life in with the mountain of carrying out a PhD thesis. Thank you both for being so understanding, supportive and compassionate to my journey.

To Peter, thank you for believing in me from day 1, for creating an environment within the team that welcomes ideas and questions, I always felt safe asking for help with any Matlab, writing etc. problem without feeling like I should know it all by now. Thank you for all the opportunities you sent my way, I am grateful for all the time at sea and trips to Germany and the US and for supporting my application to get on a once in a lifetime tip to NASA.

To Caroline thank you for all the support you have provided along the way. I always felt comfortable to reach out to you with any problem. Thank you for the space on your research surveys. Thank you for helping me get to NOAA for a month in 2019, this was the highlight of my whole PhD. Thank you for the endless advice you provided me with and for assuring me reviewers comments are not personal ☺. Thank you for all the meetings, especially in lockdown and keeping me on the straight and narrow during a difficult time for everyone.

You have both taught me so much and instilled a lot of confidence in me as a scientist that I will take forward with me throughout my career.

A big big thank you to my GRC committee: Dagmar Stengel, Joe Silke and Anthony Grehan, I thoroughly enjoyed meeting with you all each year and discussing the progress of this project and appreciate all your helpful advice and suggestions.

Thank you to The Marine Institute for funding this project and for all the travel grants along the way. Thank you to the Ryan Institute travel grant for supporting my trip to NOAA in 2019

A big thank you to all the Celtic Explorer and Celtic Voyager staff that have helped in any way to do with sampling for this PhD, especially the P&O staff who have helped with the hyperspectral radiometers especially, Liam, Clynt, Anthony, Ian, Lukasz, Darragh and others.

To all the EOS and Ryan Institute staff and postgrads who have helped me with data collection, advice or been there along the way for coffee or nights out, to Sheena, Aedin, Clynt, Dave, Eoghan, Sonny, Nadeeka, Martin, Bebhinn, Jess, Sean, Aisling, Megan, Sophie, Tom, Ana, Oisin, Ryan, Ruaihri and Leigh and a special thanks to Aidan for invaluable formatting advice and to my original office PhD buddies Monica and Alina, thank you for everything.

A special thanks goes to Shelly Tomlinson at NOAA. Shelly thank you for all your help and advice along the way, from welcoming me to your office in Silverspring for a month in 2019 to being at the end of an email every time I needed advice thank you! Also, a big thank you to Rick, Chris, Andrew and all the team at NOAA, whether it was the RBD algorithm, the HABscope or general advice, thank you all for sharing your ideas with us in Ireland and hopefully we can all continue to work together in the future.

Thank you to all the team in Oldenburg for the advice on setting up the radiometers, especially Jochen, thank you for your guidance on instrument set up, data processing and much much more.

A massive thank you to all the MI data team who have helped get the DM-QMF pack up and running, a special thanks to Ramona and Rob for the endless meetings and advice.

A big thanks to the Phytoplankton team at the MI for taking me in for a month to let me use your lab and ever since for all the data from the monitoring programme.

And a big thank you to Diego and Joe from the OCIS team in the MI for their satellite help!

Doing a PhD is a privilege, I would not be here without my family's support.

To Anne and Michael and all the O'Neills, thank you for *alllll* the babysitting and support you have given us over the years. I would not be in a position to finish this thesis without ye. Thank you for everything, Sophia and Georgia (and us) are extremely lucky to have ye.

Thank you to my brother Michael for everything, the real academic in our house. Thank you for everything from my undergrad, to my masters and finally my PhD. All the proof reading, advice and reassurance has been invaluable. I promise this is the last thesis I will do ☺.

To my Mum and Dad, there aren't enough thank yous for everything. I was 7 years old when I told you I wanted to be a marine scientist (well, this dream started off as a dolphin trainer first), you have both helped nurture my passion every day since, you have always encouraged myself and Michael to always follow our dreams and have always supported us to do so. Never in my wildest dreams did I think I would get to this stage of a completed PhD thesis. Mum a special thank you for driving me on when I could have easily given up after becoming a mother. Thank you for the endless days minding the girls and all the support. I definitely wouldn't have a completed thesis without you so I cannot thank you enough.

Donal, Thank you for everything. When I started this PhD you were my fiancé, I am ending it with you as my husband and Daddy to our two girls. Thank you for all your support throughout this journey, for all the sacrifices, building us our beautiful home and for your daily encouragement to keep going and for truly believing I was capable for this journey when a lot of the time I didn't believe it myself.

To my two beautiful daughters Sophia and Georgia.

I started this PhD a completely different person to who I am now, still a scientist but now also, a mother. I would like to thank you both for teaching me my true meaning of success. You are 2.5 years and 5 months old now, I hope when you are older and look back at this thesis it shows you, you can achieve anything. I dedicate every piece of work to you and hope it inspires you both to follow your dreams and passions, whatever they may be.

General Abstract

The main aims of this PhD thesis were

- To develop a suite of satellite derived tools for the Irish monitoring programme for Harmful Algal Blooms (HABs)
- To highlight the importance of *in situ* data for validating satellite derived data and developing regional algorithms and address the gap in the availability of such data in the North East Atlantic.

In situ data is essential for the calibration, validation and bio-optical algorithm development of ocean colour remote sensing. Chapter 2 describes in detail the difficulties associated with ocean colour measurements in Irish waters due to the persistent issue with cloud cover. This chapter introduces how invaluable the optical data collected is for ocean colour research, especially in areas that are difficult to sample frequently.

The main aims of this thesis were achieved by the successful installation and development of an operational hyperspectral radiometer system on board the RV Celtic Explorer, which collects valuable data for satellite validation, algorithm development, and water quality monitoring. Additionally, in chapters 4 and 5, I present a successful validation of the Red Band Difference (RBD) algorithm to monitor HABs in Irish coastal waters, and a preliminary feasibility study of the HABscope, an artificial intelligence technology for detecting *Karenia* spp. via their swimming pattern.

The primary goal of this thesis was accomplished by introducing the three products to the Irish monitoring programme. The developed tools, including the hyperspectral radiometry system, the RBD algorithm, and the HABscope, are valuable for monitoring marine phytoplankton and associated optically active constituents and can be utilised by the Marine Institute, Researchers, and the global ocean colour community for effective HAB monitoring and mitigation efforts.

1. General Introduction

1.1.1 Phytoplankton

Marine phytoplankton are extremely important ecosystem service providers (Naselli-Flores and Padisak, 2022). They form the base of the food web, are primary producers, provide the world with atmospheric oxygen and also importantly, are a major sink for carbon dioxide from the atmosphere, as well as via carbon storage in sediments and the deep ocean (Tweddle *et al.*, 2018). These microscopic unicellular plant-like organisms are immensely important for contributing to our marine and global production with marine phytoplankton responsible for approximately 98 % of marine system autotrophic production, and 50% of Earth's primary production (Carvalho *et al.*, 2017). As marine ecosystems are impacted and altered by changes in community composition, phytoplankton can be seen as sensitive indicators of climate change (Käse and Geurer, 2018). According to Sournia *et al.* (1991) over 5000 different species of marine phytoplankton worldwide have been discovered. Phytoplankton are planktonic photosynthesizing organisms that can range from 1µm to over 100µm. At certain times of the year, favourable conditions for algae can occur naturally, conditions such as stratification in the water column (Gohin *et al.*, 2003) an increase in nutrients in the water (Siegel *et al.*, 1999) and an increase in water temperature (Thomas *et al.*, 2003). Phytoplankton benefit from conditions such as these and because of this, cell numbers can increase, creating a low or high biomass bloom, depending on the species. The length of time a bloom is available for the cycling of carbon and nutrients and how much oxygen is produced depends on the balance between growth and mortality of the population (Steinberg and Landry, 2017). Approximately, 60-70% of phytoplankton production is consumed daily by microzooplankton (Landry and Calbet., 2004; Righetti *et al.*, 2019). Anderson and Harvey, (2019) discussed the importance of microzooplankton in marine food webs based on their prey, their growth rates and their contribution of organic biomass to higher trophic levels. For the majority of the time, the explosive growth of microscopic algae is advantageous to the ecosystem as a whole, serving as a food source for aquaculture and wild fisheries, for example (Tweddle *et al.*, 2018). A limited proportion of the species forming algal blooms do, however, have an adverse effect

on the ecosystem. These are known as harmful algal blooms (HABs), which can generate a small and large biomass bloom, and can have significant negative economic effects on marine industries like tourism, aquaculture, and fisheries in addition to having immeasurable effects on ocean health (Anderson *et al.*, 2015). A HAB event can harm an environment through two main processes: oxygen depletion brought on by high cell concentrations, and toxin production by certain phytoplankton species (Purdie, 1996). Approximately five percent of marine dinoflagellate species have been identified to produce toxins. Humans are also at risk from eating contaminated filter feeding shellfish who have consumed toxic phytoplankton and or diffused through the water column (Steidinger *et al.*, 2011; Farabegoli *et al.*, 2018). It should be noted; large phytoplankton blooms aren't always indicative of toxic events. For example, the dinoflagellate species *Dinophysis* spp., known to cause Diarrhetic Shellfish Poisoning (DSP), can be harmful at mere hundreds or thousands of cells per litre – concentrations too low to detect from space (Broullón *et al.*, 2020). This subtlety is typical for many toxin-producing species from the *Alexandrium*, *Dinophysis*, and *Azadinium* genera, which don't contribute significantly to the main biomass of a bloom, thus remaining undetectable in satellite imagery.

For these reasons it is vital that efficient mitigation strategies are in place to reduce the detrimental effects of HABs on our marine food resources. When mechanisms for warning or alerting are in place, such as monitoring programmes, aquaculture business owners can minimise damage to their stock by refraining from moving, harvesting, and/or planting new seed. Stumpf and Tomlinson, (2005) discuss the importance for mitigating against the effects of HABs, that real-time detection, monitoring, tracking, and forecasting development is vital for preparing for and determining the direction the bloom is travelling. Satellite remote sensing techniques are effective tools to observe large areas in one measurement.

As stated, the majority of phytoplankton are harmless and provide great benefits to the overall ecosystem. O'Boyle and Silke (2010) reviewed in detail the seasonal features of the phytoplankton ecology around Ireland. The authors discussed how phytoplankton growth in Irish waters is driven by the seasonal change in the vertical stability of the water column. During the winter season there is little phytoplankton growth due to large mixing depths and lack of light availability. Once the spring begins, and the water column stabilises, the spring bloom is triggered due to excess

winter nutrients and solar heating of the euphotic zone. Once the nutrients have been used up by the phytoplankton, bloom levels decline. Later in the summer months, nutrients from deeper waters promote the growth of large phytoplankton populations. During the autumn season, the thermocline breaks down completely, which in turn creates an opportunity for nutrients from the deep waters that were prevented from rising due to the thermocline, to break through into the euphotic zone. This event supports an autumn bloom. This bloom tends to be short lived due to lack of sunlight throughout the winter months. Phytoplankton use dissolved organic matter (DOM) as a nutrient source in natural environments, including marine-derived organic substances in seawater and DOM that reaches coastal zones via rivers and rainfall. This utilisation stimulates growth and can be due to trace metal complexation or direct use of organic nitrogen (N) in small molecules like urea and amino acids. Additionally, phytoplankton may indirectly access nitrogen in DOM through remineralisation by bacterivores feeding on bacteria that used the DOM as a substrate. Direct ingestion of high-molecular-weight organic molecules is another potential but underexplored mechanism. Dissolved organic matter from river water undergoes bacterial degradation and photochemical transformations as it enters coastal waters, making it more available to bacteria. In coastal areas significantly affected by river runoff and rainfall, this can lead to increased phytoplankton growth, including blooms of harmful algal species, as a result of indirect utilisation of nitrogen previously bound to DOM (Granéli and Legrand 1999).

Of course, annual cycles in phytoplankton blooms differ across the global oceans. Behrenfeld and Boss (2018) provide a comprehensive review of the variety of contrasting hypotheses that are described in the literature. The paper covers four main hypotheses:

- The bottom up hypothesis which indicates that an increase in nutrient supply to the surface layer, whether by vertical mixing or horizontal advection, is what causes phytoplankton blooms. According to this hypothesis, phytoplankton growth should increase prior to or at the beginning of the bloom.
- The top down hypothesis suggests that zooplankton grazing pressure is reduced, either as a result of seasonal migration, reproduction or predation, in turn leading to phytoplankton blooms. According to this hypothesis, the rate

of phytoplankton development should either be steady or decreasing before or at the beginning of the bloom.

- The disturbance recovery hypothesis contends that physical disturbances like storms or frontal systems, which temporarily imbalance phytoplankton growth and loss rates, are the source of phytoplankton blooms. According to this hypothesis, the phytoplankton growth rate should be larger than the loss rate at the beginning of the bloom but lower than the loss rate as the bloom declines.
- The dilution recoupling hypothesis, states that the seasonal transition from well-mixed to stratified conditions in the water column is what causes phytoplankton blooms. According to this theory, phytoplankton growth rate should be higher than loss rate after the commencement of the bloom but lower than loss rate prior to it.

The study comes to the conclusion that none of these hypotheses can adequately account for all elements of the annual cycles of phytoplankton, and that a more thorough framework is required to take into account the intricate interconnections between physical, biological, and chemical components that affect phytoplankton dynamics (Behrenfeld and Boss 2018).

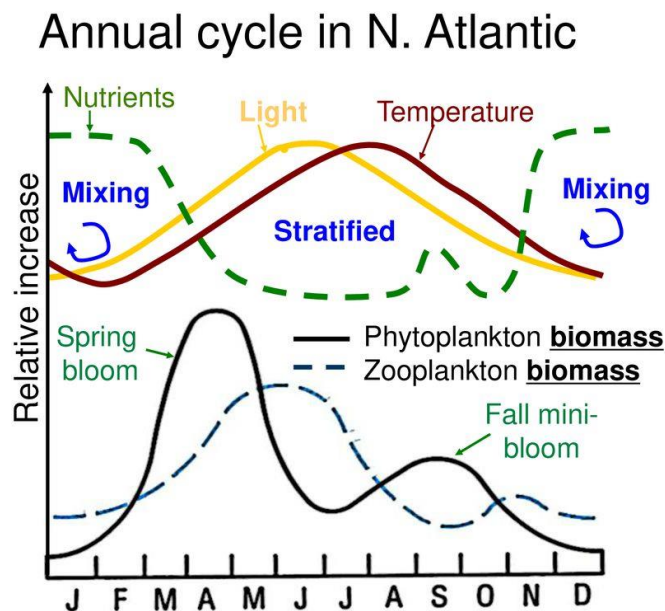


Figure 1 Diagram illustrating all the elements involved in phytoplankton blooms along with seasonal trends.
Source online: <https://slideplayer.com/slide/15767305/>

1.1.2 Aquaculture

Around the world, aquaculture is crucial for supplying food, nutrition, and employment. The FAO (2020) reports that in 2018, aquaculture production hit a record level. Between 1990 and 2018, the production of aquaculture worldwide increased by 527%. With the decline in natural fish resources and the increasing world population, aquaculture will become even more crucial than ever (FAO, 2020). Dennis and Jackson (2019) explain that, in Ireland, aquaculture outputs were between 30,000 and 50,000 tonnes, with the majority coming from the rearing of salmon and bivalves, and the country saw a net gain from under €100 million in 2009 to €180 million in 2018. In 2020, the Irish shellfish aquaculture industry was worth an estimated €51 million (Fernandes-Salvador *et al.*, 2021). Numerous factors, both environmental and biological, including temperature, salinity, oxygen levels, and the availability of food, to name a few, affect aquaculture's potential to succeed (Mydlarz *et al.*, 2006). HABs are a danger for both finfish and bivalve aquaculture (Callaway *et al.*, 2012). As described, HABs can cause a range of issues, such as oxygen depletion and the production of harmful toxins. When there is a HAB, shellfish production area may have to be closed for public safety. Shellfish production areas are generally closed due to the occurrence of Diarrhetic Shellfish Toxins (DSTs), Paralytic Shellfish Toxins (PSTs) and Amnesic Shellfish Toxins (ASTs). The length of closure time and seasonal timing varies amongst events (Fernandes-Salvador *et al.*, 2021).

1.1.3 Climate change

Climate change has profoundly impacted the ocean, primarily through warming and acidification. The absorption of anthropogenic carbon dioxide has reduced the ocean surface's pH by 0.1 since the onset of the industrial era. The ocean's increased warming, has contributed to a sea level rise of 0.19 m between 1901 and 2010. Additionally, shifts in salinity patterns and wind stress are causing noticeable changes in various regional areas. These alterations, together with human-induced factors like nutrient runoff, are transforming oceanic conditions. This not only affects biological processes but also regional climates, underscoring the broad and significant impact of climate change on the ocean's physical and ecological dynamics (Käse and Geurer 2018).

Seasonal patterns of phytoplankton blooms have been associated with Irish waters, Anderson *et al.* (2021) discusses how an increase in temperature will alter phytoplankton growth. The authors state the thermal response will vary among phytoplankton species, in particular their results showed low latitude coccolithophores will face considerable decreases while cyanobacteria will face increases in growth rates. Therefore, the seasonal patterns may change due to climate change. Gobler *et al.* (2017) suggests that there is growing evidence that the frequency and intensity of harmful algal blooms (HABs) in marine environments may already be being impacted by climate change. Using high-resolution sea-surface temperature records and temperature-sensitive growth rates of two algae species, *Dinophysis acuminata* and *Alexandrium fundyense*, the study determines that in numerous coastal Atlantic regions between 40°N and 60°N, there are notable increases in the potential mean annual growth rates and length of bloom seasons. In recent decades, HABs have emerged and expanded in several regions. According to the study's findings, rising ocean temperatures have a significant role in escalating these HABs and posing a growing risk to human health.

Wells *et al.* (2020) explores the evolving science of HABs in the context of global climate change. It acknowledges the growing concern that human-induced warming might significantly alter the distribution, patterns, and intensity of HABs. Various climate-related factors like temperature, stratification, ocean acidification, nutrients, and more are examined for their potential impacts on HAB dynamics. The study is a collection of deliberations from a symposium on HABs and climate change, discussing research challenges and new directions. This study highlights the complexity of predicting future HAB trends due to the integration of multiple climate drivers and emphasises the necessity of interdisciplinary research to understand and manage the future of HABs effectively. The study calls for a mix of laboratory and field studies, long-term observational programs, and socio-economic considerations to enhance forecasting and mitigation strategies. It is a comprehensive look at how climate change could reshape HAB occurrences and the scientific approaches needed to address these potential changes.

1.1.4 Phytoplankton Functional Types

When discussing phytoplankton, and especially in the context of remote sensing, as stated there are thousands of species identified therefore it is useful to refer to phytoplankton in terms of functional types. Phytoplankton functional types (PFT) is a commonly used phrase to describe a group of phytoplankton. A PFT or phytoplankton biogeochemical class is frequently defined as a collection of organisms (regardless of taxonomic affiliation) that perform a specific chemical process, such as calcification, silicification, nitrogen fixation, or dimethyl sulfide production (DSP); these are also occasionally referred to as "biogeochemical guilds". Some of important functional types are: Nitrogen fixers, Calcifiers, Silicifiers, Size Classes and DMSP producers (IOCCG, 2014). This is an emerging area of remote sensing to determine groups of phytoplankton from space rather than just an overall chlorophyll concentration, Moisan *et al.* (2017) summarises the studies that are developing algorithms for the certain groups.

1.1.5 Harmful Algae in Irish Waters

One of the earliest published records of discoloured water in Ireland was in 1865 (Wyatt, 2009). Toxic and harmful phytoplankton are monitored throughout the year at more than 100 Irish coastal sites. According to the Marine Institute data archive there are approximately 16 phytoplankton genera with species that can potentially cause dense blooms and 9 genera with the ability to generate biotoxins. The majority of shellfish production closures in Ireland are the result of phytoplankton species from the genera *Dinophysis*, *Azadinium*, *Pseudo-nitzschia* and *Alexandrium*. Human sicknesses caused by members of these genera include diarrhetic shellfish poisoning (DSP), azaspiracid poisoning (AZP), amnesic shellfish poisoning (ASP) and paralytic shellfish poisoning (PSP) (Cusack *et al.*, 2016). In Ireland, *Dinophysis* spp. are responsible for diarrhetic shellfish poisoning and are generally found in their highest cell densities during the summer months and normally below the limit of detection during the winter months (November to February). Blooms of *Dinophysis* spp. are believed to develop at frontal regions, in open waters and transported to coastal areas (Raine *et al.*, 2016).

The main organism causing PSP in Irish shellfish is *Alexandrium minutum* (Clarke, 2020). The highest ever PSP concentrations recorded in Irish waters was in 2020 in the Southwest of Ireland (Bresnan *et al.*, 2021).

The genes *Pseudo-nitzschia* is responsible for ASP and generally blooms are observed from March to May ranging from the Southwest up along the west coast of Ireland (Clarke, 2020).

In Ireland, AZP is primarily caused by *Azadinium spinosum* is the causative species of Azapiracids that are problematic around the Irish coastline, mainly in the northwest, west and southwest coasts (Fernandes-Salvador *et al.*, 2021).

1.1.6 Fundamentals of Ocean Colour

For satellite ocean monitoring, it is essential to comprehend the basics of ocean colour. Remote sensing is the process of gathering data about an object without coming into contact with it directly. The colour of the ocean can be determined by measuring remote sensing reflectance (R_{rs} units: sr^{-1}) or water leaving radiance (L_w) a method of measuring optically active constituents within the water column (chlorophyll-*a*, coloured dissolved organic matter (CDOM), the water itself, non-algal particles) (IOCCG, 2000). The process involves a measurement of spectral variations of water leaving radiance (L_w), or remote sensing reflectance (R_{rs}) [1] from the ocean surface, depending on what constituents the wavelengths of energy interacted with (Groom *et al.*, 2019). Some of the sunlight that interacts with the ocean's surface is reflected back into the atmosphere. The angle at which the energy penetrates the ocean determines how much energy penetrates its surface (Lotliker *et al.*, 2017). In order to identify and measure geophysical parameters, satellite sensors are designed to monitor upwelling radiation in a number of narrow bands in the visible (VIS) to near-infrared (NIR) spectral range (O'Reilly *et al.*, 1998).

$$R_{rs} = \frac{L_w}{E_s} = \frac{L_{surf} - L_{sky} * \rho}{E_s} \quad [1]$$

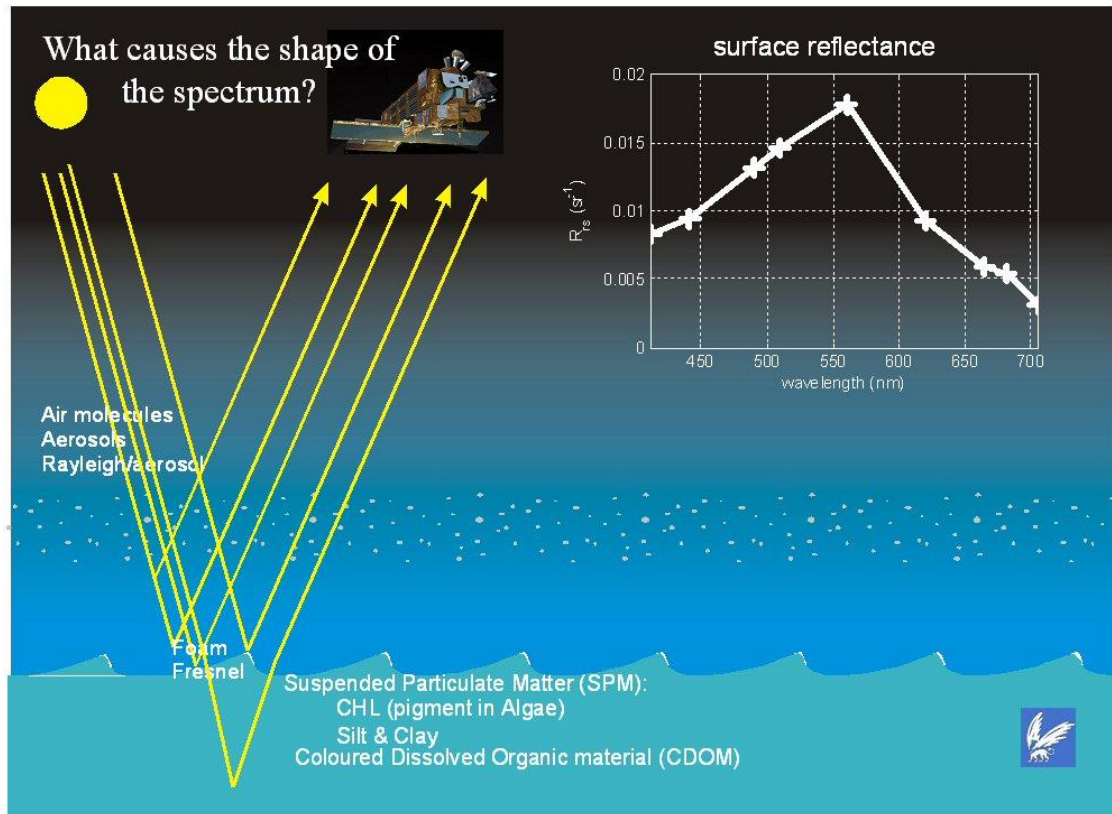


Figure 2 Diagram illustrating the wavelengths of light interacting with different properties at or just below the ocean surface, which shapes the surface reflectance. Online Source: <https://seos-project.eu/oceancolour/oceancolour-c01-p02.html>

Mobley (2001) describes how by understanding the fundamentals of how light travels to certain depths can determine different organic or inorganic optically active constituents in the water. Absorption and scattering are two processes that control the variation of downward and upward irradiance with depth, these processes are known as inherent optical properties (IOPs) (Kirk, 2011). The IOPs depend on the medium, or substance sampled, which in the case of ocean colour is seawater with dissolved and suspended particulate materials and are independent of the ambient light field. Apparent Optical Properties (AOPs) depend on both the medium IOPs and the directional structure of the ambient light field (Mobley, 2001). The water itself and optically active components in the water control the amount and spectral shape of light scattered upwards and towards the satellite sensor, which is known as the water leaving radiance. This process involves absorption and scattering of light at various wavelengths across the visible and near-infrared portions of the spectrum. The depth to which the satellite sensor can measure depends on both the wavelength of light and the optically active constituents (IOCCG, 2018). In order to obtain quantitative data on the types of compounds present in the water and their amounts, remote sensing

entails assessments of the fluctuations in magnitude and spectrum quality of the water-leaving radiation (IOCCG, 2000). The following section describes the optically active or colour producing agents the satellite sensors recognise based on the water leaving radiance but in reality, none of these constituents would exist on their own, each category would include members of the other category, and this can be a problem for algorithms, which will be discussed in this chapter and throughout the thesis.

1.1.7 Colour Producing Agents or Optically Active Constituents

Colour producing agents (CPAs) or optically active constituents (OACs) within the water include coloured dissolved organic matter (CDOM), inorganic suspended particulate material (SPM), particulate organic matter (POM) or phytoplankton, chlorophyll-a (Prieur and Sathyendranath 1981). Water gets its distinctive colour through the interaction of the OACs in the medium with the ambient light through processes of absorption and scattering (Jungblut *et al.*, 2017). The water itself also absorbs and scatters energy. Within 10 centimetres of the water surface, almost all the infrared energy (700 - 1000 nm) has been absorbed by water molecules. Longer wavelength light is absorbed more readily by pure water than shorter wavelength light. This allows for the deeper penetration of higher intensity light with short wavelengths, such as blue (Dutkiewicz *et al.*, 2015). Pegau *et al.* (1997) describe that the process of absorption by water is dependent on both temperature and salinity which can affect the molecular structure of water, which in turn affects the absorption properties of the water.

1.1.8 Case 1 and Case 2 waters

Ocean colour measurements are typically classified with two water types, Case 1 and Case 2 waters. Morel and Prieur (1977) were the first to introduce the two water types. Since then, these descriptions have been refined for use in satellite work (Gordon and Morel, 1983; Morel, 1988; IOCCG, 2000; Mobley *et al.*, 2004). Mobley *et al.* (2004) describe Case 1 waters ‘whose IOPs are dominated by phytoplankton’ and are typically classed as open ocean waters. Although Case 1 waters are associated with phytoplankton, CDOM and non-algal particles will also play a role in these waters. Case 2 waters are known as more optically complex waters due to their proximity to land and associated natural and anthropogenic effects. Bio-optical algorithms work

well in Case 1 waters due to less interference from other optical constituents. CDOM is present in Case 1 waters but is produced autochthonously by phytoplankton and the non-algal particles tend to be detritus caused by phytoplankton residues. Using this information, algorithms work well to determine phytoplankton concentration in Case 1 waters, whereas in Case 2 waters, phytoplankton or chlorophyll concentrations tend to be overestimated due to the dominance from CDOM, which are sourced from rivers and resuspension of particles from the bottom.

Mobley (1994) estimates that roughly 98% of the world's oceans fall into the Case 1 category. As Case 2 waters are heavily used by humans for the likes of recreation and fisheries, satellite remote sensing and regional algorithm development are of great interest to the scientific community.

An earlier water type classification system, developed by Jerlov (1976), is often used for *in situ* studies, but less frequently in remote sensing work. This classification was summarised by Mobley *et al.* (2021). This system classifies water bodies based on their optical properties, particularly on their light attenuation characteristics. Based on IOPs which are influenced by factors such as suspended particles, dissolved organic matter and water clarity, the Jerlov water types offer a technique to distinguish between various water masses. Jerlov categorised this data into five typical open-ocean spectra, denoted by the letters I, IA, IB, II, and III and nine typical coastal spectra, labelled 1 to 9 (Jerlov, 1976).

The Forel–Ule Index (FUI) is a colour scale for water. It categorizes water colours into 21 levels, ranging from blue to brown. This classification was first proposed by Forel in 1890 and later expanded by Ule in 1892. The scale is one of the oldest tools in optical oceanography and has been traditionally used to gauge water colour, primarily depending on water constituents. This index is advantageous as it does not rely on local retrieval algorithms and can characterize natural waters in a simple and globally effective manner. The FUI is instrumental in assessing water quality and understanding the ecological and biogeochemical states of water bodies (Ye and Sun, 2022).

Inversion algorithms, which are useful to quantitatively derive biogeochemical factors from the marine reflectance in the coastal ocean, are another method of classifying

water types in marine waters. The prevalent methods concentrate on the spectrum of optical variability unique to a designated coastal region through the creation of local or regional inversion algorithms. Although, this strategy may have a number of limitations, such as its strong reliance on the data set used to develop the algorithm and the possible restricted applicability of regional considerations for large-scale applications (Vantrepotte *et al.*, 2012).

1.1.9 Phytoplankton/Chlorophyll absorption

In marine waters, phytoplankton's optical characteristics, particularly, in vivo absorption coefficients, are crucial in determining how far radiant energy penetrates seawater and to what extent it is used for photosynthesis. Pigments found in algae play two key roles in photosynthesis: they absorb sunlight and convert it into chemical energy. Chlorophylls, which are pigments found in phytoplankton, typically have two absorption peaks, one in the blue and one in the red (Mobley *et al.*, 2021). Ocean colour is determined by radiometric quantities like Remote sensing reflectance (R_{rs}), defined as the ratio of water-leaving radiance to the total downwelling irradiance just above the water. This is a function of specific IOPs (e.g., spectral shapes of absorption and backscattering, volume scattering function) and concentrations of water constituents like chlorophyll-*a* SPM, and CDOM (Mobley, 1994). Estimation of phytoplankton biomass is generally calculated by measuring the concentration of chlorophyll-*a*, the photosynthetic pigment found in all algal species. Phytoplankton cells contain several pigments in their cells, depending on the growing conditions and species composition of the phytoplankton. These pigments include chlorophylls, carotenoids and phycobilins. The absorption process of these pigments shape the water-leaving radiance signal. Chlorophylls absorb light in the blue (440–475 nm) with a primary absorption peak near 440 nm and in the red (630–675 nm) regions of the spectrum with a secondary peak around 670 nm, while carotenoids and phycobilins do so in the 400–500 nm and 540–650 nm ranges (Meler *et al.*, 2017), see figure 3 for an example of some absorption spectra of marine algal pigments.

Light Absorption Spectra for Marine Algal Pigments

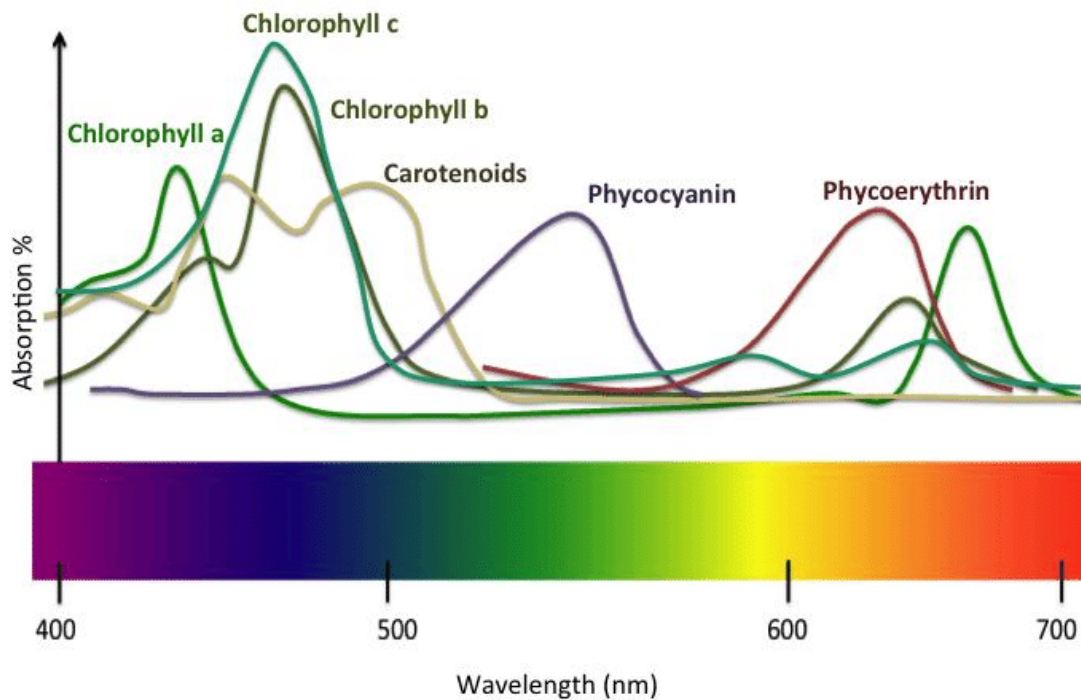


Figure 3 An example of light absorption spectra for marine algal pigments. Much of the visible spectrum is utilised by different pigments at different wavelengths. Copyright Yarish *et al.* (2012).

1.1.10 CDOM absorption

Aurin *et al.* (2018) describes CDOM, which is also known as *gilvin*, *gelbstoff*, or yellow substance, as the result from the breakdown of plants and organic matter into humic material. Kostakis *et al.* (2021) estimates CDOM is responsible for the make up of 10-90% of DOM concentration in the upper water column. CDOM absorbs light in the UV and visible wavelengths, the strongest absorption takes place in the UV and diminishes close to zero in the red region (Wei *et al.*, 2016a). One of the key constituents of marine waters is CDOM, which regulates the biogeochemical, photochemical, and biological processes that take place in marine ecosystems (Helms *et al.*, 2008), because of this, CDOM can significantly impact on the productivity of the water column due to its optical behaviour. In addition to increasing primary production and shielding marine life from radiation, CDOM can also limit production in deeper waters due to its shady impact. CDOM can protect the upper ocean from damaging UV rays. CDOM must be considered before reflectance data can be reported

for phytoplankton and suspended sediment observations since its colour signal is crucial in remote sensing investigations (Tassan 1988; Karabashev, 1992).

Figure 4 displays an example of Detritus, Phytoplankton, CDOM and Water Absorption

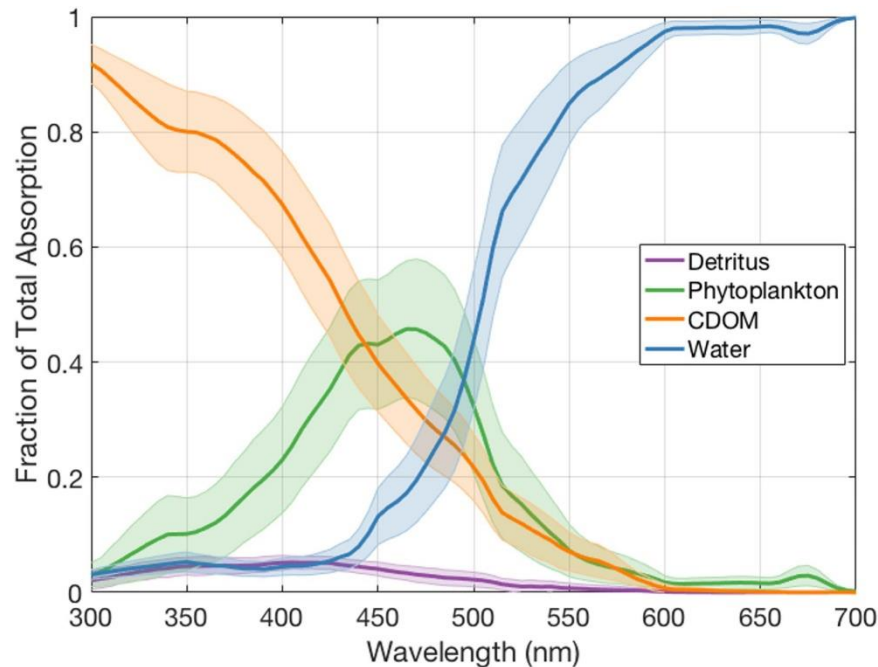


Figure 4 An example of the mean relative contributions of Detritus, Phytoplankton, CDOM, and Water to total light absorption at wavelengths between 300 and 700 nm for the NAAMES dataset. Copyright Allen et al. (2020)

1.1.11 Suspended Sediments

Myint and Walker, (2002) discuss how suspended matter/sediments are primarily responsible for scattering light, whereas as already discussed above, Chlorophyll-*a* and CDOM are chiefly responsible for absorption. Suspended sediments can impact the optical property of the water by creating turbidity. Suspended solids are generally comprised of fine particulate matter with a diameter of less than 62 μm (Waters, 1995). The level of turbidity depends on the amount of suspended particles in the water. If the turbidity is high for the specific area this can block light from travelling through the water column. Turbidity and suspended solids are important parameters in many studies due to their link between incoming light and photosynthesis for the growth of algae and plankton. The complex nature of suspended solids in the water can change the reflectance of the waterbody and cause variation in colour, because of this remotely sensed data based on just the colour of the water may not be accurate (Gholizadeh *et*

al., 2016). In summary, suspended sediments is considered a proximal parameter in evaluation the distribution of the underwater light field. It influences the light field by altering the absorption and scattering of incident light due to suspended particles. This modification by suspended sediments affects the dynamics and distribution of light underwater, which can enhance the light field under certain conditions by increasing the scattering and potentially the absorption of light, thereby affecting the penetration and distribution of light within the water column (Li *et al.*, 2022).

1.1.12 Remote Sensing

As described, a non-invasive approach of detecting optically active components within the water column is to measure R_{rs} or L_w (IOCCG, 2000). The spectral radiance of specific visible and infrared wavelengths are measured from the top of the atmosphere (TOA). Wang *et al.* (2009) describes how the ocean colour signal received by the satellite sensor is relatively small (<10%), due to light scattered by the atmosphere, and requires highly accurate correction methods. O'Reilly and Werdell (2019) discuss in detail the steps involved in deriving data from satellite measurements. To exclude the influence of the atmosphere from the overall signal and provide estimates of R_{rs} , atmospheric algorithm correction techniques are applied to the data (Mobley *et al.*, 2016). In order to estimate additional geophysical features, such as inherent optical properties (IOPs), which are the absorption and backscattering characteristics of saltwater and its particulate and dissolved constituents, bio-optical methods are then applied to the R_{rs} (Groom *et al.*, 2019).

1.1.13 Ocean Colour Sensors

The Medium Resolution Imaging Spectrometer (MERIS), Moderate Resolution Imaging Spectroradiometer (Aqua-MODIS), Sea-Viewing Wide Field-of-View Sensor (SeaWiFS), The Visible Infrared Imaging Radiometer Suite (VIIRS), and the Ocean and Land Colour Instrument (OLCI) (Groom *et al.*, 2019) are multispectral ocean colour sensors on satellites. Even though these sensors vary in band measurement, they are designed to measure the spectral radiance in several narrow bands to near infrared spectral range at the top of the atmosphere (O'Reilly *et al.*, 1998). Measurements of ocean colour from satellites began in the late 1970s with the launch of the Coastal Zone Colour Scanner (CZCS). Sensors and bio-optical

algorithms for measuring and quantifying optically active constituents have been improving since then to the most recent launch of ESA Sentinel 3B OLCI sensor in 2018 (Groom *et al.*, 2019). Werdell *et al.* (2019) describes NASA's plan to launch a hyperspectral satellite sensor: Plankton, Aerosol Cloud, Ocean Ecosystem (PACE) in 2024. This sensor will have the capability to measure a spectral resolution of 340 to 890 nm and a spatial resolution of 1 km. The PACE mission comprises of three instruments, a hyperspectral radiometer (ocean colour instrument (OCI)) and two multispectral instruments. OCI is designed to tilt 20° north in the northern hemisphere and 20° in the southern hemisphere, this tilt was also included in the SeaWiFS mission to reduce the effects of sun glint and maximise the number of ocean colour pixels retrieved. The launch of PACE and its capabilities has the potential to revolutionise retrieval of aquatic optical and biogeochemical properties (McClain *et al.*, 2022).

1.1.14 Chlorophyll Algorithms

Since the launch of the Coastal Zone Colour Scanner (CZCS) in 1978, chlorophyll-*a* has been a fundamental metric for measuring phytoplankton, marking the beginning of a significant era in ocean colour remote sensing (O'Reilly and Werdell, 2019). Its estimation is crucial for understanding various ecological and biogeochemical processes, such as the food web, marine biogeochemistry, and the carbon cycle, highlighting its importance in the broader context of marine science (Groom *et al.*, 2019).

In response to this need, the ocean colour science community has historically utilised two primary types of algorithms to derive chlorophyll-*a* from Remote Sensing Reflectance (R_{rs}). Empirical algorithms, as described by Dierseen (2010) and exemplified by the ocean colour algorithm (OC4) developed by O'Reilly *et al.* (1998), rely on a statistical relationship between the blue-to-green ratio of R_{rs} and chlorophyll concentrations via a polynomial expression. These algorithms, including variations like OC3, OC5, and OC6, have proven effective in Case 1 waters dominated by phytoplankton and are adaptable to various sensors and locations.

On the other hand, semi-analytical algorithms, outlined by IOCCG (2006) and detailed by Werdell *et al.* (2018), use radiative transfer equations to determine chlorophyll. These methods offer a more nuanced approach, incorporating the absorption and

backscattering properties of phytoplankton and are crucial in environments where the optical properties are primarily influenced by these organisms.

In summary, while blue and blue-green bands are foundational in developing algorithms for chlorophyll-*a* estimation and other water quality parameters in clearer, Case 1 waters, the complexity of Case 2 waters often necessitates additional or alternative approaches. CDOM and sediments can lead to the overestimation of chlorophyll values in more complex waters. CDOM's strong absorption in UV and blue wavelengths, particularly at 443nm, a critical absorption peak for chlorophyll-*a* (Bricaud *et al.*, 1981; O'Reilly *et al.*, 1998), requires a shift in approach. This shift helps avoid the absorption of non-algal particles that can interfere with accurate readings. This is where algorithms that measure chlorophyll fluorescence become invaluable. With chlorophyll-*a* and other components inside plankton cells having maximum absorption around 440nm and fluorescence at 685nm, this method has served as a reliable proxy for phytoplankton biomass for over five decades (Babin 2008; Lorenzen, 1996). Addressing the specific challenges of Case 2 waters, the red band difference algorithm described by Amin *et al.* (2009) has shown promising results. This algorithm is less sensitive to CDOM, sediments, and atmospheric corrections, making it an essential tool for coastal waters and has been successfully employed in monitoring HABs in various regions. This algorithm has proven successful in monitoring HABs in the Gulf of Mexico (Amin *et al.*, 2009), Chesapeake Bay (Wolny *et al.*, 2020), Alaska (Vandersea *et al.*, 2020) and the Celtic Sea (Jordan *et al.*, 2021). The upcoming hyperspectral resolution capabilities of NASA's PACE mission are set to further transform chlorophyll estimation, allowing for sophisticated discrimination of HAB species from space.

In the context of Irish waters, a pilot study in chapter 4 explores the red band difference algorithm's effectiveness compared to the traditional blue-green ratio algorithm used in the Irish monitoring program. This investigation is pivotal in adapting and refining remote sensing techniques to regional challenges, ensuring more accurate and efficient monitoring of aquatic environments. This approach, combining empirical and semi-analytical methods with advanced fluorescence measurements, represents the multifaceted strategy required to effectively understand and monitor the complex dynamics of Case 2 waters and beyond.

1.1.15 HABS from Ocean Colour

Satellite remote sensing techniques for detecting HABS typically involve measuring the concentration of chlorophyll-*a* as an indicator of algal biomass. Mueller, (1981) was the first to describe the value of remote sensing for monitoring HABS. There are key limitations to using remote sensing for determining specific HABS from satellites. Currently, ocean colour sensors are designed to measure specific wave bands as mentioned above in 1.1.13 Ocean Colour Sensors, because of this it is difficult to distinguish specific spectral signatures.

Lin *et al.* (2021) study discuss the benefit of merging satellite observations with Lagrangian particle tracking. The method enhances monitoring by predicting changes in water properties like chlorophyll-*a* concentration and spectral qualities, crucial for identifying algal species from satellite ocean colour data. Applied to coastal areas of England, this approach significantly improved satellite data interpretation, offering detailed temporal and spatial resolution. The study's findings demonstrate a high correlation between predicted and observed chlorophyll-*a* concentrations, suggesting the method's potential as a valuable tool for marine ecosystem monitoring and supporting the aquaculture industry with early warnings of HABS. Despite inherent uncertainties in modelling and methodology, the method represents a significant advancement in predicting and understanding the dynamics of HABS. Future efforts aim to extend the approach to create quantitative risk maps for key high-biomass HAB species.

Stumpf (2001) explored the use of sensors like SeaWiFS for monitoring *Karenia brevis* blooms in the Gulf of Mexico. The study highlights how integrating satellite data with field observations enhances the detection and management of HABS, despite challenges posed by the diverse nature of these organisms. Case studies demonstrate the practical application of this technology in real-world scenarios. The study concluded that while current efforts at that time focused on SeaWiFS and that future advancements in understanding phytoplankton will improve HAB monitoring and management. Wolny *et al.*, (2020) discuss how scientists in the US have moved to using Sentinel-3 satellites for detecting common HAB species like *Alexandrium monilatum*, *Karlodinium veneficum*, *Margalefidinium polykrikoides*, and *Prorocentrum minimum*. This detection is based on multispectral data products from

the OLCI sensor. These data are then analyzed in conjunction with *in situ* phytoplankton data and known ecological associations to identify the presence and extent of these specific algal species. The study highlights the potential of future hyperspectral instruments to improve species discrimination and the importance of integrating satellite data with *in situ* observations for effective resource management. It reviews how satellite data can aid in protecting shellfish resources and improving water quality monitoring. The paper also discusses how upcoming satellite missions with enhanced capabilities could further aid in understanding and managing HABs in the Chesapeake Bay, offering a more detailed and timely view of these ecological threats.

Current ocean colour missions are designed to measure the spectral radiance in several narrow bands to near infrared spectral range at the top of the atmosphere therefore identifying HABs from space requires integrating satellite data with field observations (O'Reilly *et al.*, 1998) but the unparalleled spectral coverage of the future NASA PACE satellite will enable the first-ever worldwide measurements intended to determine the makeup of phytoplankton communities. This would greatly enhance our capacity to recognise HABs by species (Werdell *et al.*, 2019).

Figure 5 shows the difference between a multispectral ocean colour sensor capabilities beside the future hyperspectral satellite for identifying HABs.

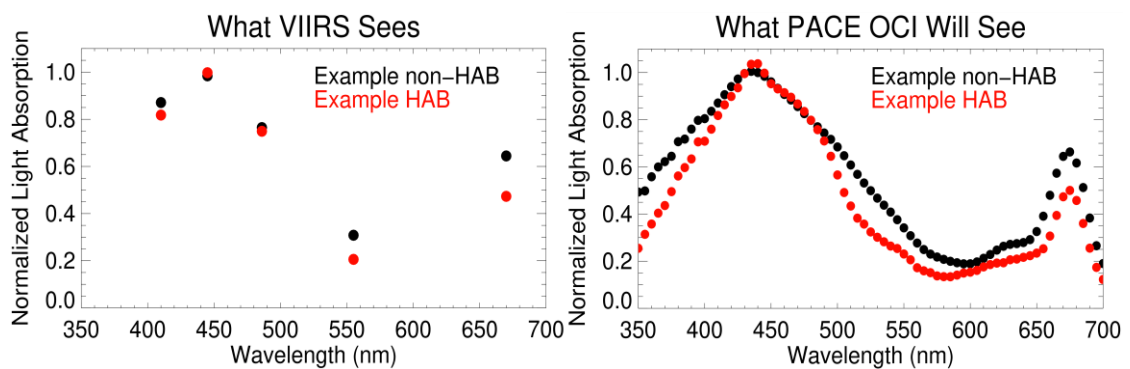


Figure 5 The difference between a multispectral ocean colour sensor (VIIRS) capabilities beside the future PACE OLI hyperspectral satellite for identifying HABs. Source: <https://pace.oceansciences.org/about.htm>

1.1.16 Deriving fluorescence from Remote Sensing

Following their absorption of sunlight, phytoplankton's energy dynamics depend heavily on chlorophyll fluorescence. This system is crucial for regulating the amount of light energy chloroplasts absorb beyond what is necessary for photosynthesis, therefore minimising potential harm from bright light (Zhao *et al.*, 2022). Chlorophyll-*a* emits fluorescence with a quantum yield, which is only a small portion of the light that is absorbed (Zhou *et al.*, 2008). A peak at 685 nm distinguishes this emission significantly (IOCCG, 2000).

One well-known metric for evaluating the physiological alterations in phytoplankton is the Fluorescence Line Height (FLH). Understanding several facets of their activities and health is especially helpful (Blondeau *et al.*, 2014). The three wavelengths that are used to calculate fluorescence loss head (FLH) are the central wavelength of maximal chlorophyll fluorescence, which is roughly 685 nm, and two additional wavelengths that aid in establishing a baseline around the fluorescence peak. According to Shehhi *et al.* (2019), these extra wavelengths are situated on either side of the peak.

The Moderate Resolution Imaging Spectroradiometer (MODIS) on the Aqua satellite, the Ocean and Land Colour Instrument (OLCI) on the Sentinel-3A/Sentinel-3B satellites, have a range of fluorescence bands for measuring this metric, for instance the OLCI sensor measures FLH using a variety of bands, including 665, 674, 681, 710, and 761 nm (Zhao *et al.*, 2022).

1.1.17 Attenuation Coefficient and K_d (490) Algorithm

As stated wavelengths of light that enters the water column will typically be absorbed and scattered by the optical constituents or the water itself. Diffuse downwelling attenuation (K_d) is defined as the reduction in the amount of downwelling irradiance (E_d) with depth, by measuring this parameter it is possible to determine the amount of light lost due to absorption and or scattering (Kirk, 2003; Moblet, 1994). One of the main causes of light attenuation in the ocean is phytoplankton. For photosynthesis, they absorb light, particularly in the blue and red part of the spectrum. In Lee *et al.* (2005), the numerous investigations and applications of measuring the diffuse attenuation coefficient $K_d(\lambda)$ are covered. These include biological activities like photosynthesis, heat transmission in the upper ocean, and the turbidity of both oceanic

and coastal waters. According to IOCCG, 2019 there are three techniques for employing satellite reflectance data to determine the diffuse attenuation coefficient, Kd (λ) or Kd (490). The first approach is based on empirical connections between the blue/green ratio ($R_{rs}(\lambda)$) of remote sensing reflectance and in situ measurements of Kd (490). The second is an actual correlation between chlorophyll and Kd . The last technique uses a quasi-analytic approach to calculate absorption and backscattering from $R_{rs}(\lambda)$. $Kd(\lambda)$ is semi-analytically estimated using the obtained values. When Lee *et al.* (2005) examined the three algorithms, they discovered that the semi-analytical method worked best for a variety of water types. SeaWiFS examines the ratio of water-leaving radiances at 443 and 490 using the Kd (490) algorithm. Remote sensing ocean colour algorithms are based on the measurement of parameters of AOPs such as Attenuation coefficients ($Kd(\lambda)$) and Remote sensing reflectance (R_{rs}) (Mobley, 2001). Joint and Groom (2000) explains the relationship between the vertical attenuation coefficient of irradiance in water and its inherent optical characteristics (IOPs), including the scattering and absorption coefficients. It is crucial to understand light behaviour in aquatic settings as this directly affects phytoplankton. 490nm is an area of the spectrum associated with phytoplankton absorption therefore can be useful to estimate the amount of light available for photosynthesis (Schanz *et al.*, 1997). The vertical attenuation of irradiance is fundamentally linked to phytoplankton through its effects on light penetration in water, a vital component of phytoplankton growth and dispersal. For marine ecosystems to be monitored effectively monitored and managed, it is essential to comprehend these processes Joint and Groom (2000).

1.1.18 Importance of Validation

As previously mentioned, satellite data is an effective tool for tracking phytoplankton blooms and water quality. It is important to note there are some limitations to satellite monitoring such as cloud, sun glint and stripe artefacts from some sensors. For these and data quality control reasons satellite derived data need to be validated with on the ground data. Results from chapter 2 are a good example of why *in situ* data is required for Irish waters. Numerous studies compare various validation efforts and highlight the significance of validation (e.g. O'Reilly *et al.*, 1998; Bailey and Werdell 2006; Zibordi *et al.*, 2012; Garaba *et al.*, 2015; Brando *et al.*, 2016, Concha *et al.*, 2021). As Wang *et al.* (2009) discussed the ocean colour signal received from the TOA is <10% due to the atmosphere therefore correction methods are needed. A crucial stage in

determining whether the observations made by satellite sensors are correct is regional validation (IOCCG, 2012). *In situ* ocean surface remote sensing reflectance measurements are routinely made using above- and in-water hyperspectral optical radiometers. Applications for R_{rs} measurements include satellite validation, water quality monitoring, bio-optical modelling, and algorithm development. These applications are especially useful in coastal regions where high-quality *in situ* radiometry is advantageous because of the close proximity to land (e.g. Mobley 1999; Zibordi *et al.*, 2002; Garaba *et al.*, 2012; 2014a, 2014b; Garaba and Zielinski 2013; Hommersom *et al.*, 2012; Zibordi *et al.*, 2012; Brando *et al.*, 2016; Tilstone *et al.*, 2017; 2020; Pitarch *et al.*, 2020; Concha *et al.*, 2021).

Measurements known as fiducial reference measurements (FRMs) are exact and traceable measurements that serve as a benchmark for verifying and adjusting measurements obtained by satellite or remote sensing technologies. These measures are used as a standard by which to evaluate how accurate the data derived from satellites is. The term "fiducial" suggests that these measurements are established, well-defined, and trustworthy as benchmarks. Banks *et al.* (2020) introduces the Copernicus Marine Environmental Monitoring Service (CMEMS) and highlights the importance of calibration and validation in satellite missions. The focus is on ocean colour radiometry (OCR) and the satellite missions (Sentinel-2 and Sentinel-3) designed to support CMEMS. The principles of calibration and validation are explained in the study, with a focus on their importance in guaranteeing the accuracy and dependability of data derived from satellites. The Fiducial Reference Measurements (FRM) programmes of the European Space Agency (ESA), in particular FRM4SOC, are presented as efforts aimed at verifying satellite data products concerning the land, ocean, and atmosphere. Establishing and sustaining SI traceable ground-based fiducial reference measurements for ocean colour is one of FRM4SOC's goals. The techniques for measuring water-leaving radiance and downwelling irradiance in the context of satellite ocean colour radiometry validation have been greatly improved by the FRM4SOC project. The project expands the scope to include all oceans, building on NASA Ocean Optics procedures and taking into account improvements since 2004. It emphasizes data collecting and processing uncertainties, which are critical in the FRM context. The specified measurement requirements include quality control, open publication of data processing software,

long-term data archiving in an open-access repository, ancillary data collection, uncertainty estimation, traceability to SI units, and in situ measurement of downwelling and water-leaving irradiance.

The process of measuring a satellite-derived product's accuracy and characterising its uncertainties through analytical comparison with reference data which are thought to be representative of reality is known as validation in remote sensing (Justice *et al.*, 2000). Concha *et al.* (2021) discusses validation strategies employed by the ocean colour community to verify satellite derived products using *in situ* data were examined in this study. Using an identical dataset of *in situ* and satellite data, two primary methodologies proposed by Bailey and Werdell (2006) and Zibordi *et al.* (2009) were compared. High spatial resolution sensors were represented by Sentinel-2A/MSI, and medium spatial resolution sensors by Sentinel-3A/OLCI. The study discovered that the amount of match-ups and validation metrics are impacted by the validation approach selected, which in turn affects how accurate satellite products are judged to be. The results highlight the necessity for consistent techniques by indicating that validation statistics presented in various research may not always be directly comparable.

Tilestone *et al.* (2021) study evaluated a range of statistical variables to assess algorithm performance, adhering to the techniques described by Muller *et al.* (2015) and Brewin *et al.* (2015). The type-II regression slope (S), intercept (I), Pearson correlation coefficient (r), bias (δ), bias-corrected root-mean-square error (Δ), and relative percentage difference (RPD) were among these measurements. Better linear consistency between *in situ* and satellite observations is indicated by a larger r . Furthermore, the data distribution around the regression line and outliers is indicated by Ψ , δ , and Δ . The relative difference between *in situ* and satellite data is represented by Ψ , which is sensitive to variations around the regression line. The bias corrected difference, denoted by Δ , is susceptible to anomalies. A value close to zero indicates that there is no systematic difference between the two datasets. The δ metric provides information on under- or overestimation of satellite data in comparison to *in situ* data.

In chapter 3 the products that can be derived from above water hyperspectral radiometers are discussed for satellite validation and applications mentioned above. This chapter focuses on the value of *in situ* measurements of remote sensing

reflectance and how it was documented using a data management quality management framework pack. Validation statistics as described by Muller *et al.* (2015), Brewin *et al.* (2015) and Concha *et al.*, (2021) are applied to the two datasets and discussed in further detail.

1.2 Chapter Summary

In summary, this introductory chapter describe various topics which will be discussed throughout the results chapters with an insight into new technologies or environmental monitoring instruments for the Irish monitoring programme. This thesis aims to advance the Irish monitoring programme for HABs by introducing and evaluating new remote sensing algorithms and technologies. Each chapter contributes to this overarching goal.

Chapter 2 delves into the diffuse attenuation coefficient (K_d 490) and its potential applications in the HAB programme. While the chapter effectively discusses the use of *in situ* point measurements of K_d (490) to validate data from Sentinel-3A OLCI, there's an inherent challenge due to cloud cover and no daily satellite data was available. The chapter concludes that Irish waters' cloudiness limits remote sensing capabilities and underscores the need for more *in situ* measurements. These type of data can be used for algorithm development alongside other data sets; this conclusion directly informs the research approach in Chapter 3.

Chapter 3 focuses on creating a data management quality management framework for a new hyperspectral radiometer system installed on the RV Celtic Explorer, which generates remote sensing reflectance (R_{rs}) measurements. This system is the first of its kind within the Marine Institute. The chapter includes a case study comparing these *in situ* R_{rs} measurements with the satellite derived CMEMS R_{rs} wavaebands, using the validation statistics previously mentioned. This system will be extremely beneficial to Irish monitoring programme for Ireland due to the potential for satellite validation, algorithm development and water quality monitoring.

Chapter 4 demonstrates the successful introduction of the Red Band Difference Algorithm to Irish waters and its potential to detect and monitor a phytoplankton

bloom, despite the challenges posed by cloudiness in chapter 2, this bloom took place during the summer months and was visible using satellite technologies.

We outline Ireland's possible use of the Red Band Difference algorithm as an additional monitoring tool within the current HAB alert system to offer an early warning approach for HABs, and specifically, blooms caused by *Karenia* spp.

In order to improve the detection capabilities presented in Chapter 4, it is important to increase the quantity and methods of *in situ* samples, as suggested by the technique presented in Chapter 5. The pilot study using the HABscope in Ireland for the first time will highlight the connection between enhancing *in situ* sample availability and developing detection techniques for *Karenia* spp and potentially other species in the future.

Overall, this thesis has effectively added a number of cutting edge instruments to the Irish monitoring programme. Significant breakthroughs have been made with the introduction of the Red Band Difference Algorithm, the deployment of a Hyperspectral Radiometer System, and the use of the HABscope, which uses artificial intelligence to detect the swimming patterns of *Karenia* spp.

2. Chapter 2:

***In situ* Attenuation Coefficient and Satellite Derived *K_d* (490) in Irish Coastal and Oceanic Waters**

Catherine Jordan^{1,2}, Caroline Cusack², Peter Croot¹

¹Earth and Ocean Sciences and Ryan Institute, School of Natural Sciences, University of Galway, H91 TK33 Galway, Ireland

²Marine Institute, Rinville, Oranmore, H91 R673 Galway, Ireland

2.1 Abstract

This study presents an extensive analysis of *in situ* and satellite derived data to understand the optical properties of Irish waters, focusing on the vertical attenuation coefficient *K_d* at 490 nm and chlorophyll-*a* concentrations over a 20-year period (1999-2019). *In situ* measurements of *K_d* (490) were collected from various research surveys, displaying a range between 0.02-0.52 m⁻¹ across different water types, including both Case 1 and Case 2 waters. Notably, the highest attenuation values were observed in the mixed waters of the Irish Sea. Complementing these *in situ* observations, satellite data from the GlobColour project, integrating measurements from MODIS, MERIS, SeaWiFS, and OLCI sensors, were analysed using the KD490-LEE algorithm. This analysis elucidated the monthly climatology trends of *K_d* (490) and chlorophyll-*a*, although data for December were consistently unavailable due to cloud coverage. The *in situ* data highlighted the presence of CDOM absorption, particularly in the CV18012 stations, and chlorophyll-*a* absorption in the CE19009 survey areas. Seasonal variation in *K_d* (490) indicated higher attenuation along coastal areas, especially during winter, aligning with increased rainfall and wind. A notable increase in attenuation and chlorophyll-*a* concentration was observed during spring and summer, suggesting a strong influence of biological and physical processes. Despite the limitations of satellite technology in capturing ocean colour under frequent cloud cover, this study emphasises the importance of *in situ* measurements, especially in under sampled areas. The integration of this algorithm into the Irish monitoring programme is proposed, offering significant benefits for comprehensive marine environment assessment and management.

2.2 Introduction

The interaction of light with sea water is essential to many oceanic processes and the fundamentals of life (Mobley, 2001). The importance of light for marine life cannot be overstated. It transfers heat to the top of the water column, causing stratification and, as a result, shaping abiotic conditions over time (McFarland, 1986). Studies of light interaction in seawater are vital for understanding processes such as primary production, climate change, biogeochemical cycling, water clarity, ocean colour remote sensing, lidar bathymetry, photochemistry and much more (Mobley, 2001; Dickey *et al.*, 2011). Remote sensing of ocean colour plays a key role in monitoring coastal and oceanic waters. Groom *et al.* (2019) provide a detailed summary of studies describing some of the practical uses of ocean colour data, including assessing water quality parameters, satellite validation, ecosystem model data assimilation, aquaculture site selection, and climate change time series, to name a few. However, as their study suggests, this is just a sampling of current and future uses of ocean colour data. Understanding the fundamentals of ocean colour is vital for satellite monitoring of our oceans.

The Diffuse Attenuation coefficient ($K_d(\lambda)$) is defined as 'the decrease with depth of ambient down welling irradiance $E_d(\lambda)$ which comprises of photons heading in all downwards direction' (Mobley, 1994). Understanding how different wavelengths travel to certain depths can help determine what materials, organic or inorganic, are in the water body (Mobley, 2001). Two processes that control the variation of downward and upward irradiance with depth are absorption and scattering and are known as inherent optical properties (IOPs) (Kirk, 1994). Inherent optical properties depend on the medium and are independent of the ambient light field. Apparent optical properties (AOPs) depend on both the medium (IOPs) and the directional structure of the ambient light field (Mobley, 2001). The Diffuse Attenuation coefficient is classed as an apparent optical property (AOP) (Preisendorfer, 1976), and varies due to direction structure of the ambient light field, solar zenith angle and depth of the water column (Mobley, 1994; Gordon, 1989). AOP's are connected to IOP's through radiative transfer theory (Preisendorfer *et al.*, 1976; Mobley, 2018; Mobley, 1994). Light absorption is a fundamental IOP and can influence the underwater light field (Kostakis *et al.*, 2021). Absorption coefficient can be quantified as $a(\lambda)$ (m^{-1}) (Mobley, 2001).

2.2.1 Phytoplankton Absorption

There are a range of processes that can be quantified by measuring absorption coefficients of constituents dissolved and suspended within the water column especially with the study of phytoplankton including pigments, taxonomic composition, size structure (Kostakis *et al.*, 2021) and primary production (Behrenfeld and Falkowski 1997). One of the most important roles light plays in the ocean is it drives photosynthesis and therefore fuels the food web. Absorption takes place for photosynthetic organisms, depending on their spectral composition and pigments, within the visible wavelengths of the electromagnetic spectrum 400 – 700 nm (Kirk, 2011), different species or groups of phytoplankton absorb light differently (Sathyendranath and Platt, 2007). Since 490 nm is an area of the spectrum associated with phytoplankton absorption this measurement can be useful to estimate the amount of light available for photosynthesis (Schanz *et al.*, 1997)

2.2.2 Water absorption

Dutkiewicz *et al.* (2015) discusses how it is not only the constituents within the water that absorb or scatter the incoming electromagnetic radiation but also the water molecules itself. Water molecules absorb very strongly in the longer wavelengths. Absorption by water is dependent on both temperature and salinity which can affect the molecular structure of water, which in turn affects the absorption properties of the water (Pegau *et al.*, 1997).

The diffuse attenuation for pure water is in the range 0.016 to 0.022 m⁻¹ for the visible spectrum (400 – 700 nm) (Smith and Baker 1981). Attenuation of light will vary in different water types, such as Case 1 and Case 2 water. Case 1 waters are associated with open waters and Case 2 with coastal waters and are more complex due to inputs (e.g. organic matter, suspended sediment) resulting from proximity to land. Morel and Prieur (1977) originally introduced these water types and the definitions have since been refined by Gordon and Morel, 1983; Morel, 1988; IOCCG, 2000; Mobley *et al.*, 2004. Waters, where the inherent optical properties are dominated by phytoplankton are defined as Case 1 waters. Due to the proximity to land Case 2 waters are more complex and have higher concentrations of optical properties, these waters generally contain higher concentrations of CDOM, SPM, and inorganic particles in addition to

phytoplankton (Mobley *et al.*, 2004). Darecki *et al.* (2003) discusses the approach by Sathendranath (IOCCG, 2000) regarding Case 2 waters. The authors consider eight classes are associated with Case 2 waters therefore one algorithm would not be adequate and all complex Case 2 waters should be assessed by area and season.

2.2.3 CDOM absorption

Another optical constituent that controls the variation of irradiance is coloured dissolved organic matter (CDOM). CDOM results from the breakdown of plants and organic matter into humic material and is also known as *gilvin*, *gelbstoff*, or yellow substance as described in Aurin *et al.* (2018). It is estimated to make up 10-90% of DOM concentration in waters and the impacts of CDOM on the upper water column are well described in Twardowski *et al.* (2004). CDOM absorbs strongly in the UV and blue wavelengths (Bricaud *et al.*, 1981) and decreases exponentially with increasing wavelengths (Dutkiewicz *et al.*, 2015). Due to the fact CDOM absorption takes place near 443nm, there is an overlap with chlorophyll-*a* absorption and this becomes a problem for remote sensing algorithms as the chlorophyll *a* values may be overestimated (O'Reilly *et al.* 1998). Jordan *et al.* (2021) describe an algorithm for monitoring phytoplankton blooms in Irish waters using a chlorophyll fluorescence algorithm rather than the traditional blue-green ratio algorithm that avoids the absorption of CDOM and sediments (Amin *et al.*, 2009). In terms of measuring algal blooms, ocean colour sensors and algorithms are being regularly updated and improved on since the launch of the first ocean colour sensor in 1978, the Coastal Zone Colour Scanner and the most recent Sentinel 3B OLCI sensor from ESA in 2018 (Groom *et al.*, 2019).

2.2.4 Remote sensing

Remote sensing of key water quality parameters using ocean colour satellite sensors is a valuable tool for monitoring our oceans. Strong practical justifications exist for using satellite remote sensing to examine the vast shelf seas of the Northeast Atlantic. It is a powerful tool to collect data over a large area in one single measurement, especially for monitoring the movement of an algal bloom (Stumpf and Tomlinson, 2005). Algal blooms are naturally occurring and the whole ecosystem generally benefits from marine phytoplankton as primary production is the source of

approximately 50% of atmospheric O₂, provide food for wild fisheries and aquaculture and provides climate regulation (Tweddle *et al.*, 2018). Algal blooms occur during specific times of the year which include, increase in temperature, stratification and increase in nutrients (Siegel *et al.*, 1999; Gohin *et al.*, 2003; Thomas *et al.*, 2003). Conditions like these are favourable for phytoplankton, and as a result, cell counts may rise and a low or high biomass bloom can result. A small percentage of the species responsible for algal blooms can cause harm to the overall ecosystem. These are known as Harmful Algal blooms (HABs). Two key mechanisms by which a HAB event might harm the environment are oxygen deprivation caused by high cell concentrations and toxin synthesis by particular dinoflagellate species (Purdie, 1996). Callaway *et al.* (2012) describes the dangers of HABs for aquaculture, both finfish and bivalve. Because phytoplankton blooms are both a benefit and can be harmful to the environment, it is vital remote sensing technology is utilised to mitigate against the impacts of HABs by providing warning systems but also to monitor the health of our oceans over a large scale.

Remote sensing ocean colour algorithms are based on the measurement of parameters of AOPs such as Attenuation coefficients ($K_d(\lambda)$) and Remote sensing reflectance (R_{rs}), and as discussed AOP's are connected to IOP's through radiative transfer theory.

The process of absorption and scattering of light at different wavelengths across the visible and near-infra-red portions of the spectrum by optically active constituents in the water and the water itself control the magnitude and spectral shape of light scattered upwards and towards the satellite sensor i.e water leaving radiance (L_w). The depth to which which the satellite sensor can measure depends on both the wavelength of light and the water properties (IOCCG, 2018).

Lee *et al.* (2005) discusses the many studies and uses of measuring the diffuse attenuation coefficient $K_d(\lambda)$, such as biological processes for instance, photosynthesis, heat transfer in the upper ocean and the turbidity of the ocean, both oceanic and coastal waters.

According to IOCCG, (2019) there are three methods for using satellite reflectance data to estimate the diffuse attention coefficient, $K_d(\lambda)$ or $K_d(490)$. The first algorithm is based on empirical relationships between *in situ* measurements of $K_d(490)$ and the blue/green ratio of remote sensing reflectance ($R_{rs}(\lambda)$). The second is an empirical

relationship between K_d and Chlorophyll. The final method is using a quasi-analytic method that derives absorption and backscattering from $R_{rs}(\lambda)$, and the values are used to semi-analytically estimate $K_d(\lambda)$. The three algorithms were compared by Lee *et al.* (2005) and the semi-analytical method was found to be the best for a range of water types. The $K_d(490)$ algorithm used by SeaWiFS compares the ratio of water-leaving radiances at 443 and 490 nm. When the uncertainty of the SeaWiFS estimation of water-leaving radiance at 443 is greater than that at 490 nm, a revised algorithm using the ratio of water-leaving radiances at 490 and 555 nm to estimate $K_d(490)$ is applied (Mueller, 2000).

Due to the high incidence of cloud cover off the Irish coast *in situ* data is vital for validating against satellite data. There is also a lack of *in situ* optical data around Ireland.

The original aim of this study was to compare *in situ* $K_d(490)$ values with satellite derived values from different water bodies around the island of Ireland. *In situ* data from two research surveys are presented here: CV18012 (NE Atlantic Ocean and the Western Irish Sea) and CE19009 (NE Atlantic Ocean). Daily satellite values to correspond with the *in situ* values was investigated. There were zero cloud free days available. *In situ* attenuation data and 20 years of $K_d(490)$ and Chlorophyll-*a* data were investigated to determine whether the $K_d(490)$ algorithm would benefit the the Irish monitoring programme.

2.3 Material and Methods

2.3.1 Study Area

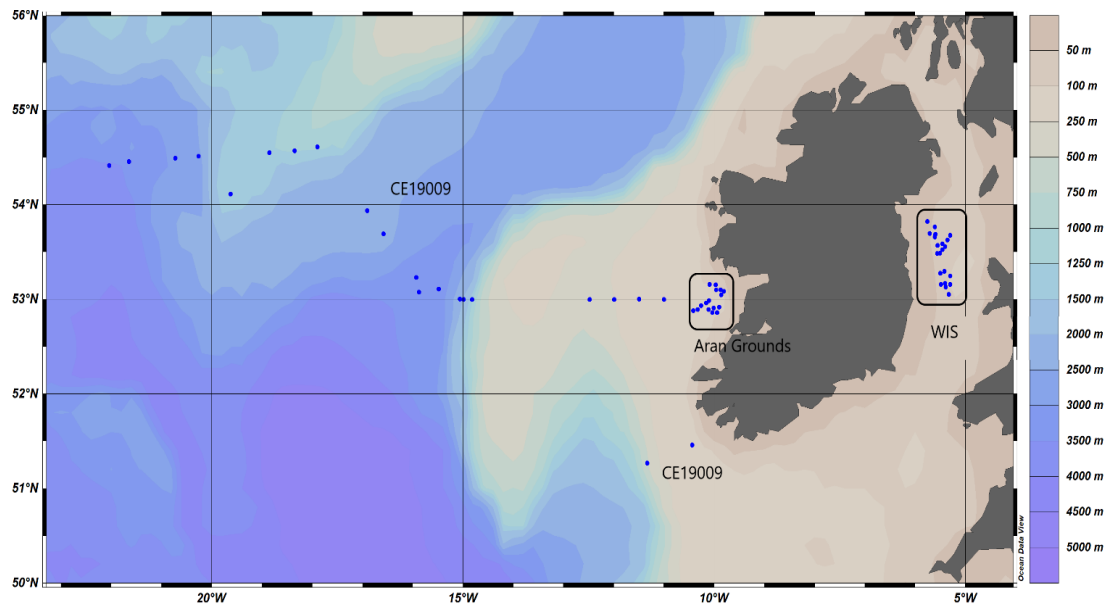


Figure 6 Study area broken into three sections: stations from CE19009 and CV18012; Aran Grounds and Western Irish Sea (WIS)

Figure 6 displays the stations sampled for this study. The study area was broken into three distinct areas, the survey area for CE19009 and the survey area for CV18012. CV18012 is broken into two areas: CV18012 West: The Aran Grounds, west of Ireland and CV18012 East: the western Irish sea (WIS), east of Ireland: Stratified and Mixed stations.

CV18012

A multidisciplinary research survey was carried out on the RV Celtic Voyager (CV18012) from the 3 - 16 April 2018 and 38 stations were sampled within this time frame. Due to the multidisciplinary nature of the survey the areas selected were commercially important fishing grounds for *Nephrops norvegicus* as the larvae was being sampled (McGeady *et al.*, 2019). The sample sites were broken into 2 main areas: The Aran grounds (West of Ireland) and the Western Irish Sea stations (East of Ireland): a mixed, a stratified area and a fixed station were sampled within this area.

CE19009

The Marine Institute's Ocean Climate Survey from Galway to the Rockall Trough was carried out from May 24 - 6 June 2019 on the RV Celtic Explorer. The main purpose of this survey was to gather high quality oceanographic data to analyse essential climate variables along a targeted section of the Atlantic Ocean starting in Galway Bay along the 53° N line and heading out to the South Rockall Trough. Stations were also sampled off the SW coast of Ireland while in transit.

2.3.2 Attenuation Coefficient

A TriOS RAMSES-ACC Hyperspectral Irradiance Sensor with a wavelength range of 320-900 nm, 256 channel and a cosine response was used on both CV18012 and CE19009 to create a profile of downwelling irradiance (E_d). The instrument has a pressure sensor incorporated to determine the depth in the water column. The instrument has an average spectral sampling of 3.3 nm per pixel and a spectral accuracy of 0.3 nm. The instrument was placed inside a frame and secured facing 'straight up' so as to detect photons travelling downwards to measure the spectral downward plane irradiance (Figure 7). The instrument was lowered at a speed of one metre per second. The TriOS RAMSES MSDA_XE software was programmed to take automatic measurements as the sensor travelled through the water column. The data acquired was stored using the software Multi-Sensor Data Acquisition (MSDA_XE ver. 8.9.2 2014-04-28) that was provided by TriOS GmbH. The data is radiometrically calibrated using the calibration files supplied by Trios GmbH. Matlab (Mathworks) was used to calculate the attenuation coefficient values at each site, determining the $K_d(490)$ *in situ* values by taking the slope of a log irradiance vs depth plot. The error estimates are derived from calculating the confidence interval for the fit of K_z at each wavelength. It is calculated using linear regression analysis.

See Appendix A1 for Matlab script.

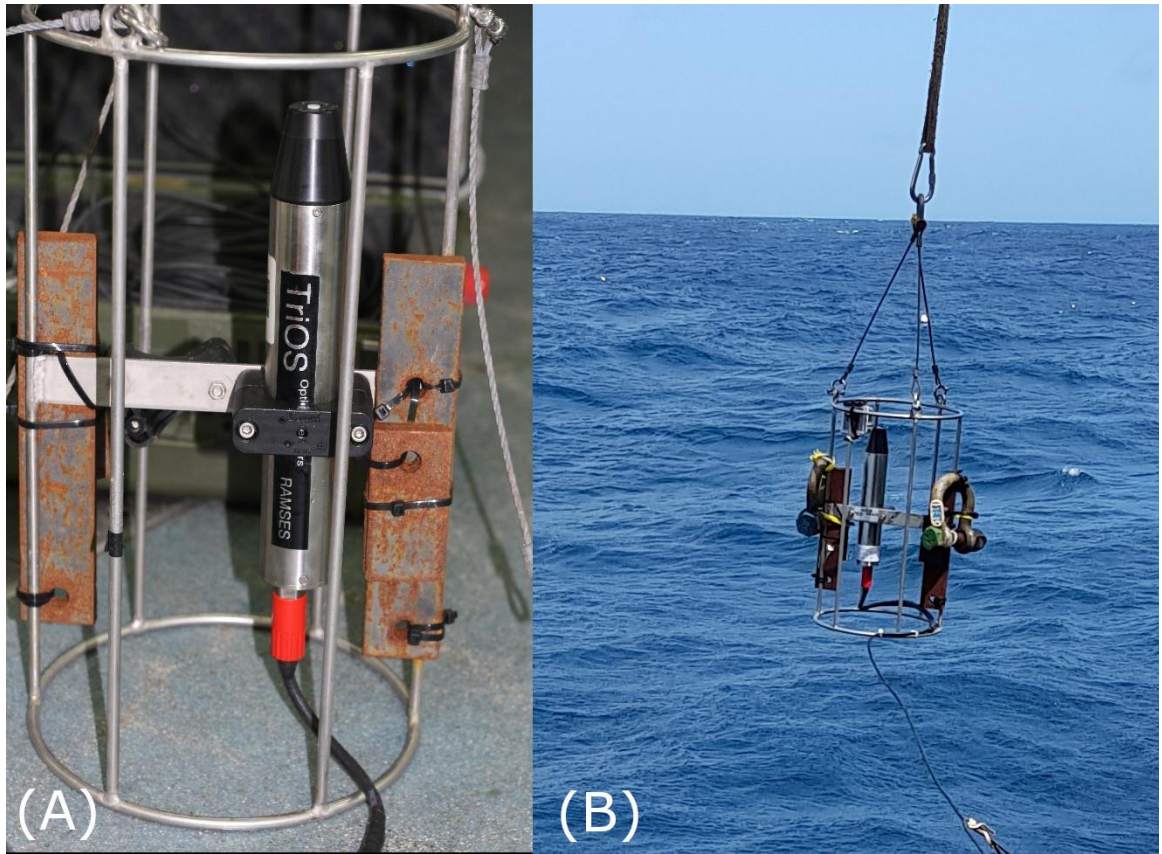


Figure 7 (A) TriOS RAMSES irradiance sensor inside frame (B) Sensor being deployed off the ship

2.3.3 Satellite Data

Satellite data from the Ocean and Land Colour Instrument (OLCI) sensor on Sentinel 3A were obtained from Copernicus Marine Service (CMEMS) (dataset-oc-atl-opt-olci_a-14-Kd490_1km_monthly-rt-v01_1628764606346.nc) and (dataset-oc-atl-opt-olci_a-14-Kd490_1km_monthly-rt-v01_1580124509985.nc). The region of interest covers all coastal waters around the island of Ireland. The multispectral OLCI sensor has 21 spectral bands from 400 to 1020nm and has a spatial resolution of 300 m. The $K_d(490)$ algorithm identifies the turbidity of the water column, i.e., how visible light in the blue-green region of the spectrum penetrates within the water column. Daily satellite data was investigated but was unavailable on all the dates surveyed. L4 monthly composites are illustrated for this study to show the monthly averages for the timeframe due to consistent cloud cover for both research surveys.

20 years of monthly $K_d(490)$ data was downloaded from GlobColour to display the climatology trends per month between 1999 and 2019. The GlobColour 1km x 1km product integrates data from multiple satellite sensors, such as MODIS, MERIS,

SeaWiFS and OLCI and all data is processed using the same algorithm, the KD490-LEE. KD490-LEE is computed from the corresponding merged fully normalised remote sensing reflectance products at 443, 490, 555 and 670 nm using the semi-analytical method of Lee and Arnone (Lee *et al.*, 2005). The data included the months January to November as December was unavailable from 1999 to 2019.

20 years of monthly Chlorophyll data was downloaded from GlobColour to illustrate Chlorophyll concentration (mg/m³) climatology trends per month between 1999 and 2019.

The data is generated by the GSM01 semianalytical bio-optical model, which involves merging of single sensor L3 normalised remote sensing reflectance. The GSM method uses the normalized reflectances at the original sensor wavelengths, without intercalibration (Maritorena and Siegel, 2005).

Monthly climatology figures were created for each month using Matlab (Mathworks) using a worksript that was created to process a climatology for each month and visualise the multi-year satellite data.

2.4 Results

In situ attenuation coefficient data from two research surveys (CV18012 and CE19009) were calculated using in house Matlab scripts as mentioned above in the methods section. Figure 8 displays the K_d (490) values from both surveys ranging from 0.02-0.52 m⁻¹ overall and 0.02 to 0.27 m⁻¹ from stations on CE19009. Waters sampled during CE19009 would generally be classed as Case 1 waters. The lowest *in situ* value during CE19009 was of 0.02 m⁻¹ Station 15. The highest *in situ* value of CE19009 was 0.27 m⁻¹ was on shelf edge station 16.

Stations sampled during CV18012 have a mix of both Case 1 and Case 2 waters. The stations to the west of Ireland, known as the Aran grounds, had K_d (490) values ranging from 0.08 to 0.33 m⁻¹. The stations in the Irish sea, east of Ireland were known as mixed water stations and stratified water stations. The stratified stations had values ranging from 0.05 to 0.22 m⁻¹ and values in the mixed water stations ranged from 0.11 to 0.52 m⁻¹, the highest attenuation recorded on both surveys.

Figure 8 displays how the majority of the stations to the west of Ireland range between 0.02 and 0.20 m^{-1} . The highest attenuation values are recorded in the Irish Sea.

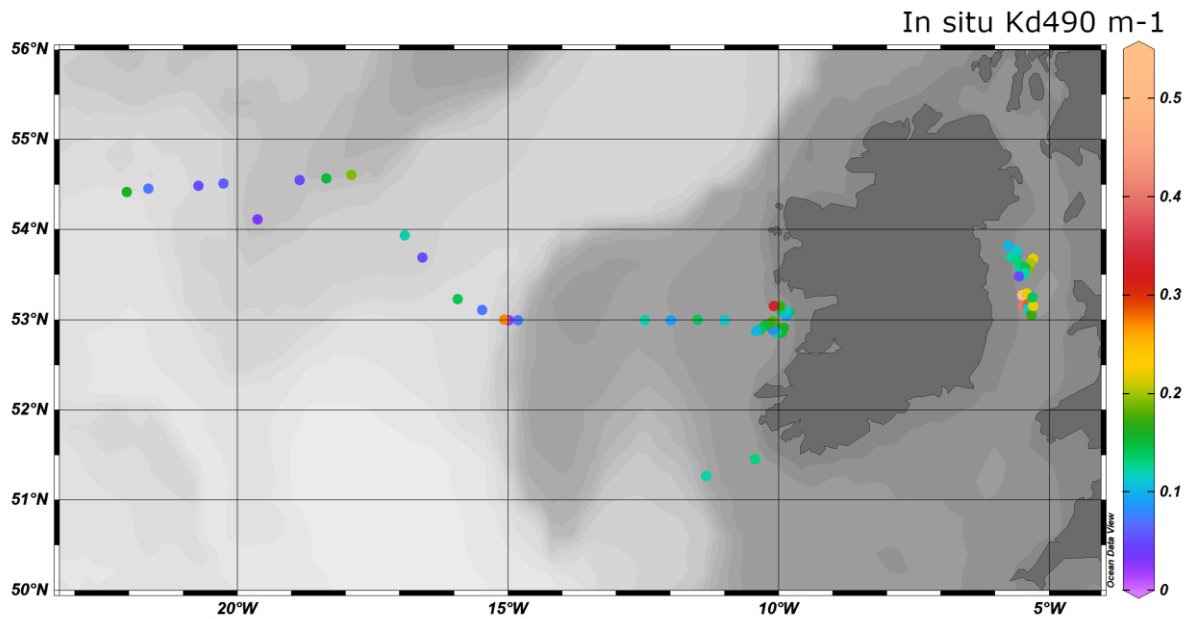


Figure 8 In situ Kd490nm values for CV18012 and CE19009 research surveys

Figure 9 displays the surface chlorophyll values for all the stations sampled on CE19009. The highest chlorophyll values were recorded at the stations within the shelf and closest to the coast.

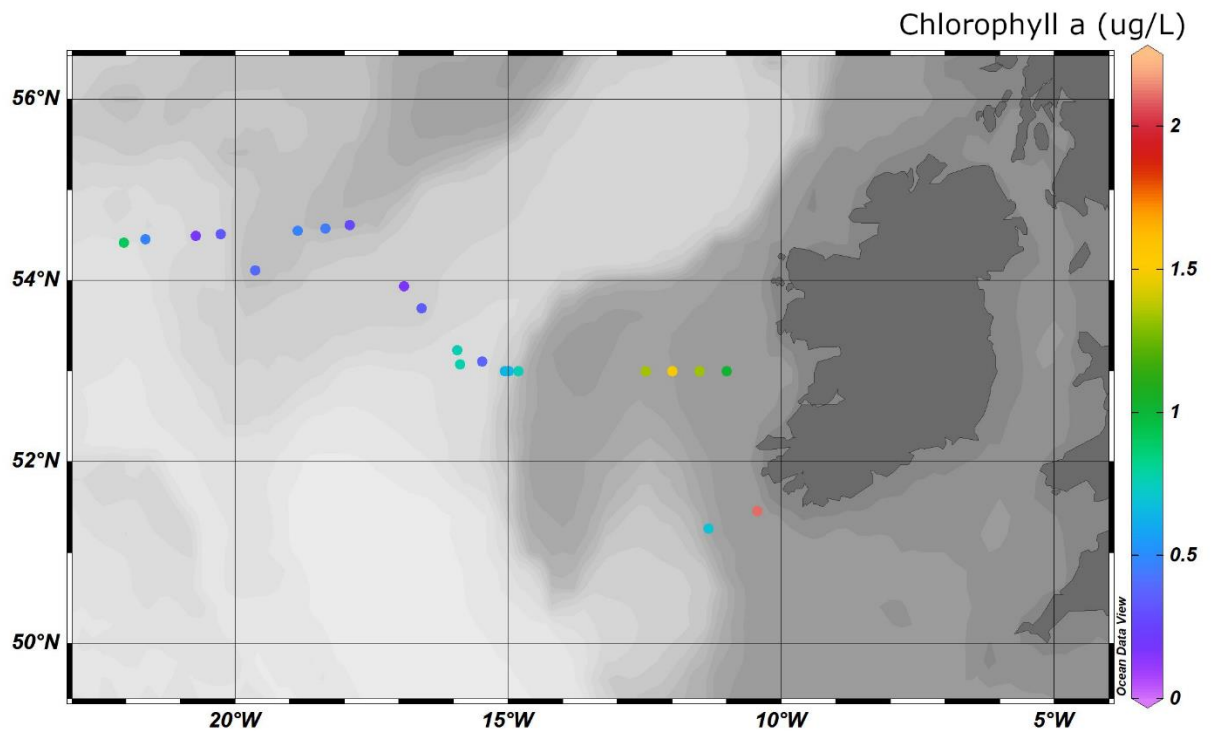


Figure 9 In situ chlorophyll surface values for all stations sampled during CE19009 (May 24th June 6th 2019)

Figure 10 displays examples of the *in situ* attenuation coefficient data generated from different survey areas such as from the survey CV18012; the Aran grounds, Stratified and Mixed waters. And data from deep oceanic waters from survey CE19009. The plots display which wavelengths were attenuated throughout the water column. The *in situ* attenuation plots can help derive what constituents were present in the water when the measurement was taken based on the absorption of specific wavelengths. It is evident from these plots that CDOM absorption took place at all the CV18012 stations displayed here with absorption peaks between 300 and 400nm in each of these plots. The CE19009 plots displayed here illustrates absorption in the red section of the spectrum, indicating chlorophyll absorption and or the red wavelengths being absorbed by the ocean water.

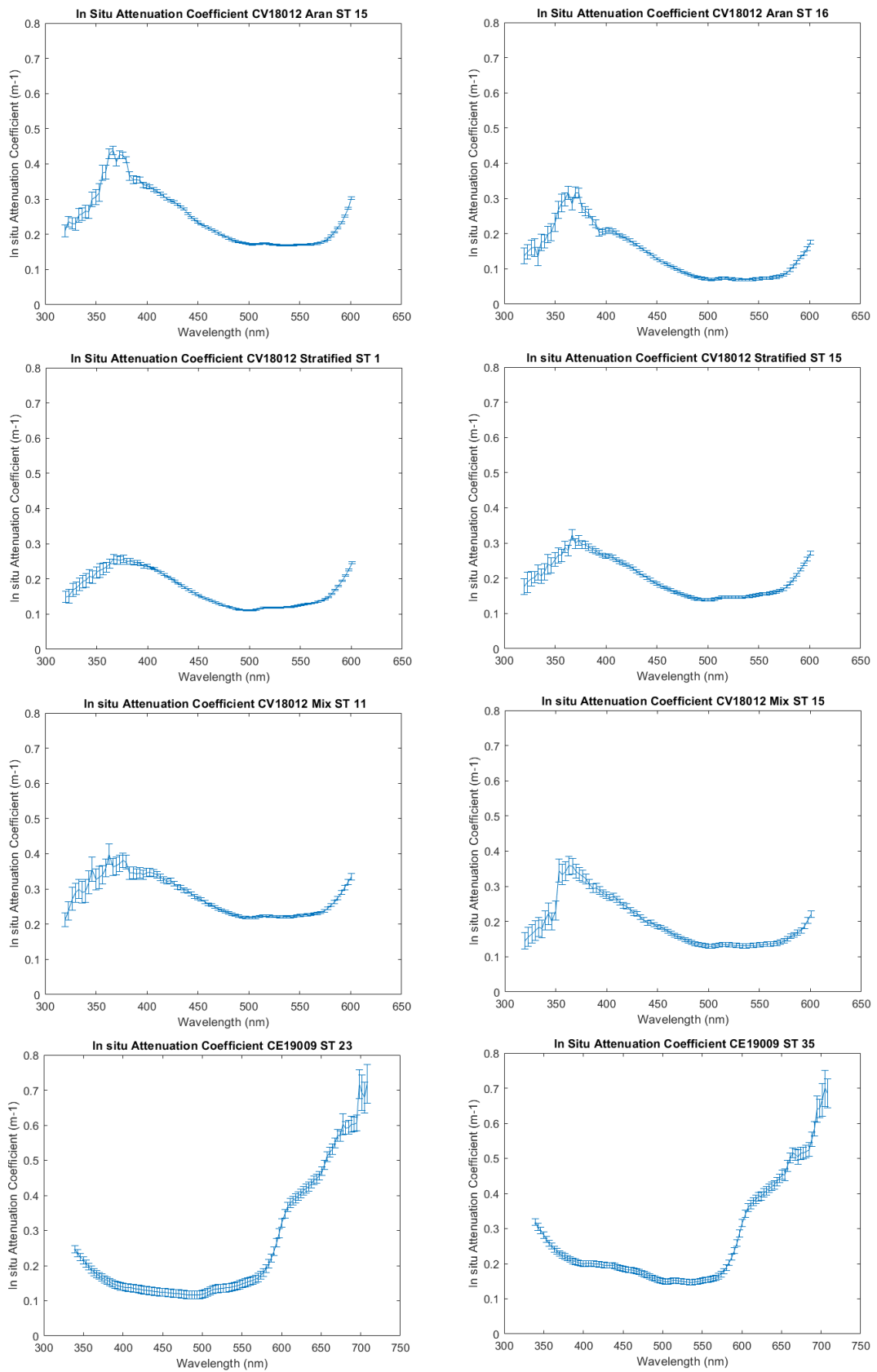


Figure 10 Examples of in situ attenuation coefficient plots generated at CV18012: Aran grounds, Stratified and Mixed water stations and open water CE19009 with error bars.

Figure 11 shows the daily data composites for dates during (A) CV18012 and (B) CE19009. The grey space represents areas covered by cloud, which in both cases is over all of the survey areas.

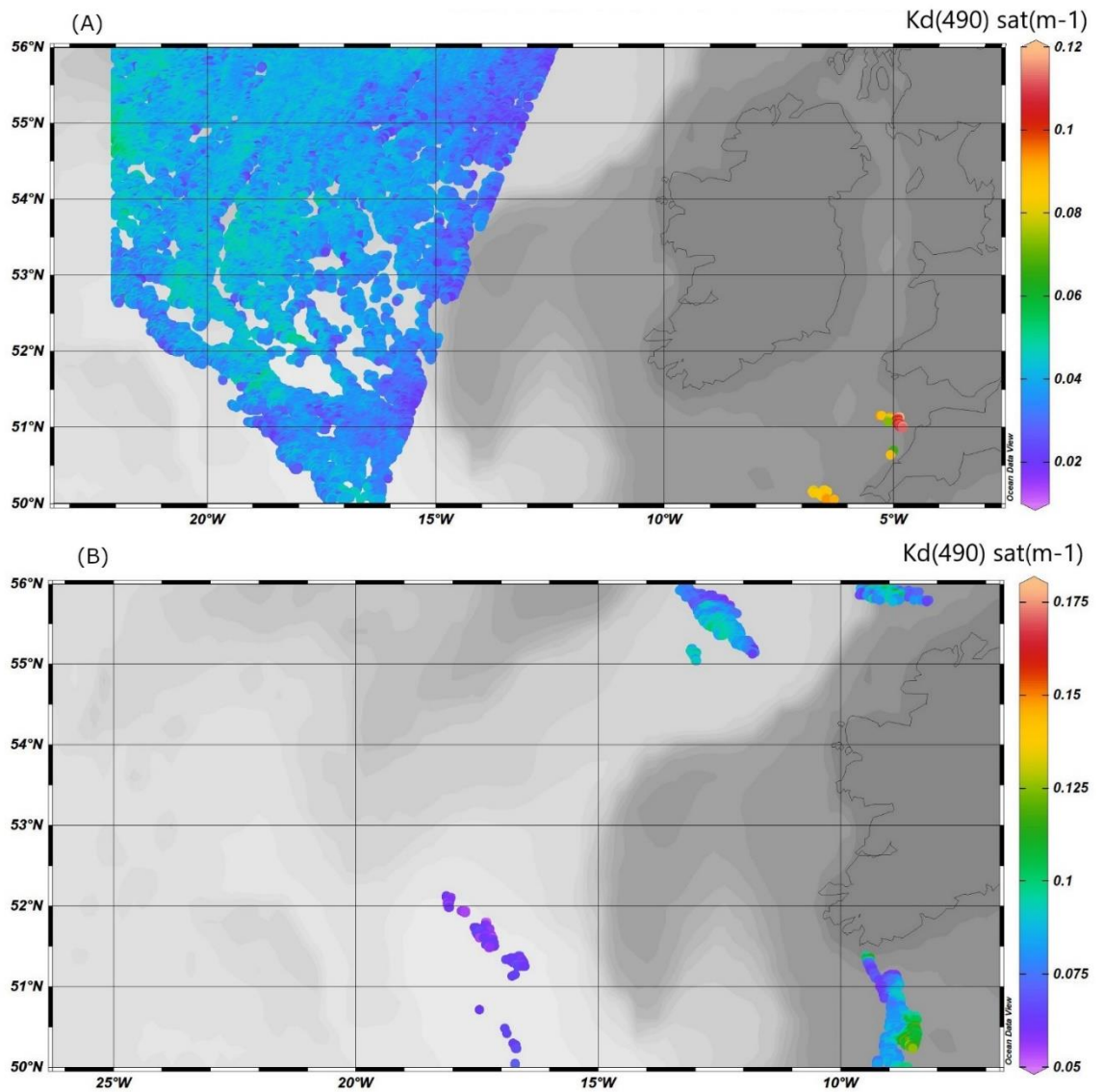


Figure 11 (A) Daily satellite derived Kd490 data from dates during CV18012. (B) Daily satellite derived Kd490 data from dates during CE19009

Figure 12 displays the average monthly data composites for dates during (A) CV18012 and (B) CE19009

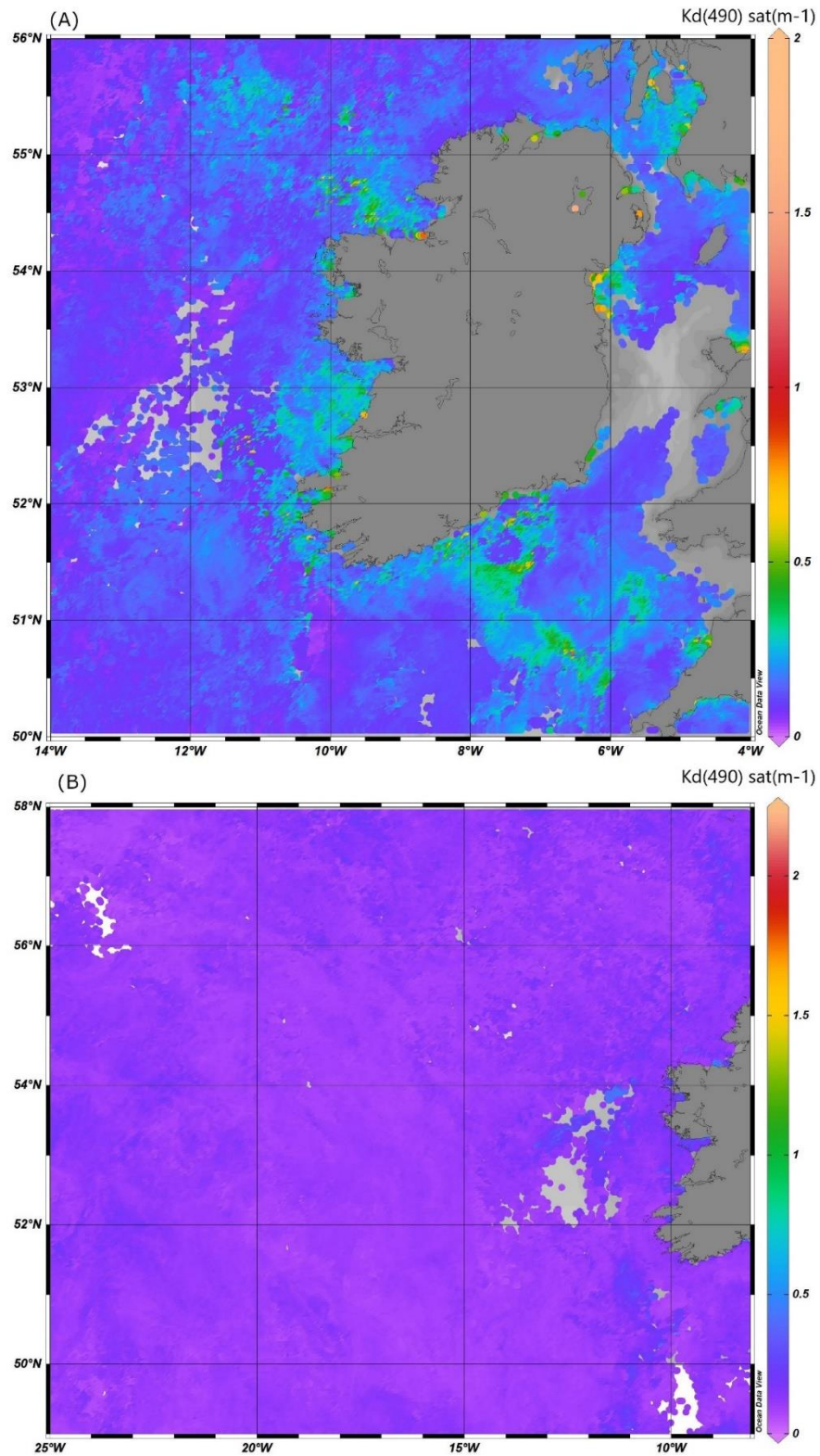


Figure 12 (A) Monthly satellite derived Kd490 average data from dates during CV18012. (B) Monthly satellite derived Kd490 average data from dates during CE19009

Figure 13 and 14 shows the $Kd(490)$ and chlorophyll 20-year climatology for January to November (1999-2019). Data received for January and November are limited and

there was no data available for December due to cloud coverage. Figure 13 illustrates the seasonal changes in Kd (490) over Irish waters over 20 years. As can be seen there is higher attenuation along coastal areas than oceanic waters in general but particularly during the winter season, coinciding with more rainfall and wind during the winter. The attenuation in the oceanic waters increases as the spring season starts. The change in attenuation of Kd (490) during spring would primarily driven by biological and physical processes in the water. This coincides with the rise in chlorophyll in spring and summer months both coastal and oceanic waters, as seen in figure 14.

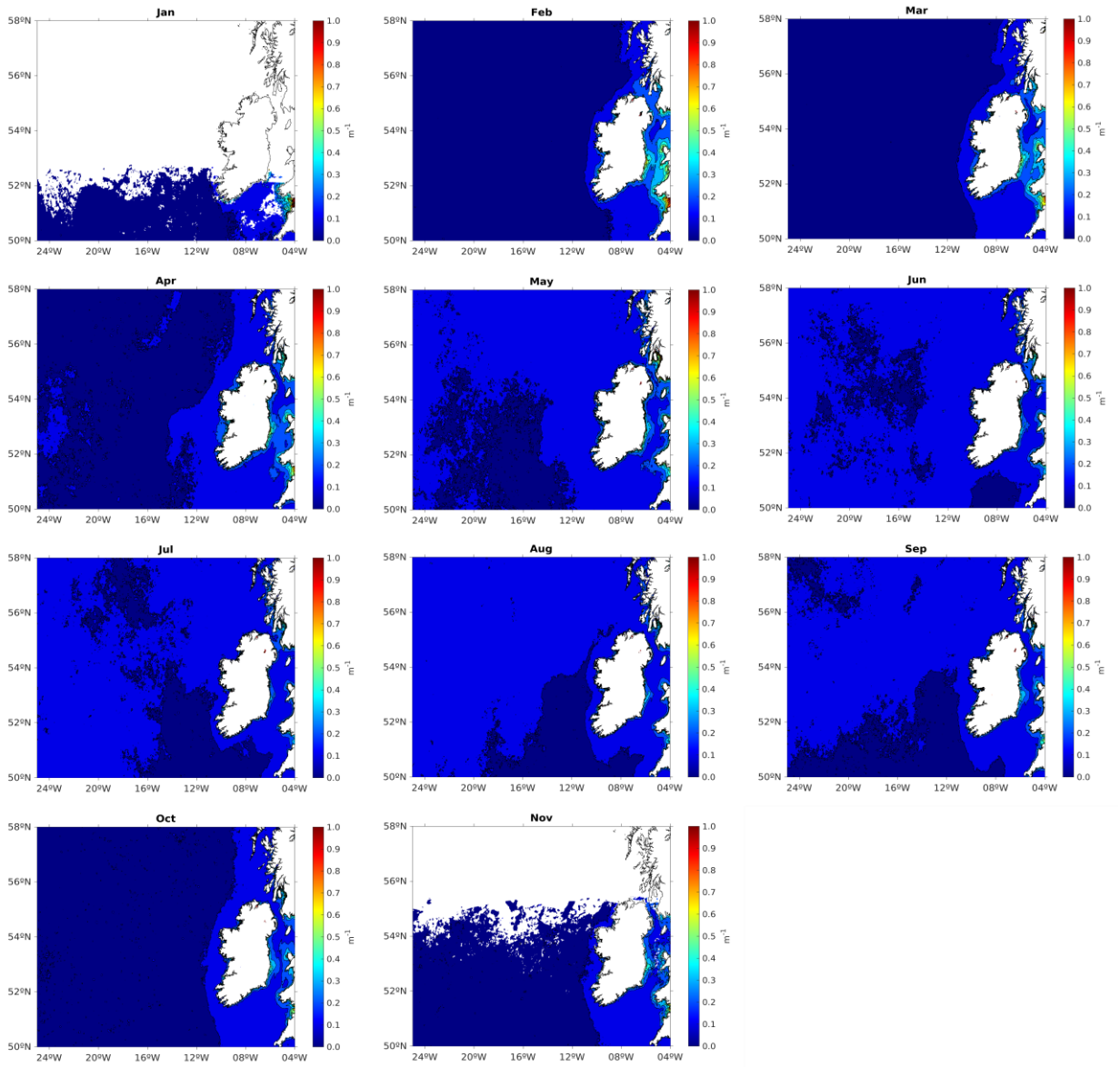


Figure 13 Monthly climatology averages for Kd(490) from January to November (1999 - 2019)

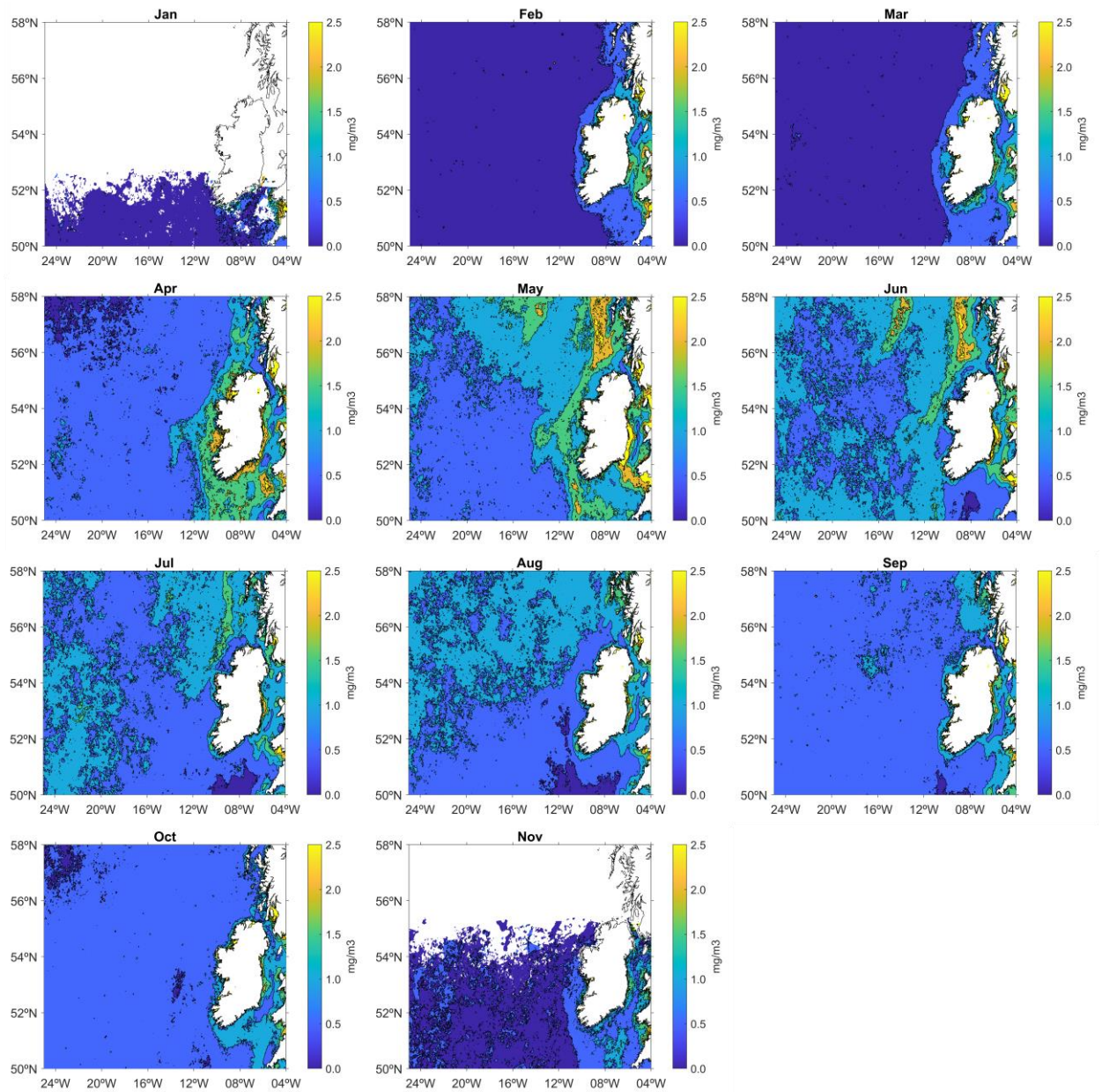


Figure 14 Monthly climatology averages for Chlorophyll from January to November (1999 - 2019)

Figure 15, which displays the data coverage percentage over Ireland from 1997 to 2019, reveals that very little data is available in December, with 0–10% coverage in certain northern Irish locations. The area around the Celtic Sea is the most covered; data coverage rises throughout July's warm months but stays relatively low in the shelf area to the west and north of Ireland. About 40% of the data is covered overall.

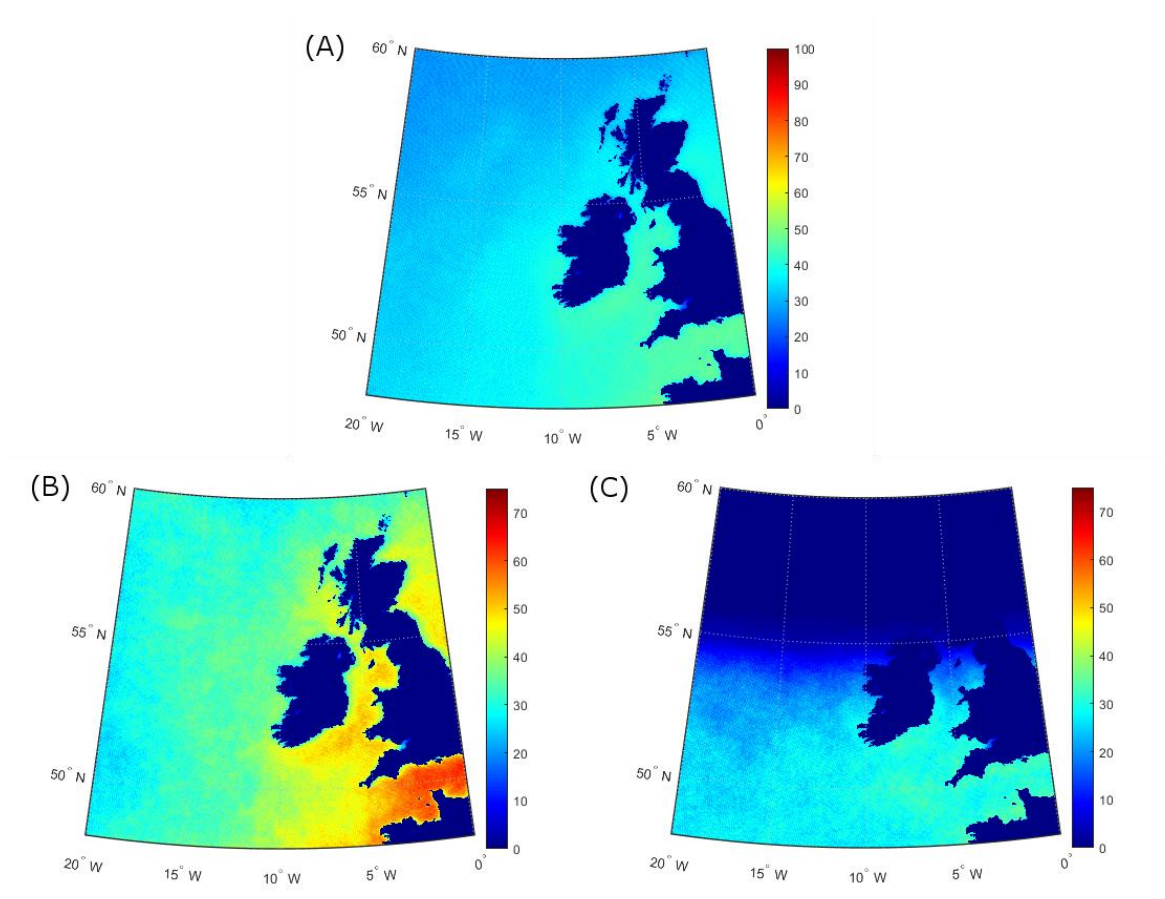


Figure 15 (A) Full year percentage data coverage generated between 1997 and 2019. (B) July percentage data coverage generated between 1997 and 2019. (C) December percentage data coverage generated between 1997 and 2019

2.5 Discussion

Algorithms used for remote sensing ocean colour are based on measurements of AOP parameters including attenuation coefficients ($Kd(\lambda)$) and remote sensing reflectance (R_{rs}). There are numerous research and applications of measuring the diffuse attenuation coefficient $Kd(\lambda)$, including biological processes like photosynthesis, heat transmission in the upper ocean, and ocean turbidity in both oceanic and coastal waters (Lee *et al.*, 2005).

In situ data is essential for checking against satellite data for many reasons but because of the high prevalence of cloud cover off the coast of Ireland, it is essential *in situ* data is measured, additionally, Irish waters lacks *in situ* optical data.

The uncertainties surrounding satellite products and how they vary between satellite missions are another factor that makes validation crucial. In their analysis employing datasets from SeaWiFS, MODIS, and MERIS, Mélin *et al.* (2016) came to the conclusion that SeaWiFS R_{rs} tend to be somewhat higher than MODIS R_{rs} and look higher than MERIS R_{rs} . Seasonal dependence may be present in biases between mission specific R_{rs} . To minimize the effects of land pixels on the satellite data, the authors of the IOCCG Protocol Series (2019), chapter 5, advocate gathering *in situ* data for ocean colour validation at least five nautical miles from the coast. In the Eumetsat (2019) recommendations of ocean colour product validation, the authors recommend comparing *in situ* values within an hour of the satellite passing, this can be extended to 3 hours to enlarge dataset match up when few data are available. In this case, zero days were available to compare *in situ* values with due to cloud cover. Figure 15 displays data for percentage of data coverage between 1997-2019. This figure further displays how cloud cover can impact data coverage. This stresses the importance of collecting *in situ* data like attenuation coefficients and remote sensing reflectance regularly. In contrast to ocean colour satellite sensors, in-water and above-water sensors have the benefit of being able to capture measurements of the ocean during days with a lot of cloud cover. Research vessels are mentioned as a source of *in situ* data for diverse parameters from the surface to the sea floor in Le Traon *et al.* (2019) and they discuss the significance of *in situ* data from various sources for The Copernicus Marine Environment Monitoring Service (CMEMS) services. The availability of *in situ* data for the Northwest European shelf region must be expanded,

according to those authors, who also emphasize the importance of data assimilation, verification, and monitoring.

McKee *et al.* (2007) discussed the feasibility of applying the $K_d(490)$ algorithm for the Irish and Celtic seas. Their results showed the algorithm performed poorly in the Case 2 waters and underestimated $K_d(490)$ values greater than 0.3 m^{-1} . Darecki *et al.* (2003) discuss the differences in how satellite ocean colour algorithms perform in Case 2 waters. Their study used case studies from waters in the Baltic and the Western Irish shelf. The authors discuss how in order for their results to be accurate in the Baltic water, a combination of spectral bands needed to be applied, whereas the more commonly used band ratio algorithm was suitable for the Irish shelf. They suggest in order for an accurate chlorophyll measurement to be made in different water bodies, a wider choice of spectral bands is needed. Multispectral ocean colour sensors with varying sensor properties that are commonly used are The Medium Resolution Imaging Spectrometer (MERIS), Moderate Resolution Imaging Spectroradiometer (Aqua-MODIS), Sea-Viewing Wide Field-of-View Sensor (SeaWiFS), The Visible Infrared Imaging Radiometer Suite (VIIRS), and the Ocean and Land Colour Instrument (OLCI) (Groom *et al.*, 2019). The NASA Plankton, Aerosol, Cloud, Ocean Ecosystem (PACE) mission, which is due to launch in 2024 will cover a spectral resolution of 340 to 890 nm and a spatial resolution of 1 km, is one of the upcoming hyperspectral satellite missions (Werdell *et al.*, 2019) and will create a lot more opportunities for accurate measurements of ocean colour.

During this study 59 stations were sampled using a TriOS RAMSES-ACC hyperspectral irradiance sensor between the dates 3 – 16 April 2018 and 24 May – 6 June 2019. *In situ* attenuation coefficients were generated for each sample location. Figure 10 illustrates examples of attenuation coefficient plots generated throughout the survey stations. *In situ* $K_d(490)$ values were calculated from this data. The lowest value recorded was 0.02 m^{-1} at station 15 at 52.999 latitude and -14.9907 longitude from CE19009 in the North Atlantic and the highest attenuation coefficient value recorded was 0.52 m^{-1} from the mixed water stations in the Irish sea at station six CV18012 53.27493 latitude and -5.49753 longitude. Station 15 from CE19009 would be classed as Case 1 waters and station six from the mixed water stations would be classed as Case 2 waters. Only 12 out of 50 stations had a value of $<0.10 \text{ m}^{-1}$ and 92% of the 12 stations were from the West coast sampling stations and classed as Case 1

waters. At 46 stations the attenuation coefficient value was $>0.10 \text{ m}^{-1}$. The 46 stations were a mix of Case 1 and Case 2 waters. 8 out of the 59 stations had values $>0.20 \text{ m}^{-1}$ and 75% of these stations were in Case 2 waters. 63% of the stations had a value of 0.10 m^{-1} - 0.20 m^{-1} and again were a mix of Case 1 and Case 2 waters. The Irish Sea displays both case 1 and case 2 traits, the optical complexity results from regional variations in tidal mixing, freshwater influx, and bathymetry that form separate hydrographic regions (Gowen *et al.*, 1995). Gowen *et al.* (1995) describe how the offshore waters of the western Irish Sea become seasonally stratified each year. During CV18012 11 stations were sampled in a stratified area of the Irish sea while nine were sampled in a mixed water area. The attenuation coefficient values from the mixed water area ranged from 0.11 m^{-1} to 0.52 m^{-1} and in the stratified area ranged from 0.05 m^{-1} to 0.22 m^{-1} , much lower values than the mixed water.

Waters that are situated away from the coast in the west of Ireland in the North Atlantic would generally be considered Case 1 waters but during the CV18012 survey in April 2018, surface water with lower salinity was observed above a warmer more saline bottom layer on the Aran grounds (McGeady *et al.*, 2019). Huang *et al.* (1993) discusses the possible origin for this is from Ireland's largest river, the River Shannon. According to Huang *et al.* (1993), as the River Shannon plume moves northward towards the Aran grounds, its temperature and salinity differ from the nearby coastal waters. With maximum temperature variations of 1.5°C , the plume is warmer in the summer and cooler in the spring relative to coastal seas. Because of the influx of fresh water, the waters can become more complex due to the influence of land.

During CE19009 and CV18012 there were zero cloud free days to directly compare *in situ* values and satellite derived values. Because there were no cloud free days during that time it is difficult to compare the monthly value to the *in situ* value as this is an average value of 30 days, and as the authors have discussed water transparency is modified by changes in the water's optical active constituents including phytoplankton, suspended sediments, and coloured dissolved organic matter which affects the water column's attenuation of light (Curtarelli *et al.*, 2020) and this can change daily.

The K_d (490) and chlorophyll-*a* 20-year climatology for January through November of 1999–2019 are displayed in Figures 13 and 14. Limited data was received for

January and November, and due to cloud coverage, no data was available for December. The seasonal variations in $K_d(490)$ over a 20-year period over Irish waters are shown in Figure 13. It is evident that there is more attenuation along coastal areas than in oceanic waters overall, but this is especially true in the winter when there is an increase in wind and precipitation. As spring arrives, the attenuation in the oceanic waters rises. The biological and physical activities occurring in the water would be the main causes of the shift in $K_d(490)$ attenuation during the spring. This is in line with the springtime increase in chlorophyll and summer months both coastal and oceanic waters, as seen in figure 14.

In order to perform photosynthesis, phytoplankton need light. The depth and intensity of light penetration in water are directly influenced by the attenuation coefficient, which in turn impacts the growth and productivity of phytoplankton. Changes in the attenuation coefficient can be a sign of altered water quality, which affects the dynamics of phytoplankton. Light penetration can be changed by elements such as increasing turbidity or the presence of other particles, which might impact phytoplankton. Understanding the vertical attenuation of irradiance is critical for remote sensing techniques used in monitoring phytoplankton from space. These methods depend on a precise interpretation of the interactions and modifications of light by phytoplankton inside the water column.

Based on this information Joint and Groom (2000) discusses how phytoplankton is essentially connected to the vertical attenuation of irradiance through its impact on light penetration in water, which is a critical factor for phytoplankton growth and distribution. Understanding these dynamics is key for effective monitoring and management of marine ecosystems.

The benefits of combining ocean colour sensors are demonstrated by the use of the GlobColour product for a 20-year climatology. By merging data from multiple sensors, this method greatly increases the accuracy and reliability of $K_d(490)$ and Chlorophyll-*a* calculations. Improved temporal and spatial coverage is the end result, which is especially useful for monitoring vast and dynamic marine environments. Combining sensors also offers a more consistent and comprehensive view of ocean conditions, supporting a range of industries from marine ecosystem management to

climate research and producing a more complex and in-depth understanding of ocean properties (Garneison *et al.*, 2019).

2.6 Conclusions

In this work we describe the collection of *in situ* attenuation coefficient values from two research surveys CV18012 and CE19009. The two research surveys took place in optically different water bodies, the open waters of the NE Atlantic (CE19009) and optically more complex waters, the Aran grounds and the Irish sea stations (CV18012). One of the original objective of this study was to compare and determine whether there was a relationship between the *in situ* dataset and satellite derived Kd (490) values. During the 26 days the *in situ* samples were collected there was constant cloud cover when the satellite passed therefore there was zero daily data to statistically compare to. We assessed the trends of 20 years worth of attenuation data around Irish waters. It is clear that attenuation around coastal areas is greater than in overall oceanic seas, and this is particularly true during the winter months when precipitation and wind are higher. The attenuation in the maritime waters increases as spring approaches. The primary causes of the change in Kd (490) attenuation in the spring would be the biological and physical activity taking place in the water. This is consistent with the rise in chlorophyll-*a* that occurs in the spring and the summer months in both marine and coastal waters, as shown in figure 14.

This chapter recognises the limitations of satellite technology in monitoring Irish seas, notably during specific periods of the year when cloud cover the ocean colour sensor, but it also emphasises the critical significance of *in situ* data, particularly in under sampled regions. *In situ* data is vital for satellite validation and algorithm development. On the other hand, the addition of a 20 year Kd (490) climatology and chlorophyll-*a* trends off the coast of Ireland highlights the considerable potential of satellite technology in clear sky situations. There are various benefits of integrating this algorithm into the Irish monitoring programme.

Large-Scale Monitoring: The study of phytoplankton distribution is made easier by satellite technology, which provides thorough coverage across large and remote oceanic areas, beyond the capabilities of *in situ* approaches.

Temporal Coverage: Observing phytoplankton populations continuously using satellites allows scientists to track long-term trends, seasonal variations, and reactions to climate change.

Water Quality and Productivity Indicator: One important measure of water clarity is the attenuation coefficient, which is obtained from satellite data. This has direct implications for phytoplankton photosynthesis, as clearer waters allow for deeper light penetration and potentially more robust phytoplankton growth.

Monitoring the health of ecosystems: Because phytoplankton is essential to marine food webs, variations in the attenuation coefficient can be used to detect changes in phytoplankton populations. In order to assess the productivity and overall health of marine ecosystems, this data is crucial.

Studies on Climate Change: By using satellite-derived attenuation coefficients to monitor phytoplankton, we can gain a better understanding of their role in sequestering carbon and the wider consequences for the global carbon cycle and climate change.

Operational Efficiency: Satellite monitoring is a viable option for frequent and comprehensive evaluations because it is less expensive and labor-intensive than in situ sampling.

The utilisation of attenuation coefficients generated from satellites offers a dynamic and all-encompassing viewpoint on phytoplankton activities, substantially expanding research endeavours in oceanography, marine resource management, and environmental protection.

The findings of this chapter form a foundation for the research presented in Chapter 3, which focuses on developing a remote sensing reflectance monitoring system. This system is designed for continuous measurements, aiding in algorithm development and satellite validation, thereby reinforcing the value of integrating satellite and *in situ* data for oceanographic studies.

3. Chapter 3:

Documenting a Continuous and Autonomous Above-Water Hyperspectral Radiometry System on a Research Vessel in the NE Atlantic

Catherine Jordan^{1,2}, Caroline Cusack², Jochen Wollschläger³, Adam Leadbetter², Ramona Carr², Rob Thomas², Peter Croot¹.

¹Earth and Ocean Sciences and Ryan Institute, School of Natural Sciences, University of Galway, H91 TK33 Galway, Ireland

²Marine Institute, Rinville, Oranmore, H91 R673 Galway, Ireland

³Institute for Chemistry and Biology of the Marine Environment, University of Oldenburg, Wihelmshaven, Germany

Submitted for peer review to *Frontiers in Remote Sensing- Optical Radiometry and Satellite Validation Research Topic*

3.1 Abstract

A five sensor above-water hyperspectral radiometry system was installed on the RV Celtic Explorer; Ireland's largest research vessel. Instrumentation set-up included a TriOS RAMSES-ACC hyperspectral cosine irradiance meter for $E_s(\lambda)$ downwelling solar irradiance E_s and four TriOS RAMSES ARC hyperspectral radiance meters: two for measuring radiance $L_{sfc}(\theta_{sfc}, \Phi_{Sun}, \lambda)$ emerging from the sea surface and two for measuring sky leaving radiance $L_{sky}(\theta_{sky}, \Phi_{Sun}, \lambda)$, with the sky and sea surface radiance sensors at zenith angles $\theta_{sfc} = 45^\circ$ and $\theta_{sky} = 135^\circ$. The radiometers collect measurements automatically at 15-minute intervals with automatic time integration throughout the survey path over a spectral range of 300-950 nm using the TriOS RAMSES software Multi Sensor Data Acquisition System- Extended Edition (MSDA_XE). Measurements are autonomous and continuous during daylight hours (07:00-21:00) resulting in over 100,000 files for a three-week scientific survey. The end-to-end pipeline of hyperspectral data collection and processing was documented under the Marine Institute's Data Management Quality Management Framework (DM-QMF) through the creation of an Implementation Pack for the TriOS RAMSES hyperspectral system on the RV Celtic Explorer. The DM-QMF implementation Pack consists of documented Standard Operating Procedures (SOPs), Process Flows, a Requirements and Acceptance Criteria Document, a Data Management Plan, a Data

Catalogue Record, Digital Object Identifiers and Performance Evaluations. The implementation pack documents cover both the operation of the hyperspectral system (including data processing) and the data management of the outputs produced by the system. The implementation of the DM-QMF by the Marine Institute fulfilled the Quality Management System requirement for accredited National Oceanographic Data Centre status, as awarded to the Marine Institute in 2019 by the International Oceanographic Data and Information Exchange of UNESCO's Intergovernmental Oceanographic Commission (IOC-IODE). Remote sensing reflectance data, derived from the TriOS RAMSES above water radiometer measurements accompanied with ocean colour satellite derived data is presented here. Data from two RV Celtic Explorer research surveys between May 2019 and July 2019 were used to determine whether a statistical relationship between the *in situ* and the satellite derived datasets was present. Comparisons are made between the RV Celtic Explorer hyperspectral above-water remote sensing reflectance and Copernicus Marine Environment Monitoring Service (CMEMS) satellite ocean colour ESA-CCI data products. Satellite derived remote sensing reflectance bands investigated included 443nm, 490nm, 510nm and 560nm. Statistical results between the two datasets all returned a positive correlation and the strongest correlation was with the 560nm band ($r = 0.8540$ $p < 0.05$) a low root mean square error value ($\Psi = 0.0012$) and a relative percentage difference of 33.5%.

The objective of this study is to highlight the ship-based above-water radiometry system to the ocean colour community and the products associated with this data (satellite validation, water quality monitoring, bio-optical modelling and algorithm development) highlighted by a case study of satellite validation from 2019.

3.2 Introduction

3.2.1 Ocean Colour

Determining the colour of the ocean by measuring remote sensing reflectance (R_{rs} , units: sr^{-1}) or water leaving radiance (L_w) is a non-invasive method of measuring optically active constituents within the water column (chlorophyll-*a*, coloured dissolved organic matter (CDOM), the water itself, non-algal particles) (IOCCG, 2000). R_{rs} is defined as the ratio of water-leaving radiance (L_w , units: $\mu\text{W cm}^{-2} \text{sr}^{-1} \text{nm}^{-1}$) to downwelling irradiance just above the sea surface (E_s , units: $\mu\text{W cm}^{-2} \text{nm}^{-1}$) (O'Reilly *et al.*, 1998).

Ocean colour satellite sensors provide large scale comprehensive observations of biogeochemical properties of the upper layer of the ocean (Groom *et al.*, 2019). These measurements from space provide important information on marine life and ecological processes. Their worldwide coverage and range of temporal and spatial scales are in good agreement with the dynamics of these processes. Applications are numerous and include managing fisheries as well as comprehending biogeochemical cycles, ecosystem health, and climate change. Complementing other marine research techniques and models with satellite observations is essential for a thorough understanding of marine ecosystems (Sathyendranath *et al.*, 2023).

3.2.2 Satellite Validation

R_{rs} is calculated from top of atmosphere (TOA) radiance and is the primary ocean colour product, this product is used to determine the optical constituents in seawater. The signal received by the satellite sensor is relatively small (<10%), due to light scattered by the atmosphere, and requires highly accurate correction methods (Wang *et al.*, 2009). Therefore, regional validation is an essential step to provide an evaluation on whether the observations from satellite sensors are accurate (IOCCG, 2012). As previously stated, satellite data is a powerful tool to monitor water quality and phytoplankton blooms. However, reference of ground validation work of satellitederived products is required. This is accomplished through the comparison of satellite products with *in situ* products using various methods, many studies highlight the importance of validation and also the comparison of different validation efforts

(e.g. O'Reilly *et al.*, 1998; Bailey and Werdell 2006; Zibordi *et al.*, 2012; Garaba *et al.*, 2015; Brando *et al.*, 2016, Concha *et al.*, 2021). Another reason why validation is essential is the uncertainties associated with satellite products and how they differ between satellite missions. Mélin *et al.* (2016) describe this, in their study using datasets from SeaWiFS, MODIS and MERIS they concluded SeaWiFS R_{rs} tend to be slightly higher than MODIS R_{rs} and appear higher than MERIS R_{rs} . Biases between mission specific R_{rs} may exhibit a seasonal dependence. In the IOCCG Protocol Series (2019), chapter 5, the authors recommend to collect *in situ* data for ocean colour validation at least five nautical miles from the coast in order to minimise the impacts of land pixels on the satellite data. For this study, statistical comparisons were made between *in situ* above-water radiometry and satellite data centered at the geographic location where the above-water measurements were collected as described in the ESA Ocean Colour Climate Change Initiative report (Calton, 2021). Concha *et al.*, (2021) reviews the various validation approaches that are used by the ocean colour community and explains that not one single approach is used to quantify and report uncertainties associated with ocean satellite measurements.

3.2.3 Hyperspectral Radiometers

To determine R_{rs} *in situ*, radiometric measurements are performed and can be used for a variety of applications such as satellite validation, water quality monitoring, bio-optical modelling, and algorithm development. These measurements can be made using above and in water approaches and from fixed platforms or ships (e.g. Mobley 1999; Zibordi *et al.*, 2002; Garaba *et al.*, 2014a, 2014b; Garaba and Zielinski 2013; Hommersom *et al.*, 2012; Zibordi *et al.*, 2012; Brando *et al.*, 2016; Tilstone *et al.*, 2017; 2020; Pitarch *et al.*, 2020; Concha *et al.*, 2021). The above-water sensors have the advantage that they can still be used to record measurements of ocean surface reflectance during days with cloud cover, unlike ocean colour satellite sensors. Many opportunities will exist in the future to develop more sophisticated algorithms for phytoplankton bloom detection with the use of both *in situ* hyperspectral radiometers and newer satellite technology, such as the PACE mission (Werdell *et al.*, 2019). Le Traon *et al.* (2019) discusses the importance of *in situ* data from different sources for The Copernicus Marine Environment Monitoring Service (CMEMS) services, with research vessels named as a source of *in situ* data for multidisciplinary parameters

from the surface to the sea floor. These authors also stress the need to increase the *in situ* data coverage for the North West European shelf region, stating that data availability for all parameters plays a key role in data assimilation, verification, and monitoring. Since 2019, five TriOS RAMSES hyperspectral radiometers have been installed on the RV Celtic Explorer, Ireland's largest research vessel. These types of radiometers are well reviewed in the literature (Garaba *et al.*, 2012; 2014a, 2014b; 2015; Alikas *et al.*, 2020; Tilstone *et al.*, 2020).

Alikas *et al.* (2020) study compared two different radiometric systems: the TriOS-Radiation Measurement Sensor with Enhanced Spectral resolution (RAMSES) and the Seabird-Hyperspectral Surface Acquisition System (HyperSAS). These systems were tested under various environmental conditions across the Atlantic Ocean. Their study aims to evaluate the consistency and reliability of these systems for measuring ocean colour and radiometry. Findings include variability in sensor responsivity, straylight effects within $\pm 3\%$, and the impact of near-infrared correction on water-leaving reflectance and radiance. The study recommends additional sensor and environmental measurement characterization to refine *in situ* uncertainty estimates. The results generally agreed within uncertainty limits and showed satisfactory consistency with Sentinel-3A OLCI data.

Tilstone *et al.* (2020) study discusses a field intercomparison of radiometer measurements conducted at the Acqua Alta Oceanographic Tower in the Adriatic Sea. This study aimed to assess the accuracy of in- and above-water radiometer measurements used for validating ocean colour products. Ten measurement systems were compared, all calibrated at the same reference laboratory. The study found good agreement among sensors for various radiometric quantities, with differences generally within acceptable limits. It highlighted the importance of minimising errors in downwelling irradiance measurements to reduce overall variability in remote sensing reflectance.

The system will ensure above-water hyperspectral radiometer data is being collected long term and along each survey path the RV Celtic Explorer takes. These are the first time measurements of this kind to will be collected on Ireland's national research vessel in Irish coastal, shelf and oceanic waters over a long period of time. The data provided by these sensors will be extremely useful for the applications mentioned

above, such as water quality monitoring, region specific bio-optical algorithm development, and satellite validation as detailed in this study. The sensors will provide data during the days that satellite measurements are limited due to cloud cover, which account for many days of the year in Ireland, as seen in figure 15, chapter 2, approximately 40% of data coverage was available over Irish waters between 1997 and 2019.

However, when using these types of instruments, whether on a fixed ocean platform (e.g. data buoy) or a moving platform (research vessel), associated errors occur due to meteorological effects. An important factor to consider when installing sensors on a platform is to ensure there is no optical interference from the platform itself, therefore it is suggested to install the sensors high and clear of any surface area from the vessel or platform (Zibordi *et al.*, 1999).

Mobley (1999) explains that all measurements taken above the water surface are subject to contamination due to solar angle. This anomaly occurs when sun or skylight is reflected directly into the optical sensor (Busch *et al.*, 2013). Principally, R_{rs} is calculated as the ratio of two properties; L_w and E_s (Equation. [1]). However, L_w (the water leaving radiance) is difficult to measure directly, as above-surface sensors always have to look at a certain angle towards the sea surface to avoid self-shadowing. Therefore, the respective measurement L_{surf} (radiance measured from the sea surface) contains also a certain proportion of skylight reflected by the sea surface (L_{sky}), which has to be measured separately in order to estimate L_w .

$$R_{rs} = \frac{L_w}{E_s} = \frac{L_{surf} - L_{sky} * \rho}{E_s} \quad [1]$$

The proportion factor ρ depends on a variety of parameters, including sea roughness (thus wind speed), wavelength, and viewing geometry (Mobley 1999, Lee *et al.*, 2010). Frequently, a value of $\rho=0.028$ is used, which is a reasonable estimate for a variety of conditions (Mobley 1999). Since L_w and E_s are obtained independently and since assumptions regarding the water reflectivity ρ had to be made to estimate L_w from the measured L_{sky} and L_{surf} data, and all measurements are subject to errors from optical interference from platforms and meteorological effects, assessment of the quality of the hyperspectral data is crucial (Wei *et al.*, 2016b).

Wei *et al.* (2016b) raised the importance of quality assessment of large hyperspectral datasets. In this context, Garaba *et al.* (2012) discuss an empirical quality control protocol for above-water measurements, these authors describe their method which consists of meteorological flags that will mask dusk, dawn, precipitation, and low light conditions, utilising incoming solar irradiance (E_s) spectra. In their work, this was achieved by testing 3,121 spectral measurements, of which 629 passed the test conditions using the meteorological flags. The three meteorological flags were $ES(\lambda = 480 \text{ nm}) > 20 \text{ mW} \cdot \text{m}^{-2} \cdot \text{nm}^{-1}$ setting a threshold for which significant $ES(\lambda)$ can be measured

$ES(\lambda = 470 \text{ nm}) / ES(\lambda = 680 \text{ nm}) < 1$ masking spectra affected by dawn/dusk radiation

$ES(\lambda = 940 \text{ nm}) / ES(\lambda = 370 \text{ nm}) < 0.25$ masking spectra affected by rainfall and high humidity

Satellite and shipborne hyperspectral radiometry data have both advantages and disadvantages. Satellite data can have global coverage and a high temporal resolution while shipborne data have local coverage with low temporal resolution meaning the data is very detailed from that point in time but a satellite can provide more frequent and consistent observations of the ocean at different points. Satellite and shipborne data have different trade-offs between temporal resolution and data quality reduction. Another difference is that satellite hyperspectral data are affected by cloud cover, as described in chapter 2, this is a very big issue in Ireland, however, shipborne hyperspectral data do not have this problem, as the data are collected directly from the ocean surface. Combining both sets of data can provide a comprehensive and detailed picture of ocean properties and processes (Groom *et al.*, 2019).

3.2.4 Data Management Quality Management Framework (DM-QMF)

Due to the large quantity of data collected using this type of system, it is vital a structured process is in place for the short and long-term storage of the data. It is also important that clear and concise instructions are available about the overall running of the hyperspectral system. For these reasons a Data Management Quality Management Framework (DM-QMF) implementation pack was developed for the hyperspectral radiometer system on board the RV Celtic Explorer. Leadbetter *et al.* (2019) provide

an in depth description of the various roles involved in the DM-QMF process such as data owner, data coordinator, data steward and data protection officer.

The DM-QMF Implementation pack was developed with a series of templates that guide data stewards and data owners throughout the process. In 2013, The International Oceanographic Data and Information Exchange of UNESCO's Intergovernmental Oceanographic Commission (IOC-IODE) released advice for National Oceanographic Data Centres (NODCs) to implement quality management systems for the successful delivery of oceanographic and related products. The IOC-IODE encourage NODCs to implement a quality management system and to demonstrate they are in conformity with ISO 9001, the international standard for quality management. A goal of the IOC-IODE's guidance is to "promote accreditation of NODCs according to agreed criteria." (Leadbetter *et al.*, 2019). The Marine Institute (as the Irish NODC) included "Quality" as a goal in their Data Strategy (2017-2020) in response to the IOC-IODE guidance and to the requirements of funding agencies. Tray *et al.* (2020) describes the benefits of using the DM-QMF system for fish scales and otolith archives. Their study describes the importance of adequate storage of long-term data and present a case study that describes an open source database which utilises the FAIR (Findable Accessible Interoperable and Reusable) open data principles (Wilkinson *et al.*, 2016). Tanhua *et al.* (2021) also discusses the importance of FAIR data while quantifying carbon relevant ocean data in an accessible location and format is key to understanding and mitigating against anthropogenic impacts on the Earth's climate. The DM-QMF process is beneficial for many reasons. It is a live system and documents can be updated as the project progresses. The documents are stored together on a shared drive within the Marine Institute. This is useful for current staff and when there is crossover of staff, all the documents on how the system works are available to new users and this helps ensure the existing sampling or processing methods are continued. The overall system is structured to include performance evaluations after the pack is complete and to ensure if the system needs improvement, it will be addressed annually to ensure continuity of the collection of high-quality data.

3.2.5 Objectives of this Chapter

The primary objective of this study is to highlight the capabilities of a recently installed above-water hyperspectral radiometry system on board the RV Celtic Explorer with the steps taken to create a DM-QMF Implementation Pack, which ensures continuity and reproducibility of data also in the post-project phase. Throughout this paper the authors provide examples on data use and some products derived from the processed data. Examples are presented to demonstrate how the end product R_{rs} data is acquired and processed. The above-water hyperspectral data is statistically compared with R_{rs} satellite data to establish how closely these datasets match to demonstrate how the data can be used for satellite validation.

3.3 Methods

3.3.1 Study Area

108 stations were carried out between two research surveys: CE19009 and CE19010. These surveys took place between dates of May 24 2019 and July 24 2019. The survey path covered ocean areas between 47° N to 58° N and 5° W to 22° W. Areas in this region include the Bay of Biscay, the Celtic Sea, the Porcupine Bank and the Rockall Trough. Throughout those 108 stations 28 *in situ* R_{rs} spectra from the above water hyperspectral radiometer sensors were analysed for comparison with satellite derived data. The decrease from 108 to 28 stations was influenced by factors such as the number of daylight hours, the timing of satellite passes, and the availability of viable data.

3.3.2 TriOS RAMSES Hyperspectral Radiometer System On Board The RV Celtic Explorer

A TriOS RAMSES three sensor above-water hyperspectral radiometry system was installed on the RV Celtic Explorer for above-water surface reflectance measurements in 2018 (Figure 16 A). This system was upgraded to five sensors in 2020 (Figure 16 B). The acquisition of two additional sensors allows for a sensor suite of dual port and starboard sensors (two reflectance angles) with one sensor measuring the overall downwelling irradiance. This design greatly increases the amount of useable data recovered while the ship is at sea under normal operation as during most operations

one set of sensors will not be impacted by solar glint, ship shadow or other interferences that result in interferences to reflectance data. It was anticipated that upon acquisition of the two additional radiance sensors that the percentage of useable reflectance data obtained from the Celtic Explorer would more than double. Thus depending on the ships's operation and the length of the expedition, it was anticipated this would result in an increase from 20-30% useable data with the 2018 three sensor operation to 60-70% coverage with the five sensor system. As such this will greatly increase both the spatial and temporal coverage for reflectance data in Irish waters and provide new data for validation of satellite estimates of ocean colour parameters and provide baseline data for new inverse models of seawater optical properties.

The instrumentation includes a TriOS RAMSES-ACC hyperspectral cosine irradiance meter for $E_s(\lambda)$ downwelling solar irradiance and TriOS RAMSES ARC hyperspectral radiance meters; two for measuring radiance $L_{sfc}(\theta_{sfc}, \Phi_{Sun}, \lambda)$ emerging from the sea surface and two for measuring sky leaving radiance $L_{sky}(\theta_{sky}, \Phi_{Sun}, \lambda)$, with the sky and sea surface radiance sensors at zenith angles $\theta_{sfc} = 45^\circ$ and $\theta_{sky} = 135^\circ$. The ACC hyperspectral cosine irradiance meter for $E_s(\lambda)$ and one pair of L_{sfc} and L_{sky} radiometers were mounted on the port side of the vessel (see Figure 16 A) and the other L_{sfc} / L_{sky} pair was mounted on the starboard side of the vessel (Figure 16 B). In the course of data processing, $E_s(\lambda)$ is used as downwelling solar irradiance for both pairs of sensors. The five instruments are mounted permanently on the vessel 13.1 m above the sea surface. The sensors are mounted above the bridge on the vessel on a platform called 'monkey island' (Figure 16 C). Field of View (FOV) is 7° for radiance sensors and 180° for the irradiance sensor. The radiometers collect irradiance and radiance measurements automatically at 15-minute intervals with automatic integration time throughout the survey path over a spectral range of 300-950 nm (λ) using the TriOS RAMSES software Multi Sensor Data Acquisition System- Extended Edition (MSDA_XE) (Figure 16 D). Measurements are autonomous and continuous during day light hours of 07:00-21:00 resulting in over 100,000 files for a three-week scientific survey. The system is sent to the TriOS factory in Germany every two years for a full calibration. See Appendix A3 for standard operating procedure for software set up.

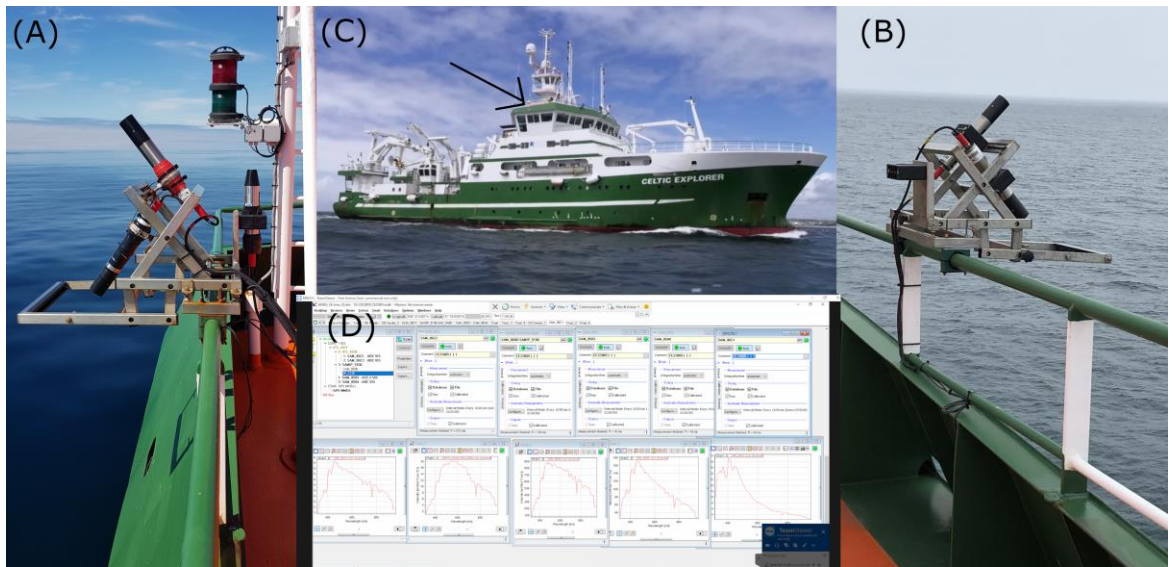


Figure 16 (A) A TriOS RAMSES-ACC hyperspectral cosine irradiance meter for $E_s(\lambda)$ downwelling solar irradiance and 2 TriOS RAMSES ARC hyperspectral radiance meters; 1 for measuring radiance $L_{sfc}(\theta_{sfc}, \Phi_{Sun}, \lambda)$ emerging from the sea surface and 1 for measuring sky leaving radiance $L_{sky}(\theta_{sky}, \Phi_{Sun}, \lambda)$ on the port side of the vessel (B) 2 TriOS RAMSES ARC hyperspectral radiance meters; 1 for measuring radiance $L_{sfc}(\theta_{sfc}, \Phi_{Sun}, \lambda)$ emerging from the sea surface and 1 for measuring sky leaving radiance $L_{sky}(\theta_{sky}, \Phi_{Sun}, \lambda)$ (C) RV Celtic Explorer with an arrow pointing to the platform the sensors are mounted on, above the bridge (D) a screen grab of the TriOS Ramses software MSDA_XE where the sensors are controlled from.

3.3.3 Process Flow

As part of the DM-QMF implementation pack, a process flow was developed to visually represent how the system works from the factory calibration of sensors to exporting data before processing (Figure 17). This visual representation is directly connected to all SOPs required to run the system and includes in-depth descriptions of the routines followed.

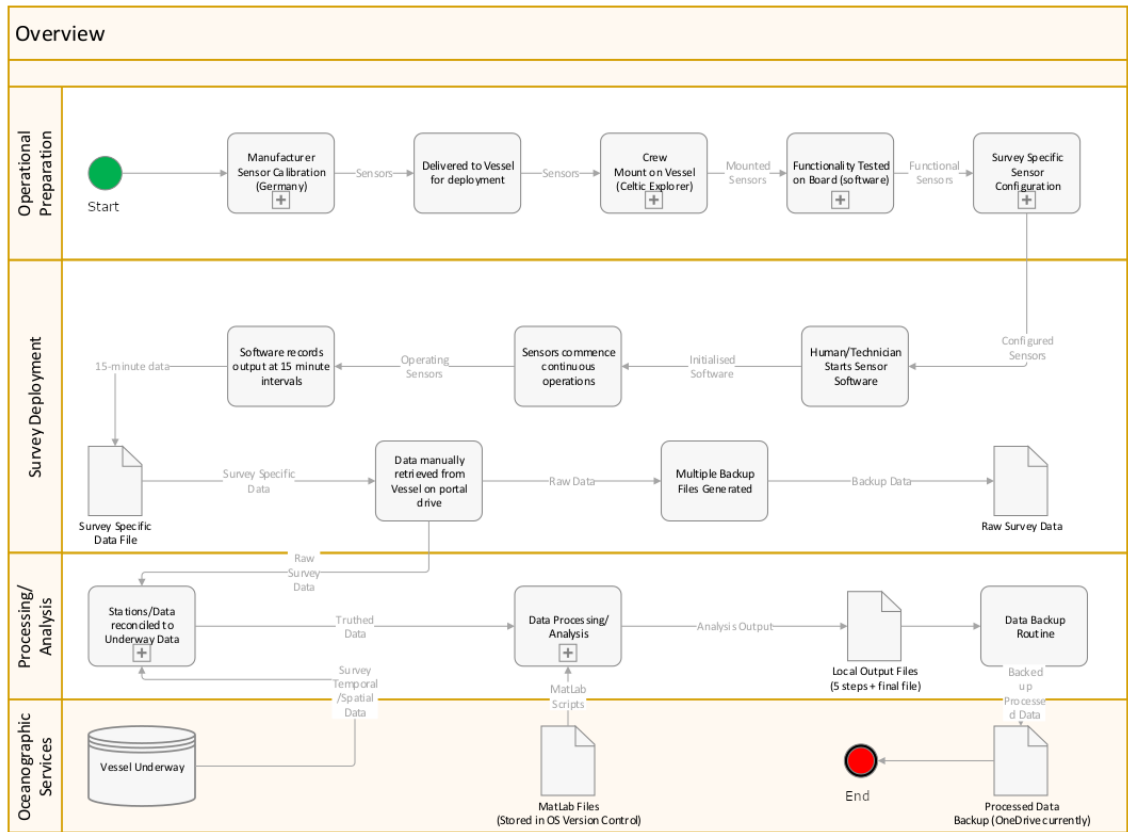


Figure 17 Process Flow that visually describes the steps from Manufacturer calibration to Rrs Data output.

TriOS RAMSES Data Processing Method

Data collected during each scientific survey has its own dataset in the MSDA_XE software with global positional system (GPS) references.

The Process Flow (Figure 17) includes a step to cross reference with the vessel underway GPS data when there is a query about ship position when the vessel is stationary, or when a GPS location is missing from the database.

Figure 18 displays a detailed Process Flow, a graphic representation of how the raw data is processed and the R_{rs} product is generated. The data files are exported in a TriOS native file format (.dat) and processed using a five-step process with a series of Matlab (Mathworks, USA) scripts described below. The individual survey specific database is accessed using MSDA_XE software. The data is then exported in TriOS format (as a *.dat file). The raw data is transferred to at least two external hard drives for back-up and further processing. The folder with the raw data is linked to Matlab where five scripts (created by Jochen Wollschläger and are listed in Appendix A1) are

used to process the data. The five steps include (1) Create daily files, (2) Calibrate daily files with the TRIOS instrument factory sensor specific calibrated settings, (3) Create working files from the calibrated data, (4) Calculate the remote sensing reflectance, (R_{rs}) following Eq. [1], assuming $\rho=0.028$ (Mobley, 1999). Prior to R_{rs} calculation, unsuitable radiometric measurements were removed following the meteorological flagging approach of Garaba and Zielinski (2013). For sunglint correction, we used the method of Garaba *et al.* (2012), thus subtracting the minimum R_{rs} value in the range from 700 to 900 nm from the whole spectrum and (5) Calculate photosynthetically active radiation (PAR). The final data is stored as a *.dat and Matlab file (*.m). In the case study presented in this paper, a number of stations along a scientific survey path were analysed. An average of 10 scans were used for each spectra. Suitable R_{rs} from the survey path were compared to available satellite derived R_{rs} measurements.

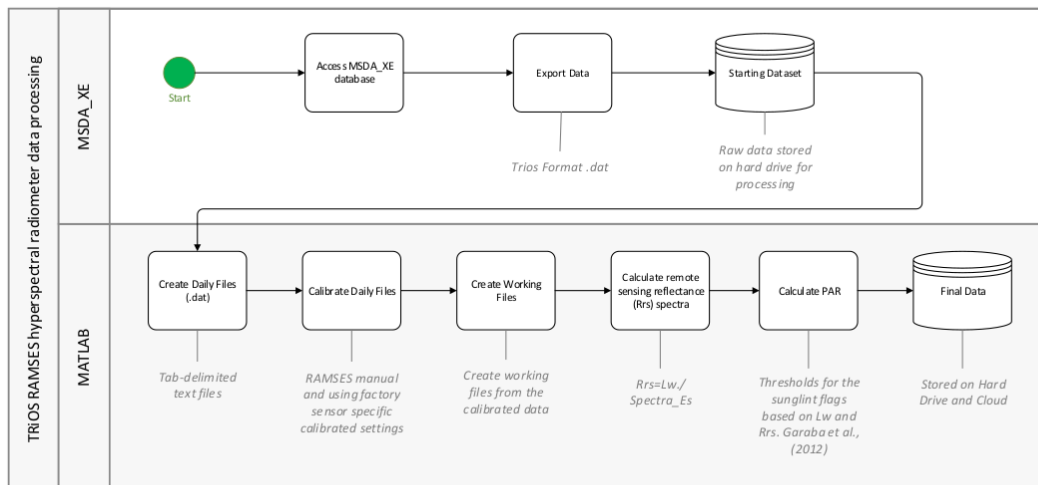


Figure 18 Detailed process flow describing each data processing step from accessing the raw data to the final data

3.3.4 Satellite Data Match Up

Level 3 daily mean satellite data was obtained from Copernicus Marine Environment Monitoring Service (CMEMS) (<https://marine.copernicus.eu/>). The R_{rs} products are available in CMEMS with a spatial resolution of 1 km x 1 km. The products downloaded for this study are part of the European space agency Climate Change Initiative (CCI). This is a two-part programme that aims to produce ‘climate quality’ merged data records from multiple sensors, derived from level 2 data produced by SeaDAS 12gen (SeaWiFS) and Polymer (MODIS, VIIRS, MERIS and OLCI-3A). All

sensors are binned to level 3. MODIS, VIIRS, MERIS and OLCI-3A were band shifted by computing inherent optical properties using the quasi-analytical algorithm (QAA) of Lee *et al.*, (2009). The output R_{rs} were cleaned of any negative values. POLYMER atmospheric algorithm was applied to the VIIRS, MERIS, MODIS and OLCI satellite data and l2gen was applied to the SeaWiFS data prior to band shifting based on published criteria (OC-CCI 2014b, OC-CCI 2014c). Satellite data was generated from the study area with geographic latitude and longitude limits of between 47° N to 58° N and 5° W to 22° W. The four products used in this study included the wavelength bands 443 nm, 490 nm, 510 nm and 560 nm.

An in-house Matlab script (see Appendix A1) was used to find the satellite derived R_{rs} values around 3 x 3 pixels centred at the geographic location where above-water measurements were collected between dates of May 24 2019 and July 24 2019. These measurements were within a few hours of satellite passing. The mean value of all 9 pixels and 2 standard deviations of the 9 pixels as the 95% confidence interval was calculated. This value was used for statistical comparison with the *in situ* measurement.

3.3.5 *In situ* Chlorophyll Analysis

A CTD rosette equipped with Niskin bottles, connected to a Seabird CTD were used to collect water in near surface waters (5-6 m max). Known volumes of water were filtered through a 25mm 0.7 μm Glass Fibre Filter (GF/F). The filters were frozen at sea (-20° C) and analysed after the survey in the laboratory for chlorophyll a, b and c values. Filter paper were ground up using a Teflon grinder and pigments were extracted with 90 and subsequent measurement of the solution absorbance using an Ocean Optics Flame spectrophotometer with a low volume 10 cm pathlength cell and DT-mini light source. The trichromatic equation of Jeffrey and Humphrey (1975) was used to calculate the chlorophyll a concentration.

3.3.6 Statistical Analysis

Taylor statistics were calculated to determine the similarity between the *in situ* and the satellite derived data sets. Taylor statistics are quantified in terms of correlation coefficient, centred root-mean-square difference, and the amplitude of their variations (represented by standard deviations) (Taylor, 2001). A matlab script was

used to calculate Regression slope (S), Intercept (I), Bias (δ) and Relative Percentage Difference (RPD) (Brewin *et al.*, 2015; Muller *et al.*, 2015; Tilstone *et al.*, 2021). Statistical analysis was computed in Matlab using the Taylor diagram function by Guillaume Maze (2022).

3.3.7 Marine Institute Data Management Quality Management Framework (DM-QMF)

A DM-QMF pack was developed for the TriOS RAMSES hyperspectral radiometer system. The implementation pack consists of several elements that structure the operation of the hyperspectral system including data processing. The elements include: (i) a Data Management Plan (Appendix A2) that describes what data are created and how they are stored and archived. (ii) Standard Operating Procedures (Appendix A3) that describe each of the elements in the DM-QMF TriOS RAMSES hyperspectral radiometer system. (iii) Documentation that is accessible to anyone using the instruments internally within the Marine Institute. (iv) Graphical representations of Process Flows (Figure 17 and 18) visually representing the different parts of the system and their connections. (v) An Acceptance and Criteria Document (Appendix A4) which contains set requirements for the data to be produced. For example, with the five-sensor hyperspectral system described in this study, in order for the R_{rs} value to be calculated, two radiance (one sky viewing and one sea viewing) and one irradiance sensor data is required. Having a set up on both sides of the vessel increases likelihood of usable data. (vi) A Data Catalogue entry, which is a central register of dataset descriptions within the Marine Institute. (vii) A Digital Objective Identifier (DOI) is assigned to data that will be made public, both are described in 3.3.8 and 3.3.9 below.

During the lifespan of the DM-QMF pack, Performance Evaluations are completed in order to highlight areas that need improvement, e.g., SOP's or a particular process. Further information is available in Leadbetter *et al.* (2019) where the authors describe each step of the DM-QMF in detail.

3.3.8 Data Catalogue

The Marine Institute operates a public facing data catalogue (<http://data.marine.ie/>). The Data Catalogue is a central register of datasets curated by the Marine Institute.

The Data Catalogue system meets the requirements of the FAIR principles of data management and provides data records for harvesting by national and international data aggregators (e.g. the Irish Spatial Data Exchange and data.gov.ie) through standards compliant metadata publication (e.g. ISO19115/19139, Schema.org). The Data Catalogue is described in more detail in Leadbetter *et al.* (2020). A Data Catalogue entry was created for the processed 2019 R_{rs} data from this study. The catalogue is created using a check list with a series of questions that describe how and when the data was collected, who is responsible for the data, where is it stored and how it can be accessed. Using the data catalogue, a digital object identifier is then created for the dataset.

3.3.9 Digital Objective Identifier

A Digital Objective Identifier (DOI) and dataset citation was created for the above-water 2019 R_{rs} data that was used in this study. The DOI for this above-water remote sensing reflectance dataset can be found at Jordan, C.; Croot, P; Cusack, C.; and Wollschlaeger, J. (2022). Remote sensing reflectance station data CE19009 & CE19010. Marine Institute, Ireland. doi: 10.20393/6410adf9-8a4e-44d3-a388-40d85827b696 as seen in figure 19.

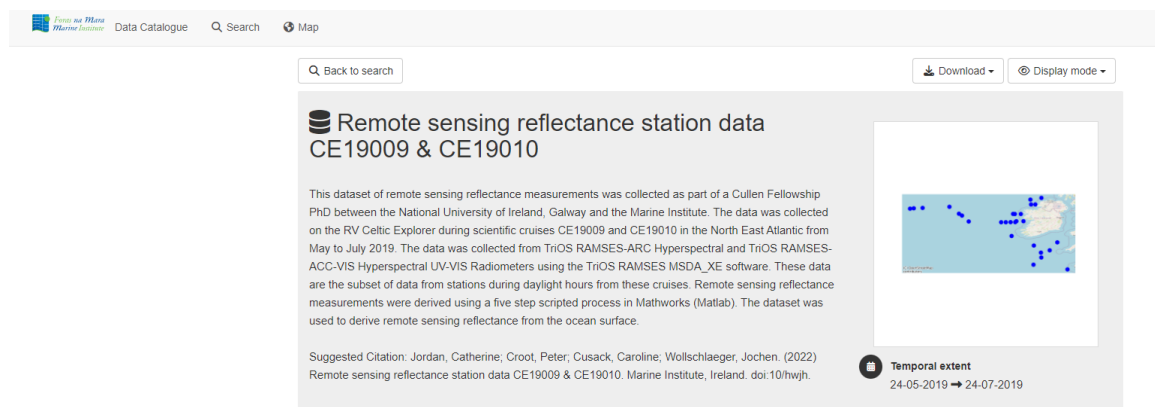


Figure 19 A screen grab from the data catalogue from www.data.marine.ie

3.3.10 Performance Evaluation

Once the Implementation pack was complete for the TriOS RAMSES hyperspectral radiometers on board the RV Celtic Explorer, a Performance Evaluation was carried out and more will be scheduled annually. The Performance Evaluation is designed to improve processes and the quality management as a whole. See Table 4 in Leadbetter

et al. (2019) for a summary of the Performance Evaluation questionnaire. Performance Evaluations will continue throughout the project to ensure the highest standards of data collection continue.

3.3.11 Celtic Explorer

The Celtic Explorer is Ireland's largest national research vessel. It conducts multidisciplinary surveys each year. The TriOS RAMSES hyperspectral radiometers are programmed to automatically collect data throughout each survey path. A survey specific database is set up prior to each survey. During 2019 for example, 16 research surveys were conducted on the RV Celtic Explorer covering a total of 42,147 nautical miles. These took place over 320 days from January to December 2019. Figure 20 displays in detail the track paths the RV Celtic Explorer travelled, covering areas such of the NE Atlantic, specifically, The Celtic Sea, Bay of Biscay, Porcupine Bank, Malin Shelf, Scottish Shelf, Hebridean Shelf, Rockall Trough, The Baltic Sea and the North Sea.

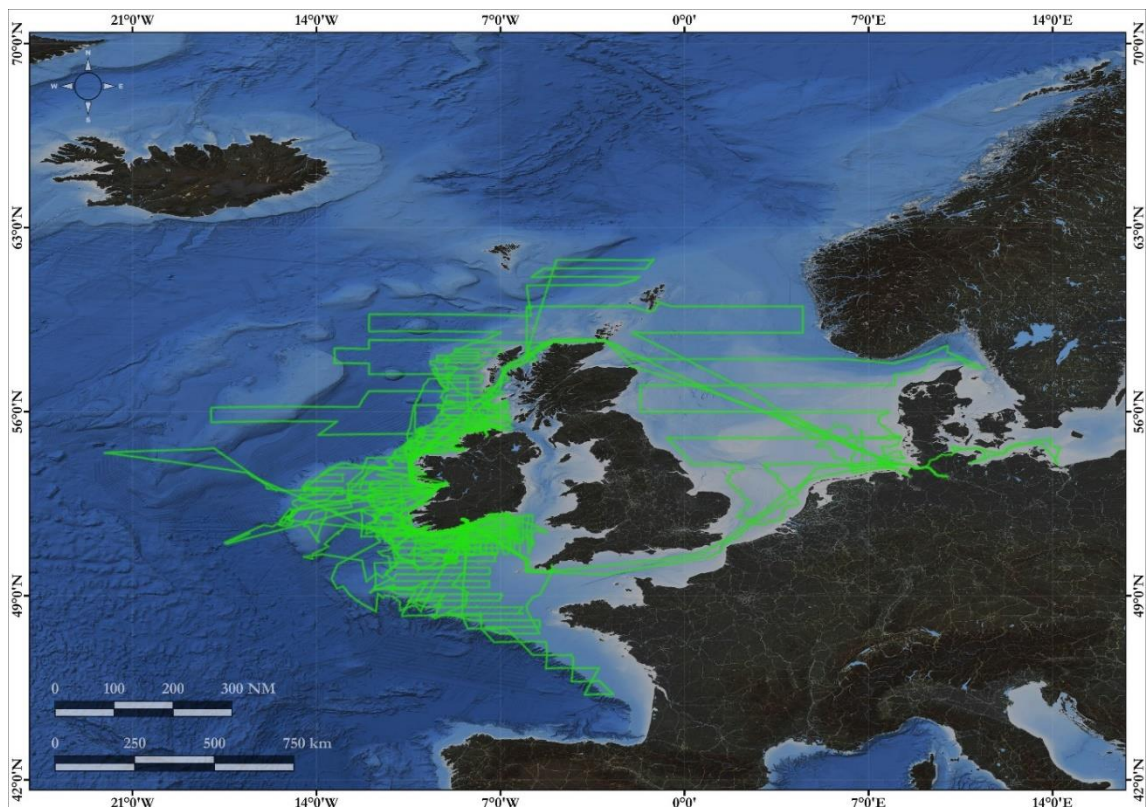


Figure 20 Track paths of the RV Celtic Explorer during 2019, 16 research surveys were conducted during this year covering a total of 42,147 nautical miles over the course of 320 days

3.4 Results

Above-water hyperspectral radiometer data from stations during two research surveys between May 2019 and July 2019 (CE19009 and CE19010) were processed using the series of Matlab scripts as described above. Figure 21 (A) displays the stations from both CE19009 and CE19010 where *in situ* R_{rs} data was collected. Figure 21 (B) displays the data points that could be matched with satellite derived R_{rs} data. Figure 22 displays an example of R_{rs} plots derived from different stations in different water bodies during CE19009 and CE19010.

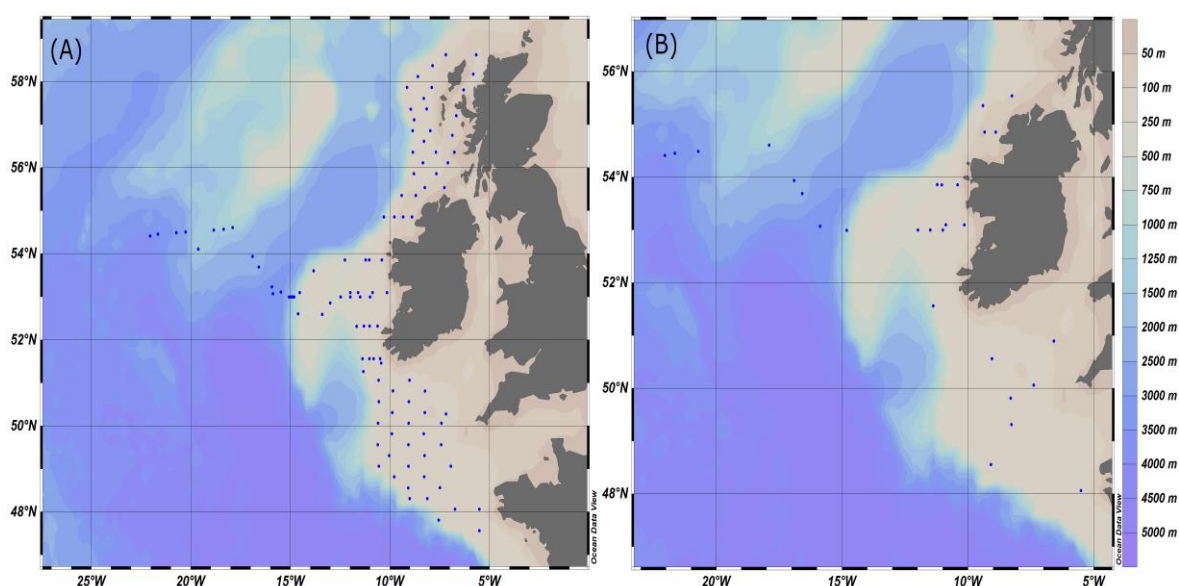


Figure 21 (A) Stations from both CE19009 and CE19010 research survey (B) Stations that were compared with satellite derived data

Figure 22 shows examples of sea surface reflectance in different areas through CE19009 and CE19010. Station 03 from CE19010 plot shows a noticeable peak in the green part of the visible spectrum around 550nm. This peak is typically indicative of the reflective properties of the water, influenced by various substances such as chlorophyll found in phytoplankton.

Station 32 CE19010, further north, this plot shows a noticeable peak in the 550-570 nm range, which could be associated with chlorophyll absorption. Additionally, there's a smaller peak around 700 nm, which might be related to the water's scattering properties or other dissolved and particulate matter.

Station 43 CE19010, west of Ireland, in this plot there is a prominent peak in the reflectance curve occurring around the 550 nm wavelength. This peak is likely due to the spectral properties of water and can be influenced by the presence of biological materials like phytoplankton, which typically absorb light in other wavelengths and reflect more in the green spectrum.

Station 60 CE19010, north west of Ireland, this plot is similar to previous with a distinct peak in the green part of the spectrum around 550 nm, again this peak is typical for oceanic waters which are influenced by chlorophyll concentration and other particulate matter, which generally have higher reflectance in the green region.

Station 26 from CE19009: There is a distinct peak around the 550 nm mark, typical of chlorophyll's reflective response, indicating phytoplankton presence.

Station 35 from CE19009: This plot shows two pronounced peaks in the reflectance curves. The first peak occurs just before 500 nm, and the second, more pronounced peak is around 550-570 nm. These peaks are characteristic of chlorophyll absorption and are commonly associated with the presence of phytoplankton in the water. Reflectance typically decreases beyond these peaks, especially after 700 nm, which is consistent with the absorption characteristics of water.

The distinctive chlorophyll peaks at stations 32 CE19010 and 35 CE19009 and reflectance of much clearer waters (less chlorophyll) at stations 43 CE19010 and 60 CE19010 are supported with *in situ* chlorophyll-*a* data from stations at 32 CE19010 0.804 (ug/l) and 35 CE19009 0.907 (ug/l) compared to lower chlorophyll-*a* values at stations 43 CE19010 0.285 (ug/l) and 60 CE19010 0.090 (ug/l).

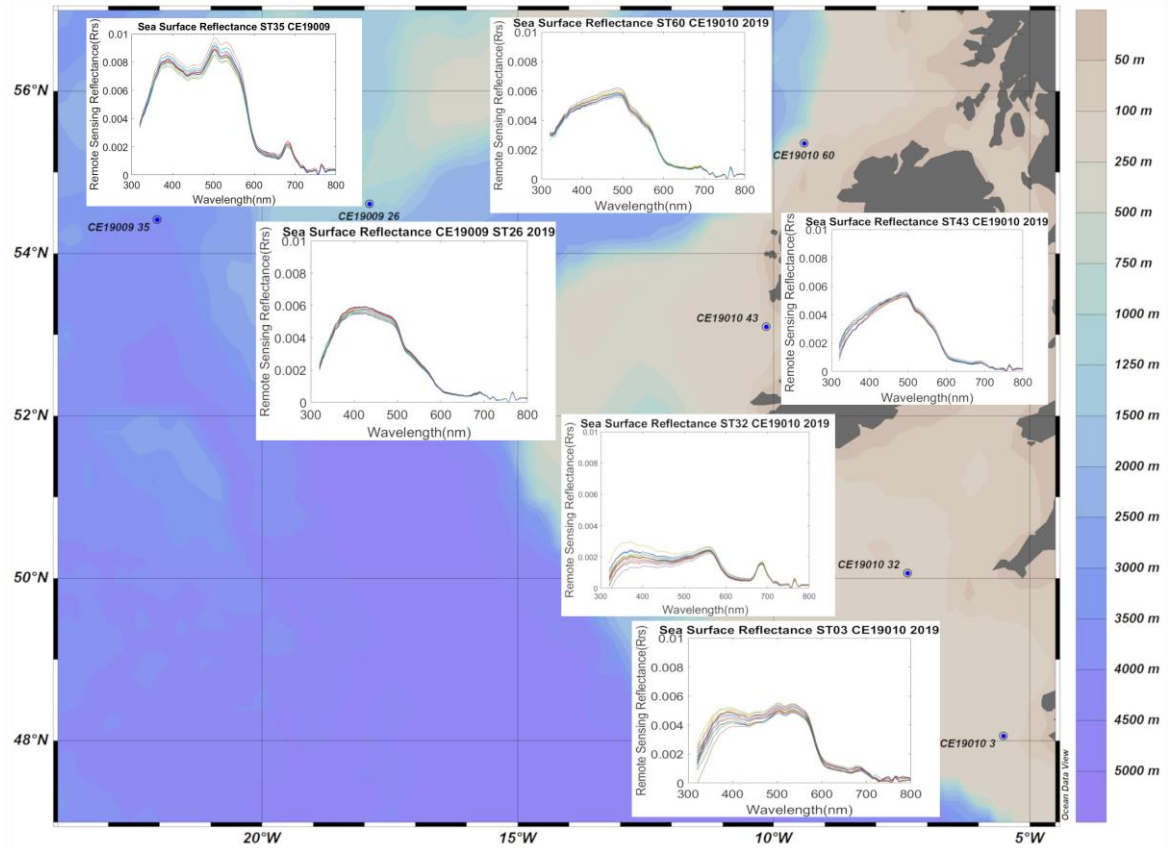


Figure 22 Remote Sensing Reflectance Plots from CE19010 ST03,32,43,60 and CE19009 ST26, 35

Four satellite R_{rs} bands were selected to statistically compare with the above-water hyperspectral values as described in the methods section. Linear regression plots (Figure 23) were created for each band comparison, and Taylor statistics (correlation coefficient, centred root-mean-square difference (Ψ), the amplitude of their variations (represented by standard deviations), regression slope (S), intercept (I), bias (δ) and RPD) were applied to the data. Results between the two datasets all returned a positive correlation. Statistical results are summarised in Table 1. For the 443 nm band, RMSE (Ψ 0.0010), indicating low error; Pearson's correlation is moderate at ($r = 0.5974$); the slope of ($S = 0.7014$) points to underestimation; the intercept and bias are very small; RPD is high at 17.3620. At 490 nm, RMSE is slightly higher at (Ψ 0.0013), with a correlation of ($r = 0.5645$) and a slope of ($S = 0.9388$); RPD is 23.8400, denoting better predictive power. For 510 nm, RMSE increases marginally to (Ψ 0.0014); correlation improves to ($r = 0.6092$); slope exceeds unity at ($S = 1.0597$); RPD further increases to 27.8900. The 560 nm band has an RMSE of (Ψ 0.0012), highest

correlation of ($r = 0.8540$), the slope is ($S = 1.3865$), indicating some overestimation; RPD is at its highest at 33.4750.

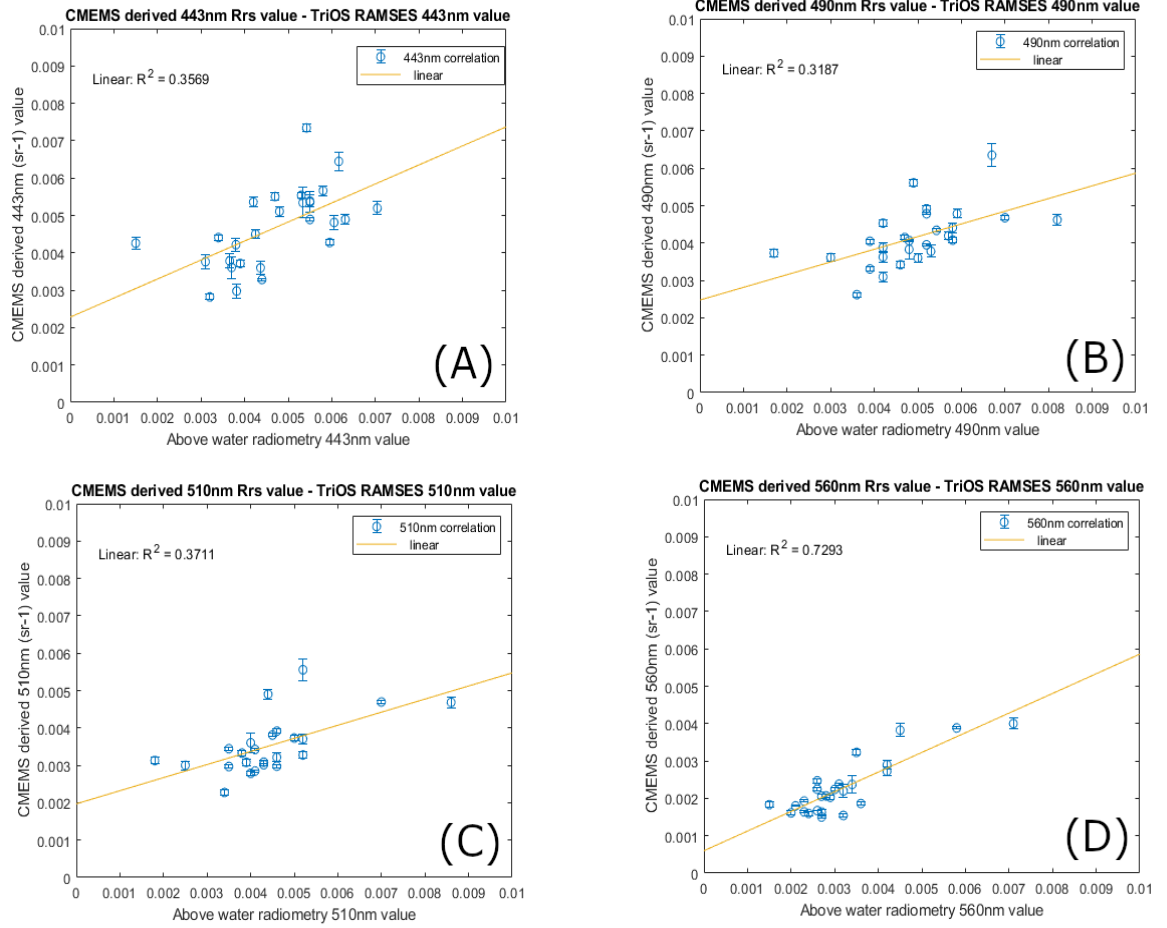


Figure 23 Linear Regression plots between ESA-CCI CMEMS derived Rrs value and above-water radiometry values (A) 443 nm, (B) 490 nm, (C) 510 nm and (D) 560 nm

Table 1 Statistics Summary Table

<i>Wavelength sr-1</i>	<i>Average In Situ</i>	<i>Average Satellite derived</i>	<i>STDV Satellite derived</i>	<i>RMSE Ψ</i>	<i>Pearson's Correlation</i>	<i>p value</i>	<i>Regression Slope (S)</i>	<i>Intercept (I)</i>	<i>Bias (δ)</i>	<i>RPD</i>
<i>Rrs 443</i>	<i>0.0047</i>	<i>0.0047</i>	<i>0.0011</i>	<i>0.0010</i>	<i>0.5974</i>	<i><0.05</i>	<i>0.7014</i>	<i>0.0014</i>	<i>-2.2042×10^{-5}</i>	<i>17.3620</i>
<i>Rrs 490</i>	<i>0.0049</i>	<i>0.0041</i>	<i>0.0008</i>	<i>0.0013</i>	<i>0.5645</i>	<i><0.05</i>	<i>0.9388</i>	<i>0.0010</i>	<i>-0.0008</i>	<i>23.8400</i>
<i>Rrs 510</i>	<i>0.0044</i>	<i>0.0035</i>	<i>0.0008</i>	<i>0.0014</i>	<i>0.6092</i>	<i><0.05</i>	<i>1.0597</i>	<i>0.0007</i>	<i>-0.0009</i>	<i>27.8900</i>
<i>Rrs 560</i>	<i>0.0032</i>	<i>0.0023</i>	<i>0.0007</i>	<i>0.0012</i>	<i>0.8540</i>	<i><0.05</i>	<i>1.3865</i>	<i>3.2921×10^{-5}</i>	<i>-0.0009</i>	<i>33.4750</i>

3.5 Discussion

Ocean Colour (OC) is a key indicator of ocean health, according to the IOCCG (2008) and was listed as an essential climate variable. Due to the fact less than 10% of the TOA radiance is due to water radiance at sea level (Gordon and Morel, 1983), it is essential there are methods of measurements closer to the sea surface to correct for uncertainties. Gilerson *et al.* (2022) summarises the primary sources of uncertainty of R_{rs} from satellite ocean colour sensors. The authors concluded that the most significant uncertainties are those related to molecular (Rayleigh) scattering. In some settings, variations in sky light reflected from the ocean surface also contributed to errors in the blue; water variability proportional to R_{rs} peaked in the green at coastal sites. The processing of atmospheric corrections is likely to be greatly enhanced with the upcoming PACE mission (Werdell *et al.*, 2019). Satellite ocean colour data is vital for the long-term monitoring of our oceans but *in situ* data is always needed validate satellite derived products (Le Traon *et al.*, 2019). Volpe *et al.* (2012) explore an ocean colour observation system tailored for the Mediterranean, addressing key operational satellite oceanography issues. These include the capability for real-time monitoring of data flow uncertainties, providing alternative solutions to users in case of system failures, and conducting scientific evaluations of the quality of the data products. This study identifies the difficulties with the SeaDAS programme in the Mediterranean environment and emphasises the useful application of the SeaWiFS mission data. It implies that even though the SeaDAS update improves for chlorophyll retrieval worldwide, the Mediterranean still does not meet quality standards. The authors state the importance for the need for these technologies to be continuously improved upon and regionally and adjusted in order to provide reliable oceanographic evaluations is emphasised in the conclusion.

Hernandez *et al.* (2015) also discuss the real-time assessment limitations due to availability and quality of observations but discuss the advancements that have been made in the past decade, highlighting operational forecasting centers have implemented mature validation and performance assessment procedures. These include diverse validation strategies, comparison of different model systems, and ensemble approaches for improved accuracy.

The focus of this project was to establish an operational above-water hyperspectral radiometer system to collect long term hyperspectral data from Irish coastal and oceanic waters. As previously stated, this data can be used for a range of products; satellite ocean colour validation, algorithm development in Case 1 and Case 2 waters, water quality assessment, climate change assessment (e.g. Mobley 1999; Zibordi *et al.*, 2002; Garaba *et al.*, 2012; 2014a, 2014b; Garaba and Zielinski 2013; Hommersom *et al.*, 2012; Zibordi *et al.*, 2012; Brando *et al.*, 2016; Tilstone *et al.*, 2017; 2020; Pitarch *et al.*, 2020; Concha *et al.*, 2021). In shipborne remote sensing, we describe a technique that is suitable for automated continuous measurements. Documenting the structure and workings of a new system, as well as having a plan in place for managing and storing data in the short and long term, is essential to a successful project. Through the development of an Implementation Pack for the TriOS RAMSES hyperspectral system on the RV Celtic Explorer, the end-to-end pipeline of hyperspectral data collection and processing was documented under the Marine Institute's Data Management Quality Management Framework (DM-QMF). The Marine Institute's implementation of the DM-QMF met the Quality Management System requirement for accredited National Oceanographic Data Centre status, which was granted to the Institute in 2019 by UNESCO's Intergovernmental Oceanographic Commission's International Oceanographic Data and Information Exchange (IOC-IODE) (Leadbetter *et al.*, 2019). There were numerous advantages to designing a DM-QMF Implementation pack for this project:

- Without having to read a lengthy document, the process flows created for this system visually show how the process works.
- Knowledge of a new system as it develops is stored in live documents on a shared place that other scientists inside the organisation can access.
- By sharing the documents, any user of the system can ensure that the system's consistency and data quality are maintained.
- Different people are involved at different stages of the process, which means that each person can go to the step that is most relevant to them while still seeing how their step fits into the larger picture.
- The Data Management plan is important for determining how data will be managed and documented throughout the project.

- The Data Catalogue is very valuable as it contains a collection of metadata that describes the dataset and guides users to where the data is stored.
- The Data Catalogue underpins the Digital Object Identifier assigned to the data
- The Performance Evaluations ensure the processes involved are continually monitored and updated if needed.

A high level of collaboration was required from the various members of the data coordinator team and the scientists involved in implementing this DM-QMF pack. Leadbetter *et al.*, (2019) study provides more detail on the DM-QMF implementation packs described above as a lot of internal information is only available within the Marine Institute.

The purpose of this study is to highlight the DM-QMF pack and a case study describing the steps involved in collecting and processing remote sensing data is presented. This initial study served as a pilot to verify the performance of the sensors and to demonstrate one of their potential applications, since it is a new system for the Marine Institute. The data analysed came from two research surveys, specifically from times when the ship was confirmed to be stationary, while on station. Future research aims to expand this work by automatically integrating data collected while the ship is moving, using scripts that can filter out effects caused by different weather conditions. Data has been collected for every survey and stored for future processing. This study highlights the use of this data for satellite validation purposes. Four remote sensing reflectance bands were selected to statistically compare the TriOS RAMSES above-water radiometry with satellite derived remote sensing data to assess how significant the comparisons are. There will be unavoidable differences in statistical analysis due to differences that may be due to atmospheric corrections on satellite data or scale effects related to the different footprints of the sensors, but all four wavelength comparisons in this study returned a positive correlation result and good agreement between the *in situ* and satellite derived data. Groom *et al.* (2019) review paper also discusses the need for *in situ* measurements for satellite validation, within this study the IOCCG, (2013) highlight that ‘uncertainty requirements for scientific applications, e.g., 5% absolute in the blue and 1% relative’. The authors describe System Vicarious Calibration (SVC) is a method used for calibrating spaceborne sensors. In this technique, the measured top-of-atmosphere radiance from the satellite is compared to

the predicted radiance, which is determined by sending the measured water-leaving light through the atmosphere using the same atmospheric model that was used to retrieve the in-water radiance. Because SVC takes into consideration the effects of the complete processing chain, it is customised to each atmospheric correction operation and a calibration that is system-specific.

Brewin *et al.* (2016) discusses the importance of recording high-quality *in situ* radiometric measurements on a regular basis in order to validate new satellite sensors and to continuously evaluate the performance of long-operating devices. Inaccurate data trends may result from adding a new sensor to a Climate Data Record (CDR) too soon, failing to resolve problems with ageing devices, or correcting inter-sensor biases.

Bio-optical equipment like flow-through absorption/attenuation instruments and above-water radiometers are being utilised more often on mobile platforms including research vessels, volunteer ships, and yachts owned by benefactors who care about the environment. It is imperative that the data collected along these routes be of a high calibre. Studies by Brewin *et al.* (2016) and Dall'Olmo *et al.* (2017) show that these systems are significantly increasing the number of satellite validation matchups.

In terms of *in situ* databases, combining several data sources is essential for Sensor Vicarious Calibration (SVC) and satellite validation. A worldwide database comprising information from many sources has been established by the ESA Ocean Colour Climate Change Initiative (CCI) project. It is described in Valente *et al.* (2016) and is reachable through PANGAEA. The most recent version, v4, includes data on spectral diffuse attenuation coefficients, chlorophyll-*a* concentrations, spectral intrinsic optical characteristics, and total suspended matter that spans the years 1997 to late 2017.

The authors discuss the issue with satellite algorithms, with the spatial differences between the satellite radiance measurement and the *in situ* value. Comparing a measurement from a 1 km² pixel and an *in situ* measurement leaves room for errors, Groom *et al.* (2019) highlights the study of Brewin *et al.* (2016) where the authors investigated obtaining multiple chlorophyll values within a satellite pixel. Their approach reduced uncertainty values to 0.157 log₁₀ Chl-*a* on average, less than half

the value recorded in previous studies. These results further highlight the value of autonomous sensors on board research vessels.

However, it has to be considered that also the processing of the *in situ* radiometric data are not straightforward, especially not when performed from a moving vessel. For example, changing measurement geometry due to the ship movement influences the amount of sunglint reaching the sensors, as well as changing the validity of the assumptions about the sea-surface reflectivity ρ (Mobley 1999, Lee *et al.* 2010). Further, there are different methods for sunglint removal, which all have their advantages and disadvantages (see discussion in Garaba *et al.* 2013). Further investigations of these factors and refinement of measurement and data processing protocols would certainly be a reasonable aim for future studies in order to improve R_{rs} quality. Nevertheless, the purpose of the satellite validation aspect of this study is to highlight one of the products associated with this data. As described in the results section *in situ* data from two research surveys are presented here. This data was derived from stations when the ship was fully stopped and *in situ* hyperspectral data was compared with satellite derived wavebands. Figure 23 displays linear regression plots associated with the data. R^2 values show results between the two datasets all returned a positive correlation and the strongest relationship was with the 560nm band. The statistical methods used to evaluate the relationship were: Average, standard deviation, Pearson's correlation, Root Mean Square Error (RMSE) is a standard statistical measure used in satellite validation to quantify the accuracy of satellite derived data compared to *in situ* (Concha *et al.*, 2021). Other metrics used were: Regression slope (S) which shows how *in situ* measurements and satellite derived data relate to one another. In principle, it indicates the change in satellite data for each unit change in *in situ* data. When the slope is closer to 1, it indicates a strong linear relationship, which means the *in situ* observations and satellite data are closely matched. A slope that deviates significantly from 1 indicates a weaker link. Intercept (I): The intercept in a regression analysis represents the value of the dependent variable (satellite derived data) when the independent variable (*in situ* data) is zero. It's important for understanding the baseline level of satellite derived data when *in situ* measurements are absent or minimal. Bias (δ): The systematic discrepancy between the *in situ* measurements and the satellite data is referred to as bias and when the bias is zero, it indicates that the satellite data is generally more accurate than the *in situ*

data. A bias that is either positive or negative means that the *in situ* measurements are regularly overestimated or underestimated by the satellite data, accordingly. Relative Percentage Difference (RPD) is used to analyse how satellite and *in situ* data differ from one other in relation to their average value. The RPD is particularly useful in satellite validation studies to understand the degree of variation or error between satellite-derived measurements and ground-truth (*in situ*) data (Brewin *et al.*, 2015; Muller *et al.*, 2015; Tilstone *et al.*, 2021).

Results between the two datasets all returned a positive correlation. Statistical results are summarised in Table 1. Results include: 443nm band: The average values are very close, indicating a good agreement between the satellite and *in situ* data at first glance. For the *in situ* data, the standard deviation is marginally higher, indicating greater more variability. The low RMSE (Ψ 0.0010) suggests that the data derived from satellite is close to measurements made *in situ*. A moderate Pearson's correlation ($r= 0.59741$) suggests a linear link between the datasets. The regression slope of 0.70139 means that the satellite readings are generally lower than the actual *in situ* measurements. Bias and the intercept are extremely close to zero, indicating little systematic bias. RPD is 17.3620, which suggests a good predictive ability at this wavelength, indicating the satellite data is quite reliable when compared to *in situ* measurements.

490nm band: The average values have a larger discrepancy compared to R_{rs} 443, standard deviation is higher for *in situ* data. RMSE (Ψ 0.0012) is slightly higher than for R_{rs} 443, indicating greater differences between datasets. Pearson's correlation ($r= 0.56452$) is slightly lower, suggesting a weaker linear relationship, but still positive. A higher proportional agreement is shown by the regression slope being closer to 1. In this case, the satellite data has a negative bias, indicating that it typically reports lower measurements than the *in situ* data. RPD is 23.8400, showing an even better predictive performance than at 443 nm, which implies a higher reliability of satellite data for this part of the spectrum.

510nm band: The discrepancy in average values is even larger than for R_{rs} 490. Standard deviation remains higher for *in situ* data. RMSE (Ψ 0.0013) is slightly higher, consistent with the larger discrepancy in averages, although still a low value. Pearson's correlation ($r= 0.60917$) is moderate and similar to R_{rs} 443. Regression Slope is greater than 1, implying that satellite data overestimates the increase in *in situ* data. Bias is

negative, indicating a systematic underestimation by the satellite. RPD of 27.8900, the satellite data's predictive capability at 510 nm is strong, suggesting a high level of accuracy in this wavelength's satellite measurements.

560nm band: The average values show the largest difference among all wavelengths. Standard deviation is consistent with other wavelengths. RMSE (Ψ 0.0011) is also low with this waveband. Pearson's correlation ($r= 0.85398$) is the highest out of all the wavebands studied, suggesting a strong linear relationship between datasets. Regression Slope is significantly greater than 1, which could indicate a stronger response in satellite data as in-situ data increases. Bias is negative, and the satellite data consistently underestimates the *in situ* data, although the bias is quite small. The highest RPD value of 33.4750 at this wavelength indicates excellent predictive ability, meaning the satellite measurements at 560 nm are very reliable when predicting *in situ* data. The metrics for validating satellite derived data against *in situ* measurements of four different wavelengths are presented here. With an RPD of 17.3620 and a regression slope of 0.7014, the satellite data at 443 nm closely match the *in situ* data, indicating a minor understatement. With RPD values of 23.8400 and 27.8900, respectively, the agreement increases at 490 and 510 nm. The regression slopes closer to or slightly above 1, indicating improved predictive ability. The RPD shows a trend of overestimation by the satellite and peaks at 33.4750 at 560 nm, with the highest regression slope of 1.3865. The Pearson correlation coefficients, which have statistically significant p-values below 0.05 and vary from moderate to strong across all bands (0.5974 to 0.8540), support the validity of the satellite data. The biases are minimal, indicating overall good sensor performance.

In situ data is essential for checking against satellite data for many reasons but because of the high prevalence of cloud cover off the coast of Ireland, it is essential *in situ* data is measured, additionally, Irish waters lack *in situ* optical data. As stated, the *in situ* sensors have an advantage to be able to generate measurements and R_{rs} data during days with cloud cover, unlike satellite technology. The DM-QMF pack will ensure data will continue to be collected, processed, managed and stored based on the standards set out in this study.

3.6 Conclusion

- We highlight an above-water radiometry system that was recently installed on the RV Celtic Explorer in this study.
- We present a case study that details the steps involved in determining the end product, remote sensing reflectance.
- We demonstrate satellite validation product using this data from two research surveys.
- We demonstrated positive statistical relationship across four wavebands
- Future research aims to expand this work by automatically integrating data collected while the ship is moving, using scripts that can filter out effects caused by different weather conditions.
- We described the DM-QMF implementation pack that was developed for this radiometry system and clarified by implementing this pack, it ensures that standards are adhered to at every stage of the process.

4. Chapter 4:

Using the Red Band Difference Algorithm to Detect and Monitor a *Karenia* spp. Bloom Off the South Coast of Ireland, June 2019

Catherine Jordan^{1,2}, Caroline Cusack², Michelle Tomlinson³, Andrew Meredith⁵, Ryan McGeady^{1,4}, Rafael Salas², Clynton Gregory¹, Peter Croot¹

¹Earth and Ocean Sciences and Ryan Institute, School of Natural Sciences, University of Galway, H91 TK33 Galway, Ireland

²Marine Institute, Rinville, Oranmore, H91 R673 Galway, Ireland

³National Centers for Coastal Ocean Science (NCCOS, NOAA) 1305 East West Highway, Silver Spring, MD 20910, United States.

⁴Zoology and Ryan Institute, School of Natural Sciences, University of Galway, H91 TK33 Galway, Ireland

⁵Consolidated Safety Services Inc., Fairfax, 22030, USA

Published Front. Mar. Sci., 30 April 2021

Sec. Marine Fisheries, Aquaculture and Living Resources

Volume 8 - 2021 | <https://doi.org/10.3389/fmars.2021.638889>

Cited by 11 on the 27/03/2023

4.1 Abstract

During the months of May, June, July and August 2019 the Red Band Difference algorithm was tested over Irish waters to assess its suitability for the Irish harmful algal bloom alert system. Over the 4 weeks of June an extensive localised surface phytoplankton bloom formed in the Celtic Sea, south of Ireland. Satellite imagery from the Sentinel-3a's Ocean and Land Colour Instrument, processed using the Red Band Difference algorithm detected the bloom in surface shelf waters and helped monitor its movement. Daily satellite images indicated that the bloom appeared at the sea surface on the 2nd June 2019 and peaked in size and surface abundance in offshore shelf waters within 4 weeks, remnants remained at the surface into July. A particle tracking approach was used to replicate oceanic circulation patterns in the vicinity of the observed algal bloom and estimate its trajectory. The initial horizontal distribution of particles in the tracking model were based on a satellite imagery polygon of the bloom when it first appeared in surface waters. Good agreement was observed between satellite imagery of the bloom and the particle tracking model. *In situ* sampling efforts

from a research survey and the national inshore phytoplankton monitoring programme confirmed that *Karenia mikimotoi* was the causative organism of the bloom. This pilot study shows great potential to use the Red Band Difference algorithm in the existing Irish harmful algal bloom alert system. In addition, satellite ocean colour data combined with particle tracking model estimates can be a useful tool to monitor high biomass harmful algal bloom forming species, such as *Karenia mikimotoi*, in surface coastal waters around Ireland and elsewhere.

4.2 Introduction

Aquaculture is extremely important for providing food, nutrition and employment around the world. According to the FAO (2020), aquaculture production reached a record high in 2018. There has been a 527% increase in global aquaculture production from 1990 to 2018. Due to wild fish stocks declining and the population increasing globally, the role of aquaculture in society is more important than ever (FAO, 2020). Aquaculture is a highly valuable industry to the Irish economy. Production in Ireland had a net gain from under €100 million in 2009 to €180 million in 2018 with aquaculture outputs between 30,000 and 50,000 tonnes mainly from salmon and bivalve farming (Dennis and Jackson, 2019). The success of aquaculture is influenced by a range of conditions, both environmental and biological such as temperature, salinity, oxygen and food availability to name a few (Mydlarz *et al.*, 2006). Harmful Algae Blooms (HABs) are a concern for both finfish and bivalve aquaculture (Callaway *et al.*, 2012). In most cases, the proliferation of microscopic algae is beneficial to the overall ecosystem, e.g., as a source of food for wild fisheries and aquaculture (Tweddle *et al.*, 2018). However, a small minority of algal bloom forming species have negative impacts on their surrounding environment. HABs, caused by either small or large biomass blooms, and depending on the species, can result in serious economic losses to marine sectors such as tourism, aquaculture and fisheries with additional, often unquantifiable, impacts on ocean health (Anderson *et al.*, 2015).

In order to mitigate against and prepare for the impacts of HABs, it is essential to detect, monitor, track and forecast their development and movement in real time (Stumpf and Tomlinson, 2005). Collecting samples in the field alone has limitations as the samples or measurements are collected at discrete points and times, and while this method generally offers high quality data from a specific point in time, temporal

and spatial limitations are a challenge. Combining different observational methods can greatly help managers detect and monitor HAB hazards. For example, satellite remote sensing techniques are powerful tools to detect and monitor the movement of surface phytoplankton blooms due to the vast area covered in one single swath measurement (Stumpf and Tomlinson, 2005). Emerging remote sensing techniques for Europe should positively impact the aquaculture industry. Ocean colour sensors and the algorithms designed to detect phytoplankton blooms or HABs have been continually improving since the launch of the first ocean colour sensor, the Coastal Zone Colour Scanner in 1978 and the most recent launch of ESA Sentinel 3B OLCI in 2018 (Groom *et al.*, 2019). Satellite technology has proven very useful in mapping the geographical extent of blooms and movement (Miller *et al.*, 2006; Stumpf *et al.*, 2009). To determine the concentration of chlorophyll-*a* (Chl-*a*) or other optically active constituents such as coloured dissolved organic matter (CDOM) or suspended particulate matter (SPM), different types of algorithms have been developed by measuring the water leaving radiance, or reflectance (Groom *et al.*, 2019). The use of satellite technology focussed on Chl-*a* and sea surface temperature (SST) combined with field sampling can support early warning systems for certain HAB types.

Standard ocean colour algorithms that estimate chlorophyll concentration or HABs from satellite sensors use the blue and green spectral bands of the visible spectrum to monitor the colour of the ocean. These algorithms are very useful, especially in open ocean water, which are classified as Case 1 waters. The algorithms are not as accurate in the more complex Case 2 waters, situated close to the coast and inland, where most aquaculture takes place and HAB detection is most critical. The two water types were originally introduced by Morel and Prieur (1977). These descriptions have since been refined (Gordon and Morel, 1983; Morel, 1988; IOCCG, 2000; Mobley *et al.*, 2004). Mobley *et al.* (2004) describe case 1 waters whose inherent optical properties (IOPs) are dominated by phytoplankton. Case 2 waters generally contain higher concentrations of CDOM, SPM, and inorganic particles in addition to phytoplankton. In Case 2 waters, as the band selection used for the standard algorithms is highly influenced by non-living suspensions, CDOM and sediment and can be misinterpreted as chlorophyll concentration.

Standard algorithms that use the blue green ratio are very important and valid methods of retrieving chlorophyll concentrations. Due to the problems with CDOM and

sediment interference it is also useful to have an algorithm measuring chlorophyll fluorescence using the red bands. Chlorophyll fluorescence can be defined by red light re-emitted by chlorophyll molecules when excited by light (Zeng and Li, 2015). Chlorophyll fluorescence in the red band of the visible spectrum has proven successful to monitor HABs in coastal areas of the United States. A good example is the Gulf of Mexico where ocean colour is used to detect *Karenia brevis* blooms (Amin *et al.*, 2009). As described by Amin *et al.* (2009) the Red Band Difference (RBD) relative fluorescence algorithm is less sensitive to CDOM, SPM, and atmospheric corrections and therefore useful in coastal waters. Vandersea *et al.* (2020) describe how the RBD algorithm is also suitable for *Karenia mikimotoi* blooms and demonstrates how it was applied to monitor a 2013 bloom in Kachemak Bay, Alaska alongside field sampling and lab techniques. The RBD algorithm is also used off the east coast of the United States and can detect several HAB dinoflagellates of interest in Chesapeake Bay, the largest estuary in the United States and a location with very turbid waters. Scattering by sediments may interfere with algorithms in environments like this (Wolny *et al.*, 2020). The benefits of using the RBD algorithm in a turbid environment is that the algorithm is less sensitive to interference by non-algal pigments as it was designed to detect Chl-*a* fluorescence in the HAB blooming species *K. brevis* without interference from sediment, the algorithm is designed to return positive values in waters where blooms occur and negative values in high scattering waters (Amin *et al.*, 2009). This is the first reported study using the RBD algorithm in Irish waters.

While *K. brevis* blooms have never been recorded in Irish waters, *K. mikimotoi* blooms frequently occur in Irish waters (Ottway *et al.*, 1979; Silke *et al.*, 2005) and have been recorded historically and in recent years, reviewed recently by Li *et al.* (2019). Gentien (1998) describes *K. mikimotoi* as a common “red tide” or large bloom forming dinoflagellates in shelf waters of the northeast Atlantic. Previously referred to as *Gyrodinium aureolum*, *Gymnodinium cf. aureolum*, *Gymnodinium nagasakiense*, and *Gymnodinium mikimotoi* in the literature *K. mikimotoi* blooms are commonly associated with marine fauna kills (Brand *et al.*, 2012; Li *et al.*, 2019). *Karenia* are thought to overwinter in low numbers as motile cells and when favourable biogeochemical and physical conditions arrive in early to late summer *Karenia* will grow and bloom (Gentien, 1998). Globally, *K. mikimotoi* has adapted to a wide range of temperatures ranging between 4 and 30°C but the European isolate has a narrower

range of 6–20°C. The salinity ranges *K. mikimotoi* can survive in are also quite extensive ranging from 9 to 35 ppt, therefore suited to a range of environments (Li *et al.*, 2019). Li *et al.*, 2019 also describe that *K. mikimotoi* is known to grow well in low light environments, however, it is not photo inhibited by high light intensities, therefore capable of adapting to conditions at both the surface and at the bottom. One important feature of *K. mikimotoi* behaviour in the environment is that, like many dinoflagellates they are capable of vertically migrating over a diurnal cycle, beginning from depth before sunrise and reaching the surface before midday. This is known as diurnal vertical migration (DVM) (Olsson and Graneli, 1991; Koizumi *et al.*, 1996; Park *et al.*, 2001; Shikata *et al.*, 2014, 2015, 2016). This phenomenon is likely why the RBD approach is so applicable to satellite detection of blooms of *K. mikimotoi* as the cells will be in the upper part of the water column at midday, close to the over pass time of the satellite, with a significant number of cells in the upper 2 m of the water column corresponding to the observable signal depth for red light in seawater (Doerffer, 1993).

The true toxicity of *K. mikimotoi* is unknown but the dinoflagellate is known to produce toxins including haemolysin (Neely and Campbell, 2006) and gymnocin A and gymnocin B (Satake *et al.*, 2002, 2005). *Karenia mikimotoi* is not known to create shellfish related biotoxins, but mass mortalities of shellfish have been associated with blooms of this species. Causes of mortalities include inhibiting larval settling rates, immune functions, gut tissue damage and larval spat mortalities. The blooms may not only impact the survival rate of shellfish but also affect the developmental processes, therefore blooms can greatly impact wild and farmed shellfish (Li *et al.*, 2019). The effects of these blooms are not limited to shellfish but also wild and farmed fish and a range of invertebrates. *Karenia mikimotoi* senescent blooms are known to deplete the water of oxygen levels when bacterial respiration associated with the breakdown of the bloom begins, and when macro-organisms start to decay, and biochemical oxygen demand rises. Diaz and Rosenberg (2008) observed mass mortalities of benthic organisms when the water became anoxic after a *Karenia* bloom. *Karenia mikimotoi* also secrete mucus (with high concentrations of extracellular polysaccharide) that can increase the likelihood of mortalities, for example, when fish gills become clogged (Gentien *et al.*, 2007). Li *et al.* (2019) describe how even at low algal densities gill damage and mortality in both wild and cultured salmon, rainbow trout and turbot were

reported, even in waters with high dissolved oxygen levels. Mortalities of a range of invertebrates, are also linked to blooms of this unarmoured dinoflagellate in European waters and evident in the literature since 1966 (Jones *et al.*, 1982). The earliest published Irish report of a *Karenia* spp. bloom related to marine life mortalities off the south coast of Ireland was made by Ottway *et al.* (1979). Two Irish examples of exceptional *Karenia* spp. blooms include the months of May, June, and July of 2005 (Silke *et al.*, 2005) and more recently, a *K. mikimotoi* bloom in the summer (May to September) of 2012 (O’Boyle *et al.*, 2016). In July 2012, *Karenia* spp. were at high concentrations, greater than one million cells per litre, in the surface waters at the Malin shelf off northwest Ireland suggesting a potential offshore origin for these blooms (Bresnan *et al.*, 2013).

Ireland has a weekly HAB bulletin, published to assist aquaculture business managers, helping them make practical decisions to mitigate against potential HAB impacts. The bulletin contains several data products based on historical and recent biotoxin and phytoplankton profiles, satellite and oceanographic *in situ* and modelled forecasting data. Products used by local scientists help to develop HAB alerts for the days ahead. In this paper, we demonstrate the potential benefits of implementing a novel bio-optical chlorophyll fluorescence algorithm within the Irish HAB monitoring framework, which has already been proven effective in the United States for detecting *K. brevis* and various other HAB species,

During the months of May, June, July and August 2019 the RBD algorithm was tested in Irish waters for the first time. During this time a phytoplankton bloom appeared in the Celtic Sea, south of Ireland.

4.2.1 Objectives of this Study

The objectives of this pilot study were:

1. To test the RBD algorithm in Irish waters and assess its suitability for use in the Irish HAB monitoring system.
2. To determine the phytoplankton taxa responsible for the bloom by analysing the drift trajectory of the bloom by using local water circulation patterns in a particle tracking model and analysing *in situ* phytoplankton data from the national inshore monitoring programme and an offshore phytoplankton survey.

4.3 Materials and Methods

4.3.1 Study Area

Figure 24 presents the study area where the phytoplankton bloom was identified via satellite imagery, including *in situ* sampling locations described in section “*In situ* Data.” The samples were from three inshore stations: Cork Harbour, Oysterhaven and Kinsale, and from eight offshore stations from the research survey CV19018; 138, 139, 140, 141, 142, 143, 144, and 148 as described in section “*In situ* Data.” Also illustrated in Figure 24 (B) is the polygon that was created based on manual interpretation of satellite imagery from when the bloom first appeared at the surface. This polygon was used for the horizontal distribution of particles deployed in the Lagrangian Particle Tracking model as described in section “Lagrangian Particle Tracking.” The study area was in the Celtic Sea, an area of the NE Atlantic Ocean bordered by Ireland in the north, the United Kingdom in the east and the Bay of Biscay (47°N) in the south. The Celtic Sea is relatively shallow with depths ranging between 100 and 200 m and decreasing in depth near the coast as illustrated in Figure 24. Tidal circulation across the Celtic Sea is weak, water movement is primarily due to wind action (Raine, 2014). In the Celtic Sea, the water tends to stabilise in April when the seasonal thermocline becomes established. Throughout the summer months, there is a deepening of the thermocline due to continued heating of the surface layer until the Autumn when the cooling phase begins, and the water column becomes well mixed again. Within the Celtic Sea there are exceptions to this in areas of tidally mixed fronts, these are found at the boundaries between thermally stratified and tidally mixed areas such as the entrance to the Irish Sea, where the Celtic Sea Front is located and at the Ushant front, located between the southwest United Kingdom and northwest France (Raine, 2014).

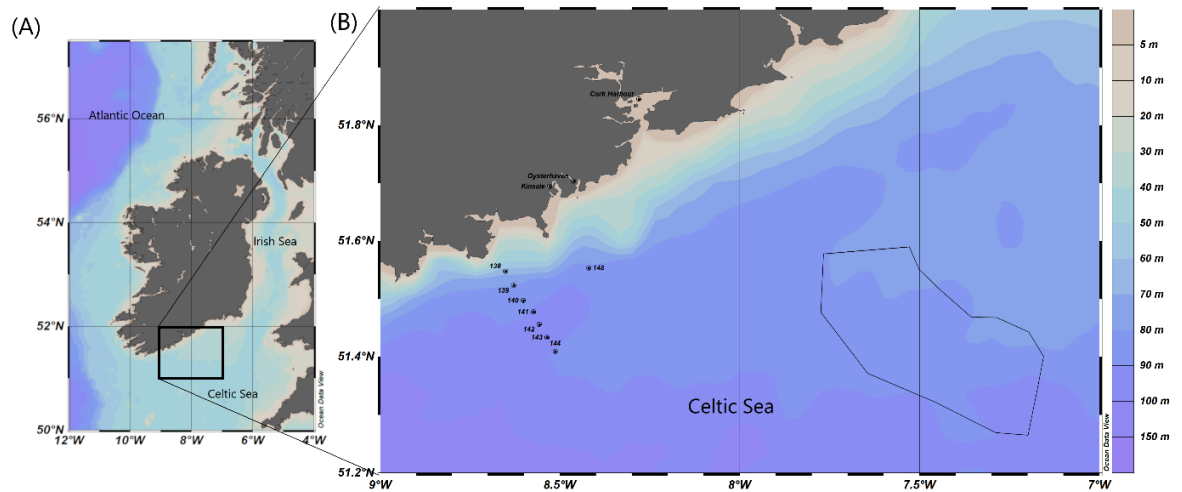


Figure 24 (A) Map of study area in the Celtic Sea. (B) In situ sample locations are noted as points and the polygon location for the particle tracking model is outlined by the black line. Bathymetry is represented in metres.

4.3.2 Satellite Imagery

The Red Band Difference satellite imagery was generated from the study area with geographic latitude and longitude limits of 47°N to 58°N, 2°W to 12°W. The region of interest covers all coastal waters around the island of Ireland. Satellite data from the Ocean and Land Colour Instrument (OLCI) sensor on Sentinel 3A were obtained from The European Organisation of Meteorological Satellites (EUMETSAT). The multispectral OLCI sensor has 21 spectral bands from 0.4 to 1.0 μm and has a spatial resolution of 300 m. The bands are optimised to measure ocean colour over open ocean and coastal zones. The whole field-of-view is shifted across track by 12.6° away from the sun to minimise the impact of sun glint. Once the OLCI L1B data were downloaded from EUMETSAT, the data were processed to L2 using the NOAA, National Centres for Coastal Ocean Science (NCCOS) satellite automated processing system which utilises NASA's 12gen software included in the Sea-viewing Wide Field-of-view Sensor (SeaWiFS) Data Analysis System (SeaDAS) package (version 7.5.3). The 12gen processing produced a surface reflectance product (R_{rhos}) that is corrected for top-of-atmosphere solar irradiance, Rayleigh radiance and molecular absorption (Wynne *et al.*, 2018).

The RBD algorithm used to highlight areas of high fluorescence, indicative of high algal biomass, uses only pixels within the valid R_{rhos} range (0–1) described by Amin *et al.*, 2009 and modified for OLCI R_{rhos} bands as follows:

$$\text{RBD} = R_{\text{rhos}}(681) - R_{\text{rhos}}(665)$$

Due to the increase in reflectance caused by Chl-*a* fluorescence at 681 nm, the RBD is positive in areas of Chl-*a* fluorescence. The RBD data products were mapped to Universal Transverse Mercator (WGS 84) projection at 300 m horizontal resolution using a nearest neighbour interpolation. A land mask was applied, and the product saved to a GeoTIFF (an image file with georeferencing information embedded in the file as metadata) and stored in a database at NCCOS. Weekly mean composites of the daily images were created using a custom ArcGIS python toolbox, RS_Tools, that was developed specifically for working with products from the NOAA-NCCOS satellite processing system.

Satellite imagery was produced for the weekly HAB bulletin using an algorithm developed by IFREMER, known as the OC5 product. The level 4 Chl-*a* product is extracted from the IFREMER FTP site¹. Matlab (MathWorks) is used to convert the level 4 Netcdf files to *.grd files. Matlab is then used to calculate chlorophyll anomalies from the 60-day median value calculated using data between current date minus 74 and current date minus 14. This anomaly data is rendered as .png files (Leadbetter *et al.*, 2018).

4.3.3 Lagrangian Particle Tracking

To examine the effect of local water circulation patterns on the drift trajectory of the *Karenia* bloom, a particle tracking simulation was conducted using outputs from a 3D hydrodynamic numerical ocean model. The northeast Atlantic Regional Ocean Modelling System (ROMS) model encompasses a large area of the northwestern European continental shelf including Irish territorial waters (NE_Atlantic model; Dabrowski *et al.*, 2016). This model has a horizontal resolution of 1.1 to 1.6 km in Irish coastal waters with 40 terrain-following vertical layers (Dabrowski *et al.*, 2016). The ROMS model output data was coupled with an offline 3D Lagrangian particle tracking mass-preserving scheme called ICHTHYOP; an individual-based model (Ichthyop v3; Lett *et al.*, 2008). This was used to simulate particle transport from the *Karenia* bloom location (i.e., the potential HAB surface transport pathways). Particle tracking simulations were conducted using hourly ROMS ocean current speed and direction outputs using a Runge–Kutta 4th order numerical scheme and a 5-min time

step. The initial horizontal distribution of the particles, representing *K. mikimotoi* cells, was based on a polygon created from satellite observations of the bloom when it was first identified at the water surface (Figure 24). In total, 50,000 particles were released with a random vertical distribution between 0 and 20 m depth in the Celtic Sea. The 50,000 particles were selected as this is the limit of detection for *K. brevis* (cells per litre) in the Gulf of Mexico, by legacy satellites (Tester *et al.*, 1998). Particles were neutrally buoyant, so any movement of particles between depths was due to vertical currents. The model simulation did not include growth or grazing of the phytoplankton. In the simulation the particles were transported for a fixed duration of 27 days from 2 to 29 June 2019. Maps were generated to show the density distribution of particles on different dates to show bloom progression and to compare with satellite imagery.

4.3.4 *In situ* Data

Availability of biological data in the region where the bloom occurred according to satellite imagery was investigated to establish the predominant phytoplankton in the area at the time. Figure 24 shows the locations where phytoplankton samples were collected at the time of the bloom.

The Irish Marine Institute runs the national biotoxin and phytoplankton monitoring programme and releases a weekly HAB bulletin. Phytoplankton abundance and composition results (freely available at <http://webapps.marine.ie/HABs/Locations/Inshore>) from southern stations close to where the bloom occurred were downloaded for this study. When the results of the particle tracking model confirmed the direction the bloom travelled, Cork Harbour, Oysterhaven, and Kinsale inshore stations were selected. Local officers from the Sea-Fisheries Protection Authority and other assigned personnel collect water and shellfish samples, at weekly intervals, from designated shellfish production areas. Samples are sent to the Marine Institute where the analyses are carried out. The programme carries an ISO 17025 quality accreditation. A 25 mL Lugol's iodine fixed seawater sample is used to determine the abundances of biotoxin producing or problematic phytoplankton using the Utermöhl test method, a recognised standard method, described in detail in UNESCO, 2010, references therein. The limit of detection is 40 cells/L⁻¹.

Coincidentally a phytoplankton field survey aboard the RV Celtic Voyager was being conducted in the Celtic Sea when the bloom was still visible via satellite imagery in July 2019. Water samples were collected at the periphery of the bloom at stations 135–144 and 148 (see Figure 29) on 10 July. A phytoplankton net vertically deployed to a maximum depth of 50 m at each station determined the predominant phytoplankton in the water column. A SeaBird 9/11 plus CTD integrated with a carousel water sampler for real-time auto-fire operations was lowered to approximately 5 m above sea floor level. Niskin water bottles were fired on the up cast at discrete depths where peaks of relative fluorescence and temperature gradients were evident on the depth profile. A fine scale sampler (FSS) was used to study the vertical thin layer distributions of dinoflagellates and to examine the correlation to the thin layer water properties. The FSS was lowered to the depth of the desired thin layer and all 15 bottles were fired simultaneously. Water samples were fixed in Lugol's iodine and stored in sterile 50 mL Sarstedt© water sampling bottles. Phytoplankton species were identified with an inverted microscope, Olympus CKX4. Aliquots and cells counted following the Utermöhl method (UNESCO, 2010).

4.4 Results

Red Band Difference satellite imagery show a phytoplankton bloom (Figure 25), appearing in surface waters in the Celtic Sea, off southern Ireland on 2 June 2019. Weekly composites of satellite images show the bloom steadily increase in size (spatially) and magnitude (elevated surface pigment), the warmer colours on the images represent higher fluorescence which indicate higher bloom concentration in the weeks that followed (Figure 25). The images also show the extent of the bloom geographically. The surface bloom peaked in magnitude on the 27 June 2019 (Figure 25) (Daily file for 27th June 2019 Appendix A5). Following this, the bloom began to disperse and dissipate in early July 2019, however, remnants remained visible in the satellite imagery until late July (Figure 25).

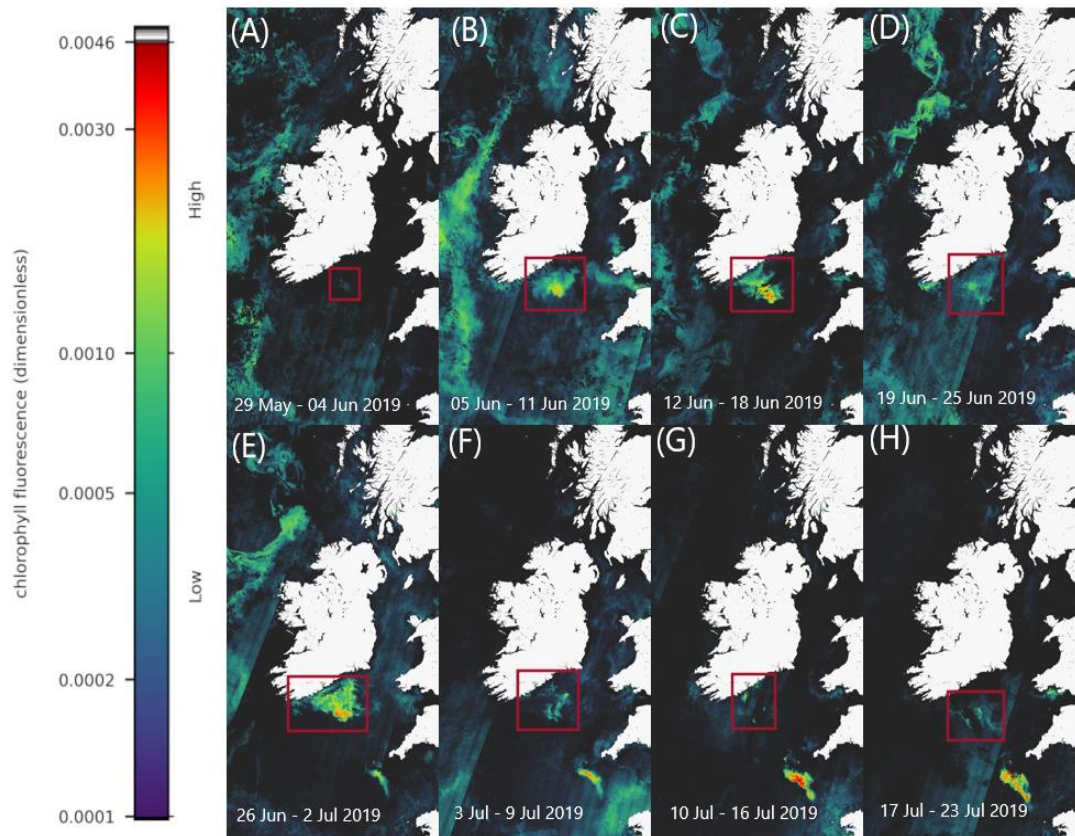


Figure 25 Sentinel-3a OLCI images with RBD algorithm displaying the phytoplankton bloom progression between 29th May 2019 and 23rd July 2019 (A–H). Colours indicate relative fluorescence, with warmer colours representing higher fluorescence indicative of higher bloom concentration.

Figure 26 displays satellite imagery from the weekly HAB bulletin, weeks 24–28 (4th June, 2019–8th July 2019). Focussing on the study area in the Celtic Sea it is clear the increase in chlorophyll concentration at the surface was detected using both algorithms. In both Figures 25, 26 B there is a noticeable rise in chlorophyll concentration in the location the bloom was detected using the RBD algorithm. There is an increase from 1 mg/m³ to 3 mg/m³ between weeks 24 and 25 in Figure 26. Chlorophyll concentration peaks in concentration between dates 23 June 2019 between and 30 June 2019 (D) and (E) using both algorithms. Comparing both Figures 25, 26 it is evident the increase in chlorophyll concentration was detected in the Celtic Sea using both algorithms, but Figure 25 displays a clearer series of images displaying the bloom’s progression and movement.

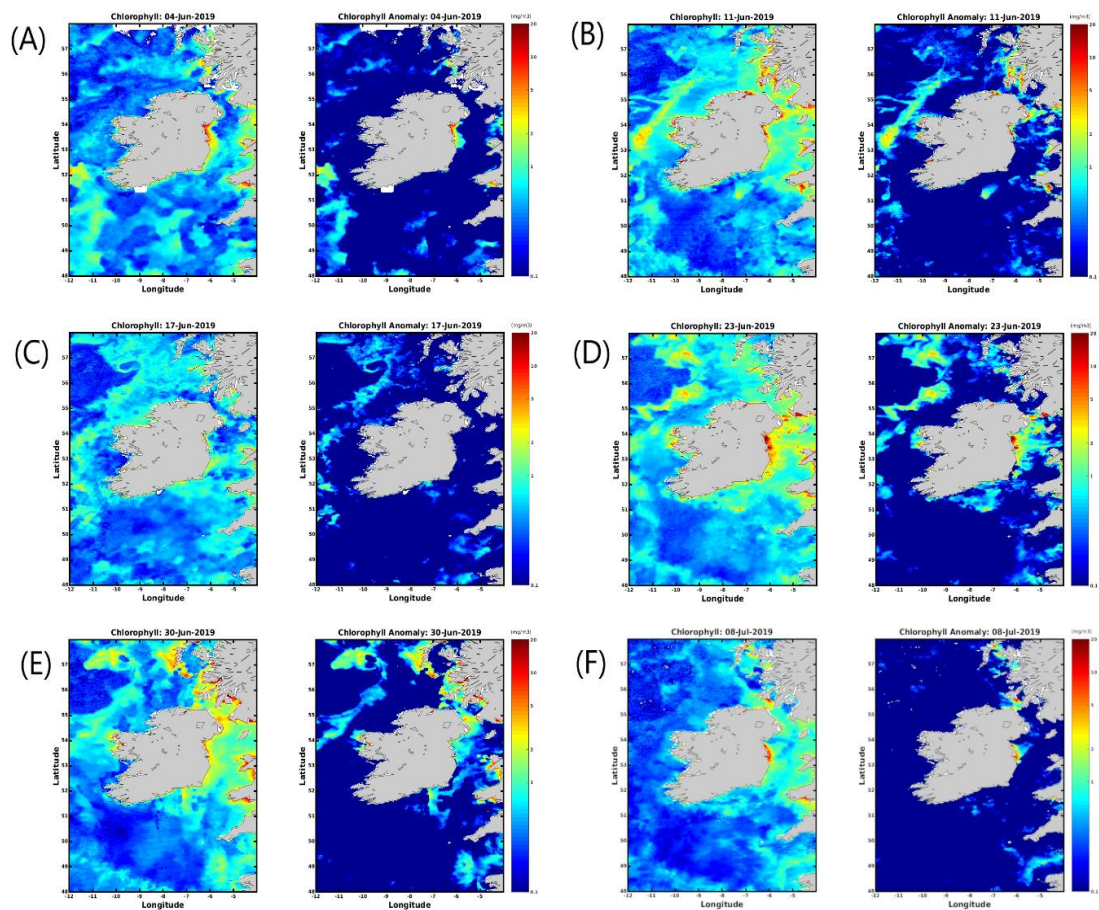


Figure 26 OC5 IFREMER Level 4 Chlorophyll a data from the HAB bulletin weeks 24–28 (A–F) 4th June 2019 to 8th July 2019.

The exact reason for the stripe artefacts in the RBD satellite imagery are not resolved at present, typically this is due to detector striping where radiometric miscalibration in the detector array elements can result in along track striping. However, it can also arise from solar glint or the “smile effect.”

Trajectories from the particle tracking simulation produced a similar pattern to that of the surface bloom in the RBD satellite images at the end of June 2019. Virtual particles that represent the bloom increase in spatial extent over the 4-week period, eventually a significant percentage of particles move toward the south coast of Ireland toward the last week of June in agreement with the Sentinel-3a OLCI RBD satellite imagery (Figure 27). Data from an inshore sampling station, in Cork Harbour confirm *Karenia* spp. as the predominant taxa recorded from late June to late July. The cell counts for *Karenia* spp. in Cork Harbour were 2,471,168 cells/L on the 30 June, 117,234 cells/L on 14 July and 257,634 cells/L on 28 July. Between June and July, *Karenia* spp. cell

counts at three inshore coastal stations (Cork Harbour, Oysterhaven, Kinsale; see Figure 24 for locations) positioned along the south coast of Ireland, showed a dramatic cell increase after being undetected at Cork Harbour and Kinsale coastal stations prior to the bloom detection in offshore waters. *Karenia* spp. had been detected in very low numbers in Oysterhaven in April 2019 (8,800 cells/L) and wasn't recorded again until the 2 June (120 cells/L). Highest cell densities of *Karenia* spp. occurred on different days at each coastal station (Cork Harbour, Oysterhaven and Kinsale) and in a westward direction. Cork Harbour displayed the highest *Karenia* spp. cell count on the 30 June (2,471,168 cells/L), Oysterhaven on the 14 July (255,432 cells/L), and Kinsale on 28 July (398,736 cells/L) (Figure 28).

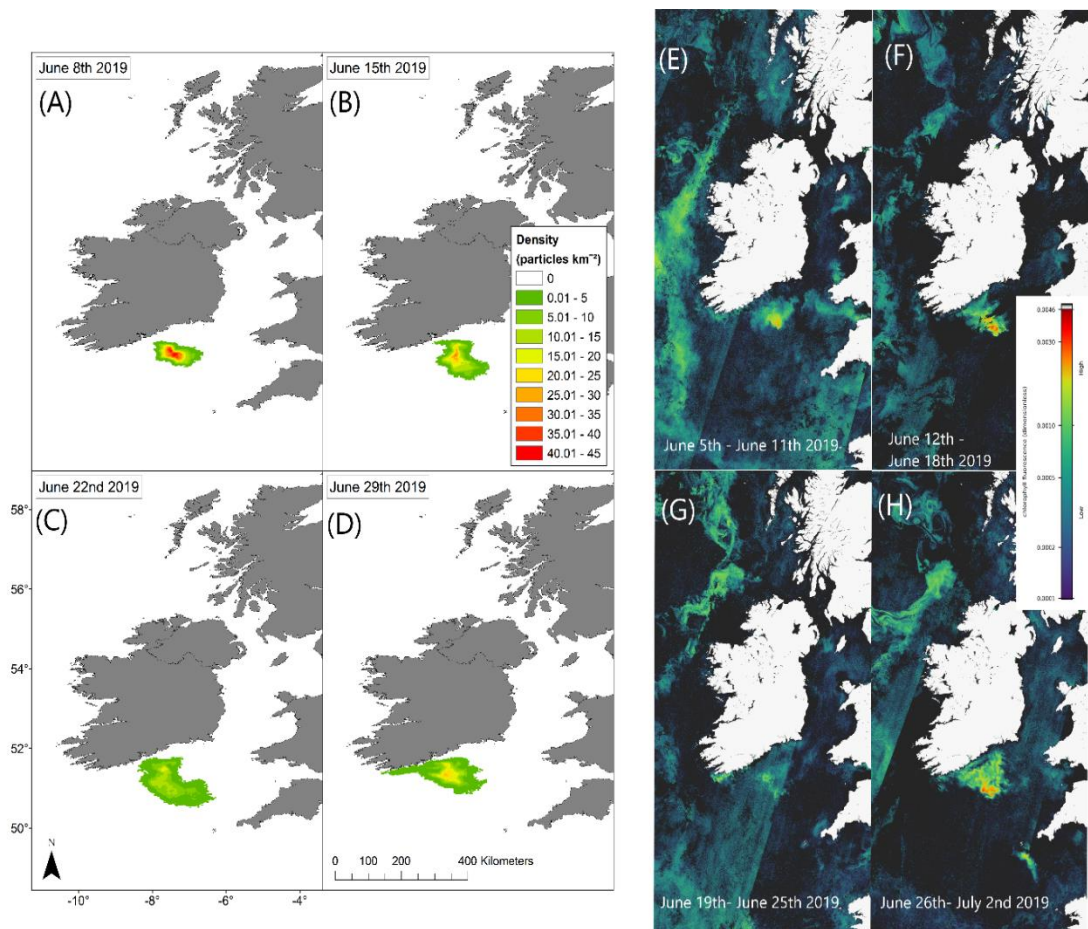


Figure 27 Particle tracking model simulation results display current driven bloom dispersal on the left (A–D). Maps show the density distribution of particles on 08/06/2019, 15/06/2019, 22/06/2019, and 29/06/2019 compared with Sentinel-3a OLCI images with RBD weekly composites on the right (E–H).

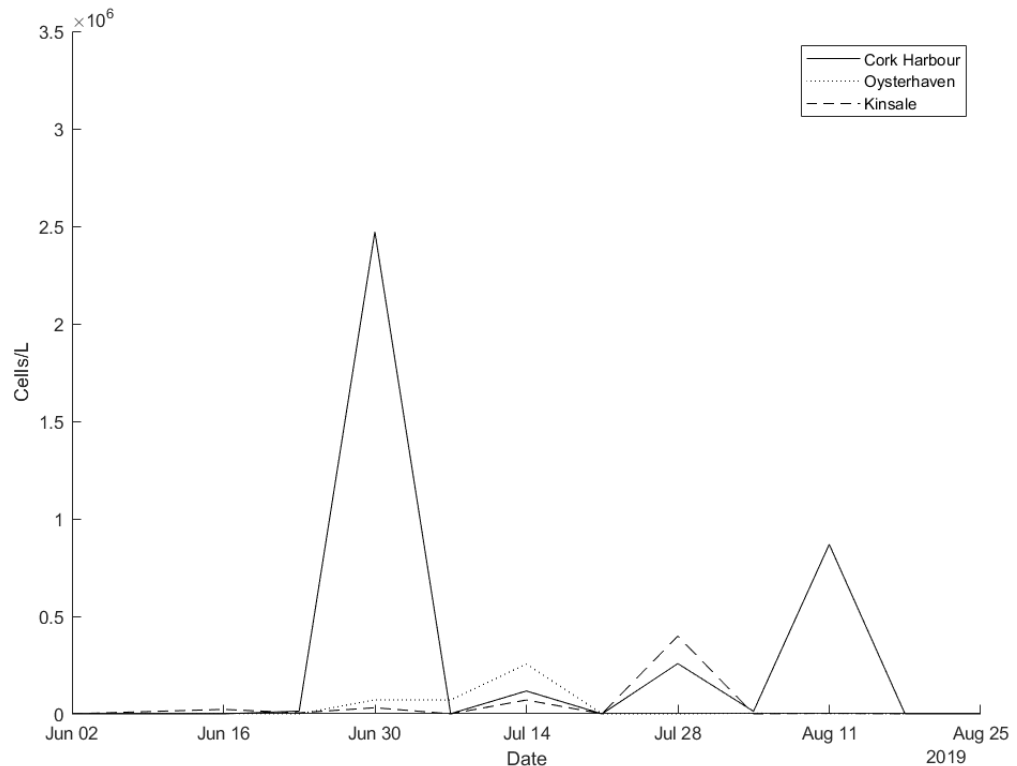


Figure 28 In situ *Karenia* spp. cells/L counts for inshore stations in Cork Harbour, Oysterhaven, and Kinsale from the national monitoring programme June–August 2019.

In 2019, the first inshore phytoplankton record of *Karenia* spp. (13,840 cells/L) in Cork Harbour was detected on 23 June. On 30 June the sharp rise in cell densities (2,471,168 cells/L) was detected, 3 days after the bloom peaked offshore. Around the same time (30 June) to the west, in Oysterhaven, 80,000 cells/L were recorded in water samples. These numbers increased to 260,000 cells/L by mid-July. Further west in Kinsale cell numbers rose from approximately 71,000 cells/L on 14 July to 398,736 by the 28 July. Many other phytoplankton taxa were identified during the above dates but *Karenia* spp. was consistently the highest cells/L recorded in each instance (Full cell counts for the three southern stations can be viewed in Appendix A6).

In July, phytoplankton cell counts from the research survey CV19018, that coincided with the time of the offshore bloom confirmed the predominant taxa observed was *K. mikimotoi*. The satellite imagery showed that stations ST134-144 were on the outer edge of the bloom and that station at ST148 was located in a high-density area of the bloom (Figure 29), the values in this graphic represent values closest to the surface. *K. mikimotoi* values of 1,710,000 cells/L at station 148 were recorded at deeper depths

but may not have been visible to satellite at that time due to the time the samples were taken and the behaviour of the phytoplankton.

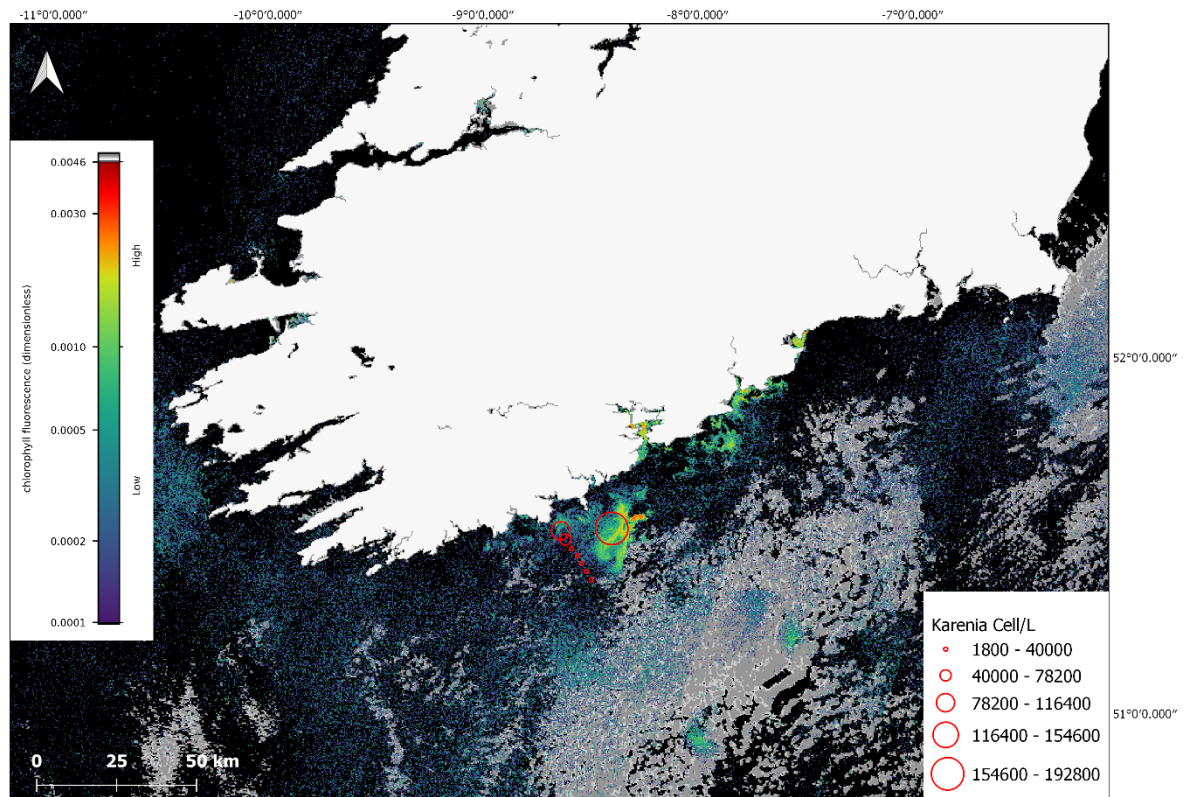


Figure 29 Sentinel-3a OLCI image with RBD algorithm from 10 July 2019. The red circles indicate cell concentrations determined using light microscopy for in situ samples collected on CV19018 on the same date. The grey colour in the image represents cloud cover

Water samples collected with the CTD at stations 135–148 had an array of phytoplankton taxa identified (e.g., *Dinophysis acuminata*, *Prorocentrum*, *Ceratium lineatum*, *Ceratium fusus*, *Ceratium furca*, *Ceratium tripos*, *Ceratium macroceros*, *Protoperdinium*, *Gyrodinium*, *Ceratium inflatum*, *Dinophysis acuta*, *Noctiluca*) with *Karenia mikimotoi* present and the most abundant taxa recorded at stations sampled. The FSS bottles were deployed at 17–19 m at station 148 at 16:48 after a thin layer was identified on the CTD cast. *K. mikimotoi* was again the predominant taxa observed throughout the 5 bottles with cell counts of 3,146,000 cells/L, 4,258,000 cells/L, 3,842,000 cells/L, 3,276,000 cells/L and 2,474,000 recorded (Full cell counts for CV19018 can be viewed in Appendix A7).

In situ K. mikimotoi cell counts from stations 138–148 closest to the surface were used to clarify whether there were any potential associations between the satellite derived

RBD value, and *in situ* cell counts. While sampling was conducted over the course of the day from 09:03 to 16:34, it was difficult to determine the exact surface counts at the time of the satellite data acquisition given the DVM behaviour of *Karenia* spp. A linear regression was calculated, $(\text{Cells/L}) = 1.97 \times 108 (\text{RBD}) - 1.49 \times 104$, with an R² value of 0.93 (n = 8) was determined (linear regression and data for this conclusion in Appendix A8). This suggests to us that an RBD value greater than approximately 0.0005 makes a useful early threshold for bloom formation as it is roughly equivalent to 1×10^6 cells/L. However, given that there are several unknowns with regard to fluorescence characteristics and the DVM nature of *K. mikimotoi*, the timing of satellite measurement, *in situ* sample timing, and the low sample size the high correlation value could have been fortuitous as the samples acquired for this study were opportunistic therefore there are spatial and temporal mismatches involved.

Future work to clarify this would require more dedicated *in situ* sampling at the time of satellite-measurement acquisition and an estimate of the *Karenia* spp. position within the water column at that time. The findings of such studies will help determine a threshold for a warning system.

4.5 Discussion

The RBD algorithm was tested in Irish waters for the first time during the months of May, June, July, and August 2019 to assess its suitability for adding to the established HAB monitoring system. A phytoplankton bloom occurred off the south coast at this time and was visible using the RBD satellite images. The results we have presented here show the RBD algorithm was proficient in assessing the timing of the initiation, movement, geographical extent, locations of the peak abundances and duration of the bloom. Although this study demonstrates the RBD's use in detecting *Karenia* spp. blooms, the algorithm would be useful for monitoring HAB events in general as the detection of bloom presence with the RBD algorithm indicates some Chl-*a* fluorescence, as the radiance returned at 681 nm is greater than that returned from 665 nm, even though 681 nm also includes strong Chl-*a* absorption (Wolny *et al.*, 2020) and already used for Chesapeake Bay for monitoring a range of dinoflagellates.

Unfortunately, there was not enough offshore data to do a rigorous validation, but, we were able to confirm the predominant phytoplankton in an area when the bloom appeared on satellite imagery using data from an offshore survey that coincided with

the bloom in July. Having confirmed the drift trajectory of the bloom based on local water circulation patterns using the particle tracking model we were confident in using the inshore data from the southern stations Cork Harbour, Oysterhaven, and Kinsale and confirmed that *Karenia* spp. was the predominate taxa identified.

Although the authors are not trying to replace the current standard chlorophyll algorithm, it is hoped the preliminary use of RBD algorithm will become an extra monitoring tool within the HAB alert system. This paper presents the results from a pilot study and future studies will help improve methodologies with the implementation of more validation methods such as the use of hyperspectral radiometry from the national research vessel.

The acquisition of new technical skills will further help support a sustainable aquaculture industry in Ireland. The use of satellite technology for observing the movement of phytoplankton blooms are well documented throughout the world (Stumpf *et al.*, 2003, 2009; Stumpf and Tomlinson, 2005; Miller *et al.*, 2006; Davidson *et al.*, 2016; Groom *et al.*, 2019). Of course, there are going to be limitations to using earth observation data, some of which include: clouds, difficulty differentiating between phytoplankton species and, depth limitations (Ruddick *et al.*, 1999). As discussed, blue-green ratio chlorophyll algorithms can overestimate chlorophyll in waters close to the coast due to contamination of CDOM and sediment in the measurements. Satellite measurements of chlorophyll fluorescence are considered proficient to detect blooms in areas like this (Gower and King, 2012; Gower *et al.*, 2013). Introducing new methods of monitoring is useful to improve current mitigation efforts, given the diversity and complexity of HAB events and the different behaviours of phytoplankton functional types (Moisan *et al.*, 2017). Understanding the history and behaviours of the most problematic species that are responsible for HAB events can help detect what type of bloom is forming offshore before it is possible to collect samples. This can be done by using algorithms with trained datasets (Martinez-Vicente *et al.*, 2020) and also it is vital to understand the typical behaviour of the species. It is established that blooms of *Karenia* spp. originate in regions of the continental shelf that have weak tidal currents and are stratified in the summer (Brand *et al.*, 2012). For example, in the Celtic Sea close to the Nympe bank, where tidal streams are weak, the spring bloom develops earliest (Pingree *et al.*, 1976; Raine, 2014). In this area, high densities of *K. mikimotoi* have been observed as early as May (Pemberton *et al.*,

2004). The Nymphe Bank is located at 51°30'0" N 7°30'0"W, an area where the centre of the bloom first appeared on satellite imagery, see Figure 24; 51°23'24" N 7°23'18"W. Large blooms of *Karenia* spp. have been recorded around Ireland in regions with similar slack circulation, areas such as the southern Malin shelf and the Irish shelf to the west of the Aran Islands (Gowen *et al.*, 1998; Silke *et al.*, 2005). Subsequent growth and transport in coastal currents can spread their impact over large areas of the coastal zone (Davidson *et al.*, 2009). Due to the proximity to land, the development of these blooms are difficult to detect without satellite technology.

Many harmful algae display diurnal vertical migration behaviour (Park *et al.*, 2001; Kononen *et al.*, 2003). The algae are known to swim toward the surface at dawn and to deeper depths at dusk (Olsson and Graneli, 1991; Koizumi *et al.*, 1996; Park *et al.*, 2001). *Karenia mikimotoi* are known to vertically migrate within an estimated daily depth range of 15–20 m (Koizumi *et al.*, 1996; Li *et al.*, 2019) they migrate before sunrise and reach the surface before midday (Li *et al.*, 2019). When the cells assemble at the surface during upward migration, this has been shown to promote the formation of the red tide (Honjo, 2004). Previous observations have suggested that *K. mikimotoi* are frequently found in thin layers near the pycnocline (Brand *et al.*, 2012) developing at or directly below the thermocline (Holligan *et al.*, 1984) particularly at frontal regions between well-mixed and stratified waters (Pingree *et al.*, 1977). Results from the FSS at station 148 on CV19018 show *Karenia* spp. between 17 and 19 m in a thin layer in extremely high densities. These samples were taken at 16:34, due to the DVM behaviour of the species, they were travelling to deeper depths before dusk and higher concentrations could have been identified at the surface if the samples were taken around midday. Knowing *Karenia* spp. exhibit these behaviours of surfacing around midday, it is a good reason to choose a fluorescence algorithm to monitor coastal waters. Fluorescence penetration depth is shallow because oceanic waters attenuate fluorescence and the signal only returns information of Chl-*a* in the subsurface waters of approximately 2 m (Xing *et al.*, 2007).

Additionally, in order to predict movement of the bloom, it is important we understand the water circulation patterns. The RBD images show the bloom was detected by satellite on the 2 June, 14 days before *Karenia* spp. was identified in the inshore samples. Historically, *K. mikimotoi* blooms are known to occur in shelf and coastal waters off the south, southwest, west and northwest of Ireland. Water circulation

around these coastal areas is heavily influenced by the Irish Coastal Current (Figure 30) that flows in a clockwise direction around the Irish Atlantic coastline (Raine, 2014). This coastal current is an important transport pathway in the northern Celtic Sea. In summer, the westward transport of planktonic organisms is heavily influenced by the Irish Coastal Current with faster flows, in a density driven current, found at depths of ~25 m (Farrell *et al.*, 2012).



Figure 30 Coastal currents (red) and the Shelf Edge Current (green) adapted from Hill *et al.* (2008)

In this study, relatively calm weather was reported in June with weak wind speeds and low significant wave heights (average 1.2 m) recorded at the M5 data buoy in the Celtic Sea, conditions suitable for the development of the *K. mikimotoi* bloom observed in offshore surface waters. The numerical hydrodynamic model used in this study was tightly coupled to meteorological data and the particle tracking model shows the advection of the *K. mikimotoi* bloom into inshore regions when the bloom was fully developed. Wind driven advection is important in this region. For example, in 1998, weak wind driven upwelling in the region uplifted a subsurface *K. mikimotoi* bloom into surface waters off the SW coast, wind also played an important part in the transport of the bloom eastwards across the Celtic Sea where it was advected into coastal areas; this bloom was recorded using satellite ocean colour and thermal infra-red sea surface temperature images alongside *in situ* measurements (Raine *et al.*,

2001). The results from the particle tracking model confirm the bloom followed the pattern of the clockwise coastal current when *Karenia* spp. counts peaked in the three southern inshore stations at different times. Cork Harbour first, Oysterhaven and then Kinsale.

The method explained in this study shows high-biomass blooms, like *Karenia* spp. can be detected and monitored with the RBD algorithm like in the Gulf of Mexico and Alaska (Amin *et al.*, 2009; Vandersea *et al.*, 2020) and now this study confirms it is a useful product to use in Irish waters. Wolny *et al.* (2020) describes how the RBD method is used to monitor the most common marine and estuarine HABs in Chesapeake Bay indicating the potential for other HAB blooms of interest in Ireland. Henderikx and Dierssen (2019) also evaluate the accuracy of Red RBD algorithms for measuring chlorophyll concentrations in coastal waters. Their study demonstrates how well RBD algorithms capture the dynamics of chlorophyll in both the summer and the winter, particularly when they use data from MERIS. The study shows that these algorithms are more dependable than other conventional approaches in complex estuarine environments and accurately reflect seasonal variations in phytoplankton concentration. The findings show that RBD algorithms could be significant in enhancing satellite-based monitoring of chlorophyll levels in coastal areas. The Le *et al.* (2013) study also assesses how accurate the RBD algorithm is at predicting the amounts of chlorophyll in coastal waters. The authors from this study also discuss about how well the RBD algorithm performs with MERIS data, showing how good it is for different ranges of chlorophyll and contrasting it with other algorithms. This study contains significant information on the algorithm's dependability and its use in satellite-based coastal water status monitoring.

Further discrimination of genus or species level is difficult with just satellite technology, but combined with particle tracking and routine monitoring programmes, can further develop a more robust warning system. Aquaculture business owners can limit damage to their stock by avoiding moving, harvesting and/or planting new seed while warning systems are in place.

Quantitative application of the RBD approach examined here, requires more data to better constrain the relationship between RBD values and cell numbers of *Karenia mikimotoi* as the observed reflectance/fluorescence is influenced by a suite of external

variables which may change with time (e.g., irradiance, photosynthetic efficiency, cell size, etc.). One such key parameter is the chlorophyll per cell of *Karenia mikimotoi*, with laboratory studies indicating it decreases with increasing irradiance and covers a wide range of values in the literature; 2–27 pg Chl cell⁻¹ (Stæhr and Cullen, 2003; Chang and Gall, 2013; Wang *et al.*, 2019; Zhao *et al.*, 2019). Values of 2–6 pg Chl cell⁻¹ (Stæhr and Cullen, 2003; Zhao *et al.*, 2019) have been found under high light conditions similar to what was observed in the Celtic Sea at the time of our study, using the Cell numbers of ~3,000,000 cells/L from the centre of the bloom at that time would indicate a value of 6–18 µg Chl/L potentially associated with *Karenia mikimotoi*.

There was limited availability of offshore data to do a full validation for this study. If this algorithm was to be used as an operational satellite product, future work will investigate combinations of inshore and offshore sampling and combining hyperspectral radiometry data.

4.6 Conclusion

- We analysed remotely sensed data for the period of May–August 2019 testing the RBD algorithm in Irish waters for the first time.
- The phytoplankton bloom we identified using the satellite technology was localised and was reflected in the inshore phytoplankton samples from around Ireland.
- Both the satellite imagery and the particle tracking simulation results confirm the movement and the direction the bloom travelled.
- *Karenia* spp. was present in high numbers only at southern stations at the time of the bloom and was not identified anywhere else along the Irish coastline.
- A sudden increase of *Karenia* spp. in Cork Harbour, Oysterhaven and Kinsale occurred shortly after the bloom developed in offshore waters.
- The appearance of *Karenia* spp. at the southern coastal stations followed an east to west pattern in line with what the expected transport of the Irish coastal current.
- We established that the predominant phytoplankton observed in offshore samples was *K. mikimotoi*.

- We describe the potential for Ireland to use the Red Band Difference algorithm as an extra monitoring tool within the established HAB alert system to provide an early warning method of HABs and in particular, *Karenia* spp. blooms.

5. Chapter 5:

Combining Satellite Imagery and the HABscope in Irish waters

Catherine Jordan^{1,2}, Caroline Cusack², Dave Clake², Sheena Fennell¹, Chris Holland³, Michelle Tomlinson³, Peter Croot¹

¹Earth and Ocean Sciences, School of Natural Sciences and Ryan Institute, University of Galway, H91 TK33 Galway, Ireland

²Marine Institute, Galway, Ireland

³National Centers for Coastal Ocean Science (NCCOS, NOAA), Silver Spring, MD, United States

This was a feasibility and preliminary study to assess the suitability of the HABscope in Irish waters.

5.1 Abstract

A feasibility study was carried out using NOAA's HABscope system in Irish waters for the first time during the summer months of 2021 on two research surveys CV21015 and CV21021. The HABscope incorporates artificial intelligence technology that can detect the swimming pattern of *Karenia* spp. and provide a confirmation of presence or absence of the phytoplankton at a particular point in time or for more thorough studies, can provide estimates of cell concentration. This can then be used as a warning tool for harmful algal blooms.

Results from research survey CV21015 in July 2021 showed that *Karenia* spp. were not detected at any surface sample during the survey and satellite results reflected low concentrations of chlorophyll fluorescence at the surface for the duration of the survey also. However, *Karenia* spp. were detected at station 17 at a depth of 38 meters at 20:00, with microscope counts indicating 250,000 cells/L and HABscope results returning an estimation of 120,000 cells/L. In August 2021, the HABscope was used on a phytoplankton dedicated survey CV21021. During this time, high concentrations of phytoplankton fluorescence were detected via satellite imagery at the surface. The HABscope was used at various points throughout different transects as an additional tool to confirm the presence or absence of *Karenia* spp.

This device would work in conjunction with the RV Celtic Explorer's Hyperspectral Radiometers from Chapter 3 and the Red Band Difference satellite algorithm from Chapter 4 to provide an early warning system for *Karenia* spp. blooms.

To summarise, implementing the HABscope technology in Ireland may enhance monitoring of the presence of *Karenia* spp. in aquaculture and marine ecosystems in general.

5.2 Introduction

Since the 1980s, Ireland's monitoring of Harmful Algal Blooms (HABs) has been conducted through a national phytoplankton and biotoxin program, using ISO 17025 standard microscopy to identify phytoplankton species. These findings are disseminated weekly in the HAB bulletin, the development of which is detailed by Leadbetter *et al.* (2018). This bulletin, crucial for aquaculture management, includes additional data like satellite and oceanographic forecasts.

Chapter 4 introduces the Red Band Difference (RBD) Algorithm, enhancing the bulletin with a satellite-based method for detecting and tracking HABs. Its effectiveness is supported by various studies (Amin *et al.*, 2009; Le *et al.*, 2013; El-habashi *et al.*, 2016; Henderikx and Dierssen 2019; Wolny *et al.*, 2020; Vandersea *et al.*, 2020; Jordan *et al.*, 2021).

NOAA's mitigation efforts include the HABscope, a new tool for detecting *K. brevis*. Developed as a citizen science project, the HABscope is a low-cost microscope paired with an iPod touch, allowing for daily sampling across many water bodies. *K. brevis*, known for producing harmful brevetoxins, is a significant concern in the US (Poli, 1986; Backer *et al.*, 2003). The HABscope's innovative approach involves citizens collecting samples, recording them with the iPod, and uploading videos for neural network analysis, focusing on *K. brevis* distinct characteristics (Hardison *et al.*, 2019).

Karenia spp. are dinoflagellates and these are more agile than most other phytoplankton types, as they can change their swimming speed and direction by adjusting their flagellar patterns. Fenchel, (2001) explains dinoflagellates have two flagella; a transversal flagellum and a trailing flagellum, which is responsible for their ability to swim. This study showed that the transverse flagellum causes the cell to rotate around its length axis, while the trailing flagella causes the cell to move forward

and also to rotate around an axis perpendicular to the length axis. The combination of these two rotations results in a helical swimming path that can be varied by changing the speed and direction of the flagella. Chang and Ryan (2004) compare the morphology and ultrastructure of a new species of *Karenia* genus that was isolated from the New Zealand coast in 2002. During this study the authors observed that when *K. concordia* cells were gently shaken within the culture flask they exhibited a falling leaf swimming pattern, meaning the cells would rotate around their longitudinal axis while descending slowly in a zigzag motion. Chang and Ryan (2004) also noted that the swimming pattern was similar to that of *K. mikimotoi*. Hardison *et al.* (2019) describes how *K. brevis* has a corkscrew swimming pattern, slightly different to *K. mikimotoi* but similar enough for the HABscope to determine the genus

While *K. brevis* hasn't been observed in Irish waters, *K. mikimotoi*, with similar traits, poses a threat to marine life (Li *et al.*, 2019). This study explores the use of the HABscope in Ireland, combined with satellite technology, to first test whether the instrument works in Irish waters and if so, can it identify *K. mikimotoi's* presence. The technology had not been used to identify *K. mikimotoi* before.

The objective of this study was to trial the HABscope in Ireland for the first time combined with satellite technology to determine whether this piece of technology would be an asset to the HAB alert system for identifying whether *K. mikimotoi* is present in a sample. Another objective was to trial the technology on a research survey, which had never been done using this system. Further studies will be completed in the future to determine the accuracy of the cell count between the HABscope and *in situ* microscope results in Irish waters.

We completed the objectives by combining satellite imagery and the HABscope on two phytoplankton research surveys during 2021. In this paper we present satellite imagery for both research surveys and how the HABscope was used to determine presence or absence of the HAB *K. mikimotoi*.

5.3 Methods

5.3.1 Phytoplankton Research Surveys CV21015 and CV21021

Two dedicated phytoplankton scientific surveys (CV21015 and CV21021) took place between 29 June and the 5 July 2021 (CV21015) and 8 August 2021 to 11 August 2021 (CV21021) in the Celtic Sea on board the RV Celtic Voyager. Figure 31 illustrates the stations from both surveys. Water samples and videos of live samples using the HABscope were taken throughout both surveys and uploaded when the ship was in 4G range, or when back on land. The water samples were fixed in Lugol's iodine and stored in sterile 50 mL Sarstedt® water sampling bottles for analysis in the laboratory at a later date. Phytoplankton species were identified with an inverted microscope, Olympus CKX4. Aliquots and cells counted following the Utermöhl method (UNESCO, 2010).

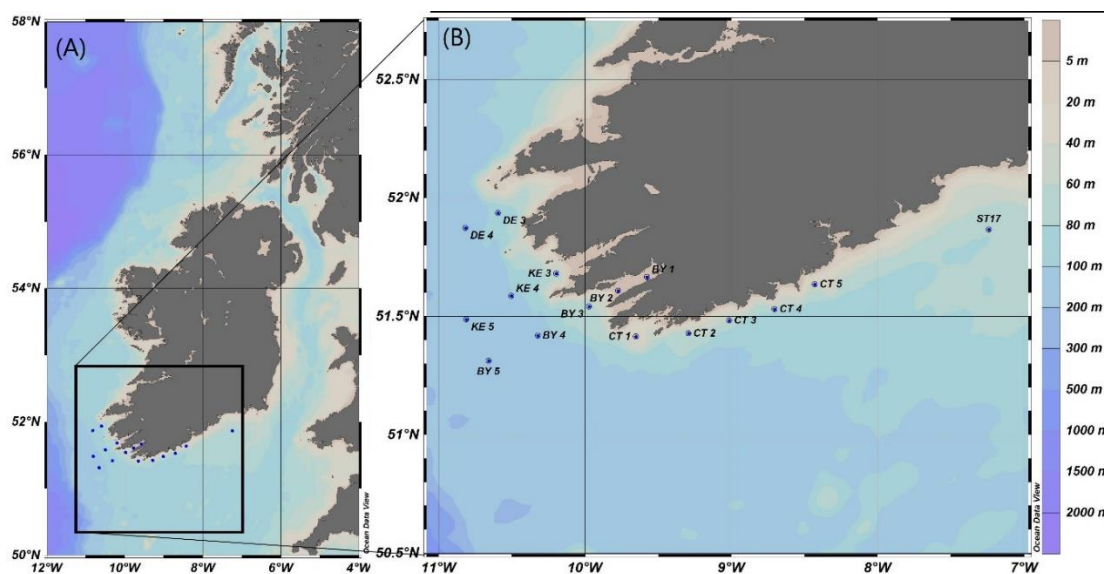


Figure 31 Stations from CV21015 and CV21021

5.3.2 Red Band Difference Satellite imagery

L1B data satellite data were downloaded from The European Organisation of Meteorological Satellites (EUMETSAT). The data was derived from Ocean and Land Colour Instrument (OLCI) sensor on Sentinel 3A. OLCI is a multispectral sensor with 21 spectral bands ranging from 400 to 1200 nm and has a spatial resolution of 300 m.

The bands are optimised to measure ocean colour. The whole field-of-view is shifted to minimise the impact of sun glint across track by 12.6° away from the sun. The L1B data were then processed to L2 using the NOAA, National Centres for Coastal Ocean Science (NCCOS) satellite automated processing system which utilises NASA's l2gen software included in the Sea-viewing Wide Field-of-view Sensor (SeaWiFS) Data Analysis System (SeaDAS) package (version 7.5.3). The l2gen processing produced a surface reflectance product (R_{rhos}) that is corrected for top-of-atmosphere solar irradiance, Rayleigh radiance and molecular absorption (Wynne *et al.*, 2018).

The RBD algorithm, described by Amin *et al.* (2009) highlights areas of high fluorescence, which suggests high algal biomass, at the surface of the water, uses only pixels within the valid R_{rhos} range (0–1) and modified for OLCI R_{rhos} bands as follows:

$$\text{RBD} = R_{\text{rhos}}(681) - R_{\text{rhos}}(665)$$

The RBD data products were mapped to Universal Transverse Mercator (WGS 84) projection at 300 m horizontal resolution using a nearest neighbour interpolation. The GeoTIFF (an image file with georeferencing information embedded in the file as metadata) created is stored in a database on the NCCOS server. Weekly mean composites of the daily images were created using a custom ArcGIS python toolbox, RS_Tools, that was developed specifically for working with products from the NOAA-NCCOS satellite processing system.

5.3.3 HABscope

The HABscope is a sampling device routinely used to sample for *Karenia brevis* in the United States. The device is designed to be used by both scientists and citizen scientists. The instrument consists of a standard classroom grade, low cost microscope, and a wireless, touchscreen controlled iPod touch (<https://www.apple.com/ipod-touch>). Figure 32 shows the HABscope set up on research survey CV21015 on board the RV Celtic Voyager. The iPod attached to the microscope enables scientists to record a short video of a three-drop water sample, approximately 60 µL using a dropper pipette placed on a 100 µL depression slide. Once the sample was focused at 40X, a 30 second video was recorded. The video is then uploaded via mobile hotspot, if in the field or using wifi if in the lab, videos are uploaded to the Gulf of Mexico

Coastal Ocean Observing System (GCOOS) website. The video is analysed using a neural network programme trained to recognise *K. brevis* cells. Cell identification is based on the size, unique shape and characteristic corkscrew swimming pattern of *K. brevis*, which helps distinguish it from co-occurring species typically found during *Karenia spp.* blooms. Once the videos are uploaded to the GCOOS website they are verified by a NOAA staff member. Hardison *et al.* (2019) describes the components of the HABscope microscope in detail. The HABscope was also tested in the laboratory using a culture of *K. mikimotoi* prior to being brought to sea to ensure it worked.



Figure 32 HABscope set up on research survey CV21015

5.4 Results

Figure 33 illustrates RBD imagery captured during the two research surveys. 33 (A) represents a weekly composite from 01 July – 07 July 2021 during CV21015 survey dates and 33 (B) represents a weekly composite from 05 August – 11 August 2021

during CV21021 dates. As can be seen in the imagery, very little phytoplankton activity was present at the surface during CV21015 dates and higher phytoplankton activity was present at the surface during CV21021 dates.

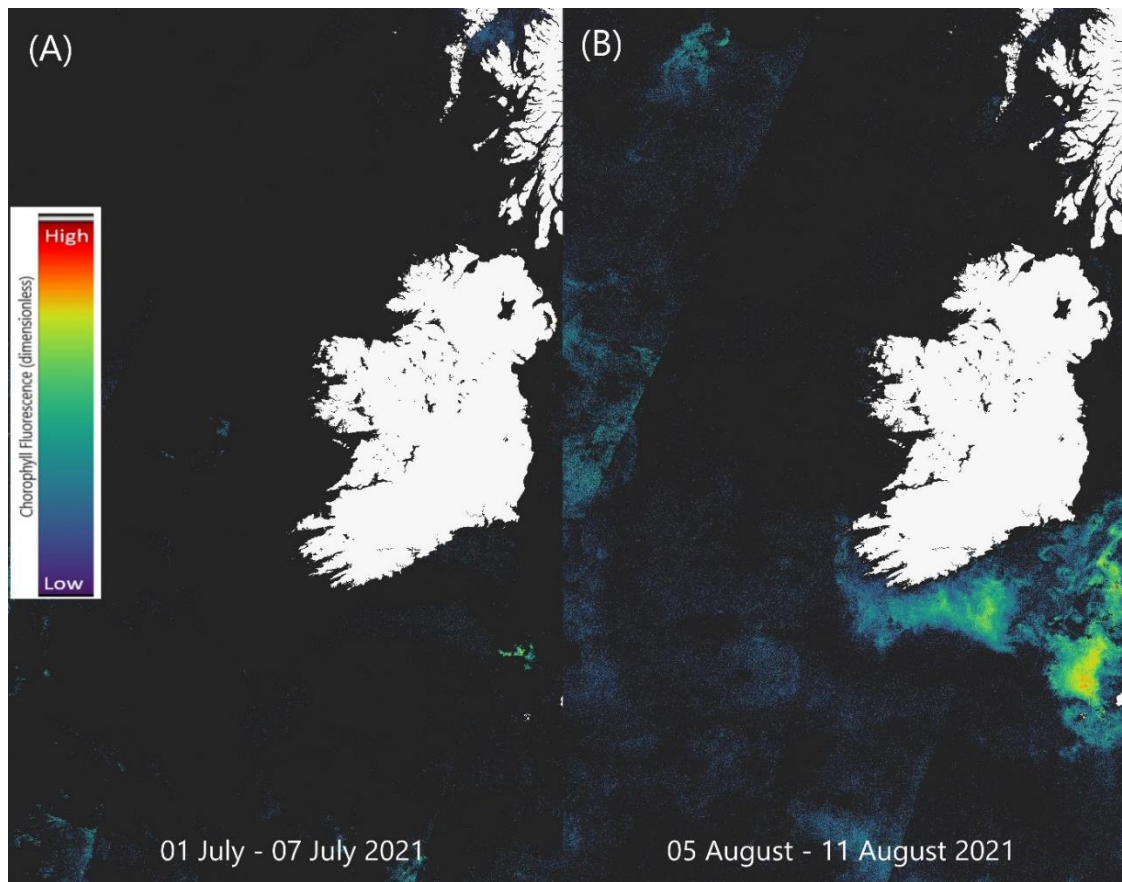


Figure 33 Red Band Difference satellite imagery from the weeks research surveys CV21015 (A) and CV21021 (B) took place

Figure 34 displays a screen grab from a HABscope video showing two cells of *K. mikimotoi* identified in a water sample during a 30 second video from station 17, CV21015 from 38 m depth. Two cells equate to 120,000 Cells/L using the HABscope conversion tool. See Appendix A9 for conversion cells to cpl. Microscope results confirmed 250,000 Cells/L were present in that water sample.



Figure 34 Screen grab from a HABscope video demonstrating two cells identified using the neural network programme trained to recognise *Karenia* spp. cells

Figure 35 displays a bubble map of *K. mikimotoi* *in situ* microscope results overlaid onto RBD satellite imagery during CV21021 survey dates. The highest cell count and largest bubble recorded using microscope analysis was 30,800 Cells/L at DE3 (Figure 31). One cell was found on the AI utilising the HABscope at this location, and the sample contained an estimated 50,000 Cells/L. Smaller dots indicate samples with less than 10,000 cells per litre. 50,000 particles this is the limit of detection for *K. brevis* (cells per litre) in the Gulf of Mexico, by legacy satellites (Tester *et al.*, 1998).

K. mikimotoi counts at KE4 (Figure 31) were 27,680 Cells/L, on the HABscope 14 cells of *K. mikimotoi* were identified from a 3 drop sample, approximately 60 μ L but this was confirmed to be an over estimation due to the mixed assemblage of phytoplankton species at that station as seen in Figure 36.

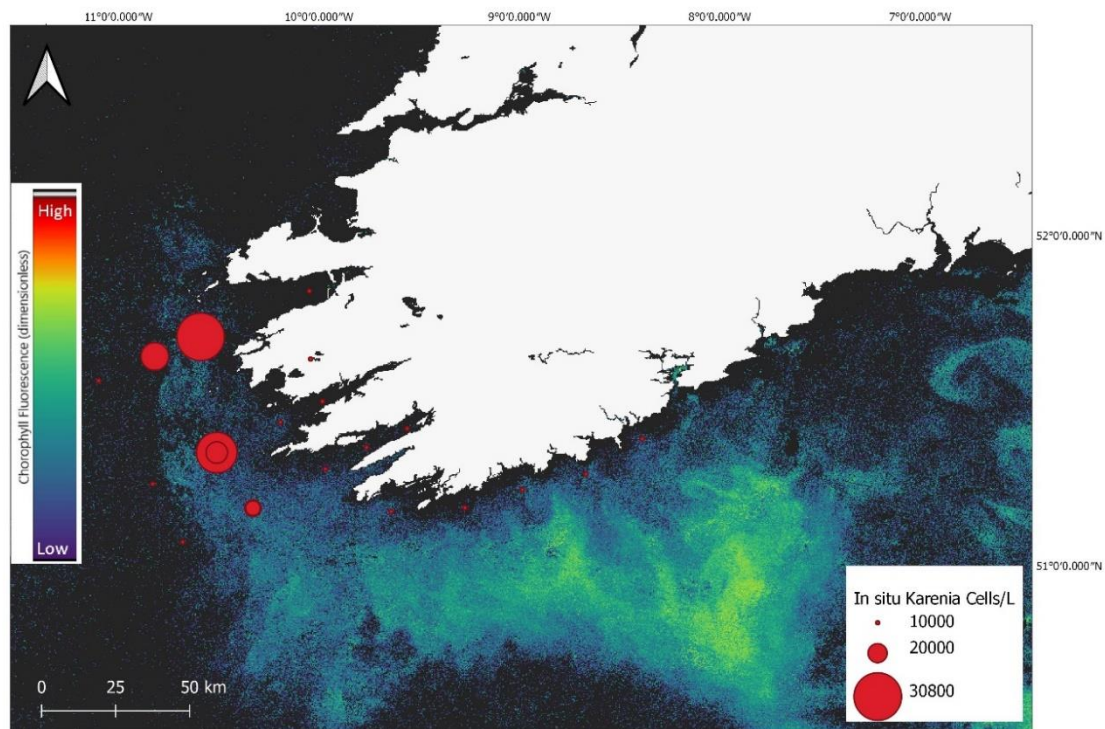


Figure 35 A bubble map of *K. mikimotoi* in situ microscope results overlaid onto RBD satellite imagery during CV21021 survey dates



Figure 36 Screen grab from the HABscope to illustrate a mixed assemblage of phytoplankton species and the neural network technology identifying *Karenia* spp. amongst other species

5.5 Discussion

The HABscope, developed by the US National Oceanic and Atmospheric Administration (NOAA) and funded by NASA is used routinely by citizen scientists to monitor the development of *K. brevis* blooms in the US (Hardison *et al.*, 2019).

The aim of this study was to evaluate the feasibility of using the HABscope technology in Irish waters and to conduct a preliminary test of the equipment during a research survey, both for the first time. Specifically, this study aimed to validate the AI's ability to detect *Karenia* spp. particularly *K. mikimotoi* in Irish waters and assess its potential for determining their presence or absence of *K. mikimotoi* without the need for labour intensive sample collection and transport to a laboratory. The technology had only identified *K. mikimotoi* in lab conditions before this study. The study's results confirmed that the HABscope would be a valuable tool for detecting presence or absence of *K. mikimotoi* in Irish waters.

A further validation study will be completed to determine how accurate the cell estimation between the HABscope and microscope counts are in future studies. Figure 35 illustrates the spread of *Karenia* spp. during one research survey. These results only became available months after the survey was finished due to time pressure while the scientists are at sea and also when they return to the lab. The HABscope was used at stations DE3 and KE4 (Figure 31) during this survey to confirm presence or absence of the species. It proved to be a valuable tool to confirm *Karenia* spp. was present at that point in time.

The RBD satellite imagery used in this study further complement the use of the HABscope technology. As stated earlier, satellite imagery is a useful tool for monitoring the ocean over vast distances, and the data provides early warnings against phytoplankton blooms (Stumpf and Tomlinson, 2005). Jordan *et al.* (2021) demonstrated the effectiveness of RBD satellite imagery as a valuable complement to the HABscope for monitoring and tracking *Karenia* spp. and other phytoplankton blooms in Ireland. In this study, Figure 33 displays RBD imagery depicting low levels of phytoplankton activity at the surface during the CV21015 survey, followed by a higher concentration of phytoplankton during the CV21021 survey. The HABscope's results corroborated these findings. Notably, *K. mikimotoi* was only observed at a depth of 38m at station 17 during CV21015, with no surface samples being recorded.

It should be noted station 17 was sampled at 20:00 therefore it is not surprising *Karenia* were found at 38m and not the surface, due to their DVM behaviour (Olsson and Graneli, 1991; Koizumi *et al.*, 1996; Park *et al.*, 2001; Shikata *et al.*, 2014, 2015, 2016). The main objective was to compare a wild *Karenia* spp. sample at sea, if found with the HABscope and *in situ* microscope data. In this instance, the HABscope estimated a cell count of 120,000 Cells/L after detecting two *Karenia* spp. cells. Subsequently, a microscope was used to validate the HABscope's estimation, and 250,000 Cells/L were identified in the same sample. This was one sample and no repeat samples were carried out at that time.

During CV21021 in August 2021, RBD satellite imagery revealed high concentration of phytoplankton at the surface, which was further confirmed by HABscope recordings that displayed abundant phytoplankton activity with many species identified (see Figure 36). Despite the high diversity of species observed, the HABscope technology was able to distinguish *K. mikimotoi* from other species within the sample, emphasizing the value of this technology. Hardison *et al.* (2019) describe in detail how they trained the AI to distinguish *K. brevis* from other similar sized free swimming dinoflagellates. To enable the CNN to train to recognise the morphological distinctions between *K. brevis* and the other species, around 5,993 photos of *K. brevis*, *Amphidinium* sp., and *Alexandrium catenella* were collected. The system's capacity to distinguish *K. brevis* cells from other material was then tested by adding *K. brevis* cells to samples of natural water. It was discovered that occasionally debris particles that were agitated by microscope vibrations were mislabelled as *K. brevis*. To solve this issue, additional photos of detritus and *K. brevis* from natural samples were used to train the CNN. Over a five-month period, the training library was updated when fresh and/or improved photos were gathered. The CNN was periodically retrained using these newly captured images, and the new model was then saved. The training library currently has 5,993 images of debris and 15,666 photographs of *K. brevis* as on 2019-04-22.

Hardison *et al.* (2019) study compared cell abundance data using HABscope software and a particle counter. Between 120,000 and 9,200,000 cells per litre, the HABscope programme found *Karenia brevis* cells with a 31% Mean Absolute Percentage Error (MAPE). The low, medium, and high cell concentrations that are important for determining respiratory hazards fall within this range. The HABscope response was

linear over the whole range when compared to the Coulter Counter data, however it tended to overestimate the lowest concentrations. There was no discernible bias at other concentrations.

The number of visible cells in the field of view (FOV) at a 40X magnification served as the HABscope's detection limit. 1-2 cells were visible in the field of view (FOV) at this magnification and concentration of 50,000 *K. brevis* cells per litre, indicating that 50,000 cells per litre is the lower detection limit of the HABscope. The quantity of cells visible in the field of view increases with increasing cell concentration.

In field tests, the HABscope exhibited a minor positive bias of 3% and a total error (mean absolute percentage error, MAPE) of 22% across a range of cell concentrations from 100,000 to 2,200,000 cells L⁻¹. Although the data generally aligned well with the 1:1 line across this range, there was a notably higher bias in two instances of low cell counts. This bias includes errors from both manual and HABscope cell counts. It's important to note that manual cell counts typically have an uncertainty of about 10–20%.

The accuracy of the HABscope system in measuring *K. brevis* and assessing respiratory risks was assessed using various criteria. The mean absolute percentage error (MAPE) was used as a key metric for assessing accuracy, and it was found to be 52%, primarily due to a negative bias of 22%. This metric was chosen because error tends to be proportional to the magnitude of the data being analysed. With an overall accuracy of 91%, the HABscope system demonstrated significant accuracy in classifying *K. brevis* concentrations into low, medium, and high respiratory risk groups. It's interesting to note that the algorithm accurately distinguished between high and low cell abundances. Based on the cell counts, 46 samples were identified as low-risk by the HABscope, which consistently placed them in that category. Nevertheless, there were variations among the group at moderate risk. Twelve samples were mistakenly identified as low-risk by the HABscope, and two were at 100,000 cells L⁻¹, the lower limit of this category. The remaining samples were manually rated as medium-risk

The system's performance was further elucidated in multiple danger categories using the HABscope categorization grid. For high-risk, the system's user accuracy was 100%; for medium-risk, it was 73%; and for low-risk, it was 98%. The overall producer accuracy was 94% in terms of the frequency of accurate classifications.

These findings demonstrate that while the HABscope system reliably detects *K. brevis* levels for respiratory risk assessment, its accuracy varies, especially in the medium-risk category (Hardison *et al.*, 2019).

As discussed in the introduction the HABscope is designed to identify *K. brevis* via its corkscrew swimming pattern, which generally helps distinguish the species from other species typically found during *K. brevis* blooms (Hardison *et al.*, 2019) and Chang and Ryan (2004) discuss the falling leaf swimming pattern which was similar to *K. mikimotoi*. Judging by the results of this study, the two swimming patterns are similar enough for the *K. mikimotoi* to be identified. Barua *et al.* (2023) discuss a rapid detection method for *K. brevis* and the authors state how different *Karenia* species are distinguished from one another by high resolution microscopy and molecular approaches which examine rRNA probes and minute physical characteristics of the organisms (such as length of epitheca and nucleus shape and location). Future *in situ* installations will increase the training database, which would be beneficial, but given that all *Karenia* species have almost similar shapes and features, it might be difficult to identify each one uniquely from their *in situ* holographic images. In this case, all *Karenia* species can be detected collectively using *in situ* holography rather than individually.

This pioneering study in Ireland has set the stage for future research, where a specialised sampling programme will be implemented to enhance the effectiveness of the HABscope. This tool will be particularly useful in improving the accuracy on research surveys and in identifying the presence of *K. mikimotoi*. Looking ahead, the HABscope could be integrated into phytoplankton research surveys, having already demonstrated its capability to detect *K. mikimotoi* at sea. It offers a practical solution for confirming the presence of *Karenia* spp. in blooms identified through satellite methods.

The HABscope, an affordable microscope, is especially proficient at automatically identifying *Karenia* spp. This makes it an essential asset for decision-makers who need quick results, enabling them to verify the presence of *Karenia* spp. in samples and to estimate cell counts.

Current challenges in distinguishing harmful algal blooms using multispectral satellites are expected to be mitigated by NASA's upcoming PACE mission. The

hyperspectral sensors on this mission will greatly enhance the ability to differentiate between harmful and non-harmful blooms.

In summary, the HABscope is a portable, user-friendly instrument, making it an invaluable asset for monitoring harmful algal blooms in coastal areas, on research surveys, and in aquaculture settings. When used in conjunction with the RBD satellite algorithm, it becomes a powerful tool for verifying the presence of *Karenia* spp. in coastal waters. Future endeavors will focus on validating cell count estimates in Irish waters and conducting pilot studies with aquaculture farms and citizen scientists. The HABscope represents a significant advancement in the detection of *Karenia* spp. blooms. Its successful application in the US paves the way for future developments, including training the AI to identify other harmful species, thereby enhancing the monitoring programs in Irish waters.

6. Summary Chapter

6.1 Summary of thesis

In summary, this thesis has effectively achieved its primary objectives by establishing an operational hyperspectral radiometer system aboard the RV Celtic Explorer, validating the Red Band Difference (RBD) algorithm for monitoring Harmful Algal Blooms (HABs) in Irish coastal waters, and conducting a preliminary feasibility study of the HABscope. These achievements have significantly enhanced our knowledge of ocean colour remote sensing in Irish waters and have introduced valuable assets to the realm of marine research and monitoring.

Throughout the thesis, the pivotal role of *in situ* data for calibrating, validating, and developing algorithms for ocean colour remote sensing has been consistently highlighted and reinforced.

Chapter 2 provided a comprehensive study of Irish waters, highlighting the challenges posed by persistent cloud cover and stressing the invaluable role of optical data collection in areas where frequent sampling is difficult. The chapter's focus on the vertical attenuation coefficient K_d at 490 nm and the 20-year climatology of K_d (490) and chlorophyll-a shed light on seasonal fluctuations and weather impacts, reinforcing the critical nature of *in situ* data for satellite validation and algorithm development.

Chapter 3 introduced the DM-QMF pack and presented a case study on *in situ* remote sensing data collection and processing. The statistical findings comparing satellite and *in situ* data across different wavelengths highlighted the importance of continued data processing and algorithm refinement.

Chapters 4 and 5 showcased the successful validation of the Red Band Difference (RBD) algorithm for monitoring Harmful Algal Blooms (HABs) in Irish coastal waters and the preliminary feasibility study of the HABscope, an AI technology for detecting *Karenia* spp. based on their swimming patterns. These developments have introduced valuable tools to the Irish monitoring program and the global ocean colour community for effective HAB monitoring and mitigation efforts.

The integration of the hyperspectral radiometry system, the RBD algorithm, and the HABscope into the Irish monitoring programme marks a substantial achievement in

marine phytoplankton and optically active constituent monitoring. These tools will not only benefit the Marine Institute but also researchers and the global ocean colour community, contributing to more effective and comprehensive HAB monitoring and mitigation strategies. This thesis serves as a valuable contribution to the field of oceanography and remote sensing.

6.1.1 Chapter 2

Chapter 2 of this thesis offers a comprehensive study of both *in situ* and satellite derived data to elucidate the characteristics of Irish waters, with a particular emphasis on the vertical attenuation coefficient K_d at 490 nm. Through various research surveys, *in situ* measurements of K_d (490) were measured, resulting in a range from 0.02-0.52 m^{-1} across diverse water types, including Case 1 and Case 2 waters. It's noteworthy that the Irish Sea's mixed waters exhibited the highest attenuation values of 0.52 m^{-1} and the lowest values of 0.02 m^{-1} was from station 15 at 52.999 latitude and -14.9907 longitude from CE19009 in the North Atlantic. The 20 year climatology of K_d (490) and chlorophyll-*a*, spanning from January through November for the years 1999–2019, are depicted in Figures 13 and 14. Limited data for January and November were obtained, and December yielded no data due to cloud coverage. Figure 13 illustrates the seasonal fluctuations of K_d (490) over these two decades in Irish waters, indicating more pronounced attenuation in coastal areas compared to oceanic waters, a trend that becomes especially pronounced during winter due to increased wind and precipitation. Conversely, as spring emerges, there's a noticeable increase in attenuation in oceanic waters. This shift during spring is attributed to the biological and physical activities in the water, correlating with the rise in chlorophyll during spring and summer, as demonstrated in Figure 14.

While acknowledging the limitations of satellite technology in monitoring Irish waters, particularly during periods of significant cloud cover, this chapter also underscores the indispensable role of *in situ* data, especially in areas that are less frequently sampled. The *in situ* data highlighted the presence of CDOM absorption, particularly in the CV18012 stations, and chlorophyll-*a* absorption in the CE19009 survey areas. *In situ* data is crucial for the validation of satellite measurements and the development of algorithms. Equally, the incorporation of a 20 year K_d (490)

climatology and chlorophyll-a trends off the Irish coast underscores the significant potential of satellite technology in clear sky conditions. The integration of this algorithm into the Irish monitoring programme offers numerous advantages, especially during the summer months in Ireland.

The insights gained in this chapter lay the groundwork for the research in Chapter 3, which focuses on the development of a remote sensing reflectance monitoring system for continuous measurements. This system will aid in algorithm development and satellite data validation, further highlighting the importance of combining satellite and *in situ* data in oceanographic research.

6.1.2 Chapter 3

Chapter 3 of this thesis introduces a DM-QMF pack explains the benefits to using a system like this and features a case study that outlines the processes of collecting and processing *in situ* remote sensing data. This preliminary investigation served as a pilot project to test the sensor performance when the ship was stationary and demonstrate its potential uses, a first of its kind for the Marine Institute. The data evaluated originated from two research surveys, CE19009 and CE19010.

The chapter outlines future research objectives, which include expanding the scope of data processing scripts to include periods when the ship is moving. This will be achieved using scripts designed to filter out effects from varying weather conditions. The analysis yielded positive correlations across both datasets. A summary of these statistical findings is provided in Table 1. Key results include:

For the 443nm band, average values were closely aligned, suggesting a strong agreement between satellite and *in situ* data. The *in situ* data exhibited slightly higher variability. A low RMSE (Ψ 0.0010) indicates a close match between satellite and *in situ* measurements. A moderate Pearson's correlation coefficient ($r= 0.59741$) points to a linear relationship between the datasets. The regression slope (0.70139) suggests satellite readings are typically lower than *in situ* measurements. The minimal bias and intercept values imply negligible systematic bias. An RPD of 17.3620 indicates reliable satellite data at this wavelength.

In the 490nm band, average values showed a larger gap compared to the 443nm band, with a higher standard deviation for *in situ* data. The RMSE (Ψ 0.0012) was slightly increased, indicating a greater divergence between datasets. The Pearson's correlation ($r= 0.56452$) was lower, indicating a weaker but still positive linear relationship. The regression slope was closer to 1, showing higher proportional agreement. The satellite data had a negative bias, suggesting it typically reported lower values than the *in situ* data. An RPD of 23.8400 demonstrated improved predictive performance compared to the 443nm band.

For the 510nm band, the discrepancy in average values was larger than in the 490nm band. The standard deviation remained higher for *in situ* data. The RMSE (Ψ 0.0013) increased slightly, in line with the larger average discrepancies. The Pearson's correlation ($r= 0.60917$) was moderate and similar to the 443nm band. The regression slope was greater than 1, indicating that satellite data overestimated the increase in the *in situ* data. A negative bias suggested systematic underestimation by the satellite. With an RPD of 27.8900, the satellite data showed strong predictive capability at this wavelength.

The 560nm band displayed the most significant difference in average values among all wavelengths. The standard deviation was consistent with other bands. A low RMSE (Ψ 0.0011) was observed for this wavelength. The Pearson's correlation ($r= 0.85398$) was the highest, indicating a strong linear relationship between the datasets. The regression slope was significantly greater than 1, suggesting an amplified response in satellite data as *in situ* data increased. Despite the small bias, satellite data consistently underestimated *in situ* data. The highest RPD value of 33.4750 at this wavelength indicated an excellent predictive ability.

The chapter concludes by summarising the metrics used for validating satellite derived data against *in situ* measurements across four different wavelengths. The results demonstrate a trend of slight underestimation by the satellite at 443 nm, with improving alignment at 490 and 510 nm, and a peak overestimation at 560 nm. The Pearson correlation coefficients, all statistically significant with p-values below 0.05, range from moderate to strong across all bands, supporting the validity of the satellite data.

The development of this system will ensure long term continued measurements of hyperspectral radiometry to build up a long term database from the Celtic Explorer survey coverage area. This chapter concludes the benefits of the DM-QMF pack for managing the long term data set and continued performance evaluations. Region specific algorithms can be developed with optical data alongside biological, chemical and physical water properties. This data will assist in the future of HAB monitoring in the Marine Institute.

Chapter 3 details the examination of four remote sensing reflectance bands (443nm, 490nm, 510nm, and 560nm) from CMEMS, seamlessly transitioning into Chapter 4. Here, the focus shifts to the Red Band Difference algorithm, which incorporates two other reflectance bands in the red part of the visible spectrum, at 681nm and 665nm, building upon the spectral insights gained previously.

6.1.3 Chapter 4

In Chapter 4, we explore a satellite derived algorithm for chlorophyll fluorescence. The analysis, which encompasses remotely sensed data from May to August 2019 marks the first application of the RBD algorithm in Irish waters. Among the significant outcomes of this analysis is the detection of a phytoplankton bloom by the RBD algorithm, a finding corroborated by inshore phytoplankton samples across Ireland that reflected a similar concentration.

Additionally, the chapter discusses the validation of the bloom's travel path and direction, supported by particle tracking simulation outcomes and satellite imagery. A notable discovery during this period was the presence of *Karenia* spp. in large concentrations (2.5 million cells per litre) specifically in Cork Harbour and other southern stations, with their absence noted in other parts of the Irish coast. This was followed by a considerable surge in *Karenia* spp. populations in locations like Cork Harbour, Oysterhaven, and Kinsale, soon after the bloom's development in offshore waters.

The appearance pattern of *Karenia* spp. at southern coastal stations was consistent with the expected east to west migration pattern of the Irish coastal current. The

analysis also determined that *K. mikimotoi* was the predominant phytoplankton in offshore samples.

Furthermore, the chapter highlights the potential of the Red Band Difference method to be integrated into Ireland's current HAB alert system as an early warning tool for HABs, with a particular focus on *Karenia* spp. blooms. The successful application of this algorithm for locating and monitoring the movement of *Karenia* spp. blooms effectively lays the foundation for the introduction of the final chapter, the HABscope.

6.1.4 Chapter 5

In the concluding chapter of the thesis, the study presents the innovative combination of the Red Band Difference (RBD) algorithm with the HABscope system. This integration utilises AI technology to specifically identify the swimming patterns of *Karenia* spp., marking a significant advancement in phytoplankton monitoring techniques. This innovative approach was tested in Irish waters during two research surveys in summer 2021 for the first time. The RBD satellite imagery, combined with HABscope recordings, successfully identified high concentrations of phytoplankton and distinguished *K. mikimotoi* from other species. For instance, during survey CV21015 in July 2021, satellite imagery showed low phytoplankton activity at the ocean surface, which was confirmed by *in situ* microscope analysis. Interestingly, *Karenia* spp. was observed at a depth of 38m, with HABscope estimates closely matching microscope counts, despite being taken from a moving vessel. The survey CV21021 showcased the effectiveness of HABscope in accurately identifying *Karenia* spp. And this initial study successfully demonstrated HABscope's capability to distinguish *Karenia* spp. from other phytoplankton in samples collected from a moving vessel at sea affirming its role as a quick and reliable tool for the Irish monitoring programme. While the study on these two surveys were preliminary, future plans include a comprehensive validation of HABscope's precision, particularly its application in shellfish aquaculture.

In summary each chapter of this thesis builds on the previous, culminating in a comprehensive approach to monitoring HABs in Irish waters using a combination of satellite and *in situ* data, and advanced algorithms.

6.2 Summary of products available from this PhD

Based on the completion of this PhD and associated research into the most cited and recent research into ocean colour topics discussed in this thesis, the following tools will be made available to the Marine Institute, NUIG and the ocean colour community for use in monitoring for marine phytoplankton and associated optically active constituents:

- A documented TriOS RAMSES hyperspectral radiometry system on board the RV Celtic Explorer.
- The Red Band Difference Algorithm for use in the current monitoring programme.
- The HABscope, that will ultimately compliment satellite imagery as a warning tool for *Karenia* spp. in Irish coastal waters.

6.3 Future Studies

I make the following recommendations for future research based on the work completed in this thesis:

- Long term- continued measurements of hyperspectral radiometry to build up a long term database from the Celtic Explorer survey coverage area.
- Further advancement and expanding the scope of data processing scripts to include periods when the ship is moving. This will be achieved using scripts designed to filter out effects from varying weather conditions.
- Intercomparison between existing chlorophyll algorithm and the red band difference algorithm to assess which products can best support *in situ* monitoring programmes / water quality / environmental assessments (Case 1 and Case 2).
- Testing other chlorophyll algorithms for Irish waters.
- Investigate Phytoplankton “functional type” discrimination - spectral signatures, changes of phytoplankton with time, growth season, environmental assessments, fisheries, etc.

- To include measurements from Case 1 and 2 waters HABs and other phytoplankton are strongly associated with complex waters (Case 2), therefore, determining optical properties is difficult from satellite (CDOM, sediment, land pixels) (IOCCG 2021).
- A feasibility study using the HABscope at aquaculture farms around Ireland.
- A spectral library with cultures in the Marine Institute labs was started during this PhD. Expand this work to include more phytoplankton cultures and unialgal blooms in the field.
- Region specific algorithms can be developed with optical data alongside biological, chemical and physical water properties as the dynamics of individual ecosystems will change from one area to another.
- With the launch of NASA's PACE satellite in 2024 the scope of this work will increase.

7. References

- Alikas, K., Vabson, V., Ansko, I., Tilstone, G. H., Dall’Olmo, G., Nencioli, F., Vendt, R., Donlon, C., & Casal, T. (2020). Comparison of above-water seabird and TriOS radiometers along an atlantic meridional transect. *Remote Sensing*, 12(10). <https://doi.org/10.3390/rs12101669>
- Amin, R., Zhou, J., Gilerson, A., Gross, B., Moshary, F., and Ahmed, S. (2009). Novel optical techniques for detecting and classifying toxic dinoflagellate *Karenia brevis* blooms using satellite imagery. *Opt. Express* 17, 9126–9144. doi: 10.1364/oe.17.009126
- Anderson, C. R., Moore, S. K., Tomlinson, M. C., Silke, J., and Cusack, C. K. (2015). “Living with harmful algal blooms in a changing world: strategies for modeling and mitigating their effects in coastal marine ecosystems,” in *Coastal and Marine Hazards, Risks, and Disasters*, eds J. T. Ellis and D. J. Sherman (Amsterdam: Elsevier), 495–561. doi: 10.1016/b978-0-12-396483-0.00017-0
- Anderson, S. R., & Harvey, E. L. (2019). Seasonal variability and drivers of microzooplankton grazing and phytoplankton growth in a subtropical estuary. *Frontiers in Marine Science*, 6 (MAR), 1–13. <https://doi.org/10.3389/fmars.2019.00174>
- Anderson, S.I., Barton, A.D., Clayton, S. *et al.* Marine phytoplankton functional types exhibit diverse responses to thermal change. *Nat Commun* 12, 6413 (2021). <https://doi.org/10.1038/s41467-021-26651-8>
- Aurin, D., Mannino, A., & Lary, D. J. (2018). Remote sensing of CDOM, CDOM spectral slope, and dissolved organic carbon in the global ocean. *Applied Sciences* (Switzerland), 8(12). <https://doi.org/10.3390/app8122687>
- Babin, M. Phytoplankton Fluorescence: Theory, Current Literature and in-situ Measurement. In *Real-Time Coastal Observing System for Marine Ecosystem Dynamics and Harmful Algal Blooms*; Marcel, B., Collin, S.R., John, J.C., Eds.; United Nations Educational, Scientific and Cultural Organization: Paris, France, 2008; pp. 237–280.
- Backer LC, Fleming LE, Rowan A, Cheng Y-S, Benson J, Pierce RH, *et al.* Recreational exposure to aerosolized brevetoxins during Florida red tide events. *Harmful Algae*. 2003;2(1):19–28.
- Bailey, S. W., & Werdell, P. J. (2006). A multi-sensor approach for the on-orbit validation of ocean colour satellite data products. *Remote Sensing of Environment*, 102(1–2), 12–23. <https://doi.org/10.1016/j.rse.2006.01.015>
- Banks, A. C., Vendt, R., Alikas, K., Bialek, A., Kuusk, J., Lerebourg, C., Ruddick, K., Tilstone, G., Vabson, V., Donlon, C., & Casal, T. (2020). Fiducial reference measurements for satellite ocean colour (FRM4SOC). *Remote Sensing*, 12(8). <https://doi.org/10.3390/RS12081322>
- Barua, R., Sanborn, D., Nyman, L., McFarland, M., Moore, T., Hong, J., Garrett, M., & Nayak, A. R. (2023). In situ digital holographic microscopy for rapid detection and monitoring of the harmful dinoflagellate, *Karenia brevis*. *Harmful Algae*, 123. <https://doi.org/10.1016/j.hal.2023.102401>

- Behrenfeld, M. J., and P. G. Falkowski. 1997. A consumer's guide to phytoplankton primary productivity models. *Limnol. Oceanogr.* 42: 1479–1491
- Behrenfeld, M. J., & Boss, E. S. (2018). Student's tutorial on bloom hypotheses in the context of phytoplankton annual cycles. *Global Change Biology*, 24(1), 55–77. <https://doi.org/10.1111/gcb.13858>
- Blondeau, P.D.; Gower, J.F.R.; Dekker, A.G.; Phinn, S.R.; Brando, V.E. A review of ocean colour remote sensing methods and statistical techniques for the detection, mapping and analysis of phytoplankton blooms in coastal and open oceans. *Prog. Oceanogr.* 2014, 123, 123–144.
- Brand, L. E., Campbell, L., and Bresnan, E. (2012). *Karenia*: the biology and ecology of a toxic genus. *Harmful Algae* 14, 156–178. doi: 10.1016/j.hal.2011.10.020
- Brando, V. E., Lovell, J. L., King, E. A., Boadle, D., Scott, R., & Schroeder, T. (2016). The potential of autonomous ship-borne hyperspectral radiometers for the validation of ocean colour radiometry data. *Remote Sensing*, 8(2). <https://doi.org/10.3390/rs8020150>
- Bresnan, E., Davidson, K., Edwards, M., Fernand, L., Gowen, R., Hall, A., *et al.* (2013). Impacts of climate change on harmful algal blooms. *MCCIP Sci. Rev.* 2013, 236–243. doi: 10.14465/2013.arc24.236-243
- Bresnan, E., Arévalo, F., Belin, C., Branco, M. A., Cembella, A. D., Clarke, D., *et al.* (2021). Diversity and regional distribution of harmful algal events along the Atlantic margin of Europe. *Harmful Algae* 102:101976. doi: 10.1016/j.hal.2021.101976
- Brewin, R. J. W., Dall'olmo, G., Pardo, S., Van Dongen-Vogels, V., and Boss, E. S. (2016). Underway spectrophotometry along the Atlantic meridional transect reveals high performance in satellite chlorophyll retrievals. *Remote Sens. Environ.* 183, 82–97.
- Brewin, R. J. W., Sathyendranath, S., Müller, D., Brockmann, C., Deschamps, P. Y., Devred, E., Doerffer, R., Fomferra, N., Franz, B., Grant, M., Groom, S., Horseman, A., Hu, C., Krasemann, H., Lee, Z. P., Maritorea, S., Mélin, F., Peters, M., Platt, T., ... White, G. N. (2015). The Ocean Colour Climate Change Initiative: III. A round-robin comparison on in-water bio-optical algorithms. *Remote Sensing of Environment*, 162, 271–294. <https://doi.org/10.1016/j.rse.2013.09.016>
- Bricaud, A., Morel, A., Prieur, L., 1981. Absorption by dissolved organic matter of the sea (yellow substance) in the UV and visible domain. *Limnology Oceanography* 26, 43–53.
- Broullón, E., López-Mozos, M., Reguera, B., Chouciño, P., Doval, M. D., Fernández-Castro, B., *et al.* (2020). Thin layers of phytoplankton and harmful algae events in a coastal upwelling system. *Prog. Oceanogr.* 189:102449. doi: 10.1016/j.pocean.2020.102449
- Busch, J. A., Hedley, J. D., & Zielinski, O. (2013). Correction of hyperspectral reflectance measurements for surface objects and direct sun reflection on surface waters. *International Journal of Remote Sensing*, 34(19), 6651–6667. <https://doi.org/10.1080/01431161.2013.804226>
- Callaway, R., Shinn, A. P., Grenfell, S. E., Bron, J. E., Burnell, G., and Cook, E. J. (2012). Review of climate change impacts on marine aquaculture in the UK and Ireland. *Aquatic Conserv. Mar. Freshw. Ecosyst.* 22, 389–421.

- Calton, B. (2021). ESA Ocean Colour Climate Change Initiative – Phase 3 Product Validation and Inter-comparison Report. 1–17.
- Carvalho, M. C., Schulz, K. G., and Eyre, B. D.: Respiration of new and old carbon in the surface ocean: Implications for estimates of global oceanic gross primary productivity, *Glob. Biogeochem. Cycles*, 31, 975–984, <https://doi.org/10.1002/2016GB005583>, 2017.
- Chang, F. H., & Ryan, K. G. (2004). *Karenia concordia* sp. nov. (Gymnodiniales, Dinophyceae), a new nonthecate dinoflagellate isolated from the New Zealand northeast coast during the 2002 harmful algal bloom events. *Phycologia*, 43(5), 552–562. <https://doi.org/10.2216/i0031-8884-43-5-552.1>
- Chang, F. H., and Gall, M. (2013). Pigment compositions and toxic effects of three harmful *Karenia* species, *Karenia concordia*, *Karenia brevisulcata* and *Karenia mikimotoi* (Gymnodiniales, Dinophyceae), on rotifers and brine shrimps. *Harmful Algae* 27, 113–120. doi: 10.1016/j.hal.2013.05.005
- Clarke, D. (2020). “New insights and perspectives from 20 years of monitoring algal events in Irish coastal waters,” in Proceedings of the 11th Irish Shellfish Safety Workshop, Marine Environment and Health Series No. 41, eds D. Clarke and M. Gilmartin (Galway: Marine Institute).
- Concha, J. A., Bracaglia, M., & Brando, V. E. (2021). Assessing the influence of different validation protocols on Ocean Colour match-up analyses. *Remote Sensing of Environment*, 259, 112415. <https://doi.org/10.1016/j.rse.2021.112415>
- Curtarelli, V. P., Barbosa, C. C. F., Maciel, D. A., Flores Júnior, R., Carlos, F. M., Novo, E. M. L. de M., Curtarelli, M. P., & da Silva, E. F. F. (2020). Diffuse attenuation of clear water tropical reservoir: A remote sensing semi-analytical approach. *Remote Sensing*, 12(17), 1–23. <https://doi.org/10.3390/rs12172828>
- Cusack, C., Dabrowski, T., Lyons, K., Berry, A., Westbrook, G., Salas, R., *et al.* (2016). Harmful algal bloom forecast system for SW Ireland. Part II: are operational oceanographic models useful in a HAB warning system. *Harmful Algae* 53, 86–101. doi: 10.1016/j.hal.2015.11.013
- Dabrowski, T., Lyons, K., Cusack, C., Casal, G., Berry, A., and Nolan, G. D. (2016). Ocean modelling for aquaculture and fisheries in Irish waters. *Ocean Sci.* 12, 101–116. doi: 10.5194/os-12-101-2016
- Dall’Olmo, G., Brewin, R. J. W., Nencioli, F., Organelli, E., Lefering, I., Mckee, D., *et al.* (2017). Determination of the absorption coefficient of chromophoric dissolved organic matter from underway spectrophotometry. *Opt. Express* 25, A1079–A1095. doi: 10.1364/OE.25.0A1079
- Darecki, M., Weeks, A., Sagan, S., Kowalczyk, P., & Kaczmarek, S. (2003). Optical characteristics of two contrasting Case 2 waters and their influence on remote sensing algorithms. *Continental Shelf Research*, 23(3–4), 237–250. [https://doi.org/10.1016/S0278-4343\(02\)00222-4](https://doi.org/10.1016/S0278-4343(02)00222-4)
- Davidson, J., Mateus, M., Reguera, B., Silke, J., and Sourisseau, M. (2016). Applied simulations and integrated modelling for the understanding of toxic and harmful algal blooms (ASIMUTH). *Harmful Algae* 53, 1–166. doi: 10.1007/978-0-387-75865-7_1

- Davidson, K., Miller, P., Wilding, T. A., Shutler, J., Bresnan, E., Kennington, K., *et al.* (2009). A large and prolonged bloom of *Karenia mikimotoi* in Scottish waters in 2006. *Harmful Algae* 8, 349–361. doi: 10.1016/j.hal.2008.07.007
- Dennis, J., and Jackson, E. (2019). *BIM National Seafood Survey Aquaculture Report*.
- Diaz, R. J., and Rosenberg, R. (2008). Spreading dead zones and consequences for marine ecosystems. *Science* 321, 926–929. doi: 10.1126/science.1156401
- Dickey, T. D., Kattawar, G. W., & Voss, K. J. (2011). Shedding new light on light in the ocean. *Physics Today*, 64(4), 44–49. <https://doi.org/10.1063/1.3580492>
- Doerffer, R. (1993). Estimation of primary production by observation of solar-stimulated fluorescence ICES mar. *Sci. Symp.* 197, 104–113.
- Dutkiewicz, S., Hickman, A. E., Jahn, O., Gregg, W. W., Mouw, C. B., & Follows, M. J. (2015). Capturing optically important constituents and properties in a marine biogeochemical and ecosystem model. *Biogeosciences*, 12(14), 4447–4481. <https://doi.org/10.5194/bg-12-4447-2015>
- El-habashi, A., Ioannou, I., Tomlinson, M. C., Stumpf, R. P., & Ahmed, S. (2016). Satellite retrievals of *Karenia brevis* harmful algal blooms in the West Florida Shelf using neural networks and comparisons with other techniques. *Remote Sensing*, 8(5). <https://doi.org/10.3390/rs8050377>
- EUMETSAT. (2019). Recommendations for Sentinel-3 OLCI Ocean Colour product validations in comparison with *in situ* measurements – Matchup Protocols. 1–10.
- FAO (2020). *The State of World Fisheries and Aquaculture 2020. Sustainability in Action*. Rome: FAO.
- Farabegoli F, Blanco L, Rodríguez LP, Vieites JM, Cabado AG. Phycotoxins in Marine Shellfish: Origin, Occurrence and Effects on Humans. *Mar Drugs*. 2018 May 29;16(6):188. doi: 10.3390/md16060188.
- Farrell, H., Gentien, P., Fernand, L., Lunven, M., Reguera, B., González-Gil, S., *et al.* (2012). Scales characterising a high density thin layer of *Dinophysis acuta* Ehrenberg and its transport within a coastal jet. *Harmful Algae* 15, 36–46. doi: 10.1016/j.hal.2011.11.003
- Fenchel, T. (2001). How dinoflagellates swim. *Protist*, 152(4), 329–338. <https://doi.org/10.1078/1434-4610-00071>
- Fernandes-Salvador, J. A., Davidson, K., Sourisseau, M., Revilla, M., Schmidt, W., Clarke, D., ... Silke, J. (2021). Current Status of Forecasting Toxic Harmful Algae for the North-East Atlantic Shellfish Aquaculture Industry. *Frontiers in Marine Science*, 8(June). <https://doi.org/10.3389/fmars.2021.666583>
- Garaba, S. P., & Zielinski, O. (2013). Methods in reducing surface reflected glint for shipborne above-water remote sensing. *Journal of the European Optical Society*, 8. <https://doi.org/10.2971/jeos.2013.13058>
- Garaba, S. P., Badewien, T. H., Braun, A., Schulz, A. C., & Zielinski, O. (2014a). Using ocean colour remote sensing products to estimate turbidity at the Wadden sea time series station Spiekeroog. *Journal of the European Optical Society*, 9. <https://doi.org/10.2971/jeos.2014.14020>

- Garaba, S. P., Schulz, J., Wernand, M. R., & Zielinski, O. (2012). Sun glint detection for unmanned and automated platforms. *Sensors (Switzerland)*, *12*(9), 12545–12561. <https://doi.org/10.3390/s120912545>
- Garaba, S. P., Voß, D., & Zielinski, O. (2014b). Physical, bio-optical state and correlations in North-Western European shelf seas. *Remote Sensing*, *6*(6), 5042–5066. <https://doi.org/10.3390/rs6065042>
- Garaba, S. P., Voß, D., Wollschläger, J., & Zielinski, O. (2015). Modern approaches to shipborne ocean colour remote sensing. *Applied Optics*, *54*(12), 3602. <https://doi.org/10.1364/ao.54.003602>
- Garnesson, P., Mangin, A., D’Andon, O. F., Demaria, J., & Bretagnon, M. (2019). The CMEMS GlobColour chlorophyll a product based on satellite observation: Multi-sensor merging and flagging strategies. *Ocean Science*, *15*(3), 819–830. <https://doi.org/10.5194/os-15-819-2019>
- Gentien, P. (1998). “Bloom dynamics and ecophysiology of the *Gymnodinium mikimotoi* species complex,” in *Physiological Ecology of Harmful Algal Blooms*, eds D. Anderson, A. D. Cembella, and G. M. Hallegraeff (Berlin: Springer).
- Gentien, P., Lunven, M., Lazure, P., Youenou, A., and Crassous, M. P. (2007). Motility and autotoxicity in *Karenia mikimotoi* (Dinophyceae). *Philos. Trans. R. Soc. B Biol. Sci.* *362*, 1937–1946. doi: 10.1098/rstb.2007.2079
- Gholizadeh, M., Melesse, A. and Reddi, L. (2016). A Comprehensive Review on Water Quality Parameters Estimation Using Remote Sensing Techniques. *Sensors*, *16*(8), p.1298.
- Gilerson, A., Herrera-estrella, E., Foster, R., & Agagliate, J. (2022). Determining the Primary Sources of Uncertainty in Retrieval of Marine Remote Sensing Reflectance From Satellite Ocean Colour Sensors. *3*(April), 1–19. <https://doi.org/10.3389/frsen.2022.857530>
- Gobler, C. J., Doherty, O. M., Hattenrath-Lehmann, T. K., Griffith, A. W., Kang, Y., & Litaker, R. W. (2017). Ocean warming since 1982 has expanded the niche of toxic algal blooms in the North Atlantic and North Pacific oceans. In *Proceedings of the National Academy of Sciences of the United States of America* (Vol. 114, Issue 19, pp. 4975–4980). National Academy of Sciences. <https://doi.org/10.1073/pnas.1619575114>
- Gohin, F., Lampert, L., Guillaud, J., Herbland, A., & Nézan, E. (2003). Satellite and *in situ* observations of a late winter phytoplankton bloom in the northern Bay of Biscay marine provinces defined by Longhurst (1998). According to chlorophyll data from the in that province: (i) mixed conditions and light limitation i. *Continental Shelf Research*, *23*(July), 1117–1141.
- Gordon, H. R., and Morel, A. Y. (1983). “In-water Algorithms,” in *Remote Assessment of Ocean Colour for Interpretation of Satellite Visible Imagery: A Review*. (Berlin, Germany: Springer-Verlag). doi:10.1007/978-1-4684-6280-710.1007/978-1-4684-6280-7_3
- Gowen, R. J., Raine, R., Dickey-Collas, M., and White, M. (1998). Plankton distributions in relation to physical oceanographic features on the southern Malin Shelf, August 1996. *ICES J. Mar. Sci.* *55*, 1095–1111. doi: 10.1006/jmsc.1998.0418

- Gowen, R. J., Stewart, B. M., Mills, D. K. *et al.* (1995) Regional differences in stratification and its effect on phytoplankton production and biomass in the northwestern Irish Sea. *J. Plankton Res.*, 17, 753–769.
- Gower, J., and King, S. (2012). Use of satellite images of Chlorophyll fluorescence to monitor the spring bloom in coastal waters. *Int. J. Remote Sens.* 33, 7469–7481. doi: 10.1080/01431161.2012.685979
- Gower, J., King, S., Statham, S., Fox, R., and Young, E. (2013). The malaspina dragon: a newly discovered pattern of the early spring bloom in the strait of georgia, British Columbia, Canada. *Prog. Oceanogr.* 115, 181–188. doi: 10.1016/j.pocean.2013.05.024
- Granéli, E., & Legrand, C. (1999). The role of C, N and P in dissolved and particulate organic matter as a nutrient source for phytoplankton growth, including toxic species. In *Aquatic Ecology* (Vol. 33).
- Groom, S. B., Sathyendranath, S., Ban, Y., Bernard, S., Brewin, B., Brotas, V., Brockmann, C., Chauhan, P., Choi, J. K., Chuprin, A., Ciavatta, S., Cipollini, P., Donlon, C., Franz, B. A., He, X., Hirata, T., Jackson, T., Kampel, M., Krasemann, H., ... Wang, M. (2019). Satellite ocean colour: Current status and future perspective. *Frontiers in Marine Science*, 6 (JUL). <https://doi.org/10.3389/fmars.2019.00485>
- Guillaume MAZE (2022). Taylor Diagram (<https://www.mathworks.com/matlabcentral/fileexchange/20559-taylor-diagram>), MATLAB Central File Exchange. Retrieved September 12, 2022.
- Hardison DR, Holland WC, Currier RD, Kirkpatrick B, Stumpf R, Fanara T, *et al.* (2019) HABscope: A tool for use by citizen scientists to facilitate early warning of respiratory irritation caused by toxic blooms of *Karenia brevis*. *PLoS ONE* 14(6): e0218489. <https://doi.org/10.1371/journal.pone.0218489>
- Helms, J. R., Stubbins, A., Ritchie, J. D., Minor, E. C., Kieber, D. J., & Mopper, K. (2008). Absorption spectral slopes and slope ratios as indicators of molecular weight, source, and photobleaching of chromophoric dissolved organic matter. *Limnology and Oceanography*, 53(3), 955–969. <https://doi.org/10.4319/lo.2008.53.3.0955>
- Henderikx Freitas, F., & Dierssen, H. M. (2019). Evaluating the seasonal and decadal performance of red band difference algorithms for chlorophyll in an optically complex estuary with winter and summer blooms. *Remote Sensing of Environment*, 231. <https://doi.org/10.1016/j.rse.2019.111228>
- Hernandez, F., Blockley, E., Brassington, G. B., Davidson, F., Divakaran, P., Drévilion, M., Ishizaki, S., Garcia-Sotillo, M., Hogan, P. J., Lagema, P., Levier, B., Martin, M., Mehra, A., Mooers, C., Ferry, N., Ryan, A., Regnier, C., Sellar, A., Smith, G. C., ... Zhang, A. (2015). Recent progress in performance evaluations and near real-time assessment of operational ocean products. *Journal of Operational Oceanography*, 8, s221–s238. <https://doi.org/10.1080/1755876X.2015.1050282>
- Hill, A. E., Brown, J., Fernand, L., Holt, J., Horsburgh, K. J., Proctor, R., Raine, R., & Turrell, W. R. (2008). Thermohaline circulation of shallow tidal seas. *Geophysical Research Letters*, 35(11). <https://doi.org/10.1029/2008GL033459>

- Holligan, P., Williams, P., Purdie, D., and Harris, R. (1984). Photosynthesis, respiration and nitrogen supply of plankton populations in stratified, frontal and tidally mixed shelf waters. *Mar. Ecol. Prog. Ser.* 17, 201–213. doi: 10.3354/meps017201
- Hommersom, A., Kratzer, S., Laanen, M., Ansko, I., Ligi, M., Bresciani, M., Giardino, C., Beltrán-Abaunza, J. M., Moore, G., Wernand, M., & Peters, S. (2012). Intercomparison in the field between the new WISP-3 and other radiometers (TriOS Ramses, ASD FieldSpec, and TACCS). *Journal of Applied Remote Sensing*, 6(1), 063615. <https://doi.org/10.1117/1.jrs.6.063615>
- Honjo, T. (2004). “*Karenia* (formerly *Gymnodinium*) *mikimotoi*,” in *Red Tides. New Zealand: Terra Scientific Publishing Company*, ed. T. Okaichi (Dordrecht: Kluwer Academic Publishers), 345–357.
- Huang, W. G., Cracknell, A. P., & Vaughan, R. A. (1993). Satellite thermal observation of the river shannon plume. In *Estuarine, Coastal and Shelf Science* (Vol. 36, Issue 3, pp. 207–219). <https://doi.org/10.1006/ecss.1993.1014>
- International Ocean Colour Coordinating Group (IOCCG). (2000). Reports of the International Ocean-Colour Coordinating Group Remote Sensing of Ocean Colour in Coastal, and Other Optically-Complex, Waters. In *Reports and Monographs of the International OceanColour Coordinating Group* (Vol. 3).
- IOCCG (2000). “Remote sensing of ocean colour in coastal, and other optically-complex, waters,” in *Reports of the International Ocean-Colour Coordinating Group*, No. 3, ed. S. Sathyendranath (Dartmouth: IOCCG).
- IOCCG. (2006). IOCCG Report Number 05: Reports of the International Ocean-Colour Coordinating Group Remote Sensing of Inherent Optical Properties: Fundamentals, Tests of Algorithms, and Applications. In *IOCCG Report 5* (Vol. 5, Issue 5).
- IOCCG. (2008). Why ocean colour? The societal benefits of ocean-colour technology. In *Reports of the International Ocean-Colour Coordinating Group* (Issue 7). <http://www.ioccg.org/reports/report7.pdf>
- IOCCG. (2012). "Mission requirements for future ocean-colour sensors." Reports of the International Ocean Colour Coordinating Group (IOCCG), Charles R. McClain and Gerhard Meister. Dartmouth, NS, Canada.
- IOCCG (2014). *Phytoplankton Functional Types from Space*. Sathyendranath, S. (ed.), Reports of the International Ocean-Colour Coordinating Group, No. 15, IOCCG, Dartmouth, Canada
- IOCCG (2018). *Earth Observations in Support of Global Water Quality Monitoring*. Greb, S., Dekker, A. and Binding, C. (eds.), IOCCG Report Series, No. 17, International Ocean Colour Coordinating Group, Dartmouth, Canada.
- IOCCG Protocol Series. (2019). IOCCG Ocean Optics and Biogeochemistry Protocols for Satellite Ocean Colour Sensor Validation. IOCCG Protocol Series, 3. <http://dx.doi.org/10.25607/OBP-691>
- Jeffrey, S. W., & Humphrey, G. F. (1975). New spectrophotometric equations for determining chlorophylls a, b, c1 and c2 in higher plants, algae and natural phytoplankton. *Biochimie Und Physiologie Der Pflanzen*, 167(2), 191–194. [https://doi.org/10.1016/s0015-3796\(17\)30778-3](https://doi.org/10.1016/s0015-3796(17)30778-3)

- Jerlov, N. G. (1976). Elsevier Oceanography Series, 14. Marine Optics, 231 pp.
- Joint, I., & Groom, S. B. (2000). Estimation of phytoplankton production from space: current status and future potential of satellite remote sensing. In *Journal of Experimental Marine Biology and Ecology* (Vol. 250). www.elsevier.nl/locate/jembe
- Jones, K. J., Ayres, P., Bullock, A. M., Roberts, R. J., and Tett, P. (1982). A red tide of *Gyrodinium aureolum* in sea lochs of the firth of Clyde and associated mortality of pond-reared salmon. *J. Mar. Biol. Assoc. U.K.* 62, 771–782. doi: 10.1017/s0025315400044040
- Jordan, C., Cusack, C., Tomlinson, M. C., Meredith, A., McGeady, R., Salas, R., Gregory, C., & Croot, P. L. (2021). Using the Red Band Difference Algorithm to Detect and Monitor a *Karenia* spp. Bloom Off the South Coast of Ireland, June 2019. *Frontiers in Marine Science*, 8. <https://doi.org/10.3389/fmars.2021.638889>
- Jungblut, S., Liebich, V., Bode, M., & Researchers, Y. M. (2017). YOUMARES 8 – Oceans Across Boundaries: Learning from each other.
- Justice, C., Belward, A., Morisette, J., Lewis, P., Privette, J., Baret, F., 2000. Developments in the ‘validation’ of satellite sensor products for the study of the land surface. *Int. J. Remote Sens.* 21, 3383–3390.
- Karabashev, G. S. 1992 On the influence of dissolved organic matter on remote sensing of chlorophyll in the straits of Skagerrak and the Kattegat. *Oceanologia Acta* 15, 255–259.
- Käse, L., & Geuer, J. K. (2018). Phytoplankton responses to marine climate change—an introduction. In *YOUMARES 8—Oceans Across Boundaries: Learning from each other: Proceedings of the 2017 conference for YOUnG MARine RESEARCHERS in Kiel, Germany* (pp. 55-71). Springer International Publishing.
- Kirk, J. T. O. (2003). The vertical attenuation of irradiance as a function of the optical properties of the water. *Limnology and Oceanography*, 48(1 D), 9–17. <https://doi.org/10.4319/lo.2003.48.1.0009>
- Kirk, J. T. O. (2011). *Light & Photosynthesis in Aquatic Ecosystems*, 3rd Edn. New York, NY: Cambridge University Press.
- Kirk, J.T.O., (1994). *Light and Photosynthesis in Aquatic Ecosystems*, second ed. Cambridge University Press, UK
- Koizumi, Y., Uchida, T., and Honjo, T. (1996). Diurnal vertical migration of *Gymnodinium mikimotoi* during a red tide in Hoketsu Bay, Japan. *J. Plank. Res.* 18, 289–294. doi: 10.1093/plankt/18.2.289
- Kononen, K., Huttunen, M., Hällfors, S., Gentien, P., Lunven, M., Huttula, T., *et al.* (2003). Development of a deep chlorophyll maximum of *Heterocapsa triquetra* Ehrenb. at the entrance to the Gulf of Finland. *Limnol. Oceanogr.* 48, 594–607. doi: 10.4319/lo.2003.48.2.0594
- Kostakis, I., Twardowski, M., Roesler, C., Röttgers, R., Stramski, D., McKee, D., Tonizzo, A., & Drapeau, S. (2021). Hyperspectral optical absorption closure experiment in complex coastal waters. *Limnology and Oceanography: Methods*, 19(9), 589–625. <https://doi.org/10.1002/lom3.10447>

- Landry, M. R., & Calbet, A. (2004). Microzooplankton production in the oceans. *ICES Journal of Marine Science*, 61(4), 501–507. <https://doi.org/10.1016/j.icesjms.2004.03.011>
- Le, C., Hu, C., Cannizzaro, J., English, D., Muller-Karger, F., & Lee, Z. (2013). Evaluation of chlorophyll-a remote sensing algorithms for an optically complex estuary. *Remote Sensing of Environment*, 129, 75–89. <https://doi.org/10.1016/j.rse.2012.11.001>
- Le Traon, P. Y., Reppucci, A., Fanjul, E. A., Aouf, L., Behrens, A., Belmonte, M., Bentamy, A., Bertino, L., Brando, V. E., Kreiner, M. B., Benkiran, M., Carval, T., Ciliberti, S. A., Claustre, H., Clementi, E., Coppini, G., Cossarini, G., De Alfonso Alonso-Muñoyerro, M., Delamarche, A., ... Zacharioudaki, A. (2019). From observation to information and users: The Copernicus Marine Service Perspective. *Frontiers in Marine Science*, 6(May). <https://doi.org/10.3389/fmars.2019.00234>
- Leadbetter, A., Carr, R., Flynn, S., Meaney, W., Moran, S., Bogan, Y., Brophy, L., Lyons, K., Stokes, D., & Thomas, R. (2019). Implementation of a Data Management Quality Management Framework at the Marine Institute, Ireland. *Earth Science Informatics*, 13(2), 509–521. <https://doi.org/10.1007/s12145-019-00432-w>
- Leadbetter, A., Meaney, W., Tray, E., Conway, A., Flynn, S., Keena, T., Kelly, C., & Thomas, R. (2020). A modular approach to cataloguing marine science data. *Earth Science Informatics*, 13(2), 537–553. <https://doi.org/10.1007/s12145-020-00445-w>
- Leadbetter, A., Silke, J., and Cusack, C. (2018). *Creating a Weekly Harmful Algal Bloom Bulletin. Version 1*. Ireland: Marine Institute.
- Lee, Z. P., Du, K. P., & Arnone, R. (2005). A model for the diffuse attenuation coefficient of downwelling irradiance. *Journal of Geophysical Research: Oceans*, 110(2), 1–10. <https://doi.org/10.1029/2004JC002275>
- Lee, Z. P., M. Darecki, K. L. Carder, C. O. Davis, D. Stramski, and W. J. Rhea (2005). Diffuse attenuation coefficient of downwelling irradiance: An evaluation of remote sensing methods. *J. Geophys. Res. Oceans* 110:2, 1–9. doi: 10.1029/2004JC002573.
- Lee, Z., Lubac, B., Werdell, J., Arnone, R. (2009), An update of the quasi-analytical algorithm (QAA_v5).
- Lee, Z. et al. (2010) ‘Removal of surface-reflected light for the measurement of remote-sensing reflectance from an above-surface platform’, *Optics Express*, 18(25), p. 26313. doi:10.1364/oe.18.026313.
- Lett, C., Verley, P., Mullon, C., Parada, C., Brochier, T., Penven, P., et al. (2008). A lagrangian tool for modelling ichthyoplankton dynamics. *Environ. Modell. Softw.* 23, 1210–1214. doi: 10.1016/j.envsoft.2008.02.005
- Li, X., Yan, T., Yu, R., and Zhou, M. (2019). A review of *Karenia mikimotoi*: bloom events, physiology, toxicity and toxic mechanism. *Harmful Algae* 90:101702. doi: 10.1016/j.hal.2019.101702
- Li, N., Zhang, Y., Shi, K., Zhang, Y., Sun, X., Wang, W., & Huang, X. (2022). Monitoring water transparency, total suspended matter and the beam attenuation coefficient in inland water using innovative ground-based proximal sensing technology. *Journal of Environmental Management*, 306. <https://doi.org/10.1016/j.jenvman.2022.114477>

- Lorenzen, C.J. A method for the continuous measurement of in vivo chlorophyll concentration. *Deep Sea Res.* 1966, 13, 223–227.
- Lotliker, Aneesh and Minu, P and Salim, Shaleen and Shafeeque, Muhammed and George, Grinson (2017) Fundamentals of ocean colour remote sensing. In: Winter School on Structure and Function of the Marine Ecosystem: Fisheries, 1-21 December 2017, Kochi.
- Maritorena, S., & Siegel, D. A. (2005). Consistent merging of satellite ocean colour data sets using a bio-optical model. *Remote Sensing of Environment*, 94(4), 429–440. <https://doi.org/10.1016/j.rse.2004.08.014>
- Martinez-Vicente, V., Kurekin, A., Sá, C., Brotas, V., Amorim, A., Veloso, V., *et al.* (2020). Sensitivity of a satellite algorithm for harmful algal bloom discrimination to the use of laboratory bio-optical data for training. *Front. Mar. Sci.* 7:582960.
- McClain, C. R., Franz, B. A., & Werdell, P. J. (2022). Genesis and Evolution of NASA's Satellite Ocean Colour Program. 3(July), 1–19. <https://doi.org/10.3389/frsen.2022.938006>
- McFarland, W. N. (1986). Light in the sea - correlations with behaviors of fishes and invertebrates. *Integr. Comp. Biol.* 26, 389–401. doi: 10.1093/icb/26.2.389
- McGeady, R., Lordan, C., & Power, A. M. (2019). Twilight migrators: Factors determining larval vertical distribution in *Nephrops norvegicus* with implications for larval retention. *Marine Ecology Progress Series*, 631, 141–155. <https://doi.org/10.3354/meps13142>
- McKee, D., Cunningham, A., & Dudek, A. (2007). Optical water type discrimination and tuning remote sensing band-ratio algorithms: Application to retrieval of chlorophyll and *Kd* (490) in the Irish and Celtic Seas. *Estuarine, Coastal and Shelf Science*, 73(3–4), 827–834. <https://doi.org/10.1016/j.ecss.2007.03.028>
- Meler, J., Ostrowska, M., Ficek, D., & Zdun, A. (2017). Light absorption by phytoplankton in the southern Baltic and Pomeranian lakes: mathematical expressions for remote sensing applications. *Oceanologia*, 59(3), 195–212. <https://doi.org/10.1016/j.oceano.2017.03.010>
- Mélin, F., Sclep, G., Jackson, T., & Sathyendranath, S. (2016). Uncertainty estimates of remote sensing reflectance derived from comparison of ocean colour satellite data sets. *Remote Sensing of Environment*, 177, 107–124. <https://doi.org/10.1016/j.rse.2016.02.014>
- Miller, P., Shutler, J., Moore, G., and Groom, S. (2006). SeaWiFS discrimination of harmful algal bloom evolution. *Int. J. Remote Sens.* 27, 2287–2301. doi: 10.1080/01431160500396816
- Mobley, C. D. (1994), *Light and Water: Radiative Transfer in Natural Waters*, 592 pp., Academic, San Diego, Calif.
- Mobley, C. D. (2001). Radiative Transfer in the Ocean. *Encyclopedia of Ocean Sciences*, 2321–2330. <https://doi.org/10.1006/rwos.2001.0469>
- Mobley, C. D. (2018). Invariant Imbedding Theory for the Vector Radiative Transfer Equation. March, 1–100. https://doi.org/10.1007/978-3-319-70796-9_1

- Mobley, C. D., Stramski, D., Bissett, W. P., and Boss, E. (2004). Optical modeling of ocean waters: is the Case 1 - Case 2 classification still useful? *Oceanography* 17, 60–67. doi: 10.5670/oceanog.2004.48
- Mobley, C. D., Werdell, J., Franz, B., Ahmad, Z., & Bailey, S. (2016). NASA / TM – 2016-217551 Atmospheric Correction for Satellite Ocean Colour Radiometry June 2016. June.
- Mobley, C., 1999. Estimation of the remote-sensing reflectance from above-surface measurements. *Applied Optics*, 38(36), p.7442.
- Mobley, C., Boss, E., Roesler, C., “Ocean optics web book: Absorption by Oceanic Constituents’ March 13th 2021
<https://www.oceanopticsbook.info/view/absorption/absorption-by-oceanic-constituents> retrieved July 1st 2022
- Moisan, T. A., Rufty, K. M., Moisan, J. R., and Linkswiler, M. A. (2017). Satellite observations of phytoplankton functional type spatial distributions, phenology, diversity, and ecotones. *Front. Mar. Sci.* 4, 1–24.
- Morel, A. (1988). Optical modeling of the upper ocean in relation to its biogenous matter content (case I waters). *J. Geophys. Res.* 93:10749. doi: 10.1029/jc093ic09p10749
- Morel, A., and Prieur, L. (1977). Analysis of variations in ocean colour1. *Limnol. Oceanogr.* 22, 709–722. doi: 10.4319/lo.1977.22.4.0709
- Mueller, J. (1981). Prospects for Measuring Phytoplankton Bloom Extent and Patchiness Using Remotely Sensed Colour Images. New York: Toxic Dinoflagellate Blooms, Elsevier, North Holland, Inc., 303–330.
- Mueller, J.L. (2000). SeaWifs Algorithm for the Diffuse Attenuation Coefficient, K(490), Using Water-Leaving Radiances at 490 And 555nm. SeaWiFS Postlaunch Calibration and Validation Analyses, 3, 51pp.
- Muller, D., Krasemann, H., Brewin, R. J. W., Brockmann, C., Deschamps, P. Y., Doerffer, R., Fomferra, N., Franz, B. A., Grant, M. G., Groom, S. B., Mélin, F., Platt, T., Regner, P., Sathyendranath, S., Steinmetz, F., & Swinton, J. (2015). The Ocean Colour Climate Change Initiative: II. Spatial and temporal homogeneity of satellite data retrieval due to systematic effects in atmospheric correction processors. *Remote Sensing of Environment*, 162, 257–270. <https://doi.org/10.1016/j.rse.2015.01.033>
- Mydlarz, L. D., Jones, L. E., and Harvell, C. D. (2006). Innate immunity, environmental drivers and disease ecology of marine and freshwater Invertebrates. *Annu. Rev. Ecol. Evol. Syst.* 37, 251–288. doi: 10.1146/annurev.ecolsys.37.091305.110103
- Myint, S.; Walker, N. Quantification of surface suspended sediments along a river dominated coast with NOAA AVHRR and SeaWiFS measurements: Louisiana, USA. *Int. J. Remote Sens.* 2002, 23, 3229–3249.
- Naselli-Flores, L., & Padišák, J. (2022). Ecosystem services provided by marine and freshwater phytoplankton. *Hydrobiologia*, 0123456789.
<https://doi.org/10.1007/s10750-022-04795-y>
- Neely, T., and Campbell, L. (2006). A modified assay to determine hemolytic toxin variability among *Karenia* clones isolated from the Gulf of Mexico. *Harmful Algae* 5, 592–598. doi: 10.1016/j.hal.2005.11.006

- O'Boyle, S., & Silke, J. (2010). A review of phytoplankton ecology in estuarine and coastal waters around Ireland. *Journal of Plankton Research*, 32(1), 99–118. <https://doi.org/10.1093/plankt/fbp097>
- O'Boyle, S., McDermott, G., Silke, J., and Cusack, C. (2016). Potential impact of an exceptional bloom of *Karenia mikimotoi* on dissolved oxygen levels in waters off western Ireland. *Harmful Algae* 53, 77–85. doi: 10.1016/j.hal.2015.11.014
- O'Reilly, J. E., & Werdell, P. J. (2019). Chlorophyll algorithms for ocean colour sensors - OC4, OC5 & OC6. *Remote Sensing of Environment*, 229(April), 32–47. <https://doi.org/10.1016/j.rse.2019.04.021>
- O'Reilly, J.E., Maritorena, S., Mitchell, B.G., Siegel, D.A., Carder, K.L., Garver, S.A., Kahru, M., McClain, C., 1998. Ocean colour chlorophyll algorithms for SeaWiFS. *Journal Geophysical Research* 103, 24937–24953.
- OC-CCI 2014b, Product Validation and Algorithm Selection Report (PVASR) Part 1 - Atmospheric Correction, D2.5, 2014-01-31, 2.0, ESA / ESRIN, AO-1/6207/09/I-LG, <http://www.esa-oceancolour-cci.org>
- OC-CCI 2014c, Product Validation and Algorithm Selection Report (PVASR) Part 2 – In-Water Algorithms, D2.5, 21/01/14, 2.0, ESA / ESRIN, AO-1/6207/09/I-LG, <http://www.esa-oceancolour-cci.org>
- Olsson, P., and Graneli, E. (1991). Observations on diurnal vertical migration and phased cell division for three coexisting marine dinoflagellates. *J. Plankton Res.* 13, 1313–1324. doi: 10.1093/plankt/13.6.1313
- Ottway, B., Parker, M., McGrath, D., and Crowley, M. (1979). Observations on a bloom of *Gyrodinium aureolum* Hulbert on the south coast of Ireland 1976, associated with mortalities of littoral and sub-littoral organisms. *Ir. Fish. Invest Ser. B* 18, 3–9.
- Park, J. G., Jeong, M. K., Lee, J. A., Cho, K.-J., and Kwon, O.-S. (2001). Diurnal vertical migration of a harmful dinoflagellate, *Cochlodinium polykrikoides* (Dinophyceae), during a red tide in coastal waters of Namhae Island, Korea. *Phycologia* 40, 292–297. doi: 10.2216/i0031-8884-40-3-292.1
- Pegau, W. S., Gray, D., & Zaneveld, J. R. V. (1997). Absorption and attenuation of visible and near-infrared light in water: dependence on temperature and salinity. *Applied Optics*, 36(24), 6035. <https://doi.org/10.1364/ao.36.006035>
- Pemberton, K., Rees, A. P., Miller, P. I., Raine, R., and Joint, I. (2004). The influence of water body characteristics on phytoplankton diversity and production in the Celtic Sea. *Cont. Shelf Res.* 24, 2011–2028. doi: 10.1016/j.csr.2004.07.003
- Pingree, R. D., Holligan, P. M., and Head, R. N. (1977). Survival of dinoflagellate blooms in the western English channel. *Nature* 265, 266–269. doi: 10.1038/265266a0
- Pingree, R. D., Holligan, P. M., Mardell, G. T., and Head, R. N. (1976). The influence of physical stability on spring, summer and autumn phytoplankton blooms in the Celtic sea. *J. Mar. Biol. Assoc. U. K.* 56, 845–873. doi: 10.1017/s0025315400020919
- Pitarch, J., Talone, M., Zibordi, G., & Groetsch, P. (2020). Determination of the remote-sensing reflectance from above-water measurements with the “3C model”: a further assessment. *Optics Express*, 28(11), 15885. <https://doi.org/10.1364/oe.388683>

- Poli M, Mende TJ, Baden DG. Brevetoxins, unique activators of voltage-sensitive sodium channels, bind to specific sites in rat brain synaptosomes. *Mol Pharmacol.* 1986;30(2):129–35. pmid:2426567
- Preisendorfer, R. W. (1976). *Hydrologic Optics*. Volume 5. Properties. 305. <http://udspace.udel.edu/handle/19716/1581>
- Prieur, L.; Sathyendranath, S. An optical classification of coastal and oceanic waters based on the specific spectral absorption curves of phytoplankton pigments, dissolved organic matter, and other particulate materials. *Limnol. Oceanogr.* 1981, 26, 671–689.
- Purdie, D. A. 1996. Marine phytoplankton blooms. *Oceanography*, 89-95.
- Raine, R. (2014). A review of the biophysical interactions relevant to the promotion of HABs in stratified systems: the case study of Ireland. *Deep Sea Res. II Top. Stud. Oceanogr.* 101, 21–31. doi: 10.1016/j.dsr2.2013.06.021
- Raine, R., Cosgrove, S., Fennell, S., Gregory, C., Bernett, M., Purdie, D., *et al.* (2016). “Origins of Dinophysis blooms which impact Irish aquaculture,” in *Proceedings of the 17th International Conference of Harmful Algae*, eds L. A. O. Proença and G. M. Hallegraeff (Florianoópolis: International Society for the Study of Harmful Algae), 46–49.
- Raine, R., O’Boyle, S., O’Higgins, T., White, M., Patching, J., Cahill, B., *et al.* (2001). A satellite and field portrait of a *Karenia mikimotoi* bloom off the south coast of Ireland, August 1998. *Hydrobiologia* 465, 187–193. doi: 10.1007/978-94-010-0434-3_19
- Righetti, D., Vogt, M., Gruber, N., Psomas, A., & Zimmermann, N. E. (2019). Global pattern of phytoplankton diversity driven by temperature and environmental variability. *Science Advances*, 5(5), 1–11. <https://doi.org/10.1126/sciadv.aau6253>
- Ruddick, K., Park, Y., Cauwer, V., Debruyne, W., and Sterckx, S. (1999). *Overview of Ocean Colour: theoretical background, sensors and applicability for the detection and monitoring of harmful algae blooms (capabilities and limitations)* Kevin. *UNESCO Monographs on Oceanographic Methodology Series, Manual on Harmful Marine Microalgae Overview*, 1–50.
- Satake, M., Shoji, M., Oshima, Y., Naoki, H., Fujita, T., and Yasumoto, T. (2002). Gymnocin-A, a cytotoxic polyether from the notorious red tide dinoflagellate, *Gymnodinium mikimotoi*. *Tetrahedron Lett.* 43, 5829–5832. doi: 10.1016/s0040-4039(02)01171-1
- Satake, M., Tanaka, Y., Ishikura, Y., Oshima, Y., Naoki, H., and Yasumoto, T. (2005). Gymnocin-B with the largest contiguous polyether rings from the red tide dinoflagellate, *Karenia* (formerly *Gymnodinium*) *mikimotoi*. *Tetrahedron Lett.* 46, 3537–3540. doi: 10.1016/j.tetlet.2005.03.115
- Sathyendranath, S. and Platt, T.: Spectral effects in bio-optical control on the ocean system, *Oceanologia*, 49, 5–39, 2007.
- Sathyendranath, S., Brewin, R. J. W., Ciavatta, S., Jackson, T., Kulk, G., Jönsson, B., Vicente, V. M., & Platt, T. (2023). Ocean Biology Studied from Space. In *Surveys in Geophysics* (Vol. 44, Issue 5, pp. 1287–1308). Springer Science and Business Media B.V. <https://doi.org/10.1007/s10712-023-09805-9>

- Schanz F, Senn P, Dubinsky Z (1997) Light absorption by phytoplankton and the vertical light attenuation: ecological and physiological significance. *Oceanography and Marine Biology: Volume 35*, 35, p.65.
- Shehhi, M.R.A.; Gherboudj, I.; Ghedira, H. Detection of algal blooms over optically complex waters of the Arabian Gulf and Sea of Oman using MODIS fluorescence data. *Int. J. Remote Sens.* 2019, 40, 3751–3771
- Shikata, T., Matsunaga, S., Nishide, H., Sakamoto, S., Onistuka, G., and Yamaguchi, M. (2015). Diurnal vertical migration rhythms and their photoresponse in four phytoflagellates causing harmful algal blooms. *Limnol. Oceanogr.* 60, 1251–1264. doi: 10.1002/lno.10095
- Shikata, T., Onitsuka, G., Abe, K., Kitatsuji, S., Yufu, K., Yoshikawa, Y., *et al.* (2016). Relationships between light environment and subsurface accumulation during the daytime in the red-tide dinoflagellate *Karenia mikimotoi*. *Mar. Biol.* 164:18.
- Shikata, T., Sakamoto, S., Onitsuka, G., Aoki, K., and Yamaguchi, M. (2014). Effects of salinity on diel vertical migration behavior in two red-tide algae, *Chattonella antiqua* and *Karenia mikimotoi*. *Plankton Benthos Res.* 9, 42–50. doi: 10.3800/pbr.9.42
- Siegel, H., Gerth, M., Neumann, T., & Doerffer, R. (1999). Case studies on phytoplankton blooms in coastal and open waters of the baltic Sea using coastal Zone colour scanner data. *International Journal of Remote Sensing*, 20(7), 1249–1264. <https://doi.org/10.1080/014311699212713>
- Silke, J., O’Beirn, F., and Cronin, M. (2005). *Karenia mikimotoi: an Exceptional Dinoflagellate Bloom in Western Irish Waters, Summer 2005*. Ireland: Marine Institute
- Smith, R. C., & Baker, K. S. (1981). Optical properties of the clearest natural waters (200–800 Nm). *Applied Optics*, 20(2), 177–184.
- Sournia, A., & Ricard, M. (1991). Marine phytoplankton: how many species in the world ocean? 13(5), 1093–1099.
- Stæhr, P. A., and Cullen, J. J. (2003). Detection of *Karenia mikimotoi* by spectral absorption signatures. *J. Plankton Res.* 25, 1237–1249. doi: 10.1093/plankt/fbg083
- Steidinger, K. A., Landsberg, J. H., Flewelling, J. L. Kirkpatrick, B. (2011). *Toxic Dinoflagellates*. Elsevier Science Publishers: New York, NY.
- Steinberg, D. K., and Landry, M. R. (2017). Zooplankton and the Ocean carbon cycle. *Ann. Rev. Mar. Sci.* 9, 413–444. doi: 10.1146/annurev-marine-010814-015924
- Stumpf, R. P. (2001). Applications of Satellite Ocean Colour Sensors for Monitoring and Predicting Harmful Algal Blooms. In *Human and Ecological Risk Assessment* (Vol. 7, Issue 5).
- Stumpf, R. P., and Tomlinson, M. C. (2005). “Remote sensing of harmful algal blooms,” in *Remote Sensing of Coastal Aquatic Environments*, eds R. L. Miller, C. E. del Castillo, and B. A. McKee (Dordrecht: Springer), 347.
- Stumpf, R. P., Culver, M. E., Tester, P. A., Tomlinson, M. C., Kirkpatrick, G. J., and Pederson, B. A. (2003). Monitoring *Karenia brevis* blooms in the Gulf of Mexico using satellite ocean colour imagery and other data. *Harmful Algae* 2, 147–160. doi: 10.1016/s1568-9883(02)00083-5

- Stumpf, R. P., Tomlinson, M. C., Calkins, J. A., Kirkpatrick, B., Fisher, K., Nierenberg, K., *et al.* (2009). Skill assessment for an operational algal bloom forecast system. *J. Mar. Syst.* 76, 151–161. doi: 10.1016/j.jmarsys.2008.05.016
- Tanhua, T., Lauvset, S. K., Lange, N., Olsen, A., Álvarez, M., Diggs, S., Bittig, H. C., Brown, P. J., Carter, B. R., da Cunha, L. C., Feely, R. A., Hoppema, M., Ishii, M., Jeansson, E., Kozyr, A., Murata, A., Pérez, F. F., Pfeil, B., Schirnick, C., ... Key, R. M. (2021). A vision for FAIR ocean data products. *Communications Earth & Environment*, 2(1), 19–22. <https://doi.org/10.1038/s43247-021-00209-4>
- Tassan, S. 1988 The effect of dissolved yellow substance on the quantitative retrieval of chlorophyll and total suspended sediment concentration from remote measurements of water colour. *International Journal of Remote Sensing* 9, 787–797.
- Taylor, K. E. (2001). *in a Single Diagram*. 106, 7183–7192.
- Tester, P. A., Stumpf, R. P., and Steidinger, K. A. (1998). “Ocean colour imagery: what is the minimum detection level for *Gymnodinium breve* blooms? in *Harmful Algae, Proceedings of the VII International Conference on Harmful Algae*, eds B. Reguera, J. Blanco, and M. Fernandez (Paris: Xunta de Galicia and Intergovernmental Oceanographic Commission of UNESCO), 149–151.
- Thomas, A. C., Townsend, D. W., & Weatherbee, R. (2003). Satellite-measured phytoplankton variability in the Gulf of Maine. *Continental Shelf Research*, 23(10), 971–989. [https://doi.org/10.1016/S0278-4343\(03\)00086-4](https://doi.org/10.1016/S0278-4343(03)00086-4)
- Tilstone, G., Mallor-Hoya, S., Gohin, F., Couto, A. B., Sá, C., Goela, P., Cristina, S., Airs, R., Icelly, J., Zühlke, M., & Groom, S. (2017). Which ocean colour algorithm for MERIS in North West European waters? *Remote Sensing of Environment*, 189, 132–151. <https://doi.org/10.1016/j.rse.2016.11.012>
- Tilstone, G., Dall’Olmo, G., Hieronymi, M., Ruddick, K., Beck, M., Ligi, M., Costa, M., D’Alimonte, D., Vellucci, V., Vansteenwegen, D., Bracher, A., Wiegmann, S., Kuusk, J., Vabson, V., Ansko, I., Vendt, R., Donlon, C., & Casal, T. (2020). Field intercomparison of radiometer measurements for ocean colour validation. *Remote Sensing*, 12(10). <https://doi.org/10.3390/rs12101587>
- Tilstone, G. H., Pardo, S., Dall’Olmo, G., Brewin, R. J. W., Nencioli, F., Dessailly, D., Kwiatkowska, E., Casal, T., & Donlon, C. (2021). Performance of Ocean Colour Chlorophyll a algorithms for Sentinel-3 OLCI, MODIS-Aqua and Suomi-VIIRS in open-ocean waters of the Atlantic. *Remote Sensing of Environment*, 260. <https://doi.org/10.1016/j.rse.2021.112444>
- Tray, E., Leadbetter, A., Meaney, W., Conway, A., Kelly, C., Maoiléidigh, N., de Eyto, E., Moran, S., & Brophy, D. (2020). An open-source database model and collections management system for fish scale and otolith archives. *Ecological Informatics*, 59(April), 101115. <https://doi.org/10.1016/j.ecoinf.2020.101115>
- Tweddle, J. F., Gubbins, M., and Scott, B. E. (2018). Should phytoplankton be a key consideration for marine management? *Mar. Policy* 97, 1–9. doi: 10.1016/j.marpol.2018.08.026
- UNESCO (2010). *Microscopic and Molecular Methods for Quantitative Phytoplankton Analysis*. Paris: UNESCO.

- Valente, A., Sathyendranath, S., Brotas, V., Groom, S., Grant, M., Taberner, M., *et al.* (2016). A compilation of global bio-optical in situ data for ocean-colour satellite applications. *Earth Syst. Sci. Data* 8, 235–252.
- Vandersea, M., Tester, P., Holderied, K., Hondolero, D., Kibler, S., and Powell, K. (2020). An extraordinary *Karenia mikimotoi* “beer tide” in Kachemak Bay Alaska. *Harmful Algae* 92:101706. doi: 10.1016/j.hal.2019.101706
- Vantrepotte, V., Loisel, H., Dessailly, D., & Mériaux, X. (2012). Optical classification of contrasted coastal waters. *Remote Sensing of Environment*, 123, 306–323. <https://doi.org/10.1016/j.rse.2012.03.004>
- Volpe, G., Colella, S., Forneris, V., Tronconi, C., & Santoleri, R. (2012). The Mediterranean Ocean Colour Observing System – System development and product validation. *Ocean Science*, 8(5), 869–883. <https://doi.org/10.5194/os-8-869-2012>
- Wang, M. H., Son, S., and Shi, W. (2009). Evaluation of MODIS SWIR and NIR-SWIR atmospheric correction algorithms using SeaBASS data. *Remote Sens. Environ.* 113, 635–644.
- Wang, X., Feng, X., Zhuang, Y., Lu, J., Wang, Y., Gonçalves, R. J., *et al.* (2019). Effects of ocean acidification and solar ultraviolet radiation on physiology and toxicity of dinoflagellate *Karenia mikimotoi*. *Harmful Algae* 81, 1–9. doi: 10.1016/j.hal.2018.11.013
- Waters, T. F. (1995) *Sediment in streams: sources, biological effects, and control*. Bethesda, Md.: American Fisheries Society (American Fisheries Society monograph, 7).
- Wei, J., Lee, Z., Ondrusek, M., Mannino, A., Tzortziou, M., & Armstrong, R. (2016a). Spectral slopes of the absorption coefficient of coloured dissolved and detrital material inverted from UV-visible remote sensing reflectance. *Journal of Geophysical Research: Oceans*, 121(3), 1953–1969. <https://doi.org/10.1002/2015JC011415>
- Wei, J., Z. Lee, and S. Shang (2016b), A system to measure the data quality of spectral remote-sensing reflectance of aquatic environments, *J. Geophys. Res. Oceans*, 121, 8189–8207, doi:10.1002/2016JC012126.
- Wells, M. L., Karlson, B., Wulff, A., Kudela, R., Trick, C., Asnaghi, V., Berdalet, E., Cochlan, W., Davidson, K., de Rijcke, M., Dutkiewicz, S., Hallegraeff, G., Flynn, K. J., Legrand, C., Paerl, H., Silke, J., Suikkanen, S., Thompson, P., & Trainer, V. L. (2020). Future HAB science: Directions and challenges in a changing climate. *Harmful Algae*, 91. <https://doi.org/10.1016/j.hal.2019.101632>
- Werdell, P. J., Behrenfeld, M. J., Bontempi, P. S., Boss, E., Cairns, B., Davis, G. T., *et al.* (2019). The Plankton, Aerosol, Cloud, ocean Ecosystem (PACE) mission: status, science, advances. *Bull. Amer. Meteorol. Soc.* 100, 1775–1794. doi: 10.1175/BAMS-D-18-0056.1
- Werdell, P. J., McKinna, L. I. W., Boss, E., Ackleson, S. G., Craig, S. E., Gregg, W. W., Lee, Z., Maritorena, S., Roesler, C. S., Rousseaux, C. S., Stramski, D., Sullivan, J. M., Twardowski, M. S., Tzortziou, M., & Zhang, X. (2018). An overview of approaches and challenges for retrieving marine inherent optical properties from ocean colour remote sensing. *Progress in Oceanography*, 160 (November 2017), 186–212. <https://doi.org/10.1016/j.pocean.2018.01.001>

- Wilkinson, M.D., Dumontier, M., Aalbersberg, I.J., Appleton, G., Axton, M., Baak, A., Blomberg, N., Boiten, J.W., da Silva Santos, L.B., Bourne, P.E., Bouwman, J., (2016). The FAIR guiding principles for scientific data management and stewardship. *Sci. Data* 3. <https://doi.org/10.1038/sdata.2016.18>
- Wolny, J. L., Tomlinson, M. C., Schollaert, Uz, S., Egerton, T. A., McKay, J. R., *et al.* (2020). Current and future remote sensing of harmful algal blooms in the chesapeake bay to support the shellfish industry. *Front. Mar. Sci.* 7:337.
- Wyatt, T., (2009) An Early *Karenia* Bloom off Southwest Ireland? *Harmful Algae News* 40, IOC of UNESCO (2009), p. 17
- Wynne, T. T., Meredith, A., Briggs, T., Litaker, W., and Stumpf, R. P. (2018). *Harmful Algal Bloom Forecasting Branch Ocean Colour Satellite Imagery Processing Guidelines*. Silver Spring, MD: NOAA.
- Xing, X. G., Zhao, D. Z., Liu, Y. G., Yang, J. H., Xiu, P., and Wang, L. (2007). An overview of remote sensing of chlorophyll fluorescence. *Ocean Sci. J.* 42, 49–59.
- Yarish, C., Redmond, S., & Kim, J. K. (2012). *Gracilaria Culture Handbook for New England. Wrack Lines. 72.* <Http://Digitalcommons.Uconn.Edu/Wracklines/72>, October 2012, 1–50. <https://www.researchgate.net/publication/311561454>
- Ye, M., & Sun, Y. (2022). Review of the Forel–Ule Index based on *in situ* and remote sensing methods and application in water quality assessment. In *Environmental Science and Pollution Research* (Vol. 29, Issue 9, pp. 13024–13041). Springer Science and Business Media Deutschland GmbH. <https://doi.org/10.1007/s11356-021-18083-0>
- Zeng, L., and Li, D. (2015). Development of *in situ* sensors for chlorophyll concentration measurement. *J. Sensors* 2015, 1–16. doi: 10.1155/2015/903509
- Zhao, T., Tan, L., Huang, W., and Wang, J. (2019). The interactions between micro polyvinyl chloride (mPVC) and marine dinoflagellate *Karenia mikimotoi*: The inhibition of growth, chlorophyll and photosynthetic efficiency. *Environ. Pollut.* 247, 883–889. doi: 10.1016/j.envpol.2019.01.114
- Zhao, M., Bai, Y., Li, H., He, X., Gong, F., & Li, T. (2022). Fluorescence Line Height Extraction Algorithm for the Geostationary Ocean Colour Imager. *Remote Sensing*, 14(11). <https://doi.org/10.3390/rs14112511>
- Zhou, J., Gilerson, A., Ioannou, I., Hlaing, S., Schalles, J., Gross, B., Moshary, F., & Ahmed, S. (2008). Retrieving quantum yield of sun-induced chlorophyll fluorescence near surface from hyperspectral in-situ measurement in productive water. http://www.ioccg.org/groups/OCAG_data.html.
- Zibordi, G. & Hooker, S. & Berthon, J. & D'Alimonte, D. (2002). Autonomous Above-Water Radiance Measurements from an Offshore Platform: A Field Assessment Experiment. *Journal of Atmospheric and Oceanic Technology*. 19. 808-819. 10.1175/1520-0426(2002)019<0808:AAWRMF>2.0.CO;2
- Zibordi, G., Doyle, J. P., & Hooker, S. B. (1999). Offshore tower shading effects on in-water optical measurements. *Journal of Atmospheric and Oceanic Technology*, 16(11 PART 2), 1767–1779. [https://doi.org/10.1175/1520-0426\(1999\)016<1767:otseoi>2.0.co;2](https://doi.org/10.1175/1520-0426(1999)016<1767:otseoi>2.0.co;2)

Zibordi, G., Ruddick, K., Ansko, I., Moore, G., Kratzer, S., Icely, J., & Reinart, A. (2012). *In situ* determination of the remote sensing reflectance: An inter-comparison. *Ocean Science*, 8(4), 567–586. <https://doi.org/10.5194/os-8-567-2012>

Appendices

Appendix A1. Matlab Scripts

Find Pixel Matlab Script Prof. Peter Croot 2019

```
function [data,pixmean,pixstd] = findpixel(filename,latpix, longpix)
%findpixel
% function to find values of 3 x 3 pixels around a point from Copernicus
% Satellite data
% this version uses Kd490 data long x lat x time
% Peter Croot NUIG Feb 2019

lon=ncread(filename,'longitude');
lat=ncread(filename,'latitude');
Kd490=ncread(filename,'KD490');
time=ncread(filename,'time');
T=datetime(time,'ConvertFrom','posixtime')

[latd,ilat]=min(abs(lat-latpix));
[lond,ilon]=min(abs(lon-longpix));

[m,n,o] = size(Kd490);

for i=1:o
    data(1:3,i)=Kd490(ilon-1:ilon+1,ilat-1,i);
    data(4:6,i)=Kd490(ilon-1:ilon+1,ilat,i);
    data(7:9,i)=Kd490(ilon-1:ilon+1,ilat+1,i);
    pixmean(i)=mean(data(:,i));
    pixstd(i)=std(data(:,i));
end
hold
plot(T,data(5,:),'r*')

% errorbar function can not handle dates need work around
plot(T,pixmean,'k+')
plot(T,pixmean+pixstd,'k*')
plot(T,pixmean-pixstd,'k*')
```

TRIOS Log Kz Matlab Script Prof. Peter Croot 2020

```
function [Kz,sm,r] = TRIOSlogKz(l,nSpec,pn,j,ln)
%Function to analyze TRIOS RAMSES underwater irradiance data
% looks at the decrease with depth
% Quick version
% Oct 2020
logl=log(abs(nSpec(:,.)));
nx=length(ln);
for i=1:nx
[Kz(i),b(i),r(i),sm(i),sb(i),xbar(i),ybar(i))] = lsqfitma(-10*pn(j),logl(j,ln(i)));
end
%plot(l(ln),Kz)
errorbar(l(ln),Kz,sm)
```


Five Hyperspectral Radiometer Data processing Matlab scripts

STEP 1

```
%Script for summarizing radiometer data into daily files
%
% The script is based on processing the ".dat" files coming from the
% radiometers (one file per measurement). The radiometer data is collected
% in daily files and is written to tab-delimited text files (.dat).
%
% All input files have to be stored in the folder specified under
% "FolderInName" (Parameters-section). Then the script can be executed.
%
% *****
%
% Jochen Wollschläger, October 2018
%
% Changelog:
%

%-----

clc
clear
BasicPath=pwd;
addpath(genpath([BasicPath,'\RequiredFiles']))

%% Parameters

%Full path of the folder that contains the input files
FolderInName='D:\Uni\TSS_Spiekeroog_Radiometer\SingleFiles\2013';

%Full path of the folder that will contain the data output files (will be created)
FolderOutName='D:\Uni\TSS_Spiekeroog_Radiometer\RawFiles\2013';

%Names of radiometers
Name_Es=[{'SAM_8503'}]; %Irradiance radiometers (Es)
Name_Lsky=[{'SAM_8504'} {'SAM_86C1'}]; %Radiance radiometers looking upward
(Lsky)
Name_Lsfc=[{'SAM_860D'} {'SAM_86C2'}]; %Radiance radiometers looking
downward (Lsfc)

%Determining which data type is considered for creation of the datily files
DesiredDataType='RAW';
% DesiredDataType='Calibrated';
```

```

%Metadata
%Write all metadata that you would like to have in the file in the
%"Metadata" variable below. For each line, use a new string enclosed in a
%cell (e.g. {'Teststring 1'}; {'Teststring 1'})
Metadata={'Time Series Station Spiekeroog'};...
    {'Measurement method: Radiometer (RAMSES, TriOS GmbH, Germany)};...
    {'Azimuth=30°'};...
    {'Nadir=30°'};...
    {'SetupHeight=13.1 m'};...
    {'Latitude=53 45 00.94095 °N'};...
    {'Longitude=7 40 16.00638 °E'};...
    {'Research project: Time Series Station Spiekeroog'};...
    {'Contact: University of Oldenburg, ICBM, Working group Marine Sensor
Systems (Oliver Zielinski)'};...
    {'E-mail: oliver.zielinski@uol.de; jochen.wollschlaeger@uol.de'};...
];

%%%%%%%%%%%%%%%%%%%%%%%%%%%%%%%%%%%%%%%%%%%%%%%%%%%%%%%%%%%%%%%%%%%%%%%%
%%%%%%%%%%%%%%%%%%%%%%%%%%%%%%%%%%%%%%%%%%%%%%%%%%%%%%%%%%%%%%%%%%%%%%%%

%% Creating list of all *.dat-files in folder

cd(FolderInName)

Content=dir;
Folders=[Content.isdir;
FileList={Content(~Folders).name}'];
Time_Index=false(size(FileList));
for i=1:length(FileList)
    if ~isempty(strfind(FileList{i},'.dat'))
        Time_Index(i)=true;
    end
end
FileList=FileList(Time_Index);
clear i Time_Index Content Folders Index

%% Create a collection variable
%%The structure is based on the first file in the folder

[~,Data]=hdrload(FileList{1});
if isempty(Data)
    Data=zeros(256,4);
end

```

```

Unit1=zeros(length(FileList),size(Data,1)+10);
Unit2=zeros(length(FileList),size(Data,1)+10);
DataID=cell(length(FileList),1);
Device=cell(length(FileList),1);
DataType=cell(length(FileList),1);
IntegrationTime=zeros(length(FileList),1);
clear Data

%% Open the files one after another and store the data

FilesToImport=length(FileList);
for i=1:length(FileList)
    [DataHeader,Data]=hdrload(FileList{i});
    if isempty(Data)
    else
        Index=strcmpi(strtok(cellstr(DataHeader)),'IDData');
        DataIDTemp=strsplit(DataHeader(Index,:));
        DataID(i,1)=DataIDTemp(3);

        Index=strcmpi(strtok(cellstr(DataHeader)),'IDDevice');
        DeviceTemp=strsplit(DataHeader(Index,:));
        Device(i,1)=DeviceTemp(3);

        Index=strcmpi(strtok(cellstr(DataHeader)),'IDDataTypeSub1');
        DataTypeTemp=strsplit(DataHeader(Index,:));
        DataType(i,1)=DataTypeTemp(3);

        Index=strcmpi(strtok(cellstr(DataHeader)),'IntegrationTime');
        IntegrationTimeTemp=strsplit(DataHeader(Index,:));
        IntegrationTime(i,1)=str2double(IntegrationTimeTemp(3));

        Unit1(i,1:size(Data,1))=transpose(Data(:,1));
        Unit2(i,1:size(Data,1))=transpose(Data(:,2));
    end

    FilesToImport=FilesToImport-1;
    display(FilesToImport)
end
clear DataHeader Data i FileList DataIDTemp DeviceTemp DataTypeTemp
TimestampTemp...
    IntegrationTimeTemp FilesToImport Index

cd(BasicPath)

```

```

%% Delete data

%Unnecessary columns
Index=sum([Unit1;Unit2],1)==0;
Unit1(:,Index)=[];
Unit2(:,Index)=[];
clear Index

%Unnecessary rows
Index=sum([Unit1,Unit2],2)==0;
DataID(Index,:)=[];
Device(Index,:)=[];
DataType(Index,:)=[];
IntegrationTime(Index,:)=[];
Unit1(Index,:)=[];
Unit2(Index,:)=[];
clear Index

%Data without the desired string in "DataType"
Index=strcmpi(DataType,DesiredDataType);
Unit1=Unit1(Index,:);
Unit2=Unit2(Index,:);
DataID=DataID(Index,:);
Device=Device(Index,:);
IntegrationTime=IntegrationTime(Index,:);
clear Index DataType

%Data-doublettes
[~,Index,~]=unique(Unit2,'rows','stable');
Unit1=Unit1(Index,:);
Unit2=Unit2(Index,:);
DataID=DataID(Index,:);
Device=Device(Index,:);
IntegrationTime=IntegrationTime(Index,:);
clear Index

%Data with incorrect integration time (< 2 ms)
Index=IntegrationTime<2;
Unit1(Index,:)=[];
Unit2(Index,:)=[];
DataID(Index,:)=[];
Device(Index,:)=[];
IntegrationTime(Index,:)=[];
clear Index

```

```

%% Taking the parameters occurring in the majority of files for all data

Parameters=unique(Unit1,'rows');
Number=zeros(size(Parameters,1),1);
for i=1:length(Number)
    Number(i)=sum(ismember(Unit1,Parameters(i,:), 'rows'));
end
 [~,Index]=max(Number);
Parameters=Parameters(Index,:);
clear i Number Index Unit1

%% Convert radiometer list and device names in upper case characters

Name_Es=upper(Name_Es);
Name_Lsky=upper(Name_Lsky);
Name_Lsfc=upper(Name_Lsfc);
Device=upper(Device);

%% Collecting the data for the different radiometers

%Irradiance radiometer (Es)
Index_Device=ismember(Device,Name_Es);
Es_Data=Unit2(Index_Device,:);
Es_Device=Device(Index_Device,:);
Es_IntegrationTime=IntegrationTime(Index_Device,:);
Es_DataID=DataID(Index_Device,:);

%Radiance radiometer upward (Lsky)
Index_Device=ismember(Device,Name_Lsky);
Lsky_Data=Unit2(Index_Device,:);
Lsky_Device=Device(Index_Device,:);
Lsky_IntegrationTime=IntegrationTime(Index_Device,:);
Lsky_DataID=DataID(Index_Device,:);

%Radiance radiometer downward (Lsfc)
Index_Device=ismember(Device,Name_Lsfc);
Lsfc_Data=Unit2(Index_Device,:);
Lsfc_Device=Device(Index_Device,:);
Lsfc_IntegrationTime=IntegrationTime(Index_Device,:);
Lsfc_DataID=DataID(Index_Device,:);

clear Index_Device Index_Deletion DataID_TimestampFormat Unit2 DataID...
Device IntegrationTime

```

```

%% Create the timestamps from the data ID

%Es
Es_Stamp=NaN(size(Es_DataID,1),6);
for i=1:size(Es_Stamp,1)
    ID_String=strsplit(Es_DataID{i},{'_','-'});

    Index=cellfun(@strfind,ID_String, repmat({'20'},size(ID_String)), 'UniformOutput',0);
    Index=~cellfun(@isempty,Index);
    [~,Index]=find(Index,1,'first');
    ID_String=ID_String(:,Index:end);
    ID_String=[ID_String{:}];
    ID_String=datevec(ID_String(1:14),'yyyymmddHHMMSS');
    Es_Stamp(i,:)=ID_String;
end
clear i ID_String

%Lsky
Lsky_Stamp=NaN(size(Lsky_DataID,1),6);
for i=1:size(Lsky_Stamp,1)
    ID_String=strsplit(Lsky_DataID{i},{'_','-'});

    Index=cellfun(@strfind,ID_String, repmat({'20'},size(ID_String)), 'UniformOutput',0);
    Index=~cellfun(@isempty,Index);
    [~,Index]=find(Index,1,'first');
    ID_String=ID_String(:,Index:end);
    ID_String=[ID_String{:}];
    ID_String=datevec(ID_String(1:14),'yyyymmddHHMMSS');
    Lsky_Stamp(i,:)=ID_String;
end
clear i ID_String Index

%Lsfc
Lsfc_Stamp=NaN(size(Lsfc_DataID,1),6);
for i=1:size(Lsfc_Stamp,1)
    ID_String=strsplit(Lsfc_DataID{i},{'_','-'});

    Index=cellfun(@strfind,ID_String, repmat({'20'},size(ID_String)), 'UniformOutput',0);
    Index=~cellfun(@isempty,Index);
    [~,Index]=find(Index,1,'first');
    ID_String=ID_String(:,Index:end);
    ID_String=[ID_String{:}];
    ID_String=datevec(ID_String(1:14),'yyyymmddHHMMSS');

```

```

    Lsfc_Timestamp(i,:)=ID_String;
end
clear i ID_String Index

%% Sort the data by timestamp

[~,Index_Es]=sort(datenum(Es_Timestamp));
[~,Index_Lsky]=sort(datenum(Lsky_Timestamp));
[~,Index_Lsfc]=sort(datenum(Lsfc_Timestamp));

Es_Data=Es_Data(Index_Es,:);
Es_DataID=Es_DataID(Index_Es,:);
Es_Device=Es_Device(Index_Es,:);
Es_IntegrationTime=Es_IntegrationTime(Index_Es,:);
Es_Timestamp=Es_Timestamp(Index_Es,:);

Lsky_Data=Lsky_Data(Index_Lsky,:);
Lsky_DataID=Lsky_DataID(Index_Lsky,:);
Lsky_Device=Lsky_Device(Index_Lsky,:);
Lsky_IntegrationTime=Lsky_IntegrationTime(Index_Lsky,:);
Lsky_Timestamp=Lsky_Timestamp(Index_Lsky,:);

Lsfc_Data=Lsfc_Data(Index_Lsfc,:);
Lsfc_DataID=Lsfc_DataID(Index_Lsfc,:);
Lsfc_Device=Lsfc_Device(Index_Lsfc,:);
Lsfc_IntegrationTime=Lsfc_IntegrationTime(Index_Lsfc,:);
Lsfc_Timestamp=Lsfc_Timestamp(Index_Lsfc,:);

clear Index_Es Index_Lsky Index_Lsfc

%% Going to or creating the folder where the data will be saved
if exist(FolderOutName,'dir')==0
    mkdir(FolderOutName)
end
cd(FolderOutName)

%% Writing irradiance radiometer (Es) data

%Writing one file per day
DayList=Es_Timestamp;
DayList(:,4:6)=0;
DayList=unique(DayList,'rows');

Es_Files_To_Write=size(DayList,1);

```

```

for i=1:size(DayList,1)

    %Indexing the data of the respective day
    Index_Day=ismember(Es_Timestamp(:,1:3),DayList(i,1:3),'rows');

    if strcmp(DesiredDataType,'RAW')
        %Creating the file name
        Es_FileName=[datestr(DayList(i,:),'yyyymmdd'),'_Es_RAW.dat'];

        %Completing the metadata
        Radiometer=Es_Device(Index_Day);
        Radiometer=Radiometer{1};
        Es_Metadata=[{'Radiometer: ',Radiometer}];{'Parameter: Irradiance
(Es)'};{'Unit: Counts'};{'';Metadata;{'}}];
        for j=1:size(Es_Metadata,1)
            Es_Metadata{j}=['#',Es_Metadata{j}];
        end
        clear j Radiometer

        %Creating the file header
        Es_DataHeader=[{'Year'} {'Month'} {'Day'} {'Hour'} {'Minute'} {'Second'}
{'IntTime [ms]'} num2cell(Parameters)];

        %Creating the file content of the respective day

        Es_Content=[Es_Timestamp(Index_Day,:),Es_IntegrationTime(Index_Day,:),Es_Data
(Index_Day,:)];
        clear Index_Day

        %Writing the file
        fid=fopen(Es_FileName,'w');
        for j=1:size(Es_Metadata,1)
            fprintf(fid,'%s\n',Es_Metadata{j});
        end
        clear j

        fprintf(fid,['%s\t%s\t%s\t%s\t%s\t%s\t%s',repmat('\t%.0f',1,size(Es_Data,2)),'\n'],Es
_DataHeader{1,:});
        for j=1:size(Es_Content,1)

            fprintf(fid,['%.0f\t%.0f\t%.0f\t%.0f\t%.0f\t%.0f\t%.0f',repmat('\t%f',1,size(Es_Data,
2)),'\n'],Es_Content(j,:));
        end
        clear j

```



```

fclose(fid);
Es_Files_To_Write=Es_Files_To_Write-1;
display(Es_Files_To_Write)

elseif strcmp(DesiredDataType,'Calibrated')

%Creating the file name
Es_FileName=[datestr(DayList(i,:), 'yyyymmdd'), '_Es_Calibrated.dat'];

%Completing the metadata
Radiometer=Es_Device(Index_Day);
Radiometer=Radiometer{1};
Es_Metadata=[{'Radiometer: ',Radiometer}];{'Parameter: Irradiance
(Es)'};{'Unit: mW m-2 sr-1'};{'';Metadata;{''}};
for j=1:size(Es_Metadata,1)
    Es_Metadata{j}=['#',Es_Metadata{j}];
end
clear j Radiometer

%Creating the file header
Es_DataHeader=[{'Year'} {'Month'} {'Day'} {'Hour'} {'Minute'} {'Second'}
num2cell(Parameters)];

%Creating the file content of the respective day
Es_Content=[Es_Timestamp(Index_Day,:),Es_Data(Index_Day,:)];
clear Index_Day

%Writing the file
fid=fopen(Es_FileName,'w');
for j=1:size(Es_Metadata,1)
    fprintf(fid,'%s\n',Es_Metadata{j});
end
clear j

fprintf(fid,['%s\t%s\t%s\t%s\t%s\t%s',repmat('\t%.0f',1,size(Es_Data,2)),'\n'],Es_DataHeader{1,:});
for j=1:size(Es_Content,1)

fprintf(fid,['%.0f\t%.0f\t%.0f\t%.0f\t%.0f\t%.0f',repmat('\t%f',1,size(Es_Data,2)),'\n'
],Es_Content(j,:));
end
clear j
fclose(fid);
Es_Files_To_Write=Es_Files_To_Write-1;

```

```

        display(Es_Files_To_Write)
    end
end
clear i Es_Files_To_Write ans fid

%% Writing upward looking radiance radiometer (Lsky) data

%Writing one file per day
DayList=Lsky_Timestamp;
DayList(:,4:6)=0;
DayList=unique(DayList,'rows');

Lsky_Files_To_Write=size(DayList,1);
for i=1:size(DayList,1)

    %Indexing the data of the respective day
    Index_Day=ismember(Lsky_Timestamp(:,1:3),DayList(i,1:3),'rows');

    if strcmp(DesiredDataType,'RAW')
        %Creating the file name
        Lsky_FileName=[datestr(DayList(i,:),'yyyymmdd'),'_Lsky_RAW.dat'];

        %Completing the metadata
        Radiometer=Lsky_Device(Index_Day);
        Radiometer=Radiometer{1};
        Lsky_Metadata=[{'Radiometer: ',Radiometer}];{'Parameter: Radiance
(Lsky)'};{'Unit: Counts'};{'';Metadata;{'}}];
        for j=1:size(Lsky_Metadata,1)
            Lsky_Metadata{j}=[ '#',Lsky_Metadata{j}];
        end
        clear j Radiometer

        %Creating the file header
        Lsky_DataHeader=[{'Year'} {'Month'} {'Day'} {'Hour'} {'Minute'} {'Second'}
{'IntTime [ms]'} num2cell(Parameters)];

        %Creating the file content of the respective day

Lsky_Content=[Lsky_Timestamp(Index_Day,:),Lsky_IntegrationTime(Index_Day,:),Ls
ky_Data(Index_Day,:)];
        clear Index_Day

        %Writing the file
        fid=fopen(Lsky_FileName,'w');

```

```

    for j=1:size(Lsky_Metadata,1)
        fprintf(fid,'%s\n',Lsky_Metadata{j});
    end
    clear j

fprintf(fid,['%s\t%s\t%s\t%s\t%s\t%s\t%s',repmat('\t%.0f',1,size(Lsky_Data,2)),'\n'],
Lsky_DataHeader{1,:});
    for j=1:size(Lsky_Content,1)

fprintf(fid,['%.0f\t%.0f\t%.0f\t%.0f\t%.0f\t%.0f\t%.0f',repmat('\t%f',1,size(Lsky_Data,2)),'\n'],Lsky_Content(j,:));
        end
        clear j
        fclose(fid);
        Lsky_Files_To_Write=Lsky_Files_To_Write-1;
        display(Lsky_Files_To_Write)

elseif strcmp(DesiredDataType,'Calibrated')

    %Creating the file name
    Lsky_FileName=[datestr(DayList(i,:),'yyyymmdd'),'_Lsky_Calibrated.dat'];

    %Completing the metadata
    Radiometer=Lsky_Device(Index_Day);
    Radiometer=Radiometer{1};
    Lsky_Metadata=[{'Radiometer: ',Radiometer}];{'Parameter:
Radiance(Lsky)'};{'Unit: mW m-2 sr-1'};{'';Metadata;{'}}];
    for j=1:size(Lsky_Metadata,1)
        Lsky_Metadata{j}=[ '#',Lsky_Metadata{j}];
    end
    clear j Radiometer

    %Creating the file header
    Lsky_DataHeader=[{'Year'} {'Month'} {'Day'} {'Hour'} {'Minute'} {'Second'}
num2cell(Parameters)];

    %Creating the file content of the respective day
    Lsky_Content=[Lsky_Timestamp(Index_Day,:),Lsky_Data(Index_Day,:)];
    clear Index_Day

    %Writing the file
    fid=fopen(Lsky_FileName,'w');
    for j=1:size(Lsky_Metadata,1)
        fprintf(fid,'%s\n',Lsky_Metadata{j});

```

```

end
clear j

fprintf(fid,['%s\t%s\t%s\t%s\t%s\t%s', repmat('\t%.0f',1,size(Lsky_Data,2)),'\n'],Lsky
_DataHeader{1,:});
for j=1:size(Lsky_Content,1)

fprintf(fid,['%.0f\t%.0f\t%.0f\t%.0f\t%.0f\t%.0f', repmat('\t%f',1,size(Lsky_Data,2)),'\
n'],Lsky_Content(j,:));
end
clear j
fclose(fid);
Lsky_Files_To_Write=Lsky_Files_To_Write-1;
display(Lsky_Files_To_Write)
end
end
clear i Lsky_Files_To_Write ans fid

%% Writing downward looking radiance radiometer (Lsfc) data

%Writing one file per day
DayList=Lsfc_Timestamp;
DayList(:,4:6)=0;
DayList=unique(DayList,'rows');

Lsfc_Files_To_Write=size(DayList,1);
for i=1:size(DayList,1)

%Indexing the data of the respective day
Index_Day=ismember(Lsfc_Timestamp(:,1:3),DayList(i,1:3),'rows');

if strcmp(DesiredDataType,'RAW')
%Creating the file name
Lsfc_FileName=[datestr(DayList(i,:), 'yyyymmdd'),' _Lsfc_RAW.dat'];

%Completing the metadata
Radiometer=Lsfc_Device(Index_Day);
Radiometer=Radiometer{1};
Lsfc_Metadata=[{'Radiometer: ',Radiometer}];{'Parameter: Radiance
(Lsfc)'};{'Unit: Counts'};{''};Metadata;{''}];
for j=1:size(Lsfc_Metadata,1)
Lsfc_Metadata[j]=['#',Lsfc_Metadata[j]];
end
clear j Radiometer

```

```

    %Creating the file header
    Lsfc_DataHeader=[{'Year'} {'Month'} {'Day'} {'Hour'} {'Minute'} {'Second'}
    {'IntTime [ms]'} num2cell(Parameters)];

    %Creating the file content of the respective day

Lsfc_Content=[Lsfc_Timestamp(Index_Day,:),Lsfc_IntegrationTime(Index_Day,:),Lsfc
_Data(Index_Day,:)];
    clear Index_Day

    %Writing the file
    fid=fopen(Lsfc_FileName,'w');
    for j=1:size(Lsfc_Metadata,1)
        fprintf(fid,'%s\n',Lsfc_Metadata{j});
    end
    clear j

    fprintf(fid,['%s\t%s\t%s\t%s\t%s\t%s\t%s',repmat('\t%.0f',1,size(Lsfc_Data,2)),'\n'],
    Lsfc_DataHeader{1,:});
    for j=1:size(Lsfc_Content,1)

    fprintf(fid,['%.0f\t%.0f\t%.0f\t%.0f\t%.0f\t%.0f\t%.0f',repmat('\t%f',1,size(Lsfc_Dat
a,2)),'\n'],Lsfc_Content(j,:));
    end
    clear j
    fclose(fid);
    Lsfc_Files_To_Write=Lsfc_Files_To_Write-1;
    display(Lsfc_Files_To_Write)

elseif strcmp(DesiredDataType,'Calibrated')

    %Creating the file name
    Lsfc_FileName=[datestr(DayList(i,:), 'yyyymmdd'),' _Lsfc_Calibrated.dat'];

    %Completing the metadata
    Radiometer=Lsfc_Device(Index_Day);
    Radiometer=Radiometer{1};
    Lsfc_Metadata=[{'Radiometer: ',Radiometer}];{'Parameter:
Radiance(Lsfc)'};{'Unit: mW m-2 sr-1'};{'';Metadata;{'}};
    for j=1:size(Lsfc_Metadata,1)
        Lsfc_Metadata{j}=['#',Lsfc_Metadata{j}];
    end
    clear j Radiometer

```

```

    %Creating the file header
    Lsfc_DataHeader=[{'Year'} {'Month'} {'Day'} {'Hour'} {'Minute'} {'Second'}
num2cell(Parameters)];

    %Creating the file content of the respective day
    Lsfc_Content=[Lsfc_Timestamp(Index_Day,:),Lsfc_Data(Index_Day,:)];
    clear Index_Day

    %Writing the file
    fid=fopen(Lsfc_FileName,'w');
    for j=1:size(Lsfc_Metadata,1)
        fprintf(fid,'%s\n',Lsfc_Metadata{j});
    end
    clear j

    fprintf(fid,['%s\t%s\t%s\t%s\t%s\t%s',repmat('\t%.0f',1,size(Lsfc_Data,2)),'\n'],Lsfc_
DataHeader{1,:});
        for j=1:size(Lsfc_Content,1)

    fprintf(fid,['%.0f\t%.0f\t%.0f\t%.0f\t%.0f\t%.0f',repmat('\t%f',1,size(Lsfc_Data,2)),'\
n'],Lsfc_Content(j,:));
        end
        clear j
        fclose(fid);
        Lsfc_Files_To_Write=Lsfc_Files_To_Write-1;
        display(Lsfc_Files_To_Write)
    end
end
clear i Lsfc_Files_To_Write ans fid

cd(BasicPath)

```

STEP 2

%Script for calibrating radiometer data according to the RAMSES manual

```
clc
clear
BasicPath=pwd;
addpath(genpath([BasicPath,'\RequiredFiles']))

%% Parameters

%Full path of the folder that contains the uncalibrated files
FolderInName='D:\TRIOS\Celticexplorer_Radiometer\RawFiles';

%Full path of the folder that will contain the calibrated data output files (will be
created)
FolderOutName='D:\TRIOS\Celticexplorer_Radiometer\CalibratedFiles';

%Full path of the folder that contains instrument calibration files
FolderInstrumentFiles='C:\Users\CatherineJordan\Documents\MATLAB\Scripts\Data
aProcessing_Radiometer\InstrumentData';

%%%%%%%%%%%%%%%%%%%%%%%%%%%%%%%%%%%%%%%%%%%%%%%%%%%%%%%%%%%%%%%%%%%%%%%%
%%%%%%%%%%%%%%%%%%%%%%%%%%%%%%%%%%%%%%%%%%%%%%%%%%%%%%%%%%%%%%%%%%%%%%%%

%% Import of *.ini-files for the radiometers

cd(FolderInstrumentFiles)

%Creating list of all *.ini-files in folder
Content=dir;
Folders=[Content.isdir];
FileList={Content(~Folders).name}';
Index=false(size(FileList));
for i=1:length(FileList)
    if ~isempty(strfind(FileList{i},'.ini'))
        Index(i)=true;
    end
end
IniFileList=FileList(Index);
clear i Index Content Folders FileList

%Open the files and store the data
IniFilesContent=cell(length(IniFileList),8);
```

```

for i=1:length(IniFileList)

    fid=fopen(IniFileList{i});
    Data=textscan(fid,'%s%s%s%s','Delimiter',' ','MultipleDelimsAsOne',1);
    fclose(fid);

    Data=[Data{:}];

    IniFilesContent{i,1}=Data{ismember(Data(:,1),'IDDevice'),3};
    IniFilesContent{i,2}=Data{ismember(Data(:,1),'c0s'),3};
    IniFilesContent{i,3}=Data{ismember(Data(:,1),'c1s'),3};
    IniFilesContent{i,4}=Data{ismember(Data(:,1),'c2s'),3};
    IniFilesContent{i,5}=Data{ismember(Data(:,1),'c3s'),3};
    IniFilesContent{i,6}=Data{ismember(Data(:,1),'DarkPixelStart'),3};
    IniFilesContent{i,7}=Data{ismember(Data(:,1),['DarkPixelEnd'
'DarkPixelStop'])},3};
    IniFilesContent{i,8}=[Data{ismember(Data(:,1),'DateTime'),3},
'Data{ismember(Data(:,1),'DateTime'),4}];
end
clear i Data ans fid
clc

IniFilesContent(:,2:7)=num2cell(str2double(IniFilesContent(:,2:7)));

%Check for and delete data-doublettes
[~,Index,~]=unique(str2double(IniFilesContent(:,2:end)),'rows','stable');
IniFilesContent=IniFilesContent(Index,:);
clear Index

cd(BasicPath)

%% Import of BACK and CAL files for the radiometers

cd(FolderInstrumentFiles)

%Creating list of all *.dat-files in folder
Content=dir;
Folders=[Content.isdir];
FileList={Content(~Folders).name}';
Index=false(size(FileList));
for i=1:length(FileList)
    if ~isempty(strfind(FileList{i},'.dat'))
        Index(i)=true;
    end
end

```



```

end
FileList=FileList(Index);
clear i Index Content Folders Index

%Create a collection variable
%The structure is based on the first file in the folder

[~,Data]=hdrload(FileList{1});
if isempty(Data)
    Data=zeros(256,4);
end
Instrument_Pixel=zeros(length(FileList),size(Data,1)+10);
Instrument_Spectrum=zeros(length(FileList),size(Data,1)+10);
Instrument_ErrorCounts=zeros(length(FileList),size(Data,1)+10);
Instrument_DataID=cell(length(FileList),1);
Instrument_Device=cell(length(FileList),1);
Instrument_DataType=cell(length(FileList),1);
Instrument_IntTime=zeros(length(FileList),1);
clear Data

%Open the files one after another and store the data
for i=1:length(FileList)
    [DataHeader,Data]=hdrload(FileList{i});
    if isempty(Data)
    else
        Index=strcmpi(strtok(cellstr(DataHeader)),'IDData');
        DataIDTemp=strsplit(DataHeader(Index,:));
        Instrument_DataID(i,1)=DataIDTemp(3);

        Index=strcmpi(strtok(cellstr(DataHeader)),'IDDevice');
        DeviceTemp=strsplit(DataHeader(Index,:));
        Instrument_Device(i,1)=DeviceTemp(3);

        Index=strcmpi(strtok(cellstr(DataHeader)),'IDDataTypeSub1');
        DataTypeTemp=strsplit(DataHeader(Index,:));
        Instrument_DataType(i,1)=DataTypeTemp(3);

        Index=strcmpi(strtok(cellstr(DataHeader)),'IntegrationTime');
        IntegrationTimeTemp=strsplit(DataHeader(Index,:));
        Instrument_IntTime(i,1)=str2double(IntegrationTimeTemp(3));

        Instrument_Pixel(i,1:size(Data,1))=transpose(Data(:,1));
        Instrument_Spectrum(i,1:size(Data,1))=transpose(Data(:,2));
        Instrument_ErrorCounts(i,1:size(Data,1))=transpose(Data(:,3));
    end
end

```

```

end
end
clear DataHeader Data i FileList DataIDTemp DeviceTemp DataTypeTemp...
    IntegrationTimeTemp Index

%Delete unnecessary columns
Index=sum([Instrument_Pixel;Instrument_Spectrum;Instrument_ErrorCounts],1)==
0;
Instrument_Pixel(:,Index)=[];
Instrument_Spectrum(:,Index)=[];
Instrument_ErrorCounts(:,Index)=[];
clear Index

%Delete unnecessary rows
Index=sum([Instrument_Pixel,Instrument_Spectrum,Instrument_ErrorCounts],2)==
0;
Instrument_DataID(Index,:)=[];
Instrument_Device(Index,:)=[];
Instrument_DataType(Index,:)=[];
Instrument_IntTime(Index,:)=[];
Instrument_Pixel(Index,:)=[];
Instrument_Spectrum(Index,:)=[];
Instrument_ErrorCounts(Index,:)=[];
clear Index

%Getting the timestamp from the data ID
Instrument_Timestamp=NaN(size(Instrument_DataID,1),6);
for i=1:size(Instrument_Timestamp,1)
    ID_String=strsplit(Instrument_DataID{i},{ '_' , '-' });

Index=cellfun(@strfind,ID_String,repmat({'20'},size(ID_String)), 'UniformOutput',0);
    Index=~cellfun(@isempty,Index);
    [~,Index]=find(Index,1,'first');
    ID_String=ID_String(:,Index:end);
    ID_String=[ID_String{:}];
    ID_String=datevec(ID_String(1:14),'yyyymmddHHMMSS');
    Instrument_Timestamp(i,:)=ID_String;
end
clear i Index ID_String

%Taking the pixel occurring in the majority of files for all data
Instrument_Pixel=unique(Instrument_Pixel,'rows');
if size(Instrument_Pixel,1)>1
    errordlg('Different pixel information in the BACK and CAL files! Script aborted!')

```

```

    return
end

%Converting the device names in upper case letters
Instrument_Device=upper(Instrument_Device);

cd(BasicPath)

%% Calibrate the radiometer rawdata
%according to the procedures given in the TriOS RAMSES manual

cd(FolderInName)

%Creating list of all *RAW.dat-files in folder
Content=dir;
Folders=[Content.isdir];
FileList={Content(~Folders).name}';
Index=false(size(FileList));
for i=1:length(FileList)
    if ~isempty(strfind(FileList{i},'RAW.dat'))
        Index(i)=true;
    end
end
FileList=FileList(Index);
clear i Index Content Folders Index

cd(BasicPath)

FilesToCalibrate=size(FileList,1);
for i=1:size(FileList,1)

    cd(FolderInName)

    %Open the radiometer file
    fid=fopen(FileList{i},'r');
    [Metadata, Data]=hdrload(FileList{i});
    Metadata=cellstr(Metadata);
    Metadata=Metadata(1:end-1,:);
    fclose(fid);
    clear ans fid

    %Getting the radiometer name from the metadata
    Radiometer=Metadata{~cellfun(@isempty,strfind(Metadata,'Radiometer'))};
    Radiometer=strsplit(Radiometer,' ');

```

```

Radiometer=upper(Radiometer{2});

%Getting the parameter name from the metadata
Parameter=Metadata{~cellfun(@isempty,strfind(Metadata,'Parameter'))};
Parameter=strsplit(Parameter,');
Parameter=upper(Parameter{3});

%Dividing the radiometer data
Timestamp=Data(:,1:6);
IntTime=Data(:,7);
Spectra=Data(:,8:end);
clear Data

cd(BasicPath)

%% Get the BACK data for the radiometer

%By data type and device type
Instrument_DataID_Temporary=Instrument_DataID;
Instrument_DataType_Temporary=Instrument_DataType;
Instrument_Device_Temporary=Instrument_Device;
Instrument_ErrorCounts_Temporary=Instrument_ErrorCounts;
Instrument_IntTime_Temporary=Instrument_IntTime;
Instrument_Spectrum_Temporary=Instrument_Spectrum;
Instrument_Timestamp_Temporary=Instrument_Timestamp;

Index=ismember(Instrument_DataType_Temporary,'BACK')&ismember(Instrument
_Device_Temporary,Radiometer);
Instrument_DataID_Temporary=Instrument_DataID_Temporary(Index,:);
Instrument_DataType_Temporary=Instrument_DataType_Temporary(Index,:);
Instrument_Device_Temporary=Instrument_Device_Temporary(Index,:);

Instrument_ErrorCounts_Temporary=Instrument_ErrorCounts_Temporary(Index,:);
Instrument_IntTime_Temporary=Instrument_IntTime_Temporary(Index,:);
Instrument_Spectrum_Temporary=Instrument_Spectrum_Temporary(Index,:);
Instrument_Timestamp_Temporary=Instrument_Timestamp_Temporary(Index,:);
clear Index

%From all BACK data available select the one that is closest to the radiometer file
Diff=datenum(Instrument_Timestamp_Temporary)-datenum(Timestamp(1,:));
Index=ismember(Diff,max(Diff(Diff<0)));
if sum(Index)~=1

```

```

        errorlg(['No or wrong BACK data for radiometer ',Radiometer,' available!
Script aborted!'])
        return
    end
    BackSpectrum=Instrument_Spectrum_Temporary(Index,:);
    BackErrorCounts=Instrument_ErrorCounts_Temporary(Index,:);
    BackID=Instrument_DataID_Temporary(Index,:);
    Back_Timestamp=datestr(Instrument_Timestamp_Temporary(Index,:), 'yyyy-mm-
dd HH:MM:SS');
    clear Index Diff Instrument_DataID_Temporary
Instrument_DataType_Temporary...
        Instrument_Device_Temporary Instrument_ErrorCounts_Temporary...
        Instrument_IntTime_Temporary Instrument_Spectrum_Temporary...
        Instrument_Timestamp_Temporary

%% Get the CAL data for the radiometer

%By data type and device type
Instrument_DataID_Temporary=Instrument_DataID;
Instrument_DataType_Temporary=Instrument_DataType;
Instrument_Device_Temporary=Instrument_Device;
Instrument_ErrorCounts_Temporary=Instrument_ErrorCounts;
Instrument_IntTime_Temporary=Instrument_IntTime;
Instrument_Spectrum_Temporary=Instrument_Spectrum;
Instrument_Timestamp_Temporary=Instrument_Timestamp;

Index=ismember(Instrument_DataType_Temporary,'CAL')&ismember(Instrument_
Device_Temporary,Radiometer);
    Instrument_DataID_Temporary=Instrument_DataID_Temporary(Index,:);
    Instrument_DataType_Temporary=Instrument_DataType_Temporary(Index,:);
    Instrument_Device_Temporary=Instrument_Device_Temporary(Index,:);

Instrument_ErrorCounts_Temporary=Instrument_ErrorCounts_Temporary(Index,:);
    Instrument_IntTime_Temporary=Instrument_IntTime_Temporary(Index,:);
    Instrument_Spectrum_Temporary=Instrument_Spectrum_Temporary(Index,:);
    Instrument_Timestamp_Temporary=Instrument_Timestamp_Temporary(Index,:);
clear Index

%From all CAL data available select the one that is closest to the radiometer file
Diff=datenum(Instrument_Timestamp_Temporary)-datenum(Timestamp(1,:));
Index=ismember(Diff,max(Diff(Diff<0)));
if sum(Index)~=1

```

```

        errordlg(['No or wrong CAL data for radiometer ',Radiometer,' available! Script
aborted!'])
        return
    end
    CalSpectrum=Instrument_Spectrum_Temporary(Index,:);
    CalErrorCounts=Instrument_ErrorCounts_Temporary(Index,:);
    CalID=Instrument_DataID_Temporary(Index,:);
    Cal_Timestamp=datestr(Instrument_Timestamp_Temporary(Index,:), 'yyyy-mm-
dd HH:MM:SS');
    clear Index Diff Instrument_DataID_Temporary
Instrument_DataType_Temporary...
        Instrument_Device_Temporary Instrument_ErrorCounts_Temporary...
        Instrument_IntTime_Temporary Instrument_Spectrum_Temporary...
        Instrument_Timestamp_Temporary

%% Get the INI data for the radiometer

%By device type
IniFilesContent_Temporary=IniFilesContent;
IniFileList_Temporary=IniFileList;
Index=ismember(IniFilesContent_Temporary(:,1),Radiometer);
IniFilesContent_Temporary=IniFilesContent_Temporary(Index,:);
IniFileList_Temporary=IniFileList_Temporary(Index,:);

%By timestamp
Diff=datetime(IniFilesContent_Temporary(:,8), 'yyyy-mm-dd HH:MM:SS')-
datetime(Timestamp(1,:));
Index=ismember(Diff,max(Diff(Diff<0)));
if sum(Index)~=1
    errordlg(['No or wrong INI data for radiometer ',Radiometer,' available! Script
aborted!'])
    return
end
IniData=IniFilesContent_Temporary(Index,:);
IniFileName=IniFileList_Temporary(Index,:);
clear Diff Index IniFilesContent_Temporary IniFileList_Temporary

%% Converting pixels into wavelengths

Wavelengths=repmat(IniData{2},size(Instrument_Pixel));
Wavelengths=Wavelengths+(Instrument_Pixel+1).*IniData{3};
Wavelengths=Wavelengths+((Instrument_Pixel+1).^2).*IniData{4};
Wavelengths=Wavelengths+((Instrument_Pixel+1).^3).*IniData{5};
Wavelengths=[Instrument_Pixel(:,1) Wavelengths(2:end)];

```

```

%% Calibration

Spectra_Cal=Spectra./65535;

Background= repmat(BackSpectrum,size(Spectra_Cal,1),1)+repmat(IntTime,size(BackSpectrum))./8192.*repmat(BackErrorCounts,size(Spectra_Cal,1),1);
Spectra_Cal=Spectra_Cal-Background;

Offset=mean(Spectra_Cal(:,Instrument_Pixel(Instrument_Pixel==IniData{6}+1):Instrument_Pixel(Instrument_Pixel==IniData{7}+1)),2,'omitnan');
Spectra_Cal=Spectra_Cal-repmat(Offset,1,size(Spectra_Cal,2));
Spectra_Cal=Spectra_Cal.*8192./repmat(IntTime,1,size(Spectra_Cal,2));
Spectra_Cal=Spectra_Cal./repmat(CalSpectrum,size(Spectra_Cal,1),1);
Spectra_Cal=[Spectra(:,1) Spectra_Cal(:,2:end)];
Spectra_Cal(:,Instrument_Pixel(Instrument_Pixel==IniData{6}):end)=NaN;
clear Background Offset Index_Device Index_Ini

%% Replacing "inf" and "-inf" values by NaN

Index=isinf(Spectra_Cal);
Spectra_Cal(Index)=NaN;
clear Index

%% Saving the data

%Going to or creating the folder where the CALIBRATED data will be saved
if exist(FolderOutName,'dir')==0
    mkdir(FolderOutName)
end

cd(FolderOutName)

%Changing the file name
SaveFileName=FileList{i};
SaveFileName=strrep(SaveFileName,'RAW','Calibrated');

%Supplementing the metadata
Metadata_Calibrated=Metadata;
if strcmp(Parameter,'(ES)')

Metadata_Calibrated(~cellfun(@isempty,strfind(Metadata_Calibrated,'Unit')))=='#Unit: mW m-2';
else

```

```

Metadata_Calibrated(~cellfun(@isempty,strfind(Metadata_Calibrated,'Unit')))=='#U
nit: mW m-2 sr-1';
end
Metadata_Calibrated=[Metadata_Calibrated;...
    {'#Instrument initialization file: ',IniFileName{:},'; ',IniData{8}}];...
    {'#c0: ',num2str(IniData{2})};...
    {'#c1: ',num2str(IniData{3})};...
    {'#c2: ',num2str(IniData{4})};...
    {'#c3: ',num2str(IniData{5})};...
    {'#DarkPixelStart: ',num2str(IniData{6})};...
    {'#DarkPixelStop: ',num2str(IniData{7})};...
    {'#'}];
Metadata_BackgroundSpectrum=['#Background spectrum:
',num2cell(BackSpectrum(2:end))];
Metadata_BackgroundErrorCounts=['#Background error counts:
',num2cell(BackErrorCounts(2:end))];
Metadata_CalibrationSpectrum=['#Calibration spectrum:
',num2cell(CalSpectrum(2:end))];
Metadata_CalibrationErrorCounts=['#Calibration error counts:
',num2cell(CalErrorCounts(2:end))];

%Creating the data header
Header={'Year'} {'Month'} {'Day'} {'Hour'} {'Minute'} {'Second'}
num2cell(Wavelengths)];

%Creating the file content
Content=[Timestamp Spectra_Cal];

%Writing the file
fid=fopen(SaveFileName,'w');
for j=1:size(Metadata_Calibrated,1)
    fprintf(fid,'%s\n',Metadata_Calibrated{j});
end
clear j
fprintf(fid,'%s\n',['#Background file: ',BackID{:},'; ',Back_Timestamp]);
fprintf(fid,['%s',repmat('%f ',1,size(Metadata_BackgroundSpectrum,2)-
1),'\n'],Metadata_BackgroundSpectrum{:});
fprintf(fid,['%s',repmat('%f ',1,size(Metadata_BackgroundErrorCounts,2)-
1),'\n'],Metadata_BackgroundErrorCounts{:});
fprintf(fid,'%s\n','#');
fprintf(fid,'%s\n',['#Calibration file: ',CalID{:},'; ',Cal_Timestamp]);
fprintf(fid,['%s',repmat('%f ',1,size(Metadata_CalibrationSpectrum,2)-
1),'\n'],Metadata_CalibrationSpectrum{:});

```



```

    fprintf(fid,['%s',repmat('%f ',1,size(Metadata_CalibrationErrorCounts,2)-
1),'\n'],Metadata_CalibrationErrorCounts{:});
    fprintf(fid,'%s\n','#');

fprintf(fid,['%s\t%s\t%s\t%s\t%s\t%s',repmat('\t%.0f',1,size(Wavelengths,2)),'\n'],Header{1,:});
    for j=1:size(Content,1)

fprintf(fid,['%.0f\t%.0f\t%.0f\t%.0f\t%.0f\t%.0f',repmat('\t%f',1,size(Spectra_Cal,2))
,'\n'],Content(j,:));
    end
    clear j
    fclose(fid);
    clear Metadata_Calibrated Metadata_BackgroundSpectrum...
        Metadata_BackgroundErrorCounts Metadata_CalibrationSpectrum...
        Metadata_CalibrationErrorCounts

    cd(BasicPath)

    FilesToCalibrate=FilesToCalibrate-1;
    display(FilesToCalibrate)
end

```

STEP 3

%Script for creating working data from the calibrated radiometer data

```
clc
clear
BasicPath=pwd;
addpath(genpath([BasicPath,'\RequiredFiles']))

%% Parameters

%Full path of the folder that contains the calibrated files
FolderInName='D:\TRIOS\Celticexplorer_Radiometer\CalibratedFiles';

%Full path of the folder that will contain the working data output files (will be
created)
FolderOutName='D:\TRIOS\Celticexplorer_Radiometer\WorkingFiles';

%Wavelength range and resolution for the working files
Wavelength_Min=320;
Wavelength_Max=950;
Resolution=2;

%Threshold for outlier spectra (Spectra containing lower values will be omitted)
Outlier=-1;

%%%%%%%%%%%%%%%%%%%%%%%%%%%%%%%%%%%%%%%%%%%%%%%%%%%%%%%%%%%%%%%%%%%%%%%%
%%%%%%%%

%% Creating list of all *.dat-files in folder

cd(FolderInName)

Content=dir;
Folders=[Content.isdir];
FileList={Content(~Folders).name}';
Index=false(size(FileList));
for i=1:length(FileList)
    if ~isempty(strfind(FileList{i},'.dat'))
        Index(i)=true;
    end
end
FileList=FileList(Index);
clear i Index Content Folders
```

```

cd(BasicPath)

%% Create working data

FilesToProcess=size(FileList,1);
for i=1:size(FileList,1)

    cd(FolderInName)

    %Get the metadata
    [Metadata,~]=hdrload(FileList{i});
    Metadata=cellstr(Metadata);
    Metadata=Metadata(1:end-1,:);

    %Get the header
    fid=fopen(FileList{i},'r');
    Wavelengths=textscan(fid,[repmat('%s', 1, 3000) '%*[\n]'],1, 'delimiter',
'\t','CommentStyle','#', 'collectoutput', true);
    Wavelengths=[Wavelengths{:}];
    fclose(fid);
    clear fid ans

    %Get the data
    fid=fopen(FileList{i},'r');
    Data=textscan(fid,[repmat('%f', 1, 3000) '%*[\n]'], 'delimiter',
'\t','HeaderLines',size(Metadata,1)+1, 'collectoutput', true);
    Data=[Data{:}];
    fclose(fid);
    clear fid ans

    %Delete empty cells
    Index=cellfun(@isempty,Wavelengths);
    Wavelengths(:,Index)=[];
    Data(:,Index)=[];
    clear Index

    %Convert the wavelengths into numerical data
    Wavelengths=cellfun(@str2double,Wavelengths);

    %Refine the wavelengths and divide data into timestamps and real data
    Index=isnan(Wavelengths);
    Wavelengths(:,Index)=[];
    Wavelengths=Wavelengths(:,2:end);
    Timestamp=Data(:,Index);

```

```

Spectra=Data(:,~Index);
Spectra=Spectra(:,2:end);
clear Data Index

%Deletion of outlier spectra
Index=logical(sum(Spectra<=Outlier,2));
Spectra(Index,:)=[];
Timestamp(Index,:)=[];

%In case all data has been deleted, a dummy spectrum is created
if isempty(Spectra)
    Spectra=NaN(size(Wavelengths));
end

%Interpolate the spectra on the desired range and resolution
Wavelengths_interpol=Wavelength_Min:Resolution:Wavelength_Max;
if size(Spectra,1)==1
    Spectra=interp1(Wavelengths,Spectra,Wavelengths_interpol,'linear');
else

Spectra=transpose(interp1(Wavelengths,transpose(Spectra),Wavelengths_interpol,'
linear'));
end
Wavelengths=Wavelengths_interpol;
clear Wavelengths_interpol

cd(BasicPath)

%% Save the data

%Going to or creating the folder where the WORKING data will be saved
if exist(FolderOutName,'dir')==0
    mkdir(FolderOutName)
end

cd(FolderOutName)

%Changing the file name
SaveFileName=FileList{i};
SaveFileName=strrep(SaveFileName,'Calibrated','Working');

%Creating the data header
Header={['Year'} {'Month'} {'Day'} {'Hour'} {'Minute'} {'Second'}
num2cell(Wavelengths)];

```

```

%Creating the file content
Content=[Timestamp Spectra];

%Writing the file
fid=fopen(SaveFileName,'w');
for j=1:size(Metadata,1)
    fprintf(fid,'%s\n',Metadata{j});
end
clear j

fprintf(fid,['%s\t%s\t%s\t%s\t%s\t%s', repmat('\t%.0f',1,size(Wavelengths,2)),'\n'],Header{1,:});
for j=1:size(Content,1)

fprintf(fid,['%.0f\t%.0f\t%.0f\t%.0f\t%.0f\t%.0f', repmat('\t%f',1,size(Spectra,2)),'\n'],Content{j,:});
end
clear j
fclose(fid);

cd(BasicPath)

FilesToProcess=FilesToProcess-1;
display(FilesToProcess)
end

```

STEP 4

%Script for calculation of Rrs spectra from Ramses radiometer data

clc

clear

BasicPath=pwd;

addpath(genpath([BasicPath,'\RequiredFiles']))

%% Parameters

%Full path of the folder that contains the radiometer working files

FolderInName='D:\TRIOS\Celticexplorer_Radiometer\WorkingFiles_correctedEs';

%Full path of the folder that will contain the working data output files (will be created)

FolderOutName='D:\TRIOS\Celticexplorer_Radiometer\RemoteSensingReflectance'

;

%Threshold for the minimum light condition flag (at Es480)

Threshold_Es=10;

%Ranges for the meteorological condition flag (Ratio Es940/Es370)

Threshold_Meteo_Min=0.2;

Threshold_Meteo_Max=0.25;

%Thresholds for the sunglint flags

Threshold_Lw=2; %mean values from 700-900 nm

Threshold_Rrs=0.01; %min value from 700-900 nm

%Reflectivity of water used in Lw calculation

rho=0.0265;

%%%

%%%

% *****FROM HERE, ONLY MAKE CHANGES IF YOU KNOW WHAT YOU ARE
DOING!***** %

%%%

%%%

%% Creating list of all *.dat-files in folder

cd(FolderInName)

Content=dir;

```

Folders=[Content.isdir];
FileList={Content(~Folders).name}';
Index=false(size(FileList));
for i=1:length(FileList)
    if ~isempty(strfind(FileList{i},'.dat'))
        Index(i)=true;
    end
end
FileList=FileList(Index);
clear i Index Content Folders

%% Creating list of available days

DayList=cell(size(FileList));
for i=1:size(FileList,1)
    CurrentDay=strsplit(FileList{i},'_');
    DayList(i)=CurrentDay(1);
end
DayList=unique(DayList,'stable');
clear i CurrentDay

%% Omitting days where not all radiometers were available

%Creating a temporary file list
FileList_Temporary=cell(size(FileList));
for i=1:size(FileList,1)
    FileList_Temporary{i}=strsplit(FileList{i},'_');
end
clear i
FileList_Temporary=vertcat(FileList_Temporary{:});

OmittedFiles=false(size(FileList));

for i=1:size(DayList,1)
    Index=ismember(FileList_Temporary(:,1),DayList(i));
    Parameters=FileList_Temporary(Index,2);
    if sum(ismember(Parameters,['Es' {'Lsky'} {'Lsfc'}]))<3
        OmittedFiles(Index,:)=true;
    end
end
FileList(OmittedFiles)=[];
clear i Index Parameters FileList_Temporary OmittedFiles DayList

cd(BasicPath)

```

```

%% Creating new list of available days

DayList=cell(size(FileList));
for i=1:size(FileList,1)
    CurrentDay=strsplit(FileList{i},'_');
    DayList(i)=CurrentDay(1);
end
DayList=unique(DayList,'stable');
clear i CurrentDay

%% Creating a new temporary file list
FileList_Temporary=cell(size(FileList));
for j=1:size(FileList,1)
    FileList_Temporary{j}=strsplit(FileList{j},'_');
end
clear j
FileList_Temporary=vertcat(FileList_Temporary{:});

%% Process each day

DaysToProcess=size(DayList,1);
for i=1:size(DayList,1)

    cd(FolderInName)

    %% Opening the irradiance (ES) files of the specific day

    Index=ismember(FileList_Temporary(:,1),DayList(i)) &
ismember(FileList_Temporary(:,2),{'Es'});

    %Get the metadata
    [Metadata_Es,~]=hdrload(FileList{Index});
    Metadata_Es=cellstr(Metadata_Es);
    Metadata_Es=Metadata_Es(1:end-1,:);

    %Get the header
    fid=fopen(FileList{Index},'r');
    Wavelengths_Es=textscan(fid,[repmat('%s', 1, 3000) '%*[\n]'],1, 'delimiter',
'\t','CommentStyle','#', 'collectoutput', true);
    Wavelengths_Es=[Wavelengths_Es{:}];
    fclose(fid);
    clear fid ans

```



```

%Get the data
fid=fopen(FileList{Index},'r');
Data_Es=textscan(fid,[repmat('%f', 1, 3000) '%*[\n]'], 'delimiter',
\t','HeaderLines',size(Metadata_Es,1)+1, 'collectoutput', true);
Data_Es=[Data_Es{:}];
fclose(fid);
clear fid ans Index

%Delete empty cells
Index=cellfun(@isempty,Wavelengths_Es);
Wavelengths_Es(:,Index)=[];
Data_Es(:,Index)=[];
clear Index

%Convert the wavelengths into numerical data
Wavelengths_Es=cellfun(@str2double,Wavelengths_Es);

%Refine the wavelengths and divide data into timestamps and real data
Index=isnan(Wavelengths_Es);
Wavelengths_Es(:,Index)=[];
Timestamp_Es=Data_Es(:,Index);
Spectra_Es=Data_Es(:,~Index);
clear Data_Es Index

%% Opening the upward looking irradiance (Lsky) files of the specific day

Index=ismember(FileList_Temporary(:,1),DayList(i)) &
ismember(FileList_Temporary(:,2),{'Lsky'});

%Get the metadata
[Metadata_Lsky,~]=hdrload(FileList{Index});
Metadata_Lsky=cellstr(Metadata_Lsky);
Metadata_Lsky=Metadata_Lsky(1:end-1,:);

%Get the header
fid=fopen(FileList{Index},'r');
Wavelengths_Lsky=textscan(fid,[repmat('%s', 1, 3000) '%*[\n]'],1, 'delimiter',
\t','CommentStyle','#', 'collectoutput', true);
Wavelengths_Lsky=[Wavelengths_Lsky{:}];
fclose(fid);
clear fid ans

%Get the data
fid=fopen(FileList{Index},'r');

```

```

    Data_Lsky=textscan(fid,[repmat('%f', 1, 3000) '%*[\n]'], 'delimiter',
'\t','HeaderLines',size(Metadata_Lsky,1)+1, 'collectoutput', true);
    Data_Lsky=[Data_Lsky{:}];
    fclose(fid);
    clear fid ans Index

%Delete empty cells
Index=cellfun(@isempty,Wavelengths_Lsky);
Wavelengths_Lsky(:,Index)=[];
Data_Lsky(:,Index)=[];
clear Index

%Convert the wavelengths into numerical data
Wavelengths_Lsky=cellfun(@str2double,Wavelengths_Lsky);

%Refine the wavelengths and divide data into timestamps and real data
Index=isnan(Wavelengths_Lsky);
Wavelengths_Lsky(:,Index)=[];
Timestamp_Lsky=Data_Lsky(:,Index);
Spectra_Lsky=Data_Lsky(:,~Index);
clear Data_Lsky Index

%% Opening the downward looking radiance (Lsfc) files of the specific day

Index=ismember(FileList_Temporary(:,1),DayList(i)) &
ismember(FileList_Temporary(:,2),{'Lsfc'});

%Get the metadata
[Metadata_Lsfc,~]=hdrload(FileList{Index});
Metadata_Lsfc=cellstr(Metadata_Lsfc);
Metadata_Lsfc=Metadata_Lsfc(1:end-1,:);

%Get the header
fid=fopen(FileList{Index},'r');
Wavelengths_Lsfc=textscan(fid,[repmat('%s', 1, 3000) '%*[\n]'],1, 'delimiter',
'\t','CommentStyle','#', 'collectoutput', true);
Wavelengths_Lsfc=[Wavelengths_Lsfc{:}];
fclose(fid);
clear fid ans

%Get the data
fid=fopen(FileList{Index},'r');
Data_Lsfc=textscan(fid,[repmat('%f', 1, 3000) '%*[\n]'], 'delimiter',
'\t','HeaderLines',size(Metadata_Lsfc,1)+1, 'collectoutput', true);

```

```

Data_Lsfc=[Data_Lsfc{:}];
fclose(fid);
clear fid ans Index

%Delete empty cells
Index=cellfun(@isempty,Wavelengths_Lsfc);
Wavelengths_Lsfc(:,Index)=[];
Data_Lsfc(:,Index)=[];
clear Index

%Convert the wavelengths into numerical data
Wavelengths_Lsfc=cellfun(@str2double,Wavelengths_Lsfc);

%Refine the wavelengths and divide data into timestamps and real data
Index=isnan(Wavelengths_Lsfc);
Wavelengths_Lsfc(:,Index)=[];
Timestamp_Lsfc=Data_Lsfc(:,Index);
Spectra_Lsfc=Data_Lsfc(:,~Index);
clear Data_Lsfc Index

%% Checking data availability

Available_Es=true;
Available_Lsky=true;
Available_Lsfc=true;

if isequal(isnan(Spectra_Es),isnan(NaN(1,size(Spectra_Es,2))))
    Available_Es=false;
end

if isequal(isnan(Spectra_Lsky),isnan(NaN(1,size(Spectra_Lsky,2))))
    Available_Lsky=false;
end

if isequal(isnan(Spectra_Lsfc),isnan(NaN(1,size(Spectra_Lsfc,2))))
    Available_Lsfc=false;
end

if Available_Es==true && Available_Lsky==true && Available_Lsfc==true

    %% Assigning the closest measurements of Es and Lsky to the Lsfc
measurements
    %The difference in time has to be smaller than the measurement interval of
Lsfc

```

```

%Conversion of timestamps
Timestamp_Es=datenum(Timestamp_Es);
Timestamp_Lsky=datenum(Timestamp_Lsky);
Timestamp_Lsfc=datenum(Timestamp_Lsfc);

%Calculate the measurement interval of Lsfc
if size(Timestamp_Lsfc,1)==1
    Interval_Lsfc=1;
else
    Interval_Lsfc=abs(Timestamp_Lsfc(1)-Timestamp_Lsfc(2));
end

%Creating new Es and Lsky variables
Timestamp_Es_New=NaN(size(Timestamp_Lsfc,1),1);
Timestamp_Lsky_New=NaN(size(Timestamp_Lsfc,1),1);
Spectra_Es_New=NaN(size(Spectra_Lsfc));
Spectra_Lsky_New=NaN(size(Spectra_Lsfc));

%Assigning Es
for j=1:size(Timestamp_Lsfc,1)
    Diff=Timestamp_Es-Timestamp_Lsfc(j);
    Index=find(Diff<=0,1,'last');
    Value=abs(Diff(Index));
    if Value<Interval_Lsfc
        Timestamp_Es_New(j,:)=Timestamp_Es(Index,:);
        Spectra_Es_New(j,:)=Spectra_Es(Index,:);
    end
end
clear Diff Value Index j

%Assigning Lsky
for j=1:size(Timestamp_Lsfc,1)
    Diff=Timestamp_Lsky-Timestamp_Lsfc(j);
    Index=find(Diff<=0,1,'last');
    Value=abs(Diff(Index));
    if Value<Interval_Lsfc
        Timestamp_Lsky_New(j,:)=Timestamp_Lsky(Index,:);
        Spectra_Lsky_New(j,:)=Spectra_Lsky(Index,:);
    end
end
clear Diff Value Index j Interval

%Replacing the old variables by the new ones

```

```

Timestamp_Es=Timestamp_Es_New;
Timestamp_Lsky=Timestamp_Lsky_New;
Spectra_Es=Spectra_Es_New;
Spectra_Lsky=Spectra_Lsky_New;
clear Timestamp_Es_New Timestamp_Lsky_New...
    Spectra_Es_New Spectra_Lsky_New

%Deleting all rows where in one measurement is a NaN
Index=logical(sum(isnan([Timestamp_Es Timestamp_Lsfc
Timestamp_Lsky]),2));
Timestamp_Es(Index,:)=[];
Timestamp_Lsky(Index,:)=[];
Timestamp_Lsfc(Index,:)=[];
Spectra_Es(Index,:)=[];
Spectra_Lsky(Index,:)=[];
Spectra_Lsfc(Index,:)=[];
clear Index

%Conversion of timestamps back to vectors
Timestamp_Es=datevec(Timestamp_Es);
Timestamp_Lsky=datevec(Timestamp_Lsky);
Timestamp_Lsfc=datevec(Timestamp_Lsfc);

%Taking the Lsfc timestamp and wavelengths as the final ones
Timestamp=Timestamp_Lsfc;
Wavelengths=Wavelengths_Lsfc;
clear Wavelengths_Es Wavelengths_Lsfc Wavelengths_Lsky...
    Timestamp_Es Timestamp_Lsfc Timestamp_Lsky
end

%% Check again data availability

if isempty(Spectra_Es)
    Available_Es=false;
end

if isempty(Spectra_Lsky)
    Available_Lsky=false;
end

if isempty(Spectra_Lsfc)
    Available_Lsfc=false;
end

```

```

if Available_Es==true && Available_Lsky==true && Available_Lsfc==true

%% Calculate Rrs

%To avoid divisions by zero, replace all zeros by NaN
Spectra_Es(Spectra_Es==0)=NaN;
clear Index

%Lw
Lw=Spectra_Lsfc-(rho.*Spectra_Lsky);

%Remote sensing reflectance Rrs
Rrs=Lw./Spectra_Es;

%Interpolate the NaN values in the corrected Rrs spectra
for j=1:size(Rrs,1)
    Index=isnan(Rrs(j,:));
    if Index>0
        Rrs(j,:)=interp1(Wavelengths(~Index),Rrs(j,~Index),Wavelengths);
    end
end
clear j Index

%Smoothing the spectra by interpolation with loess to reduce noise
Rrs=loess_matrix(Wavelengths,Rrs,Wavelengths,0.03);

%Correct the spectra for reflectance in the infrared region
Rrs_min=min(Rrs(:,Wavelengths>=700&Wavelengths<=900),[],2,'omitnan');
Rrs_corr=Rrs-repmat(Rrs_min,1,size(Rrs,2));

%% Creating flags

%Creating minimum light flag based on intensity of Es at 480 nm
Flag_Light=ones(size(Rrs,1),1);
Index=Spectra_Es(:,Wavelengths==480)<Threshold_Es;
Flag_Light(Index)=0;
clear Index

%Create light quality flag based on the shape of Es
Flag_Daylight=ones(size(Rrs,1),1);
Index=(Spectra_Es(:,Wavelengths==480)./Spectra_Es(:,Wavelengths==680))<1;
Flag_Daylight(Index)=0;
clear Index

```

```

%Create flag for meterological conditions based on Es
Flag_Weather=ones(size(Rrs,1),1); %Weather conditions ok

Index_1=(Spectra_Es(:,Wavelengths==940)./Spectra_Es(:,Wavelengths==370))<=
Threshold_Meteo_Min;
Index_2=(Spectra_Es(:,Wavelengths==940)./Spectra_Es(:,Wavelengths==370))>
Threshold_Meteo_Min &...
(Spectra_Es(:,Wavelengths==940)./Spectra_Es(:,Wavelengths==370))<
Threshold_Meteo_Max;
Flag_Weather(Index_1)=2; %Precipitation
Flag_Weather(Index_2)=3; %High humidity
clear Index_1 Index_2

%Create sunglint flag based on Lw (Garaba et al. (2012): Sunglint detection for
unmanned and automated platforms)
Flag_Glint_Lw=ones(size(Rrs,1),1);
Index=mean(Lw(:,ismember(Wavelengths,700:1:900)),2)>Threshold_Lw;
Flag_Glint_Lw(Index,:)=0;
clear Index

%Create sunglint flag based on Rrs (Garaba et al. (2012): Sunglint detection for
unmanned and automated platforms)
Flag_Glint_Rrs=ones(size(Rrs,1),1);
Index=Rrs_min>Threshold_Rrs;
Flag_Glint_Rrs(Index)=0;
clear Index

%% Creating new metadata

Radiometer=[strsplit(Metadata_Es{1});strsplit(Metadata_Lsky{1});strsplit(Metadata
_Lsfc{1})];

Index_Written=find(ismember(Metadata_Lsfc,'#'),2,'first');

Metadata={['#Parameter: Rrs'];...
['#Irradiance sensor (Es): ',Radiometer{1,2}];...
['#Upward radiance sensor (Lsky): ',Radiometer{2,2}];...
['#Downward eadiance sensor (Lsfc): ',Radiometer{3,2}];...
['#Unit: sr-1'];...
['#Rrs is corrected for sunglint by subtracting the minimum at 700-900
nm.'];...

```

```

        {'#However, the sunglint flags were determined by the original
spectrum.'};...
        {'#To get the original spectrum, just add the minRrs value to the
spectrum.'};...
        Metadata_Lsfc(Index_Written(1):Index_Written(2),:);...
        {'#Correction procedures: Irradiance (Es) has been corrected for drift
(Period 1: 2004-2012; Period 2: 2013-2016)'};...
        {'#'};...
        {'[#Sea surface reflectivity (rho): ',num2str(rho)]};...
        {'#'};...
        {'#Flagging for light availability'};...
        {'[#Threshold [mW m-2 s-1]: ',num2str(Threshold_Es)]};...
        {'#1 = Sufficient light'};...
        {'#0 = Light too low'};...
        {'#'};...
        {'#Flagging for light quality'};...
        {'#1 = Daylight conditions'};...
        {'#0 = Twilight conditions'};...
        {'#'};...
        {'#Flagging for weather state'};...
        {'[#Threshold min/max: ',num2str(Threshold_Meteo_Min),' /
',num2str(Threshold_Meteo_Max)]};...
        {'#1 = Weather ok'};...
        {'#2 = Precipitation'};...
        {'#3 = Humidity'};...
        {'#'};...
        {'#Flagging for sunglint (based on water leaving radiance Lw)'};...
        {'[#Threshold [mW m-2 s-1]: ',num2str(Threshold_Lw)]};...
        {'#1 = Mean value of 700-900 nm is below the threshold (no sunglint)'};...
        {'#0 = Mean value of 700-900 nm is above the threshold (sunglint)'};...
        {'#'};...
        {'#Flagging for sunglint (based on remote sensing reflectance Rrs)'};...
        {'[#Threshold [sr-1]: ',num2str(Threshold_Rrs)]};...
        {'#1 = Minimum value of 700-900 nm is below the threshold (no
sunglint)'};...
        {'#0 = Minimum value of 700-900 nm is above the threshold (sunglint)'};...
        {'#'};
        clear Radiometer Index_Written

%% Saving the data

%Going to or creating the folder where the Rrs data will be saved
if exist(FolderOutName,'dir')==0
    mkdir(FolderOutName)

```



```

end

cd(FolderOutName)

%Creating the file name
SaveFileName=[DayList{i},'_Rrs.dat'];

%Creating the data header
Header=[{'Year'} {'Month'} {'Day'} {'Hour'} {'Minute'} {'Second'}...
        {'Flag Light Availability'} {'Flag Light Quality'} {'Flag Weather'} {'Flag
Sunlint (Lw)'} {'Flag Sunlint (Rrs)'}...
        {'minRrs'} num2cell(Wavelengths)];

%Creating the file content
Content=[Timestamp Flag_Light Flag_Daylight Flag_Weather Flag_Glint_Lw
Flag_Glint_Rrs Rrs_min Rrs_corr];

%Writing the file
fid=fopen(SaveFileName,'w');
for j=1:size(Metadata,1)
    fprintf(fid,'%s\n',Metadata{j});
end
clear j

fprintf(fid,['%s',repmat('\t%s',1,11),repmat('\t%.0f',1,size(Wavelengths,2)),'\n'],Hea
der{1,:});
for j=1:size(Content,1)

fprintf(fid,['%.0f',repmat('\t%.0f',1,10),repmat('\t%f',1,size(Rrs_corr,2)+1),'\n'],Cont
ent(j,:));
end
clear j
fclose(fid);

cd(BasicPath)

end
clear Available_Es Available_Lsky Available_Lsfc

DaysToProcess=DaysToProcess-1;
display(DaysToProcess)
end

```


STEP 5

%Script for calculating PAR from "Working" radiometer data (Es)

```
clc
clear
BasicPath=pwd;
addpath(genpath([pwd,'\RequiredFiles']))
%% Parameters

%Full path of the folder that contains WORKING files
FolderInName='D:\TRIOS\Celticexplorer_Radiometer\WorkingFiles_correctedEs';

%Full path of the folder that will contain the output files (will be created)
FolderOutName='D:\TRIOS\Celticexplorer_Radiometer\PAR\';

%Threshold for minimum light condition (in mW at 480 nm)
Threshold_Es=10;

%%%%%%%%%%%%%%%%%%%%%%%%%%%%%%%%%%%%%%%%%%%%%%%%%%%%%%%%%%%%%%%%%%%%%%%%
%%%%%%%%

%% Creating list of all irradiance (Es) *.dat-files in folder

cd(FolderInName)

Content=dir;
Folders=[Content.isdir];
FileList={Content(~Folders).name}';
Index=false(size(FileList));
for i=1:length(FileList)
    if ~isempty(strfind(FileList{i},'.dat'))
        Index(i)=true;
    end
end
FileList=FileList(Index);
clear i Index Content Folders

FileList_Temporary=cell(size(FileList,1),3);
for i=1:size(FileList,1)
    FileList_Temporary(i,:)=strsplit(FileList{i},'_');
end
clear i
```

```

Index=ismember(FileList_Temporary(:,2),{'Es'});
FileList=FileList(Index,:);
clear Index FileList_Temporary

cd(BasicPath)

%% Processing the data

FilesToProcess=size(FileList,1);
for i=1:size(FileList,1)

    cd(FolderInName)

    %% Get the metadata
    [Metadata,~]=hdrload(FileList{i});
    Metadata=cellstr(Metadata);
    Metadata=Metadata(1:end-1,:);

    %% Get the header
    fid=fopen(FileList{i},'r');
    Wavelengths=textscan(fid,[repmat('%s', 1, 3000) '%*[\n]'],1, 'delimiter',
'\t','CommentStyle','#', 'collectoutput', true);
    Wavelengths=[Wavelengths{:}];
    fclose(fid);
    clear fid ans

    %% Get the data
    fid=fopen(FileList{i},'r');
    Data=textscan(fid,[repmat('%f', 1, 3000) '%*[\n]'], 'delimiter',
'\t','HeaderLines',size(Metadata,1)+1, 'collectoutput', true);
    Data=[Data{:}];
    fclose(fid);
    clear fid ans

    %% Delete empty cells
    Index=cellfun(@isempty,Wavelengths);
    Wavelengths(:,Index)=[];
    Data(:,Index)=[];
    clear Index

    %% Convert the wavelengths into numerical data
    Wavelengths=cellfun(@str2double,Wavelengths);

    %% Refine the wavelengths and divide data into timestamps and real data

```

```

Index=isnan(Wavelengths);
Wavelengths(:,Index)=[];
Timestamp=Data(:,Index);
Spectra=Data(:,~Index);
clear Data Index

%% Calculating Photon Flux (PAR & Total)
Index_PAR=ismember(Wavelengths,400:1:700);
E_photon=(6.63e-34.*2.998e8)./(Wavelengths./1000000000);%Energy of a single
photon of the respective wavelength
E_total=Spectra./1000;%Conversion mW in W
N_photons=E_total./repmat(E_photon,size(E_total,1),1);%Calculation of the
number of photons
uMol_photons=(N_photons./6.022e23).*1000000;%Convert the number of
photons in  $\mu\text{mol}$ 
PhotonFlux_PAR=trapz(uMol_photons(:,Index_PAR),2);%Integrate over the PAR-
spectrum (400-700 nm)
PhotonFlux_Total=trapz(uMol_photons,2);%Integrate over the whole available
spectrum
clear E_photon E_total uMol_photons Index_PAR N_photons

%% Calculating Irradiance in  $\text{W m}^{-2}$  (PAR & Total)
Index_PAR=ismember(Wavelengths,400:1:700);
Irradiance_PAR=trapz(Spectra(:,Index_PAR)./1000,2);
Irradiance_Total=trapz(Spectra./1000,2);
clear Index_PAR

%% Setting all values below zero to zero
PhotonFlux_PAR(PhotonFlux_PAR<0)=0;
PhotonFlux_Total(PhotonFlux_Total<0)=0;
Irradiance_PAR(Irradiance_PAR<0)=0;
Irradiance_Total(Irradiance_Total<0)=0;

%% Saving the data

%Going to or creating the folder where the PAR data will be saved
if exist(FolderOutName,'dir')==0
    mkdir(FolderOutName)
end

cd(FolderOutName)

%Changing the file name
SaveFileName=FileList{i};

```

```

SaveFileName=strrep(SaveFileName,'Working','Irradiance_PhotonFlux');

%Complementing the metadata
Metadata_Temporary=[Metadata;...
    {'#'};...
    {'#Correction procedures:'};...
    {'#Irradiance spectra (Es) have been corrected for drift (Period 1:
2004-2012; Period 2: 2013-2016.}';...
    {'#Furthermore, all values for irradiance and photon flux below zero
have been set to zero.}';...
    {'#'};...
    {'#PAR: 400-700 nm'};...
    [{'#Total spectrum: ',num2str(min(Wavelengths)),'-
',num2str(max(Wavelengths)),' nm'}];...
    {'#'}];

%Creating the header
Header=[{'Year'} {'Month'} {'Day'} {'Hour'} {'Minute'} {'Second'}...
    {'Photon Flux (PAR) [ $\mu\text{mol photons m}^{-2}$ ]} {'Photon Flux (Total) [ $\mu\text{mol photons m}^{-2}$ ]}...
    {'Irradiance (PAR) [ $\text{W m}^{-2}$ ]} {'Irradiance (Total) [ $\text{W m}^{-2}$ ]}];

%Creating the file content
FileContent=[Timestamp PhotonFlux_PAR PhotonFlux_Total Irradiance_PAR
Irradiance_Total];

%Writing the file
fid=fopen(SaveFileName,'w');
for j=1:size(Metadata_Temporary,1)
    fprintf(fid,'%s\n',Metadata_Temporary{j});
end
clear j
fprintf(fid,['%s',repmat('\t%s',1,size(Header,2)-1),'\n'],Header{1,:});
for j=1:size(FileContent,1)
    fprintf(fid,['%.0f\t%.0f\t%.0f\t%.0f\t%.0f\t%.0f',repmat('\t%f',1,size(FileContent,2)-
6),'\n'],FileContent(j,:));
end
clear j
fclose(fid);

clear Metadata_Temporary

cd(BasicPath)

```

```
FilesToProcess=FilesToProcess-1;  
display(FilesToProcess)  
end
```

Appendix A2. Data Management Plan Checklist

Data Management Plan Checklist

Dataset Overview	
Process Flow Title	Trios Ramses Hyperspectral Radiometer on the Celtic Explorer
Dataset Description	Reflectance data collected from the Celtic Explorer sensors
Date of First Version	17/01/2020
Date of Second Version	03.03.2021

Data Collection
What data will you collect or create?
Remote sensing reflectance data is being automatically created using the 5 Trios Ramses sensors on the Celtic Explorer, connected to a PC in the dry lab on the Celtic Explorer.
How will the data be collected or created?
The data is created using 5 Trios Ramses hyperspectral sensors that measure light reflectance off the surface of the ocean. The sensors are mounted permanently on the side of the vessel on monkey island on the Explorer and the cables run from there to the dry lab. Raw data is being fed to a PC in the dry lab every 15 minutes during day light hours and stored on an external hard drive specifically for the reflectance data. The data is then removed post survey and a new database is set up for the next survey

Documentation and Metadata
What documentation and metadata will accompany the data?
Underway data is requested from the Marine institute after each survey to accompany the data to determine GPS locations. Each data point will have a data and time stamp associated with the measurements in order to determine place and time sample was recorded.

Ethics and Legal Compliance
How will you manage any ethical issues?
Not applicable
How will you manage copyright and Intellectual Property Rights (IPR) issues?
<p>Once operational Data will have an 'Open' classification.</p> <p>From grant aid agreement of Catherine Jordan's Cullen fellowship: The Grantee is required to take all necessary steps to:</p> <p>15.2.1 Preserve and protect such Intellectual Property Rights (IPR) including, where appropriate, by applying for patent registration; and</p> <p>15.2.2 Actively to exploit in a timely fashion any discoveries, inventions or processes resulting from the research, by means of commercial licensing arrangements and otherwise.</p> <p>15.2.3 Whenever possible, intellectual property shall be managed for the benefit of enterprise development in Ireland</p>

Storage and Backup
How will the data be stored and backed up during the research?
<p>The data is collected at the end of each survey by Catherine Jordan and stored on an external hard drive</p> <p>Request has been submitted to IT-Ops for 14GB annually</p>
How will you manage access and security?
<p>The data is part of a Cullen Fellowship PhD and access is only needed by Catherine Jordan currently but this will be readdressed once the PhD is coming to an end and the sensors are operational for the Marine Institute</p>

Selection and Preservation
Which data are of long term value and should be retained, shared, and/or preserved?
The raw data are of long term value and should be retained.
What is the long-term preservation plan for the dataset?
Currently the 4 years of the PhD, this will be updated

Data Sharing
How will you share the data?
Open access data
Are any restrictions on data sharing required?
Pre-operational - Currently the data will only be used for Catherine Jordan's PhD. Sharing the data would have to be discussed with the Catherine Jordan's supervisor's Peter Croot (NUIG) and Caroline Cusack (OSIS, MI) and Catherine Jordan.

Responsibilities and Resources
Who will be responsible for data management?
Catherine Jordan Cullen Fellow
What resources will you require to deliver your plan?
Disk storage is the primary resource requirement to cope with the expanding database over time. 14GB of annual storage has been requested from the Marine Institute

Appendix A3. Hyperspectral Radiometer Software Set Up

TriOS RAMSES MSDA_XE Software SOP

At the beginning of each survey a new database will be set up. Software to be set this prior to each survey:

How to set up a new database at the beginning of each survey

Store the empty database in a single folder on the hard drive/desktop

Store calibration files for each sensor in same folder

In MSDA_XE software click on database

Clicked on configuration

-Databases

-Create new database

Under Target

Path- clicked on folder with empty database

name- named it the survey eg: CE19009

Create new database

Restart software

Re add in calibration files for the sensors.

Open MSDA_XE software on the desktop

Device manager should be open with the sensors 'On-line' Sensors are called SAM_8504 SAM_8503, SAM_860D, SAM_86C2 and SAM_86C1

If they are not showing up click on one (eg SAM_8504) and click Scan

If the sensors are still not showing up click **Options**, **Port manager** and make sure the active COM port is selected)

Five boxes SAM_8504 and SAM_8503, SAM_860D, SAM_86C2 and SAM_86C1 should be open side by side (resize each window to fit them in onto the screen)

If the boxes are not open on the screen click on one sensor in device manager and click **Control** and repeat for 2nd, 3rd, 4th and 5th sensor (again, resize boxes if needed to fit across the screen)

Keep SAM_8504 and SAM_8503 SAM_860D SAM_86C2 and SAM_86C1 open side by side

In SAM_8504 check these options are selected or do the following if starting from scratch:

Comment box. To edit click the symbol. Comment should be the survey name eg: CE19009

Click OK

Click the arrow beside (More...)

In the General tab:

Measurement: Integration automatic

Storing: Boxes to be ticked- Database, File, Raw and Calibrated

Automatic Measurements: Click Configure: Click Interval and select 15 minutes (00:15:00), then click the box beside Restrict down the bottom and select the hours 07:00 and 21:00 then click OK

Select bursts of 10 (10 measurements will be taken by each sensor every 15 minutes)

Calibration Tabs: Check Calibration driver files are there, if not, they can be added in by clicking database- import files and select calibration files

Repeat same steps with SAM_8503

Repeat same steps with SAM_860 D

Repeat same steps with SAM_86C2 and SAM_86C1

Once ALL sensors have been set up have the 5 boxes (SAM_8504 SAM_8503 SAM_860D SAM_86C2 and SAM_86C1) open side by side.

Click Auto in each box one after the other, this will start the sensors taking measurements every 15 minutes

If you are unable to select Auto check the top right hand corner of that box and make sure the red circle is green by clicking on it once.

To check data is being collected check the database after 5 minutes by clicking Database- Data and you should see new measurements for that day (make sure each sensor is recording 10 measurements each, every 15 minutes)

Once Auto has been selected you can minimise the software and it can be left running in the background. Make sure it is minimised and not x'd out of.

Trouble shooting

- Cannot get the sensors to show up in Device Manager? Click Options, Port Manager, search through COM ports that are available and go back to device manager, click on SCAN and sensors should now show up, continue with searching through COM ports if the sensors don't show up.
- Software keeps crashing? A new database needs to be set up prior to each survey* as once the database goes past 1500MB it will start to crash and will be difficult taking data off post survey, therefore if the software is crashing, check the size of the database (DB- bottom left hand corner of screen, remove data and set up a new database).

***Before a new database is set up make sure ALL data is exported to another hard drive as it is difficult to recover once a new database has been set up.**

- Error message: **No reaction on measurement of device... after... sec**

Temporary communication problem with the device. No answer received, after command was sent by the computer.

If taking automatic measurements. Press AUTO on each of the sensor box (this will stop the sensors taking measurements).

Disconnect the cable of the sensor with the error from the IPS for around 10 seconds or all of them if unsure which sensor is which.

Reconnect the cable(s) and click SCAN on the device manager.

Click AUTO on all sensors which should start each sensor taking measurements again.

Still getting an error message? check the sensors are recording every 15 minutes, if anything less, it can overwhelm the software so this is why it is set to 15 minutes.

Connecting GPS to TRIOS Software:

The GPS output from the ship is normally 9600 baud, 8 bytes, 0, 1, Software Xon/Xoff

Make sure this is what the input to the TRIOS is by looking in Port Manager in MSDA_XE. Check also that you have the right com port.

To change the baudrate (or other settings), please do the following:

1. Close MSDA_XE
2. Go to the folder MSDA_XE on your computer (standard setting: C:\Users\Public\Documents\MSDA_XE\UserData\Ini Files) and open the .ini file.
3. Scroll down to ports, there you will see a list of ports
4. Change the baudrate of the port to be used accordingly
5. Save the .ini file
6. Open MSDA_XE again

You can also use a terminal program to check the output from the GPS feed:

MSDA_XE only interprets rows with \$GPGGA. Here is an example:

```
$GPGGA,hhmmss.ss,lll.ll,a,yyyy.yy,a,x,xx,x.x,x.x,M,x.x,M,x.x,xxxx*hh
```

hhmmss.ss = UTC of position

lll.ll = latitude of position

a = N or S

yyyy.yy = Longitude of position

a = E or W

x = GPS Quality indicator (0=no fix, 1=GPS fix, 2=Dif. GPS fix)

xx = number of satellites in use

x.x = horizontal dilution of precision

x.x = Antenna altitude above mean-sea-level

M = units of antenna altitude, meters

x.x = Geoidal separation

M = units of geoidal separation, meters

x.x = Age of Differential GPS data (seconds)

xxxx = Differential reference station ID

These rows should show up in your terminal program.

If data flow stops or fails to initiate, try switching off the active connection and then turn it on again within the programme as this often restarts it.

Appendix A4. Requirements and Acceptance Criteria

Requirements and Acceptance Criteria

Requirements for Cullen Project (Grant-aid Agreement No. CF/17/03/01)

WP3: Install and collect hyperspectral irradiance and radiance sensors on the Celtic Explorer or Celtic Voyager for the collection of *in situ* reflectance data.

Objectives: Obtain hyperspectral sea surface reflectance for the validation of satellite retrievals along the Irish west coast.

Task 3.1: Installation of the Trios RAMSES hyperspectral sensors on the Celtic Explorer or Celtic Voyager for long term determination of at sea reflectance data. Optimize the installation to minimize the impact of solar glint. Develop quality controls for processing the data impacted by solar glint, sunrise or sunset and rain events.

Deliverable 3.3: Database of values of the measured parameters obtained during the ship board expeditions

Requirements (why do we need this data)

Ocean colour satellite sensors provide measurements of spectral remote sensing reflectance (R_{rs}). Bio optical algorithms are applied to R_{rs} measurements to produce estimates of optical and geophysical quantities such as phytoplankton pigment concentration and spectral marine inherent optical properties (IOPs). Time series of remotely sensed IOPs provide long valuable data sets for studying long term changes in our ocean-ecosystems. IOPs, spectral absorption and scattering properties of seawater and its particulate and dissolved constituents can be used to interpret the contents of the upper ocean. This information is critical for our understanding of biogeochemical oceanic processes such as phytoplankton community dynamics, carbon exchanges and ecosystem responses to disturbances.

Remote sensing ocean colour algorithms are also based on the measurement of parameters of Apparent optical properties (AOPs) such as Attenuation coefficients (K_d) as well as Remote sensing reflectance (R_{rs}).

Calibration and validation of satellite observations are essential to ensure that processing methods accurately account for atmospheric and environmental effects, in order to have valid data for calibration/validation it is necessary to measure the light field both above and in the water column.

To determine Rrs in a non-invasive manner that can be used in sensor validation, automated above-water hyperspectral radiometers can be mounted to a moving platform such as a research vessel to collect continuous spectral data while the ship is at sea. Ships can provide a suitable platform to collect spatially diverse data for regional validation purposes. The continuous spectral acquisition along the ships track enables spatial resampling to match the satellite footprint.

In order to determine the water leaving Rrs above the sea surface the Marine Institute currently have 1 x hyperspectral cosine irradiance hyperspectral meter that measures the incoming solar radiation/downwelling spectral plane irradiance incident onto the sea surface, 4x hyperspectral radiance meters with a field of view of 7° in air, that measure the radiance emanating from the sea surface and the sky, L_{sf}, L_{sky} (θ , Φ , λ), respectively. A frame is designed by the Trios Ramses to hold the irradiance meter facing upward and the sky and surface radiance meters at zenith angles $\theta = 45^\circ$ and 135° . The sensor set up currently on the RV Celtic Explorer is mounted on the port and starboard side of the vessel on monkey island. The five sensor set up is required because the sensors are collecting data continuously while the ship is at sea therefore would encounter a lot of issues such as sun glint, ships shadow and foam reflected glint therefore being able to switch between sides is the most effective way of getting reliable data.

Acceptance:

Radiance sensors on the Celtic Explorer: SAM_8504, SAM_860D, SAM_86C2 and SAM_86C1

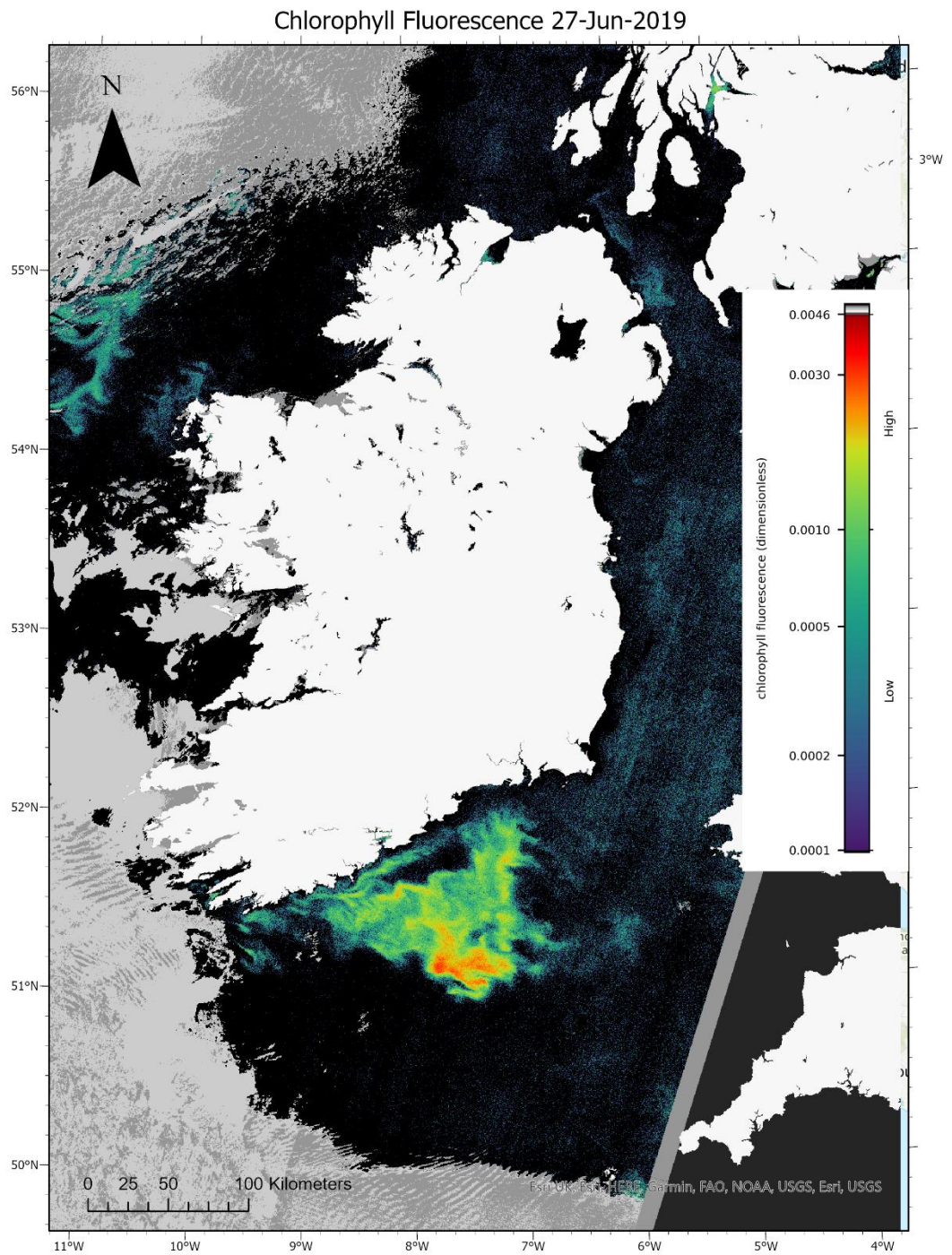
Irradiance sensor on the Celtic Explorer: SAM_8503

In order to calculate reflectance two radiance and one irradiance sensor data is required.

The complete set up of five sensors ensures approximately 60-70% useable data from the full length of a scientific survey. Data from only three sensors will amount to approximately 20-30% useable data due to the unavoidable conditions such as sunglint and ships shadow.

All Data must include: Date|Time, IDData, Device, DataType (Raw/Calibrated), Latitude|Longitude (if GPS fails during a survey, use underway data to match up location)

Appendix A5. Daily RBD image for the 27th June 2019.



Appendix A6. Full Species count lists for Cork, Oysterhaven and Kinsale

Date	Cork	Species	Cells/L		
04/08/2019	Cobh (CK-CH-CH)	Armoured dinoflagellate	560		
		Chaetoceros (Hyalochaete) spp.	1840		
		Cylindrotheca closterium/ Nitzschia longissima	12200		
		Detonula confervacea	20920		
		Dinophysis acuminata	600		
		Dinophysis acuta	400		
		<i>Karenia mikimotoi</i>	12960		
		Leptocylindrus minimus	18440		
		Oxyrrhis spp.	400		
		Prorocentrum micans	680		
		Prorocentrum triestinum	720		
		Rhizosolenia spp.	2840		
		Rhizosolenia styliformis	680		
		Scrippsiella spp.	480		
		Thalassiosira nordenskiöldii	600		
		Thalassiosira spp.	560		
		Tintinnids	920		
		Tripos furca	160		
		11/08/2019	Cobh (CK-CH-CH)	Amphiprora spp.	2680
				Chaetoceros (Hyalochaete) spp.	72384
Dinophysis acuminata	80				
Dinophysis acuta	80				
<i>Karenia mikimotoi</i>	868770				
Leptocylindrus minimus	1563786				
Oxyrrhis spp.	480				
Pleurosigma sp	1400				
Prorocentrum micans	480				
Prorocentrum triestinum	92568				
Protoperidinium spp.	160				
Rhizosolenia spp.	640				
Rhizosolenia styliformis	160				
Scrippsiella spp.	5320				
Scrippsiella trochoidea	4280				
Thalassiosira rotula/gravida	2280				
Tripos furca	120				
18/08/2019	Cobh (CK-CH-CH)	Alexandrium spp.	2240		
		Amphidinium spp.	40		

	Armoured dinoflagellate	1520
	Centric diatom	320
	Ceratium spp.	40
	Ciliates	280
	Cylindrotheca closterium/ Nitzschia longissima	73776
	Dinophysis acuminata	120
	Diplopsalis spp.	640
	Gyrodinium spirale	40
	Heterocapsa triquetra	40
	<i>Karenia mikimotoi</i>	200
	Lauderia / Detonula sp	160
	Leptocylindrus danicus	2160
	Leptocylindrus minimus	1312808
	Mesodinium rubrum	800
	Naked dinoflagellate	1520
	Nematodinium spp.	80
	Paralia sp.	1000
	Pennate diatom	200
	Pleurosigma/Gyrosigma	480
	Polykrikos spp.	440
	Prorocentrum balticum/minimum	40
	Prorocentrum micans	280
	Prorocentrum spp.	53592
	Protoperdinium spp.	80
	Pseudo-nitzschia seriata complex	280
	Rhizosolenia spp.	1040
	Scrippsiella spp.	88392
	Tintinnids	40
Cobh (CK- 25/08/2019 CH-CH)	Asterionellopsis glacialis	23880
	Ceratium fusus	40
	Ceratium tripos	80
	Ciliates	1800
	Dinobryon spp.	120
	<i>Karenia mikimotoi</i>	120
	Leptocylindrus minimus	36640
	Prorocentrum micans	280
	Pseudo-nitzschia seriata complex	4640
	Scrippsiella trochoidea	960
	Skeletonema costatum	8200
	Thalassiosira rotula/gravida	560
	Tintinnids	2880

Date	Oysterhaven	Species	Cells/L
02/06/2019	Oysterhaven (CK-ON-ON)	Amphiprora spp.	560

	Ciliates	1680
	Coscinodiscus radiatus	160
	Heterocapsa triquetra	680
	<i>Karenia mikimotoi</i>	120
	Leptocylindrus danicus	16880
	Leptocylindrus minimus	6280
	Licmophora spp.	3280
	Pennate diatom	4160
	Pseudo-nitzschia seriata complex	1880
	Skeletonema costatum	8160
	Skeletonema spp.	7080
	Tintinnids	480
16/06/2019	Oysterhaven (CK-ON-ON)	
	Alexandrium spp.	80
	Armoured dinoflagellate	440
	Azadinium/heterocapsa spp.	440
	Cerataulina spp.	1360
	Ceratium fusus	320
	Coccolithophorids	160
	Cylindrotheca closterium/ Nitzschia longissima	960
	Dinophysis acuminata	40
	Dinophysis acuta	200
	Gyrodinium lachryma	560
	<i>Karenia mikimotoi</i>	2160
	Leptocylindrus minimus	5400
	Licmophora spp.	2560
	Phalacroma rotundatum	80
	Protopteridinium spp.	80
	Pseudo-nitzschia seriata complex	4920
	Scrippsiella trochoidea	480
	Tripos lineatus	2200
30/06/2019	Oysterhaven (CK-ON-ON)	
	Armoured dinoflagellate	1240
	Ceratium fusus	160
	Chaetoceros (Hyalochaete) spp.	5640
	Dinophysis acuminata	480
	Dinophysis acuta	680
	Gyrodinium lachryma	2680
	Heterocapsa spp.	4200
	Heterocapsa triquetra	1280
	<i>Karenia mikimotoi</i>	71688
	Oxyrrhis spp.	2080
	Paralia sulcata	1880
	Phalacroma rotundatum	120
	Polykrikos kofoidii	3760
	Prymnesiophytes	164952

	Scrippsiella spp.	2240
	Scrippsiella trochoidea	3480
	Thalassiosira rotula/gravida	600
Oysterhaven (CK-ON-07/07/2019 ON)	Armoured dinoflagellate	4320
	Dinophysis acuminata	600
	Dinophysis acuta	560
	Euglena/Eutreptiella spp.	3880
	Gymnodinium spp.	4160
	Gyrodinium lachryma	1880
	Heterocapsa spp.	1080
	Heterocapsa triquetra	560
	<i>Karenia mikimotoi</i>	70992
	<i>Karenia</i> spp.	6280
	Microcystis (colony)	120
	Navicula spp.	680
	Noctiluca scintillans	80
	Paralia sp.	2240
	Paralia sulcata	4080
	Phalacroma rotundatum	80
	Protoperidinium spp.	200
	Rhizosolenia setigera	400
	Rhizosolenia spp.	600
	Skeletonema spp.	122496
	Striatella unipunctata	3320
	Thalassiosira rotula/gravida	5480
	Thalassiosira spp.	178872
	Tripos furca	1520
	Tripos lineatus	2920
Oysterhaven (CK-ON-14/07/2019 ON)	Akashiwo sanguinea	280
	Armoured dinoflagellate	5000
	Azadinium/heterocapsa spp.	4880
	Cerataulina spp.	2560
	Ceratium trichoceros	80
	Cylindrotheca closterium/ Nitzschia longissima	87000
	Dinophysis acuminata	80
	Dinophysis acuta	400
	Euglena/Eutreptiella spp.	96744
	Heterocapsa spp.	12720
	<i>Karenia mikimotoi</i>	255432
	Navicula spp.	3520
	Paralia sp.	9480
	Paralia sulcata	8280
	Polykrikos kofoidii	4960
	Prorocentrum micans	2960

	Protopteridinium quinquecorne	41040
	Protopteridinium spp.	1360
	Rhizosolenia spp.	4320
	Rhizosolenia styliformis	3520
	Striatella unipunctata	8640
	Tintinnids	8760
Oysterhaven (CK-ON- 21/07/2019 ON)	Actinoptychus spp.	760
	Ceratium fusus	1360
	Chaetoceros (Hyalochaete) spp.	14440
	Chaetoceros affinis	18280
	Coscinodiscus centralis	200
	Coscinodiscus granii	80
	Coscinodiscus spp.	120
	Dinophysis acuminata	2560
	Dinophysis acuta	1280
	Favella ehrenbergii	160
	Gyrodinium lachryma	1240
	Gyrodinium spirale	200
	Gyrodinium spp.	880
	<i>Karenia mikimotoi</i>	240
	<i>Karenia</i> spp.	160
	Noctiluca scintillans	200
	Oxyrrhis spp.	640
	Paralia sulcata	280
	Phalacroma rotundatum	80
	Prorocentrum micans	15240
	Protopteridinium spp.	400
	Pseudo-nitzschia seriata complex	4200
	Rhizosolenia spp.	9640
	Rhizosolenia styliformis	4200
	Scrippsiella spp.	840
	Scrippsiella trochoidea	760
	Thalassiosira rotula/gravida	480
	Tintinnids	1200
	Tripos furca	3920
	Tripos lineatus	2360
	Tripos longipes	240
Oysterhaven (CK-ON- 28/07/2019 ON)	Ceratium fusus	160
	Dinophysis acuminata	320
	Dinophysis acuta	80
	Leptocylindrus minimus	153036
	Prorocentrum micans	2760
	Protopteridinium quinquecorne	160
	Protopteridinium spp.	200
	Pseudo-nitzschia seriata complex	2680

	Rhizosolenia setigera	1040
	Rhizosolenia spp.	3880
	Tintinnids	55440
	Tripos furca	480
Oysterhaven (CK-ON- 04/08/2019 ON)	Armoured dinoflagellate	3880
	Azadinium/heterocapsa spp.	480
	Ceratium fusus	200
	Ciliates	2240
	Cylindrotheca closterium/ Nitzschia longissima	7520
	Dinophysis acuminata	120
	Heterocapsa triquetra	1160
	<i>Karenia mikimotoi</i>	3360
	Leptocylindrus minimus	24440
	Navicula spp.	1760
	Noctiluca scintillans	200
	Odontella spp.	14640
	Paralia sp.	4280
	Paralia sulcata	8760
	Phalacroma rotundatum	80
	Prorocentrum micans	1200
	Proto-peridinium quinquecorne	20640
	Pseudo-nitzschia seriata complex	8560
	Scrippsiella spp.	4960
	Scrippsiella trochoidea	3640
	Striatella unipunctata	640
	Tintinnids	2240
	Tripos furca	240
	Tripos lineatus	160
Oysterhaven (CK-ON- 11/08/2019 ON)	Amphiprora spp.	1200
	Ciliates	1680
	Detonula sp.	218544
	Euglena/Eutreptiella spp.	5680
	Gymnodinium spp.	1280
	<i>Karenia mikimotoi</i>	1640
	<i>Karenia</i> spp.	680
	Katodinium spp.	600
	Leptocylindrus minimus	117624
	Licmophora spp.	3600
	Navicula spp.	16200
	Paralia sulcata	1320
	Pennate diatom	16760
	Prorocentrum micans	1880
	Pseudo-nitzschia seriata complex	6920
	Rhizosolenia setigera	160

	Rhizosolenia spp.	880
	Scrippsiella spp.	2880
	Scrippsiella trochoidea	3200
	Skeletonema spp.	13084
Oysterhaven (CK-ON- 25/08/2019 ON)	Ciliates	1040
	Lauderia / Detonula sp	178872
	Leptocylindrus danicus	72384
	Leptocylindrus minimus	297192
	Prasinophytes	70296
	Prorocentrum micans	80
	Protoperidinium quinquecorne	200
	Pseudo-nitzschia delicatissima complex	22920
	Pseudo-nitzschia seriata complex	16240
	Rhizosolenia setigera	600
	Rhizosolenia spp.	1080
	Scrippsiella spp.	3680
	Scrippsiella trochoidea	960
	Striatella unipunctata	120
	Thalassiosira nordenskiöldii	7520
	Thalassiosira rotula/gravida	680
	Thalassiosira spp.	5280
	Tintinnids	2040

Date	Sampling location	Species	Cells/L
02/06/2019	Kinsale Bridge (CK- KE-KB)	Actinoptychus spp.	Present
		Armoured dinoflagellate	Present
		Azadinium/heterocapsa spp.	440
		Chaetoceros (Hyalochaete) spp.	Present
		Chaetoceros curvisetus	Present
		Chaetoceros debilis	Present
		Chaetoceros socialis	Present
		Dinophysis acuminata	160
		Dinophysis acuta	120
		Gonyaulax spp.	Present
		Gonyaulax verior	Present
		Gyrodinium lachryma	Present
		Haptophytes	Present
		Heterocapsa triquetra	Present
		<i>Karenia mikimotoi</i>	160
		Lauderia / Detonula sp	Present
		Navicula spp.	Present
		Nitzschia spp.	Present
		Protoperidinium spp.	280

	Prymnesiophytes	Present
	Pseudo-nitzschia seriata complex	1880
	Scrippsiella spp.	Present
	Scrippsiella trochoidea	Present
	Skeletonema costatum	Present
	Skeletonema spp.	Present
	Thalassiosira nordenskiöldii	Present
	Thalassiosira spp.	Present
	Tintinnids	Present
Kinsale Bridge (CK- 16/06/2019 KE-KB)	Alexandrium spp.	400
	Armoured dinoflagellate	Present
	Azadinium/heterocapsa spp.	680
	Centric diatom	Present
	Ceratium fusus	Present
	Chaetoceros (Hyalochaete) spp.	Present
	Chaetoceros curvisetus	Present
	Chaetoceros debilis	Present
	Chaetoceros socialis	Present
	Dinophysis acuminata	400
	Dinophysis acuta	200
	Guinardia flaccida	Present
	Gyrodinium lachryma	Present
	<i>Karenia mikimotoi</i>	22760
	Mesodinium rubrum	Present
	Navicula spp.	Present
	Phalacrocoma rotundatum	40
	Prorocentrum micans	Present
	Protoperidinium bipes	240
	Protoperidinium spp.	1840
	Scrippsiella spp.	Present
	Scrippsiella trochoidea	Present
	Thalassiosira anguste-lineata	Present
	Thalassiosira rotula/gravida	Present
	Thalassiosira spp.	Present
	Tintinnids	Present
	Tripos furca	Present
Kinsale Bridge (CK- 23/06/2019 KE-KB)	Amphidinium spp.	120
	Azadinium/heterocapsa spp.	1160
	Ceratium horridum	Present
	Chaetoceros socialis	Present
	Dinophysis acuminata	160
	Dinophysis acuta	840
	Gyrodinium britannicum	Present
	Gyrodinium fusiforme	Present
	Gyrodinium lachryma	Present

	Gyrodinium spirale	6040
	Heterocapsa spp.	10760
	<i>Karenia mikimotoi</i>	5320
	Phalacroma rotundatum	80
	Pleurosigma angulatum	Present
	Pleurosigma sp	Present
	Prorocentrum micans	Present
	Prorocentrum triestinum	Present
	Protoperidinium brevipes	600
	Protoperidinium marie-lebouriae	280
	Protoperidinium spp.	280
	Pseudo-nitzschia seriata complex	3720
	Scrippsiella spp.	Present
	Scrippsiella trochoidea	Present
	Thalassiosira nordenskiöldii	Present
	Thalassiosira rotula/gravida	Present
	Torodinium robustum	Present
Kinsale Bridge (CK- 30/06/2019 KE-KB)	Actinoptychus spp.	Present
	Alexandrium spp.	320
	Ceratium fusus	Present
	Cylindrotheca closterium/ Nitzschia longissima	Present
	Dinophysis acuminata	160
	Dinophysis acuta	1240
	Gyrodinium lachryma	Present
	Gyrodinium spirale	2080
	Heterocapsa spp.	600
	Heterocapsa triquetra	Present
	<i>Karenia mikimotoi</i>	31320
	Leptocylindrus minimus	Present
	Noctiluca scintillans	80
	Oxyrrhis spp.	Present
	Pennate diatom	Present
	Phalacroma rotundatum	80
	Pleurosigma sp	Present
	Polykrikos kofoidii	Present
	Protoperidinium spp.	1080
	Scrippsiella spp.	Present
	Scrippsiella trochoidea	Present
	Skeletonema costatum	Present
	Skeletonema spp.	Present
Kinsale Bridge (CK- 14/07/2019 KE-KB)	Alexandrium spp.	280
	Armoured dinoflagellate	Present
	Azadinium/heterocapsa spp.	600
	Cerataulina pelagica	Present

	Coscinodiscus granii	Present	
	Dinophysis acuminata	2560	
	Dinophysis acuta	360	
	Dinophysis spp.	440	
	Gyrodinium lachryma	Present	
	Heterocapsa spp.	6200	
	<i>Karenia mikimotoi</i>	70902	
	Prorocentrum micans	Present	
	Protoperidinium quinquecorne	2160	
	Protoperidinium spp.	1040	
	Pseudo-nitzschia delicatissima complex	11760	
	Pseudo-nitzschia seriata complex	5160	
	Scrippsiella spp.	Present	
	Scrippsiella trochoidea	Present	
	Thalassiosira rotula/gravida	Present	
	Tintinnids	Present	
	Tripos furca	Present	
Kinsale Bridge (CK- 21/07/2019 KE-KB)	Ceratium fusus	Present	
	Dictyocha fibula	160	
	Dinophysis acuminata	160	
	Dinophysis acuta	160	
	Diploneis spp.	Present	
	<i>Karenia mikimotoi</i>	400	
	<i>Karenia</i> spp.	80	
	Licmophora spp.	Present	
	Melosira spp.	Present	
	Navicula spp.	Present	
	Plagiogrammopsis spp.	Present	
	Pleurosigma angulatum	Present	
	Pleurosigma sp	Present	
	Protoperidinium depressum	80	
	Pseudo-nitzschia delicatissima complex	2400	
	Striatella unipunctata	Present	
	Tripos furca	Present	
	Kinsale Bridge (CK- 28/07/2019 KE-KB)	Akashiwo sanguinea	80
		Ceratium fusus	Present
		Dinophysis acuminata	560
Dinophysis acuta		520	
Eucampia zodiacus		Present	
Guinardia delicatula		Present	
<i>Karenia mikimotoi</i>		398736	
Leptocylindrus danicus		Present	
Leptocylindrus minimus		Present	
Navicula spp.		Present	
Noctiluca scintillans		200	

	Prorocentrum micans	Present
	Protoperidinium spp.	160
	Rhizosolenia spp.	Present
	Thalassiosira rotula/gravida	Present
	Tintinnids	Present
	Tripos furca	Present
	Tripos lineatus	Present
Kinsale Bridge (CK-04/08/2019 KE-KB)	Actinoptychus spp.	Present
	Akashiwo sanguinea	680
	Bacillaria paxillifera	Present
	Dinophysis acuta	80
	Euglena/Eutreptiella spp.	Present
	Guinardia flaccida	Present
	Navicula spp.	Present
	Noctiluca scintillans	920
	Prorocentrum micans	Present
	Prorocentrum triestinum	Present
	Protoperidinium spp.	160
	Thalassiosira rotula/gravida	Present
	Tripos furca	Present
	Tripos lineatus	Present
	Tripos macroceros	Present
Kinsale Bridge (CK-11/08/2019 KE-KB)	Akashiwo sanguinea	30040
	Alexandrium spp.	3480
	Armoured dinoflagellate	Present
	Ciliates	Present
	Coscinodiscus centralis	Present
	Coscinodiscus spp.	Present
	Dactyliosolen fragilissimus	Present
	Dinophysis acuminata	80
	Euglena/Eutreptiella spp.	Present
	Guinardia flaccida	Present
	Gymnodinium spp.	Present
	Gyrodinium lachryma	Present
	Heterocapsa triquetra	Present
	<i>Karenia mikimotoi</i>	2440
	Navicula spp.	Present
	Noctiluca scintillans	40
	Paralia sp.	Present
	Paralia sulcata	Present
	Pennate diatom	Present
	Prorocentrum micans	Present
	Prorocentrum triestinum	Present
	Protoperidinium spp.	440
	Prymnesiophytes	Present

	Scrippsiella spp.	Present
	Scrippsiella trochoidea	Present
	Thalassiosira rotula/gravida	Present
	Tintinnids	Present
	Tripos furca	Present
Kinsale Bridge (CK- 18/08/2019 KE-KB)	Alexandrium spp.	880
	Armoured dinoflagellate	Present
	Cylindrotheca closterium/ Nitzschia longissima	Present
	Dactyliosolen fragilissimus	Present
	Diplopsalis spp.	Present
	Heterocapsa triquetra	Present
	Lauderia / Detonula sp	Present
	Leptocylindrus minimus	Present
	Mesodinium rubrum	Present
	Paralia sp.	Present
	Pennate diatom	Present
	Pleurosigma/Gyrosigma	Present
	Polykrikos spp.	Present
	Protoperidinium spp.	40
	Pseudo-nitzschia seriata complex	280
	Rhizosolenia spp.	Present
	Scrippsiella spp.	Present
	Skeletonema spp.	Present
	Striatella spp.	Present
Kinsale Bridge (CK- 25/08/2019 KE-KB)	Actinoptychus spp.	Present
	Alexandrium spp.	2200
	Armoured dinoflagellate	Present
	Detonula confervacea	Present
	Lauderia / Detonula sp	Present
	Leptocylindrus minimus	Present
	Odontella spp.	Present
	Plagiogrammopsis spp.	Present
	Pleurosigma angulatum	Present
	Pseudo-nitzschia delicatissima complex	1760
	Pseudo-nitzschia seriata complex	720
	Scrippsiella spp.	Present
	Scrippsiella trochoidea	Present
	Skeletonema costatum	Present

Date	Cork Harbour <i>Karenia</i> cells/L	Oysterhaven <i>Karenia</i> cells/L	Kinsale <i>Karenia</i> cells/L
02/06/2019	0	120	160
16/06/2019	0	2160	22760
23/06/2019	13840	0	5320
30/06/2019	2471168	71688	31320
07/07/2019	760	70992	0
14/07/2019	117234	255432	70902
21/07/2019	0	240	400
28/07/2019	257634	0	398736
04/08/2019	12960	3360	0
11/08/2019	868770	1640	2440
18/08/2019	200	0	0
25/08/2019	120	0	0

Appendix A7. Phytoplankton counts from CV19018

Counts of individuals per 1/2 base scanning	Column n1	Column n2	Column n3	Column n4	Column n5	Column n6	Column n7	(1T) = 1 transect	Column n8	1T x 2000 = Cells per litre	Column n9	Column n10	Column n11	Column n12	Column n13	Column n14	
Station	Date	Depth (m)	Sample (ml)	<i>Karenia</i>	<i>C. lineatum</i>	<i>C. furca</i>	<i>C. fusus</i>	<i>C. tripos</i>	<i>C. macroceros</i>	<i>C. inflatum</i>	Noctiluca	Protoperidinium	Prorocentrum	<i>D. acuta</i>	<i>D. tripos</i>	<i>D. acuminata</i>	<i>Gyrodinium spirale</i>
136	N/A																
137	N/A																
138	10/07/2019	11	10	533	1	2	0	0	0	1	0	4	33	51	0	4	0
		12	11.5	7953	1	9	14	0	1	7	5	5	15	51	0	42	46
		15	10	4062	10	1	21	0	2	6	3	7	9	22	0	1	21
		17	11.5	4232	10	1	34	0	1	5	1	4	17	33	1	1	15
139	10/07/2019	5	10	254	2	3	2	0	0	0	0	3	99	9	0	6	4
		10	10	260	1	4	0	0	0	0	1	3	25	14	0	2	9
		13	11.5	321(1T)	12	6	1	0	0	5	3	12	30	28	0	33	83
		14	11.5	316(1T)	24	1	5	0	0	1	5	5	12	40	1	75	151

		15	10	40 3(1 T)	27	5	10	0	1	8	10	8	19	68	0	51	210
		18	10	34 0	14	0	51	2	0	11	3	4	23	9	0	3	12
140	10/0 7/20 19	8	11.5	10	0	4	4	0	0	1	1	1	48	3	0	4	4
		14	11.5	11 2	5	1	4	1	2	1	3	4	17	20	0	11	10
		18	10	21 7	3	3	6	0	3	4	5	2	7	26	0	12	16
		23	10	36 2	13	0	17	1	3	25	6	1	12	14	0	2	38
		25	11.5	52 1	11	3	3	0	0	1	2	4	12	6	0	11	26
141	10/0 7/20 19	7	11.5	21	0	5	1	0	0	1	1	6	14	4	1	0	1
		9.8	10	6	0	5	3	0	0	1	1	0	1	2	0	1	6
		16	11.5	6	0	1	2	2	0	0	2	0	17	2	0	1	1
		24	11.5	41	0	3	1	1	0	0	9	1	0	3	0	0	10
142	10/0 7/20 19	14. 75	10	9	0	4	1	1	0	0	0	1	3	5	0	0	7
		17. 84	10	14	1	1	0	1	1	0	1	0	3	49	0	1	21
		21. 55	10	21	3	2	4	1	0	1	2	0	5	3	0	1	7
		28. 81	11.5	11 5	0	6	5	0	0	3	2	2	11	0	0	1	5

		48. 86	11.5	2	0	1	0	0	0	0	0	0	1	1	0	0	0	2
143	10/0 7/20 19	10. 6	11.5	22	1	2	0	2	0	0	0	0	0	3	0	0	1	9
		14. 5	11.5	44	21	4	0	2	0	0	2	1	1	4	0	1	8	
		30. 48	10	17 8	4	4	3	0	1	1	2	0	9	2	0	3	19	
		45. 01	10	4	0	2	0	0	0	0	0	0	2	1	0	0	3	
144	10/0 7/20 19	9.4 5	10	30	0	8	0	1	0	0	1	0	4	4	0	0	11	
		14. 9	10	63	0	3	0	0	0	0	0	0	1	5	0	1	3	
		19. 3	11.5	0	0	1	0	0	0	0	0	0	2	10	0	0	0	
		25. 88	11.5	29	10	3	7	0	0	1	0	0	0	0	0	3	21	
		35. 7	10	62	21	1	1	0	0	0	0	1	1	0	0	3	29	
148	10/0 7/20 19	10. 3	10	96 4	7	3	3	0	1	0	3	13	14	28	0	3	35	
		13. 29	11.5	95 0	9	6	7	1	2	4	4	7	36	34	0	7	24	
		16. 72	11.5	85 5(1 T)	21	3	10	0	0	2	5	6	20	161	0	29	47	

		18. 51	10	82 2(1 T)	11	1	16	2	2	4	1	12	19	25	0	134	45
		20. 41	10	60 3(1 T)	6	2	30	1	7	19	9	6	10	44	0	65	24
		24. 81	11.5	39 6(1 T)	5	3	12	1	0	7	1	2	9	6	0	6	6
		35. 2	11.5	59 8	4	5	6	0	0	0	3	1	19	5	0	0	2
FSS-6		1	10	15 73(1T)	35	9	23	3	5	24	23	15	52	189	0	36	4
		2	11.5	21 29(1T)	57	14	37	3	9	28	21	16	69	267	1	21	5
		3	11.5	19 21	50	10	42	4	12	27	19	15	56	217	0	14	8
		4	11.5	16 38	42	11	47	2	8	25	17	15	52	211	0	20	10
		5	10	12 37	22	10	40	1	12	25	12	11	76	206	0	10	7

Counts in cells per litre (individual counts x200)	136 and																	
	Co lu mn 1	Co lu m n2	Co lum n3	Co lu m n4	137 totals not taken	Co lu m n5	Co lu m n6	Co lu m n7	(1T) = 1 tran sect	Co lu mn 8	1T x 2000 = Cells per litre	Colu mn9	Col um n10	Co lu mn 11	Co lu mn 12	Col um n13	Colu mn14	
Station	Date	Depth (m)	Sample (ml)	Karenia	C. lineatum	C. furca	C. fusus	C. tripos	C. maceros	C. inflatum	Noctiluca	Protooperidium	Prorocentrum	D. acuta	D. tripos	D. acuminata	Gyrodinium spirale	
136	N/A																	
137	N/A																	
138	10/07/2019	11	10	106,600	200	400	0	0	0	200	0	800	6,600	10,200	0	800	0	
		12	10	1,590,600	200	1,800	2,800	0	200	1,400	1,000	1,000	3,000	10,200	0	8,400	9,200	
		15	10	812,400	2,000	200	4,200	0	400	1,200	600	1,400	1,800	4,400	0	200	4,200	
		17	10	846,400	2,000	200	6,800	0	200	1,000	200	800	3,400	6,600	200	200	3,000	
139	10/07/2019	5	10	50,800	400	600	400	0	0	0	0	600	19,800	1,800	0	1,200	800	

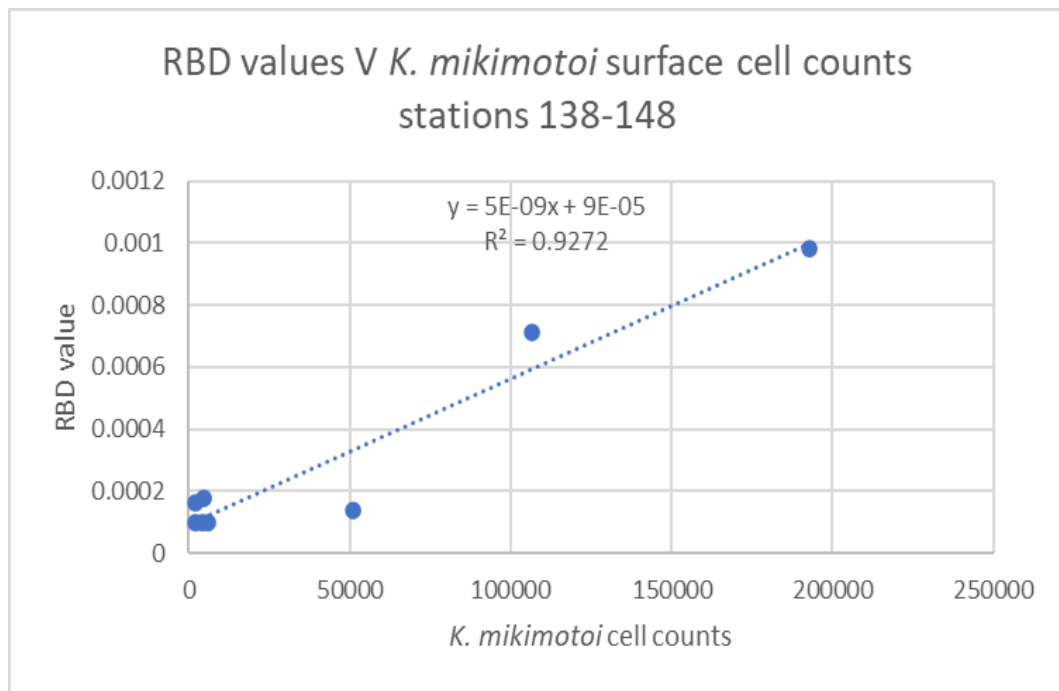
		10	10	52,00	200	800	0	0	0	0	200	600	5,000	2,800	0	400	1,800
		13	11.5	64,200	2,400	1,200	200	0	0	1,000	600	2,400	6,000	5,600	0	6,600	16,600
		14	11.5	63,200	4,800	200	1,000	0	0	200	1,000	1,000	2,400	8,000	200	1,500	30,200
		15	10	80,600	5,400	1,000	2,000	0	200	1,600	2,000	1,600	1,800	13,600	0	10,200	42,000
		18	10	68,000	2,800	0	10,200	400	0	2,200	600	800	4,600	1,800	0	600	2,400
140	10/07/2019	8	11.5	2,000	0	800	800	0	0	200	200	200	9,600	600	0	800	800
		14	11.5	22,400	1,000	200	800	200	400	200	600	800	3,400	4,000	0	2,200	2,000
		18	10	43,400	600	600	1,200	0	600	800	1,000	400	1,400	5,200	0	2,400	3,200
		23	10	72,400	2,600	0	3,400	200	600	5,000	1,200	200	2,400	2,800	0	400	7,600
		25	11.5	104,200	2,200	600	600	0	0	200	400	800	2,400	1,200	0	2,200	5,200

141	10/07/2019	7	11.5	4,200	0	1,000	200	0	0	200	200	1,200	2,800	800	200	0	200
		9.8	10	1,200	0	1,000	600	0	0	200	0	200	0	200	0	200	1,200
		16	11.5	1,200	0	200	400	400	0	0	400	0	3,400	400	0	200	200
		24	11.5	8,200	0	600	200	200	0	0	1,800	200	0	600	0	0	2,000
142	10/07/2019	14.75	10	1,800	0	800	200	200	0	0	0	200	600	1,000	0	0	1,400
		17.84	10	2,800	200	200	0	200	200	0	200	0	600	9,800	0	200	4,200
		21.55	10	4,200	600	400	800	200	0	200	400	0	1,000	600	0	200	1,400
		28.81	11.5	23,000	0	1,200	1,000	0	0	600	400	400	2,200	0	0	200	1,000
		48.86	11.5	400	0	200	0	0	0	0	0	200	200	0	0	0	400
143	10/07/2019	10.6	11.5	4,400	200	400	0	400	0	0	0	0	600	0	0	200	1,800
		14.5	11.5	8,800	4,200	800	0	400	0	0	400	200	200	400	0	200	1,600
		30.48	10	35,600	800	800	600	0	200	200	400	0	1,800	400	0	600	3,800

		45.01	10	800	0	400	0	0	0	0	0	0	0	400	200	0	0	600	
144	10/07/2019	9.45	10	6,000	0	1,600	0	200	0	0	0	200	0	800	800	0	0	2,200	
		14.9	10	12,600	0	600	0	0	0	0	0	0	0	200	1,000	0	200	600	
		19.3	11.5	0	0	200	0	0	0	0	0	0	0	400	2,000	0	0	0	
		25.88	11.5	5,800	2,000	600	1,400	0	0	0	200	0	0	0	0	0	0	600	4,200
		35.7	10	12,400	4,200	200	200	0	0	0	0	0	200	200	0	0	600	5,800	
148	10/07/2019	10.3	10	19,280	1,400	600	600	0	200	0	600	2,600	2,800	5,600	0	0	600	7,000	
		13.29	11.5	19,000	1,800	1,200	1,400	200	400	800	800	1,400	7,200	6,800	0	0	1,400	4,800	
		16.72	11.5	1,710,000	4,200	600	2,000	0	0	400	1,000	1,200	4,000	32,200	0	0	5,800	9,400	
		18.51	10	1,644,000	2,200	200	3,200	400	400	800	200	2,400	3,800	5,000	0	0	26,800	9,000	

		20.41	10	1,206,000	1,200	400	6,000	200	1,400	3,800	1,800	1,800	2,000	8,800	0	13,000	4,800
		24.81	11.5	792,000	1,000	600	2,400	200	0	1,400	200	400	1,800	1,200	0	1,200	800
		35.2	11.5	1,196,000	800	1,000	1,200	0	0	0	600	200	3,800	1,000	0	0	400
FSS-6	10/07/2019	1	10	3,146,000	70,000	18,000	46,000	6,000	10,000	48,000	46,000	30,000	104,000	37,800	0	72,000	8000
148		2	11.5	4,258,000	114,000	28,000	74,000	6,000	18,000	56,000	42,000	32,000	138,000	53,400	20,000	42,000	10000
		3	11.5	3,842,000	100,000	20,000	84,000	8,000	24,000	54,000	38,000	30,000	112,000	43,400	0	28,000	16,000
		4	11.5	3,276,000	84,000	22,000	94,000	4,000	16,000	50,000	34,000	30,000	104,000	42,200	0	40,000	20,000
		5	10	2,474,000	44,000	20,000	80,000	2,000	24,000	50,000	240,000	22,000	152,000	41,200	0	20,000	14,000

Appendix A8. RBD values V Surface Cell counts



Station	<i>K. mikimotoi</i> in situ cell concentration cells/L	RBD satellite value
138	106600	0.000713
139	50800	0.00014
140	2000	0.0001
141	4200	0.0001
142	1800	0.000161
143	4400	0.000179
144	6000	0.0001
148	192800	0.000985

Appendix A9. HABscope conversion chart

Cells: 0 = 50000 c/L Cells: 1 = 120000 c/L Cells: 2 = 590000 c/L Cells: 3 = 642000 c/L Cells: 4 = 694000 c/L Cells: 5 = 698000 c/L Cells: 6 = 703000 c/L Cells: 7 = 1055000 c/L Cells: 8 = 1103000 c/L Cells: 9 = 1151000 c/L Cells: 10 = 1868000 c/L Cells: 11 = 1936000 c/L Cells: 12 = 2004000 c/L Cells: 13 = 2072000 c/L Cells: 14 = 2258000 c/L Cells: 15 = 2444000 c/L Cells: 16 = 2631000 c/L Cells: 17 = 2817000 c/L Cells: 18 = 3004000 c/L Cells: 19 = 3190000 c/L Cells: 20 = 3377000 c/L Cells: 21 = 3563000 c/L Cells: 22 = 3750000 c/L Cells: 23 = 3936000 c/L Cells: 24 = 4123000 c/L Cells: 25 = 4309000 c/L Cells: 26 = 4496000 c/L Cells: 27 = 4744000 c/L Cells: 28 = 4992000 c/L Cells: 29 = 5240000 c/L Cells: 30 = 5488000 c/L Cells: 31 = 5737000 c/L Cells: 32 = 5985000 c/L Cells: 33 = 6233000 c/L Cells: 34 = 6481000 c/L Cells: 35 = 6729000 c/L Cells: 36 = 6978000 c/L Cells: 37 = 7226000 c/L Cells: 38 = 7474000 c/L Cells: 39 = 7722000 c/L Cells: 40 = 7970000 c/L Cells: 41 = 8219000 c/L Cells: 42 = 8467000 c/L Cells: 43 = 8715000 c/L Cells: 44 = 8963000 c/L Cells: 45 = 9212000 c/L Cells: 46 = 9839000 c/L Cells: 47 = 10467000 c/L Cells: 48 = 11095000 c/L Cells: 49 = 11722000 c/L Cells: 50 = 12350000 c/L Cells: 51 = 12978000 c/L Cells: 52 = 13606000 c/L Cells: 53 = 14233000 c/L Cells: 54 = 14861000 c/L Cells: 55 = 15489000 c/L Cells: 56 = 16116000 c/L Cells: 57 = 16744000 c/L Cells: 58 = 17372000 c/L Cells: 59 = 18000000 c/L Cells: 60 = 18279000 c/L Cells: 61 = 18558000 c/L Cells: 62 = 18837000 c/L Cells: 63 = 19116000 c/L Cells: 64 = 19395000 c/L Cells: 65 = 19674000 c/L Cells: 66 = 19953000 c/L Cells: 67 = 20232000 c/L Cells: 68 = 20511000 c/L Cells: 69 = 20790000 c/L Cells: 70 = 21069000 c/L Cells: 71 = 21348000 c/L Cells: 72 = 21627000 c/L Cells: 73 = 21906000 c/L Cells: 74 = 22186000 c/L Cells: 75 = 22465000 c/L Cells: 76 = 22744000 c/L Cells: 77 = 23023000 c/L Cells: 78 = 23302000 c/L Cells: 79 = 23581000 c/L Cells: 80 = 23860000 c/L Cells: 81 = 24139000 c/L Cells: 82 = 24418000 c/L Cells: 83 = 24697000 c/L Cells: 84 = 24976000 c/L Cells: 85 = 25255000 c/L Cells: 86 = 25534000 c/L Cells: 87 = 25813000 c/L Cells: 88 = 26093000 c/L Cells: 89 = 26372000 c/L Cells: 90 = 26651000 c/L Cells: 91 = 26930000 c/L Cells: 92 = 27209000 c/L Cells: 93 = 27488000 c/L Cells: 94 = 27767000 c/L Cells: 95 = 28046000 c/L Cells: 96 = 28325000 c/L Cells: 97 = 28604000 c/L Cells: 98 = 28883000 c/L Cells: 99 = 29162000 c/L Cells: 100 = 29441000 c/L Cells: 101 = 29720000 c/L Cells: 102 = 30000000 c/L Cells: 103 = 30000000 c/L Cells: 104 = 30000000 c/L Cells: 105 = 30000000 c/L Cells: 106 = 30000000 c/L Cells: 107 = 30000000 c/L Cells: 108 = 30000000 c/L Cells: 109 = 30000000 c/L Cells: 110 = 30000000 c/L

Appendix A10. Communication of PhD thesis to the public

NOAA Science Seminar June 2021

<https://noaabroadcast.adobeconnect.com/pb5txbj5895u/>

RTE brainstorm article July 2021 <https://www.rte.ie/brainstorm/2021/0726/1237300-harmful-algal-blooms-seas-oceans-satellites-algorithms/>

Marine Institute Cullen Profile 2022 <https://www.marine.ie/site-area/news-events/news/cullen-scholar-catherine-jordan>

Soapbox Science Presenter June 2019 <http://soapboxscience.org/2019/05/28/take-pride-in-your-work-meet-catherine-jordan/>

<https://www.marine.ie/site-area/news-events/news/marine-institute-and-nui-galway-phd-student-speak-soapbox-science>

April 2018 CV218012 Celtic Voyager Nephrops Larvae Survey Blog No 2

Celtic Voyager - Distribution of *Nephrops* larvae and associated oceanographic conditions http://scientistsatsea.blogspot.com/2018/04/celtic-voyager-nephrops-larvae-survey_10.html

Blog for Ocean Climate survey June 2019 <http://scientistsatsea.blogspot.com/2019/06/>

Press releases on the HABscope trial:

<https://www.marine.ie/site-area/news-events/press-releases/irish-scientists-collaborate-noaa-test-new-habscope>

<https://www.siliconrepublic.com/innovation/habscope-algal-blooms-marine-institute-nui-galway>